Numerical Simulation of Gas-Lubricated Journal Bearings for Microfabricated Machines

by

Edward Stanley Piekos

B.S.E. (Aerospace E.), University of Michigan (1992)
S.M. (Aeronautics and Astronautics), M.I.T. (1995)

Submitted to the Department of Aeronautics and Astronautics
in partial fulfillment of the requirements for the degree of

Doctor of Philosophy in Aeronautics and Astronautics

at the

MASSACHUSETTS INSTITUTE OF TECHNOLOGY

February 2000

Submitted by .....
Department of Aeronautics and Astronautics
December 16, 1999

Certified by ..... Kenneth S. Breuer
Visiting Associate Professor of Aeronautics and Astronautics

Certified by ..... Alan H. Epstein
R.C. Maclaurin Professor of Aeronautics and Astronautics

Certified by ..... Jaime Peraire
Professor of Aeronautics and Astronautics

Certified by ..... Martin A. Schmidt
Professor of Electrical Engineering

Accepted by ..... Nesbitt W. Hagood
Associate Professor of Aeronautics and Astronautics
Chairman, Department Graduate Committee

Numerical Simulation of Gas-Lubricated Journal Bearings for Microfabricated Machines

by

Edward Stanley Piekos

Submitted to the Department of Aeronautics and Astronautics
on December 16, 1999, in partial fulfillment of the
requirements for the degree of
Doctor of Philosophy in Aeronautics and Astronautics

Abstract

Numerical simulations of gas-lubricated journal bearings for microfabricated machines are performed with specialized tools. To maximize flexibility, an orbit method formulation is chosen for the primary tool. Its pseudospectral fluid equation solver enables run-time resolution adjustment while maintaining the efficiency advantage of spectral methods. A design framework is established for microfabricated bearings, including several new charts that reflect the unique constraints of MEMS. A duality between applied load and imbalance level is demonstrated and a method for experimentally determining appropriate loads for unknown imbalance is suggested. A large-amplitude whirling mode is shown to exist on both sides of the fixed-point threshold speed, in agreement with experimental observation. A quasi-static method for calculating shock tolerance is suggested and evaluated against unsteady simulations. Simulations of loads applied via noncircumferentially-uniform pressure at the bearing end are shown to increase the attitude angle and decrease the allowable nondimensional mass compared to the equivalent gravity-loaded case. Furthermore, the associated axial pressure gradients are shown to produce a hydrostatic stiffness via inertial effects. A nondimensional model is constructed for this stiffness and its dependence on various parameters is studied. It is shown that the load capacity advantage reported in the literature for noncircular bearings can be canceled by microfabrication constraints. The stability advantage, however, survives. Tapered axial clearance is shown to have an extremely deleterious effect on performance while bowed clearance proves less detrimental. Navier-Stokes solutions of infinite-length bearings with unity inertial parameters are performed using a second specially-built tool. Little change is found in the steady-state results from inertial and curvature effects in the MIT microengine's parameter space.

Thesis Supervisor: Kenneth S. Breuer
Title: Visiting Associate Professor of Aeronautics and Astronautics

Acknowledgments

This document represents the conclusion of a very long process. Consequently, I'm sure I will forget to mention someone who has helped me along the way and I offer my apologies in advance. Also, after spending a fair amount of time sweating the accuracy of my English in this document, I reserve the right to use a more conversational tone in this section.

First off, my successful negotiation of the numerous obstacles I encountered during this process can only be described as miraculous. I'm deeply indebted to the grace of God for bringing me to this point. In addition, while I tend to be interested in a wide range of things, I feel quite blessed to find myself in an area (fluids + MEMS) I still find absolutely fascinating even after many (many, many) hours of study.

Next, I certainly could not have spent this amount of time in an expensive city at an expensive school without financial support. I am therefore grateful for the resources provided by the ARO under MURI #DAAH04-95-0093, monitored by Dr. Richard Paur, and the AFOSR under grant number F49620-93-1-0376, monitored by Dr. James McMichael.

On the faculty front, I'd first like to thank my advisor Kenny Breuer for paying me to ask questions, my favorite pastime in the world, and for teaching me volumes about management. I am also indebted to him for involving me in the microengine project, which was always technically fascinating as well as intellectually and personally challenging.

On this note, the microengine project itself wouldn't exist without the creativity, determination, and fund-gathering skills of Alan Epstein. I also wish to thank him for freely offering his advice and opinion on a wide range of topics and for always having a good story to make his point memorable.

Rounding out my committee, I am deeply thankful to Jaime Peraire and Marty Schmidt for taking their time, an *extremely* precious commodity around here, to be truly helpful whenever I was in need.

I'd also like to thank a few faculty members who are not on my committee. First, I am grateful to Dave Darmofal and Earll Murman for giving me the opportunity to TA 16.100 during its redesign. I hope to never forget the lessons I learned. I am also inspired by your willingness to expend exceptional effort to ensure an enriching, and even pleasant, experience for the students. Second, I will forever be inspired by Mark Drela's deep knowledge and fascination with all things fluid, especially in relation to flight. He has also provided me with valuable pearls of wisdom on design and programming over the years.

On the non-faculty front, I am indebted to the other members of the microbearing team, and the microengine team as a whole, for broadening my horizons, both technically and personally. In particular, I'd like to thank Stu Jacobson for his extensive and very thoughtful comments on my thesis draft. It is much improved as a result of your effort. Also, I am indebted to Arturo Ayón for cheerfully providing an endless stream of SEM's as well as microfabrication wisdom; Luc Fréchette and John Protz for pictures and current information on the devices; and C.C. Lin for trying a few of my suggestions on the rig and for digging up some useful papers.

Off of the microengine team (there's still a few), I am thankful to Bob Haimes for many valuable discussions of all things computational, as well as for all the great machines to work on. I also enjoyed receiving his unrestrained opinion on a wide variety of topics. I am thankful to Jean Sofronas for helping me track down Kenny and Jaime and for providing an endless supply of supplies. Similarly, Lori Martinez was always helpful and entertaining when hunting for a piece of Alan's calendar. Also, this document wouldn't be

official (and thus I wouldn't have graduated) without the thoughtful assistance of Marie Stuppard.

I can say without reservation that MIT would not be what it is without the marvelous students it attracts. I have benefited from the knowledge and enthusiasm of a number of people, only a tiny fraction of whom are mentioned here. I am thankful to: Anj for being a great officemate and lending me all the food and music; Tolu for providing a wall to bounce ideas from, as well as for showing me scary programming tricks I hope I'm never tempted to implement; Dave for the great music, as well as warnings about JAVA; Ruben for teaching me how to make trifle and beer - and for all the long conversations over them; Christine for discussions about feminism and the outdoors and for weathering all the good-natured pokes at Canada, Ali for spiritual discussions and giving me insight into Islam not available in the U.S. media; Alex also for conversations of spirituality and for insight into all things aesthetic (and for giving me periodic updates on our house this past few weeks); Laura for lunches outside and for keeping VSG and FoodFest going when I was burned to a crisp; Errol and Kerri for wonderful Thanksgivings and an unblinking opinion; Ray for providing a comfortable couch outside my office, a goring target, and a good laugh; Graeme for good music and great stories (and, with Ray, for being an example of *not* letting this place make you tense); and T, Matt, and Anj (again) for exploration of the 'Tute's darkest corners and for various nonacademic projects.

DJ Orr is in a class by himself as coworker, friend, and long-time roommate. He deserves heartfelt thanks for all the long hours of conversation about things technical, and things not, as well as for serving as a fearless sampler of my culinary experiments. I have no doubt that any remaining sanity is largely attributable to him providing an ear and an honest opinion, especially on bearings at their deepest level when I was beginning to think I was speaking a foreign language.

Off campus, I'd like to thank Christi and Sisia for conversations about the really "big picture" topics; Jen for her patience in socializing me after so many years in the lab; Michelle, Matt, and April for the tea and laid-back attitude; the "Capetrip" crew for providing a solid foundation of friendship from which I draw much strength; and the Holly's for being like a second family.

I am thankful to the MIT SKA karate club, and Johnson Chung in particular, for keeping my mind and body in shape and in communication with each other. The opportunity to let out a little frustration in the form of an exhausting workout and a good kiai made this process bearable, not to mention all the wonderful people I met through the organization. Sandy Lett also deserves thanks for giving us a place to practice, even when I turned the forms in late.

Last, but certainly not least, I am grateful to my family for their constant love, support, and encouragement, as well as their patience during this process. In particular, I thank my mother for her insight while I was (am?) growing up and my father for expending considerable effort to be there, as well as for making it back up the hill every time in his roller-coaster ride of late. Finally, I thank my sister for being the trailblazer; I rode most of my childhood on her coattails. I love you all

"The known is finite, the unknown infinite; intellectually we stand on an islet in the midst of an illimitable ocean of inexplicability. Our business in every generation is to reclaim a little more land, to add something to the extent and solidity of our possessions."

Thomas Huxley, on the reception of *Origin of Species* (1887)

Contents

List of Figures

Nomenclature

Symbol	Description	Section
A_{nc}	noncircularity amplitude, m	4.1
C	clearance: $R_b - R$, m	1.2.1
C_{nc}	mean clearance of noncircular bearing, m	4.1
D	bearing diameter, m	1.2.3
H	channel height, m	B.4
F_{hs}	hydrostatic restoring force, N	5.2.2
F_v	viscous drag, N	3.1.2
K_∞	fully-developed axial flow incremental pressure defect	5.2.2
L	bearing length, m	1.2.1
M	Mach number	1.2.3
$\bar{M}$	dimensionless mass: $\frac{mP_a}{72L\mu^2}\left(\frac{C}{R}\right)^5$	1.2.3
P_a	ambient pressure at bearing ends, Pa	1.2.1
P_ℓ	pressure at entry length, Pa	5.2.2
P_i	axial inlet pressure, Pa	5.2.2
P_o	axial outlet pressure, Pa	5.2.2
P_H	pressure on high side of loading plenum, Pa	5.1.1
P_L	pressure on low side of loading plenum, Pa	5.1.1
$\vec{V}$	journal velocity, m/s	1.2.3
W	bearing load, N	1.2.1
R	journal radius, m	1.2.1
R_b	bearing radius, m	1.2.1
X	distance from axial flow entrance, m	5.2.2

X_ℓ	axial flow entry length, m	5.2.2
U_{ax}	axial flow speed, m/s	5.2.2
U_i	uniform axial flow inlet speed, m/s	5.2.2
$\mathcal{F}$	nondimensional friction variable: $\frac{F_v C}{2\pi\mu R^2 \omega L}$	3.1.2
$\mathcal{I}$	entry length pressure integral	5.2.2
$\mathcal{L}$	nondimensional entry length: $\frac{4\mu X_\ell}{\rho U_i H^2}$	5.2.2
$\mathcal{P}$	nondimensional pressure at entry length: $\frac{P_i - P_{\ell l}}{\frac{1}{2}\rho U_i^2}$	5.2.2
a_s	acceleration due to shock loading, $g's$	3.2.5
a_{nc}	normalized noncircularity amplitude: A_{nc}/C_{nc}	4.1
d	minimum distance between solid surfaces, m	3.2.1
d_u	distance between geometric and mass centers, m	3.2.4
e	distance between journal and bearing centers, m	1.2.1
g	gravitational acceleration, m/s^2	3.2.5
h	normalized channel height: H/C	1.2.3
k	wavenumber of trigonometric expansion	2.2.2
m	journal mass, kg	1.2.1
n	degree of Chebyshev polynomial	2.2.2
n_w	number of wave cycles	4.1
p	nondimensional pressure: $\frac{P}{P_a}$	1.2.3
$\hat{p}$	nondimensional hydrostatic correction pressure	5.2.2
r	distance from center in radial direction, m	2.1.1
t	time, s	1.2.3
u_i	normalized axial inlet flow speed: $\frac{12\mu}{C^2}\frac{L}{P_i - P_o}U_i$	5.2.2
$\hat{u}$	normalized axial flow speed: $\frac{U}{U_i}$, $1 \leq \hat{u} < 1.5$	5.2.2
$\vec{v}$	normalized journal velocity: $\frac{V}{C\omega}$	1.2.3
α	wave phase angle, rad	4.1
δ	nondimensional minimum running clearance: $\frac{d}{C}$	4.1.2
δ_u	nondimensional imbalance distance: $\frac{d_u}{C}$	3.2.4

ϵ	eccentricity ratio: $\frac{e}{C}$	1.2.1
ϵ_o	initial eccentricity when shock is applied	1.2.1
ϵ_f	final eccentricity ratio under shock load	1.2.1
Δp	nondimensional axial pressure drop: $\frac{P_i - P_o}{P_o}$	5.2.3
Λ	bearing number: $\frac{6\mu\omega}{p_a}\left(\frac{R}{C}\right)^2$	1.2.3
μ	dynamic viscosity, $Pa \cdot s$	1.2.3
ϕ	attitude angle, rad	1.2.1
ρ	fluid density, kg/m^3	1.2.3
ρ_{Si}	silicon density, kg/m^3	1.3.3
ω	rotation rate, rad/s	1.2.1
χ	inertial parameter: $\frac{\rho\omega C^2}{\mu}$	1.2.3
χ_{ax}	axial inertial parameter: $\frac{\rho C^4 P_o}{12\mu^2 L^2}$	5.2.3
τ	nondimensional time: $t\omega$	1.2.3
ζ	load parameter: $\frac{W}{2RLP_a}$	1.2.3
ζ_g	load parameter due to weight: $\frac{mg}{2RLP_a}$	3.2.5

subscripts

c	condition in equivalent circular bearing	4.1.1
nc	noncircular	4.1

superscripts

$\tilde{}$	renormalized condition	4.1.2

Chapter 1

Introduction

1.1 Microfabricated Machines

MicroElectroMechanical Systems, or MEMS, are a novel class of devices appearing in a rapidly expanding range of applications. As a group, they are characterized by manufacturing techniques closer to those of integrated circuit (IC) chips than those of conventional machines. Their advantages include the mass-producibility responsible for IC's ubiquity as well as low weight, small size, rapid response, and low power consumption.

Recently, a new class of MEMS, *power MEMS*, has emerged. This term describes heat engines with power densities comparable to their full-sized counterparts, resulting in centimeter-scale packages with power outputs of 10 to 100 Watts [2]. A number of potentially revolutionary turbomachines in this class are currently under development at MIT. These machines include gas turbine engines for propulsion or electrical power generation, electrically-driven compressors for refrigeration or fuel cells, and turbopumps for rocket motors.

The great promise of power MEMS has an accompanying cost: complexity. In general, these devices emphasize the "systems" component of the MEMS acronym. As an example, a 3-D cutaway view of the MIT microengine is shown in Fig. 1.1. In this figure, the rotating components are shaded and the flow path is indicated with a dashed line. The operation is as follows: fluid enters the engine at its center, passes through a centrifugal compressor and moves radially outward. Fuel is added as the flow travels around and then into the combustor, where it is burned. The resulting hot gases are expanded through the turbine and exhausted from the center at the chip's aft surface. Radial rotor motion is controlled by a journal bearing at the turbine rim and axial motion is controlled by an opposed pair of thrust bearings located at the rotor center.

Successful operation of this device requires many subsystems to operate efficiently together, including compression, combustion, electromechanical energy conversion, expansion, and, the subject of this document: bearings. In addition, construction of this machine requires six wafers with microfabricated features on both sides, five precision-

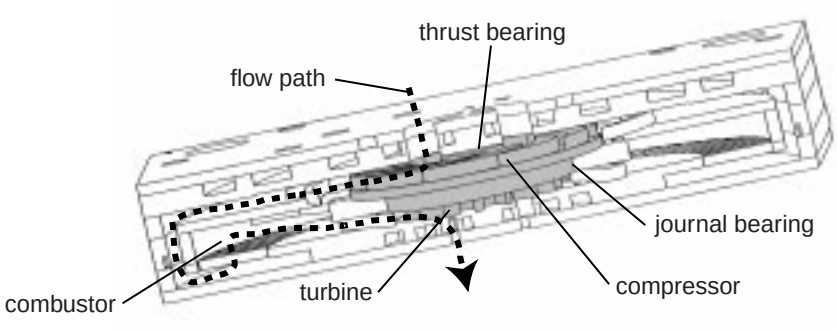

Figure 1.1: Three-dimensional cutaway drawing of the baseline MIT microengine. The rotating portion is shaded gray and the flow path is indicated with a dashed line. Figure courtesy of J. Protz.

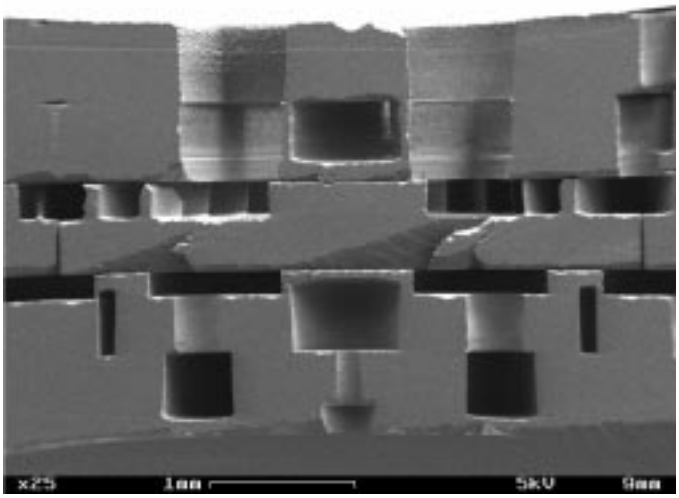

Figure 1.2: Scanning electron micrograph (SEM) of a cross-sectioned silicon micro-bearing test rig. Many features of the microengine shown in Fig. 1.1 are visible in this device. Figure courtesy of C.C. Lin [3].

aligned (within 1-2μm) bonds between them, and a process complexity comparable to that of modern CMOS devices [2]. The experimental rig built to test the bearings is, in itself, a complex device, containing many of the engine's features, as shown (in cross-section) in Fig. 1.2.

Bearings represent an important subsystem in power MEMS due to the presence of high speed rotating machinery. While rotating members have been previously demonstrated in microdevices [4–6], rim speeds have been limited to a few meters per second. This limitation stems, in part, from bearing drag associated with controlling axial and radial rotor movement. In the axial direction, passive magnetic levitation has been implemented [5] as a first step toward solution of this problem. In the radial direction, electrostatic bearings were investigated for the MIT microengine [7] but this topic has received little external attention. Consequently, lateral loads experienced in MEMS often result in "dry rubbing", where the rotating members make direct contact with their adjoining surfaces. At the large rim speeds required by high power density micro-turbomachines, such contact results in unacceptably high drag and short service life.

1.2 Journal Bearings

Gas journal bearings have comparable fabrication simplicity (for a microdevice) to dry-rubbing bearings but they have much lower drag and little to no running wear. Unfortunately, these attractive attributes are balanced by a penchant for instability that can produce destructive contact between rotating and stationary components if the geometry and operating conditions are not carefully controlled.

This stability issue, combined with their relatively low load capacity, has prevented the widespread application of gas journal bearings. To date, they have appeared primarily in devices where contamination of the working fluid by lubricants is unacceptable, low drag is essential, and or long life at high rotation rates are required. Examples of such applications include navigational gyros [8], cryogenic expansion turbines [9], and air cycle machines (ACM) [10].

1.2.1 Geometry and Nomenclature

The cross-section of a typical journal bearing is shown in Fig. 1.3. The inner (shaded) and outer members are referred to as the "journal" and the "bearing", respectively. Either or both members may rotate in the general case.

The simplicity of this arrangement is striking; the bearing consists of nested members connected only by a fluid film. The complete separation of moving solid surfaces is responsible for journal bearings' low drag and near-zero running wear. Unfortunately, because the operating characteristics are thus entirely dependent on the fluid dynamics of the film,

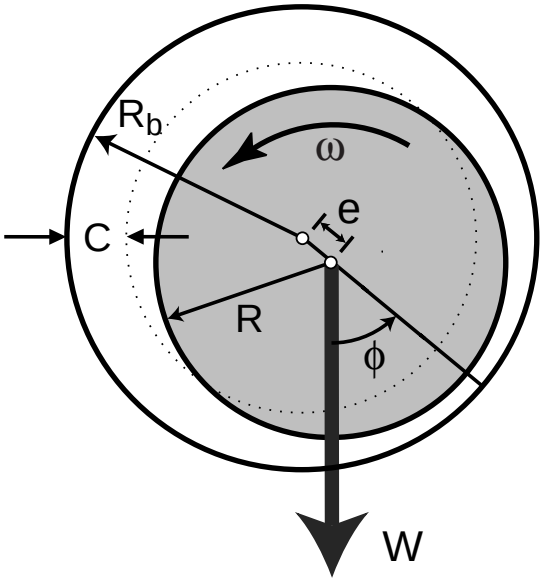

Figure 1.3: Journal bearing cross-section with relevant nomenclature.

there is a very strong sensitivity to the geometry. This consideration complicates fabrication because the geometry must be carefully controlled, often with unusually stringent tolerances on dimension, roundness, and roughness.

Much of the nomenclature used in this document appears in Fig. 1.3: ω denotes the rotation rate, W is the applied load, R_b is the bearing radius, R is the journal radius and their difference is the clearance, C. The attitude angle, ϕ is the angle between the applied load and a line connecting the journal and bearing centers. The excursion of the journal center from the bearing center is known as the "eccentricity" and denoted by e. It is most often normalized by C and expressed as an "eccentricity ratio", ϵ, so ϵ=0 and ϵ=1 represent fully-centered and "crashed" journals, respectively. Finally, the journal has mass m and, though not visible in this cross-sectional view, the bearing has length L and its ends are either exhausted to ambient conditions or treated with a nonuniform pressure distribution, to be described in Sec. 5.1.

1.2.2 Operation Description

Due to the complete separation of its solid surfaces, a journal bearing's drag and load-carrying characteristics are generated solely by fluid action. In most configurations, the drag is determined primarily by viscous shear from journal rotation. The load-carrying capacity, however, may be due to a pressure field generated by relative motion of the surfaces, an operating mode termed "hydrodynamic" or "self-acting", or by externally-supplied pressures, a mode termed "hydrostatic" or "externally-pressurized". If both of these effects are significant, the operating mode is termed "hybrid". The majority of this document will deal with hydrodynamic bearings, though a hydrostatic mode of particular

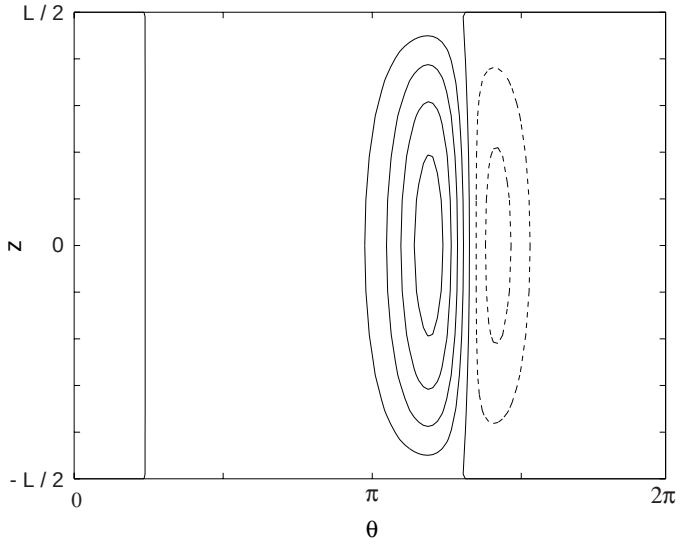

Figure 1.4: Typical pressure distribution of a journal bearing operating in an eccentric position. z is the axial coordinate and θ is the azimuthal coordinate. Fluid motion is left to right, dashed lines signify sub-ambient pressures, and the applied load acts toward $\theta = \pi$. The attitude angle is 43^o so the minimum channel height occurs at $\theta = 1.24\pi$

importance to microfabricated bearings will be discussed in Sec. 5.2.

The load-carrying capacity of a hydrodynamic journal bearing is derived from a viscous pumping action. This action is a result of shear stress at the rotating journal imparting kinetic energy to the fluid in the gap. When operating in a concentric position, the moving surface-induced (Couette) flow moves through a uniform passage between journal and bearing. It will therefore have a linear velocity profile, varying from zero at the bearing surface to $R\omega$ at the journal surface. In this situation, the pressure is constant around the circumference, thus the load capacity is zero. When the journal moves to an eccentric position, however, the rotational symmetry of the fluid passage is broken as it assumes a converging-diverging shape. Now, as the journal rotates, the fluid is forced through a passage of varying height. Consequently, the linear velocity profile, which has the same endpoints regardless of passage height, no longer satisfies mass conservation. In order to maintain continuity, a pressure-forced (Poiseuille) mechanism appears which is manifested as a strong negative pressure gradient in the direction of motion near the narrowed region and positive gradients on either side of this region. The resulting pressure field is shown in Fig. 1.4, where the azimuthal coordinate has been "unwrapped". The resultant rotational asymmetry of the pressure produces a net force that may be used to support a load.

Because the asymmetric pressure field results from a viscous action, and because gases have relatively low viscosity, gas-lubricated bearings tend to have lower load capacity than their oil-filled counterparts and much lower capacity than their rolling-element cousins. Furthermore, compressibility tends to reduce load capacity as well [11]. As noted previ-

ously, however, gas journal bearings have a problem more serious than modest load capacity preventing their widespread application: they have a tendency to become unstable.

Journal bearing instability is caused by misalignment between the applied load and its corresponding reaction force, measured by the attitude angle, ϕ, shown in Fig. 1.3. This misalignment is visible in Fig. 1.4 by the appearance of the peak pressure downstream of the load application point ($\theta = \pi$). In this case, the journal has moved to $\phi = 0.24\pi$ so the minimum channel height is located at $\theta = 1.24\pi$.

The force misalignment is caused by the pressure distribution's asymmetry around the narrowest point in the passage. The distribution shown in Fig. 1.4 is typical: the highest pressure occurs upstream of the "throat" (to borrow a term from supersonic nozzles) while the lowest occurs downstream. Motion in a direction tending to narrow the throat will therefore be answered by a force with components both against the motion as well as perpendicular to it, with the latter component acting in the direction of rotation. The rate of change of these forces with displacement are often referred to as "direct stiffness" and "cross stiffness", respectively.

Due to the nonzero cross-stiffness, the journal's reaction vector following a perturbation will not point toward the equilibrium position, producing an orbit instead of a straight-line oscillation. Due to its self-excited nature, this orbit occurs at a frequency less than half the rotational frequency. (For a circular bearing, a whirl at exactly half the rotational speed implies that the mean lubricant flow speed equals the rate at which throat is moving away, thus the load capacity falls to zero because the fluid is no longer, on average, forced through the throat.) Consequently, this type of motion is sometimes referred to as "half frequency whirl," though a more proper term is "fractional frequency whirl," (FFW) because it may occur at a frequency much less than half the rotation frequency.

Because a unique journal location is associated with each speed-loading pair for a given bearing, it may be expected that the disturbed journal would certainly return to its equilibrium position, despite the circuitous path implied above. This is indeed the case; unless it has mass.

Finite journal mass implies finite accelerations. Consequently a nonzero centripetal force must be provided by the fluid film to decrease the orbit radius (stable case), producing an inward spiral toward the static point. Smaller centripetal forces result in either periodic orbits (neutrally stable case) or outward spirals that may end in wall contact (unstable case). The nonzero cross-stiffness complicates this process by contributing force components in the whirling direction. Further complication arises from the fact that time-dependent terms appear in the fluid equations. For an incompressible fluid, the reaction felt by the journal is a function not only of its position, but of its velocity. Density variation adds a dependence on the path taken to a given position known as a "history" effect. The flowfield can therefore differ significantly from the static prediction for a given journal position and the journal can depart increasingly from its static position, either entering a

stable orbit mode or crashing into the bearing.

One well-known means of stabilizing a bearing is to force it to a high eccentricity. Physically, increasing eccentricity increases the direct stiffness with respect to the cross-stiffness. This fact is evidenced by a decreasing attitude angle with increasing eccentricity shown, for example, in [11]. In addition, squeeze-film damping becomes stronger when the separation between surfaces is reduced [12]. The bearing design must therefore reflect the proper combination of load and geometry to be stable at a given speed. Changing any one of these quantities will usually require a change in the others, though it will be shown in this document that regions of insensitivity to certain parameters can be found.

1.2.3 Nondimensional Parameters

A number of nondimensional parameters are used in the bearing literature to generalize the data and enable comparison of outwardly disparate bearings. The parameter sets employed reflect a combination of the particular needs of the authors as well as the prevailing tradition.

Throughout this research, the evolution of a consistent and meaningful set of parameters and their associated diagrams was a primary goal. Studying the diverse set of parameters used in the literature was a first step toward this goal. A broad classification of the three types of parameters necessary to specify bearing problems was then developed. The resulting classes will be termed “fluid condition”, “loading condition”, and “geometric condition”.

Fluid Condition

The parameters in this set emerge naturally upon nondimensionalization of the fluid equations for lubrication problems. These equations are developed from the Navier-Stokes equations by first dropping terms of order $(C/R)^2$. This simplification is rarely questionable because, referring back to the operation description of the previous section, a geometry with C comparable to R would be an extremely weak viscous pump and would therefore not be a useful bearing because it could not generate a significant load-carrying pressure distribution.

Under this simplification, the momentum equations become:

$$\rho\left(\frac{\partial \mathcal{U}}{\partial t}+\mathcal{U}\frac{\partial \mathcal{U}}{\partial X}+\mathcal{V}\frac{\partial \mathcal{U}}{\partial Y}+\mathcal{W}\frac{\partial \mathcal{U}}{\partial Z}\right) = \mu\frac{\partial^2 \mathcal{U}}{\partial Z^2}-\frac{\partial P}{\partial X} \tag{1.1}$$

$$\rho\left(\frac{\partial \mathcal{V}}{\partial t}+\mathcal{U}\frac{\partial \mathcal{V}}{\partial X}+\mathcal{V}\frac{\partial \mathcal{V}}{\partial Y}+\mathcal{W}\frac{\partial \mathcal{V}}{\partial Z}\right) = \mu\frac{\partial^2 \mathcal{V}}{\partial Z^2}-\frac{\partial P}{\partial Y} \tag{1.2}$$

$$\rho\left(\frac{\partial \mathcal{W}}{\partial t}+\mathcal{U}\frac{\partial \mathcal{W}}{\partial X}+\mathcal{V}\frac{\partial \mathcal{W}}{\partial Y}+\mathcal{W}\frac{\partial \mathcal{W}}{\partial Z}\right) = \mu\frac{\partial^2 \mathcal{W}}{\partial Z^2} \tag{1.3}$$

where ρ is the density, t is the time, and P is the pressure. In common with most bearing

analyses, the coordinate axes are oriented such that X measures distance along the circumference, Y measures distance along the axis of rotation, and Z measures radial distance. Under this coordinate system, $\mathcal{U}$, $\mathcal{V}$, and $\mathcal{W}$ are the fluid velocities in the circumferential, axial, and radial directions, respectively.

The "unwrapping" of the circumferential coordinate such that the fluid passage is expressed in a Cartesian frame implies another common assumption in bearing analyses: that the effect of curvature is negligible. This assumption is slightly more restrictive than the last because the curvature terms are of order C/R (see, for example, the momentum equations in Nataraj *et al.* [13], which were developed in cylindrical coordinates). For most bearings, however, C/R is of order 1 / 1000, so it is entirely reasonable to neglect curvature. The effect of this assumption will be discussed in Sec. B.5.

Removing the units via the nondimensionalizations:

$$\begin{array}{rclrclrcl} t &=& \omega\tau & P &=& P_a p & \rho &=& \tilde{\rho}\rho_a \\ X &=& R\theta & Y &=& R\xi & Z &=& Cz \\ \mathcal{U} &=& R\omega u & \mathcal{V} &=& R\omega v & \mathcal{W} &=& R\omega w \end{array}$$

the momentum equations become:

$$\chi\tilde{\rho}\left(\frac{\partial u}{\partial\tau} + u\frac{\partial u}{\partial\theta} + v\frac{\partial u}{\partial\xi} + \frac{R}{C}w\frac{\partial u}{\partial z}\right) = \frac{\partial^2 u}{\partial z^2} - \frac{6}{\Lambda}\frac{\partial p}{\partial\theta} \tag{1.4}$$

$$\chi\tilde{\rho}\left(\frac{\partial u}{\partial\tau} + u\frac{\partial v}{\partial\theta} + v\frac{\partial v}{\partial\xi} + \frac{R}{C}w\frac{\partial v}{\partial z}\right) = \frac{\partial^2 v}{\partial z^2} - \frac{6}{\Lambda}\frac{\partial p}{\partial\xi} \tag{1.5}$$

$$\chi\tilde{\rho}\left(\frac{\partial u}{\partial\tau} + u\frac{\partial w}{\partial\theta} + v\frac{\partial w}{\partial\xi} + \frac{R}{C}w\frac{\partial w}{\partial z}\right) = \frac{\partial^2 w}{\partial z^2} \tag{1.6}$$

From these equations, it can be seen that two new parameters have emerged: χ and Λ.

The first parameter, χ, is called the "inertial parameter" and is given by:

$$\chi = \frac{\rho R\omega C}{\mu}\frac{C}{R} = Re_c\frac{C}{R} \tag{1.7}$$

where Re_c is the Reynolds number based on the clearance and the tangential speed at the journal surface. The inertial parameter is is thus sometimes called the "modified Reynolds number." Because it is a coefficient on all inertial terms in the momentum equations, this parameter measures the importance of inertial "forces" relative to pressure and viscous forces. For most bearing systems, χ is small because Reynolds numbers are typically of order unity and C/R is of order 1 / 1000. For this reason, the inertial terms are often neglected in bearing analyses, eliminating the left-hand side of all three momentum equations. The effects lost under this assumption will be discussed in Sec. B.1.

The second parameter, Λ, is called the "bearing number" and is given by:

$$\Lambda = \frac{6\mu\omega}{p_a}\left(\frac{R}{C}\right)^2, \tag{1.8}$$

Also sometimes called the "compressibility number," Λ is the sole remaining fluid parameter if terms involving χ are dropped. Its clear origin has led to a near universal adoption in the gas bearing literature for nondimensionalizing the journal rotation speed, ω.

It is sometimes useful to note that, for an ideal gas, the bearing number may be also be expressed in variables more familiar to the fluid dynamicist:

$$\Lambda = \frac{6\gamma M^2}{Re_c}\frac{R}{C}, \tag{1.9}$$

where γ is the ratio of specific heats and M is the Mach number based on the tangential speed at the journal surface $(r\omega)$.

Under these assumptions, the left-hand side of the momentum equations disappear and they can be integrated in the cross-channel, or z, direction to yield u, v and w . These velocities may then be used in the continuity equation and, further assuming isothermal ideal gas, the following equation results (see, for example, Hamrock [12] Chap. 7):

$$\frac{\partial}{\partial\theta}\left(ph^3\frac{\partial p}{\partial\theta}\right) + \frac{\partial}{\partial\xi}\left(ph^3\frac{\partial p}{\partial\xi}\right) = \Lambda\left(\frac{\partial(ph)}{\partial\theta} + 2\frac{\partial(ph)}{\partial\tau}\right) \tag{1.10}$$

where h is the passage height, normalized by the clearance. This expression is a form of the "Reynolds equation," which was named to honor Osborne Reynolds who published it in 1886 [14]. The Reynolds equation is a striking simplification because it represents all three momentum equations plus continuity and it has only two dependent variables: the pressure and the channel height. Furthermore, the cross-channel, or z, direction has vanished. Only two computational dimensions are therefore required to describe flow in three-dimensional geometries. Finally, the equation only requires one nondimensional variable, Λ, to fully specify the fluid-dynamic state of the problem.

Loading Condition

Even for steady flows, Eq. 1.10 still contains two dependent variables once Λ is fixed: p and h. Another equation or parameter is therefore necessary. In this work, the parameter will be referred to as the "loading condition." For plain bearings, this condition may be specified in two ways: applied load (which implies a pressure distribution) or running eccentricity (which implies a height distribution). This choice exists because applied load and eccentricity have a one-to-one relationship once the bearing number is fixed. (In reality, the attitude angle, ϕ, presents a third option, but it is rarely exercised due to the difficulty in physical interpretation.) For nonplain bearings, as will be shown in Sec. 4.1.2, the load-eccentricity relationship may not be one-to-one. In this case, the loading condition is best specified in terms of applied load only.

The applied load, W, is commonly normalized by the ambient pressure acting on the bearing's projected area. The resulting term is referred to as the "load parameter", ζ:

$$\zeta = \frac{W}{2RLP_a}, \tag{1.11}$$

Owing to its straightforward definition and meaning, ζ, like Λ, is employed in the vast majority of gas bearing publications.

Geometric Condition

Though it is hidden in the nondimensionalization of Eq. 1.10, a geometric condition is necessary for even steady-state problems. Once again, an almost unanimous agreement exists in the literature on the definition of this parameter. Sometimes referred to as a "slenderness ratio" and assigned a symbol, the ratio of a bearing's length to its diameter is most often simply referred to as an "L over D" and written as "L/D".

For moving journal cases, a second geometric condition is required because the inclusion of a time-dependent height implies the addition of Newton's second law to determine accelerations from forces:

$$\vec{F} = m\frac{\partial \vec{V}}{\partial t} \tag{1.12}$$

where $\vec{V}$ is the journal velocity.

Again following the procedure of normalizing the equation to discover the appropriate nondimensional parameters, Eq. 1.12 becomes:

$$\vec{\zeta} = \bar{M}\Lambda^2\frac{\partial \vec{v}}{\partial \tau} \tag{1.13}$$

where $\vec{v}$ is the journal velocity normalized by $C\omega$, or the velocity of its center if it were in a synchronous whirl at $\epsilon = 1$, and t is the time normalized by ω. The force has been normalized by $2RLP_a$ to become a load parameter, as introduced in the previous section.

The new parameter, $\bar{M}$ is given by:

$$\bar{M} = \frac{mP_a}{72L\mu^2}\left(\frac{C}{R}\right)^5. \tag{1.14}$$

While the variables in Eq. 1.14 are not strictly constant, they change very little along the operating line in most devices. Thus, $\bar{M}$ is largely fixed at manufacture, hence its classification as a "geometric condition."

It instructive to note that $\bar{M}$ may also be expressed as:

$$\bar{M} = \frac{1}{\Lambda}\left(\frac{mC\omega^2}{2RLP_a}\right)\left(\frac{P_aC^3}{6\pi\mu R^2C\omega}\right) = \frac{1}{\pi\Lambda}\frac{\zeta_{cent}}{\zeta_{sqz}} \tag{1.15}$$

where the first parenthetical term is a load parameter for the centripetal force necessary to keep a journal whirling at the rotation speed in an orbit at $\epsilon = 1$. The second parenthetical term is an inverse load parameter for squeeze film force resulting from moving the journal from zero eccentricity at a linear speed of $C\omega$ [12]. In addition, bearing load capacity is proportional to bearing number, so the Λ term is also an indicator of fluid forces. The quantity denoted by $\bar{M}$ therefore expresses the ratio of the bearing's mass to the fluid's ability to resist its motion. This interpretation highlights a similarity in reasoning between $\bar{M}$ and a parameter recently proposed by Belforte *et al.* [15], which was the nondimensional centripetal force divided by the square of the sum of the external and squeeze film forces.

Unlike the previous cases, considerable disagreement exists in the literature as to the proper nondimensionalization for the Newton's second law. Parameters used for this purpose include the "speed parameter," Γ, in [16], [17]:

$$\Gamma = \omega \left(\frac{mC}{W} \right)^{1/2}$$

and Ω in [18], [19]:

$$\Omega = \frac{mC\omega^2}{\pi D L P_a}$$

In the current work, both of these parameters were found to be inconvenient, because they include the bearing rotation speed, which is a variable logically associated with the fluid condition. Furthermore, the speed parameter includes ω as well as W, which mixes all three of the conditions used in this document. Interdependent conditions make it difficult to determine an operating line on stability maps because the coordinates are strongly coupled. One can therefore encounter a "tail chasing" situation where a parameter is changed to move to the other side of a stability boundary only to discover that the boundary has moved in the same direction.

Notably, Rentzepis and Sternlicht were the first authors to propose a parameter set in which ω appeared on only one axis, though it was not nondimensional [20]. This work was later extended and the parameters nondimensionalized by Pan and Sternlicht [21], who proposed two parameter sets:

$$\bar{c} = \left[\left(\frac{mR}{W} \right) \left(\frac{P_a}{6\mu} \right)^2 \right]^{1/5} \frac{C}{R} \qquad \bar{\omega} = \left[\left(\frac{mR}{W} \right)^2 \left(\frac{6\mu}{P_a} \right)^2 \right]^{1/5} \omega$$

and

$$c^+ = \left[\left(\frac{m}{2P_a L} \right) \left(\frac{P_a}{6\mu} \right)^2 \right]^{1/5} \frac{C}{R} \qquad \omega^+ = \left[\left(\frac{m}{2P_a L} \right)^2 \left(\frac{6\mu}{P_a} \right)^2 \right]^{1/5} \omega$$

depending on whether the load was fixed at the rotor weight or variable. In both cases, the load parameter fixed the loading condition and the above parameters fixed the clearance

(geometric condition) and the rotor speed (fluid condition).

The identification of a fluid, geometric, and loading condition as a useful parameter space may be supported by noting that, despite the different appearance of the nondimensional parameter sets used in the current work and in Pan and Sternlicht's varying load case, the variables appearing only once in their nondimensional set are ω, c, and W. In the current work, these parameters are ω, m, and W. In both cases, the set of independent variables has a logical representative in each of the fluid, geometric, and loading conditions.

Conversely, when using Γ, ζ, Λ, and L/D, the independent variables are r, μ, and m. Substituting Ω for Γ changes the set to ω, μ, and m. In both cases, the parameter set has duplicate representation in one of the three conditions and no representation in another. Not coincidentally, both Γ and Ω have generated criticism in the literature in terms of their applicability in a design situation [16, 21].

1.3 Design Space

In a microfabrication environment, features are generally cut by line-of-sight etching, built up by deposition, or formed by a combination of these techniques. These production methods differ considerably from the casting, forging, and machining operations typically performed on the macro scale so the constraints they transmit to the design are often quite different and, in many cases, more limiting. At the same time, the system's intended function implies constraints for thermodynamic and structural considerations, for example, that apply to devices of all sizes. As a result, the design of microdevices is, by nature, a difficult problem. The complexity of power MEMS increases this difficulty considerably.

1.3.1 Fabrication-Related Constraints

Production cost and complexity targets lead to a design requirement of monolithic fabrication at the wafer level. As a result, the journal and bearing are defined simultaneously by etching the bearing gap between them, instead of creating them independently and performing a subsequent assembly. This method presents a significant challenge when designing bearings because, as will be shown in later chapters, their performance typically improves as length increases and clearance decreases while the opposite trend holds for all presently available etching techniques.

Features become more difficult and slow to form as they become narrower and deeper due to issues of introducing etch chemicals, removing etch products, and preventing the widening of the trench due to erosion of its sidewalls while etching its floor. The microfabrication of tall, close-clearance structures is, in fact, a perennial problem for the MEMS community and the subject of a great deal of development work [22–24].

While time multiplexed deep etching (TMDE) [25] has precipitated significant strides in this area, it is still difficult to create bearings that even roughly approximate their macroscale counterparts by etching alone. The only viable means proposed so far for alleviating this problem, besides separate etching and hand assembly, is lengthening the bearing by bonding multiple, separately-etched wafers together. This solution, however, requires extremely precise wafer alignment at the bonding step to avoid unacceptable imbalance and to allow axial movement and tilting of the journal without solid surface contact. In addition, bonding is a sensitive operation so adding bonding steps typically reduces overall yield.

In summary, monolithic fabrication technology implies a minimum C/L, leading to a trade-off between the smallness of C/R and the largeness of L/D, which are both desirable from bearing standpoint (see, for example, [26]), that is strictly a function of R. The choice of radius is, in turn, constrained by manufacturing and drag concerns. Manufacturing concerns impart a desire to keep the die size small to maximize the number of devices per wafer and to minimize cross-chip variation arising from non-uniformities in the etching chamber. Drag increases with surface area, which is proportional to R for the journal and R^2 for the rotor face.

In addition to imposing limitations on the achievable performance of a plain bearing, microfabrication constraints greatly complicate or preclude the application of many of the suggested improved bearing types, such as herringbone groove, foil, and tilting pad, a number of which are surveyed by Fuller [27].

Herringbone grooves [28] are difficult to microfabricate because photolithographic techniques generally produce only shapes that are extrusions of the 2-dimensional mask. Axial grooves are therefore straightforward to create, but tilting these grooves off the normal axis, as in a herringbone arrangement, is not. Foils and tilting pads, while satisfying the extruded shape requirement, are excluded by material concerns due to the silicon construction of most microdevices, in addition to a combination of the monolithic fabrication and minimum etch aspect ratio constraints.

Microfabrication gains an advantage over conventionally-fabricated bearings through the one-mask-for-several-bearings nature of photolithography. This feature implies that shapes that fulfill the 2-D extrusion requirement, such as elliptic, Rayleigh step [29], and wave bearings [30], may be produced without a per-piece increase in cost from shape complexity. This issue will be explored in Sec. 4.1.

1.3.2 Application-Related Constraints

Additional constraints apply to microfabricated turbomachine bearings. These requirements apply to turbomachines of any size, though the methods of satisfying them may differ significantly at the microscale. The most important of these requirements for the bearings is transonic compressor tip speeds, which stems from a desire to maximize the

stage pressure ratio [31]. For millimeter-scale rotors, this requirement leads to rotation rates in millions of RPM.

In addition, mass flow requirements, driving the inlet area and blade height, place restrictions on the allowable R due to structural considerations. Finally, thermal and stress-induced rotor expansion can cause the clearance to vary between operating points.

1.3.3 Relation to Conventional Bearings

Due to the above constraints, the design space available for bearings in the MIT microengine project is well outside that of conventional bearings. The most striking departure is in terms of the bearing length. The baseline L/D of 0.075 is more than a factor of three smaller than the *shortest* bearings reported in the literature. It is an order of magnitude smaller than commonly reported values. Second, due to the scale-independence of the transonic tip-speed constraint, the rotation rate is two orders of magnitude larger than commonly reported because the radii are two orders of magnitude smaller. Finally, the baseline C/R is approximately 0.005, which is a factor of five larger than typically encountered in the literature. While this ratio is not large enough to call the curvature simplifications into serious question (this issue is discussed in Sec. B.5), it could have serious implications for the nondimensional parameters outlined in Sec. 1.2.3 due to their strong C/R dependence. Interestingly, however, due to an interplay between the small mass and the large rotation rates with C/R, neither $\bar{M}$ nor Λ are especially unusual. The former is of order 10^{-1} and the latter is of order unity.

The inertial parameter also represents a serious departure from the conventional design space. Usually on order 1/1000, χ is order unity for the microengine bearings due to the large Reynolds number and large C/R. Because the smallness of χ was invoked when inertia was neglected during the Reynolds equation development, another means must be found for investigating its effect. This issue is discussed in Sec. B.1.

Another unusual feature typical of microbearings is their low load parameter due to weight. This is a consequence of the "cube-square law", where the surface area is proportional to the length scale squared, while the mass is proportional to the length scale cubed. Consequently, as devices shrink, their functionality (which generally scales with area) per unit mass increases. In the bearing case, the effect is a direct reduction of the load parameter:

$$\zeta = \frac{W}{2RLP_a} = \frac{\pi R^2 L \rho_{Si} g}{2RLP_a} \propto R \tag{1.16}$$

Thus the load parameter can be two orders of magnitude smaller for the microbearing than for a macro-scale bearing. This difference is increased further by the fact that silicon has approximately 1/3 the density of steel.

Specifically, for millimeter-scale radii and a silicon density of $\rho_{Si} = 2330 kg/m^3$, devices

operating at atmospheric pressure will have a load parameter with order of magnitude:

$$\zeta = \frac{\pi R \rho_{Si} g}{2 P_a} = \frac{(10^{-3})(10^{3})(10^{1})}{(10^{5})} = (10^{-4}) \tag{1.17}$$

Low weight is one of MEMS' most attractive features in many applications. For vehicles, this attraction is felt in terms of fuel savings and maneuverability. For instruments, the attraction is in terms of low inertia, which implies previously unattainable frequency response (see, for example [32]). Low inertia, as will be shown in Sec. 3.2.5, also implies a very high tolerance to shock loading, making MEMS very attractive as crash-tolerant safety devices on aircraft-carried weapons, for example [33].

For a microfabricated bearing, low weight presents a complication because, as noted earlier, the journal must be forced to an eccentricity to be stable. In macro-devices, the rotor weight is often sufficient for this purpose, hence the widespread appearance of charts involving the "threshold speed", which is the maximum stable speed under a fixed load. In microdevices, as will be shown in Sec. 3.2.1, low weight combined with high eccentricities required for stability usually lowers the threshold speed below their design speed. Applying load via noncircumferentially-uniform pressure at one of the bearing ends will be explored as a possible solution to this problem in Sec. 5.1.

An interesting effect of these constraints is they imply a rearrangement of the bearing design process. A microbearing designer is tasked with determining a loading condition to enable a bearing of a tightly-constrained geometry to run at a given speed. The typical macrobearing designer, on the other hand, is tasked with creating a geometry to enable a bearing to carry a given load at a given speed. The context in which the data are presented in this document reflect the former case.

The absence of data in the literature at these unusual conditions makes design of microbearings based on existing work difficult. In fact, extrapolation of reported data to the needed range often yields unsettling predictions. For example, Reynolds and Gross [26] calculated a threshold eccentricity ratio as a function of length and clearance from their experimental data. Their results are presented in Fig. 1.5. Extrapolating these results to $L/D = 0.075$, $C/R = 5 \times 10^{-3}$ appears to indicate an impossible threshold eccentricity ratio of much greater than unity for the baseline microbearing.

1.4 Analysis Methods

Because the existing data did not cover the range of parameters needed for microbearings, generation of new data was necessary. When choosing a method for this task, its applicability to small L/D, large C/R, and large eccentricities were primary considerations.

A second requirement for an analysis method was flexibility because, due to the difficulty in producing stable bearings in this regime implied by the current literature, a num-

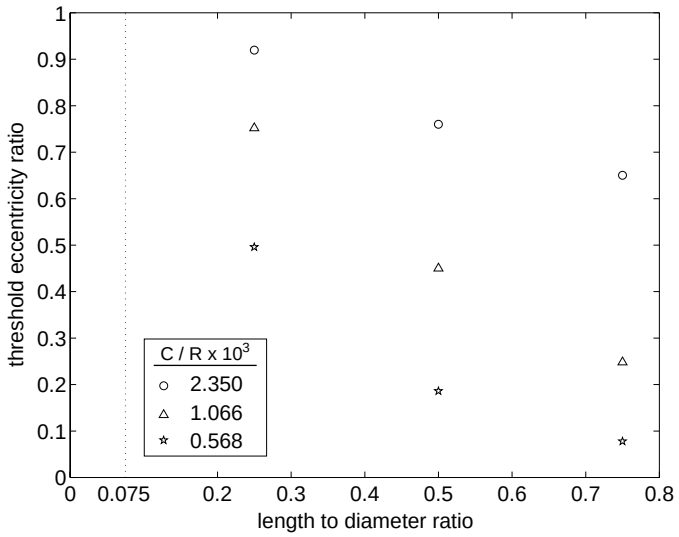

Figure 1.5: Experimental threshold eccentricity ratio, or minimum ϵ for stability, from Reynolds and Gross [26] for bearings of varying length and clearance. Extrapolation from this chart to the microbearing baseline ($L/D = 0.075$, $C/R = 5 \times 10^{-3}$) appears to predict an impossible threshold eccentricity of greater than unity.

ber of design options would likely be investigated to improve performance. In addition, this work was to be undertaken in tandem with an ongoing design effort and experiments on the micro [3] and macro [34] scale. The ability to model phenomena such as imbalance and geometric imperfection was therefore desired.

1.4.1 Previous Work

Several analytical solutions have been presented for the steady-state load capacity and attitude angle at a given eccentricity and speed [35–37]. Currently, however, these quantities are most often computed directly from the relevant fluid equations with straightforward numerical techniques. Raimondi [11] published a series of careful finite-difference solutions in 1961 that is still a common reference for this type of data. Modern computers and more sophisticated numerical techniques have decreased the time necessary to obtain such solutions [38], but little controversy exists regarding the resulting data.

Methods for determining journal bearing stability, and their results, are considerably more diverse. The vast majority of methods, both analytical and numerical, are based on a linearization to enable an eigenvalue analysis of system stability. The primary distinguishing feature between the various methods is their handling of time-dependent terms in the fluid equations. The two extremes are time-accurate methods, which couple the rotordynamic and fluid equations, and uncoupled, “quasi-static”, methods. Pan and Sternlicht surveyed most of these methods in their 1964 paper [21], comparing them to each other and to experimental data. The analytic methods discussed in their work, however, become questionable at large eccentricities due to application of Ausman’s “linearized

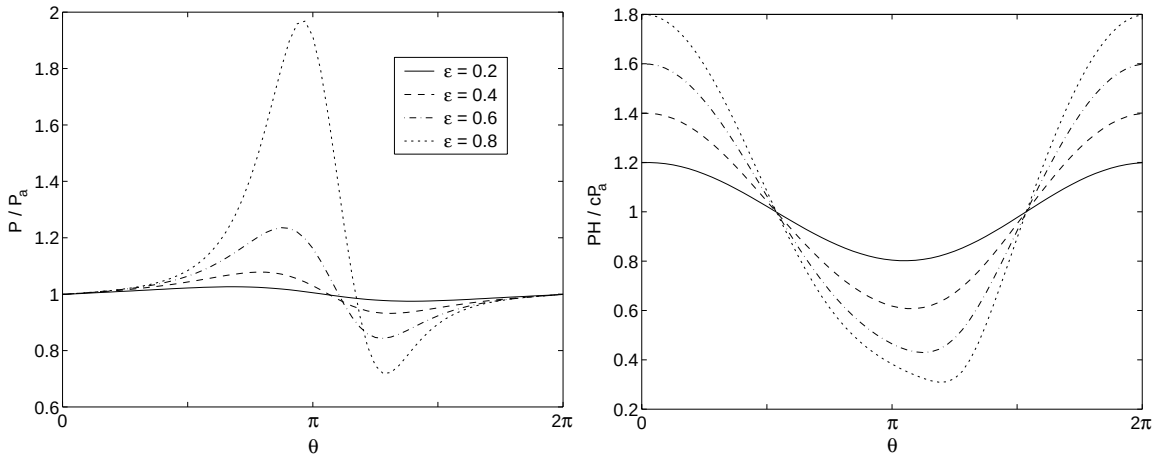

(a) pressure **(b)** pressure×height

Figure 1.6: Typical variation of normalized pressure and normalized pressure times height with eccentricity. Minimum channel height occurs at $\theta = \pi$. Multiplying the pressure by the height smoothes the distribution considerably, but the curve still becomes sharper as eccentricity increases.

PH" assumption [36]. The only remaining method in [21] valid for finite bearings, that of Rentzepis and Sternlicht [20], also becomes questionable at high ϵ because it relies on stiffnesses generated by finite difference differentiation of the load curve, which becomes extremely nonlinear at high ϵ.

One year after Pan and Sternlicht's comparison was published, Cheng and Pan [16] published an extension of Cheng and Trumpler's infinite-length bearing Galerkin method solution [39] to finite bearings. This method was unique at the time because it fully-coupled the rotordynamic and fluid equations and it did not contain explicit linearizing assumptions about the pressure distribution or eccentricity. It was thus theoretically capable of calculating the equilibrium position and, by linearizing for small perturbations about this position, the stability of any plain journal bearing at any eccentricity.

Despite the relative absence of assumptions in Cheng and Pan's work, implicit limitations are imposed by the low order of their Galerkin approximation. Due to the difficulty in carrying out the expansion by hand (evidenced by the complexity of Eqs. 10-16 in their paper), they included only two Fourier modes in the circumferential direction and a single cosine mode in the axial direction. As shown in Fig. 1.6(a), however, the circumferential pressure distribution in a journal bearing has increasingly sharp extremes as the eccentricity increases. From a spectral perspective, the decreased minimum radius of curvature in the distribution implies larger higher order modes and, thus, increased truncation error for a fixed-order expansion.

In an attempt to extend their useful ϵ range, Cheng and Pan employed pressure times channel height as their dependent variable because its distribution is typically smoother.

As shown in Fig. 1.6(b), however, this distribution also begins to show increasing skew and decreasing radius of curvature as ϵ increases. As a result, Figs. 2 and 3 in their paper show increasing error in steady-state load capacity with ϵ. Furthermore, it will be demonstrated in Sec. 2.2.2 of the current document that Cheng and Pan's stability results become suspect at roughly $\epsilon = 0.6$, for $L/D = 0.25$.

Despite the great promise of their method, there have been few attempts to extend Cheng and Pan's work to more modes in the 30 years since its publication. In support of early MIT microengine designs, Jacobson [40] solved the Reynolds equation with a finite difference technique and expanded the resulting PH distribution in a Fourier series. In this manner, he showed that 85% of the spectral power in the axial direction for an $L/D = 0.075$ bearing at $\epsilon = 0.6$ is captured by the first mode, while four modes are required to reach comparable power in the circumferential direction. He then extended Cheng and Pan's work to four modes in the circumferential direction and one in the axial direction using symbolic mathematics software to execute the expansion.

Recently, Orr [34] showed that brute-force expansion with symbolic mathematics software becomes intractable at approximately seven modes in the circumferential direction with a single mode in the axial direction. He then circumvented this difficulty by using pattern-recognition techniques to eliminate trigonometric terms that evaluate identically to zero and extended the method to 24 circumferential modes. In view of the efficiency issues to be discussed in Sec. 2.2.2 this order of approximation is likely to be accurate for an extremely wide range of problems, effectively putting the numerical issues of linear stability analysis to rest for plain, short journal bearings.

Taking a different approach, Pan [19] published an analysis of gas bearing systems through periodic excitation at a range of frequencies in 1965. The goal of his method is to decouple the stability analysis from the particulars of the bearing configuration and calculation method. Pan reached this goal by showing that the forces on a gas bearing under periodic perturbation can be used to compute effective damping and stiffness coefficients. The state of neutral stability is then identified as the frequency of perturbation at which the effective damping coefficient vanishes and the rotor mass has a critical value that is in resonance with the effective stiffness. Instability is then indicated if the effective damping coefficient at this point increases with frequency. The calculation therefore requires knowledge of bearing reactions to perturbations for the entire frequency spectrum but it is not dependent on how those reactions are calculated.

An even more general, and highly intuitive, means of generalizing bearing analysis was proposed by Castelli and Elrod [41]. Their suggestion, known as an "orbit method," was to simply march the fluid and motion equations together in time. The computation then becomes, in effect, a numerical experiment with a full suite of non-invasive instruments unavailable to the physical experimentalist. Though this technique is the most direct and, thus, the most computationally-expensive, Castelli and Elrod were able to perform

such calculations in 1965 for an infinite-length bearing by hand, on a Univac, and later, on an IBM 7090 . Their work involved a finite-difference discretization and a trapezoidal integration of the pressures to determine forces on the journal. The system was marched forward in time using a Crank-Nicolson method.

Due to the expense of their calculation, Castelli and Elrod used it only to spot-check the stability boundary produced by a semi-numerical method, also presented in [41], by showing cases on either side of the stability boundary behaved as predicted. They also mention the existence of stable limit cycles and the stabilizing effect of imbalance but note that a systematic investigation of these phenomena was impractical with the current computers.

Despite the orders-of-magnitude increase in computing power since Castelli and Elrod's investigation, there have been few direct simulations of gas bearings, most likely due to the general dearth of research in this area. Liquid-filled bearings, however, have been treated with this method [42, 43]. In this case, the time integration is extremely rapid because the fluid equations may be solved analytically for very short or very long bearings.

1.4.2 Current Analysis Method

A key enabler for investigating the wide variety of effects in the current work is an extension of Castelli and Elrod's orbit method concept to finite-length bearings. Furthermore, the efficiency of the scheme is increased by use of a pseudospectral technique. This technique allows the numerical resolution to be adjusted at run time to avoid truncation error at high eccentricity and unneeded computation at low eccentricity.

A second code was also written for this work that solves the full viscous flow equations instead of the simplified set employed by the methods of the previous section. Full advantage was taken of the journal bearing geometry and boundary conditions to improve the speed of this tool over that of general-purpose flow solvers. This formulation enables the investigation of phenomena assumed negligible in standard bearing analyses that may be appreciable in microbearings.

These codes are both described in detail in Chap. 2.

1.5 Dissertation Objective and Outline

This work is intended to fill a void existing in the gas bearing literature in the very low L/D regime occupied by most microbearings. Following the type of data presented in the literature, steady-state operating results as well as fixed-point stability boundaries are computed. In addition, a framework for design that is appropriate to microbearings is outlined, including a number of new presentation methods for stability data. Investigation of the tradeoffs peculiar to microbearings are also presented.

Taking advantage of the orbit method's flexibility, more complex phenomena are also treated. Some of these phenomena, such as imbalance, large-amplitude whirl, and shock

tolerance have been observed experimentally but no systematic computational investigation in gas bearings has been previously reported.

In addition, topics particular to microfabricated bearings are discussed. First, noncircular bearing shapes are evaluated in the fixed minimum clearance context of microfabricated bearings. Also, the impact of varying clearance in the axial direction due to etching concerns is assessed. The implications of loading via application of a noncircumferentially-uniform pressure at one axial end are also presented. Finally, a model and nondimensionalization is developed for a hydrostatic mode due to axial flow inertia that emerged during experiments for the MIT microengine.

Because microturbomachine bearings may violate some of the assumptions commonly made in lubrication analyses, the importance of several neglected effects is discussed in the last chapter.

Chapter 2

Numerical Tools

The results presented in this dissertation are derived from two original and distinct codes: BASICS and SPECTRES. BASICS, for *B*earing *A*nalysis *S*uite for *I*nvestigating *C*ommon *S*implifications, is a Navier-Stokes solver formulated specifically for efficient treatment of journal bearing flowfields. Its purpose is to explore the effect of terms neglected in the lubrication equations when operating outside their conventional envelope. SPECTRES, for *SPEC*tral *R*eynolds *E*quation *S*olver, is based around a pseudospectral Reynolds equation solver for fluid effects and time-marching of the motion equations for journal path determination. Common lubrication assumptions are therefore implicit in SPECTRES' calculation of hydrodynamic forces, but the journal motion is free of non-physical constraints. This chapter describes these codes in detail and presents their validation measures.

2.1 BASICS

As shown in Sec. 1.3.3, preliminary calculations for the MIT microturbomachine bearings indicated that fluid inertia, normally neglected in lubrication analyses, may be significant. In addition, due to the appreciable Mach numbers at the journal surface, non-isothermal flow was a distinct possibility, violating another typical assumption of lubrication analyses. BASICS was written to investigate these effects with the understanding that the computational cost associated with solving more complex fluid equations would preclude its use as a design tool.

2.1.1 Equations and Nondimensionalizations

BASICS is based on the unsteady, compressible Navier-Stokes equations. In consideration of the journal bearing geometry, these equations were written in a normalized cylindrical coordinate system. The calculation is two-dimensional, treating the circumferential and cross-channel (radial) directions and neglecting the axial direction. This formulation implies negligible side-leakage or, strictly, an infinite-length bearing.

The nondimensionalizations chosen for this work are similar to those used by Nataraj *et al.* [13]:

$$\begin{array}{lllllllll} \tilde{t} & = & \dfrac{\omega t}{\kappa} & \tilde{r} & = & \dfrac{R-r}{C} & \tilde{\rho} & = & \dfrac{\rho}{\rho_\infty} \\ \tilde{p} & = & \dfrac{P}{\rho_\infty (r\omega)^2} & \tilde{v_r} & = & \dfrac{v_r}{\kappa r \omega} & \tilde{v_\theta} & = & \dfrac{v_\theta}{r\omega} \\ \tilde{\mu} & = & \dfrac{\mu}{\mu_\infty} & \tilde{\tau_{..}} & = & \dfrac{\tau_{..}}{\rho_\infty (r\omega)^2} & \tilde{e} & = & \dfrac{e}{(r\omega)^2} \end{array} \tag{2.1}$$

$\kappa = C/R$ is the clearance ratio. It should be noted that the nondimensional radial coordinate, $\tilde{r}$, is unity at the journal surface and zero at the bearing surface. This introduces minus signs at a few unusual locations in the fluid equations.

With these nondimensionalizations, the Navier-Stokes equations may be expressed as:

$$\frac{\partial U}{\partial t} - \frac{\partial F}{\partial \tilde{r}} + \frac{\partial G}{\partial \theta} + H = 0 \tag{2.2}$$

where

$$U = \frac{R}{r} \begin{bmatrix} \tilde{\rho} \\ \kappa \tilde{\rho} \tilde{v_r} \\ \tilde{\rho} \tilde{v_\theta} \\ \tilde{\rho} \tilde{e}_t \end{bmatrix}$$

$$F = \begin{bmatrix} \kappa \tilde{\rho} \tilde{v_r} \\ \tilde{p} + \kappa^2 \tilde{\rho} \tilde{v_r}^2 - \tilde{\tau}_{rr} \\ \kappa \tilde{\rho} \tilde{v_r} \tilde{v_\theta} - \tilde{\tau}_{r\theta} \\ \kappa \tilde{v_r} (\tilde{\rho} \tilde{e}_t + p) - \kappa \tilde{v_r} \tilde{\tau}_{rr} - \tilde{v_\theta} \tilde{\tau}_{r\theta} + q_r \end{bmatrix}$$

$$G = \frac{\kappa}{1 - \kappa \tilde{r}} \begin{bmatrix} \tilde{\rho} \tilde{v_\theta} \\ \kappa \tilde{\rho} \tilde{v_r} \tilde{v_\theta} - \tilde{\tau}_{r\theta} \\ \tilde{p} + \tilde{\rho} \tilde{v_\theta}^2 - \tilde{\tau}_{\theta\theta} \\ \tilde{v_\theta} (\tilde{\rho} \tilde{e}_t + p) - \kappa \tilde{v_r} \tilde{\tau}_{r\theta} - \tilde{v_\theta} \tilde{\tau}_{\theta\theta} - \frac{\kappa}{1-\kappa\tilde{r}} q_\theta \end{bmatrix}$$

$$H = \frac{\kappa}{1 - \kappa \tilde{r}} \begin{bmatrix} \kappa \tilde{\rho} \tilde{v_r} \\ \kappa^2 \tilde{\rho} \tilde{v_r}^2 - \tilde{\rho} \tilde{v_\theta}^2 - \tilde{\tau}_{rr} + \tilde{\tau}_{\theta\theta} \\ 2\kappa \tilde{\rho} \tilde{v_r} \tilde{v_\theta} - 2\tilde{\tau}_{r\theta} \\ \kappa \tilde{v_r} (\tilde{\rho} \tilde{e}_t + \tilde{p}) - \kappa \tilde{v_r} \tilde{\tau}_{rr} - \tilde{v_\theta} \tilde{\tau}_{r\theta} + q_r \end{bmatrix}$$

$$\tilde{\tau}_{rr} = -\frac{2\kappa\tilde{\mu}}{Re_c}\left[\frac{\partial\tilde{v}_r}{\partial r} - \frac{1}{3(1-\kappa\tilde{r})}\left(\frac{\partial(1-\kappa\tilde{r})\tilde{v}_r}{\partial r} - \frac{\partial\tilde{v}_\theta}{\partial\theta}\right)\right]$$

$$\tilde{\tau}_{r\theta} = -\frac{\tilde{\mu}}{Re_c}\left[\frac{\partial\tilde{v}_\theta}{\partial r} + \frac{\kappa}{(1-\kappa\tilde{r})}\left(\tilde{v}_\theta - \kappa\frac{\partial v_r}{\partial\theta}\right)\right]$$

$$\tilde{\tau}_{\theta\theta} = \frac{2\tilde{\mu}}{Re_c}\frac{\kappa}{1-\kappa\tilde{r}}\left[\frac{\partial\tilde{v}_\theta}{\partial\theta} + \kappa\tilde{v}_r + \frac{1}{3}\left(\frac{\partial(1-\kappa\tilde{r})\tilde{v}_r}{\partial r} - \frac{\partial\tilde{v}_\theta}{\partial\theta}\right)\right]$$

$$q_r = \frac{\tilde{\mu}}{Re_c M_\infty^2 Pr(\gamma-1)}\frac{\partial T}{\partial r}$$

$$q_\theta = \frac{\tilde{\mu}}{Re_c M_\infty^2 Pr(\gamma-1)}\frac{\partial T}{\partial\theta}$$

2.1.2 Algorithm

Equation 2.2 is discretized in space with a vertex-based finite volume scheme. Time integration is performed via an explicit four-step Runge-Kutta scheme. Local time stepping is implemented to accelerate convergence. The viscous fluxes are calculated on an intermeshing grid. They are calculated only on the first Runge-Kutta step and frozen for the remaining steps to reduce the computational cost.

The physical domain is mapped onto a structured grid of quadrilateral cells with one of the computational grid directions aligned with the radial direction of physical space. This alignment reduces the number of metrics and fluxes that must be calculated while still enabling most shapes of interest to be modeled. A sample of this grid is provided in Fig. 2.1. Note that the step in θ between radial gridlines is constant, but the step in r between circumferential gridlines is not when the journal is in an eccentric position.

The boundary conditions are relatively straightforward. A periodicity condition is imposed between the left and right edges of the computational domain. The journal and bearing surfaces are treated with a no-slip condition, *i.e.* rarefaction effects are neglected, the validity of which is explored in Sec. B.4. Moreover, the journal and bearing surfaces are held at a constant temperature that may be specified independently for each surface.

During intermediate state vector updates, densities at surfaces are calculated using the continuity equation with modifications to the fluxes and cell areas for the solid wall. During final state vector updates, the surface densities are calculated with the continuity equation but also corrected with a centripetal acceleration-based pressure boundary condition using the known local flow curvature and speed. This well-known condition is given by:

$$\frac{\partial P}{\partial n} = -\frac{\rho V^2}{R_s} \tag{2.3}$$

where V is the flow speed at the surface and n is the surface outward normal direction. R_s

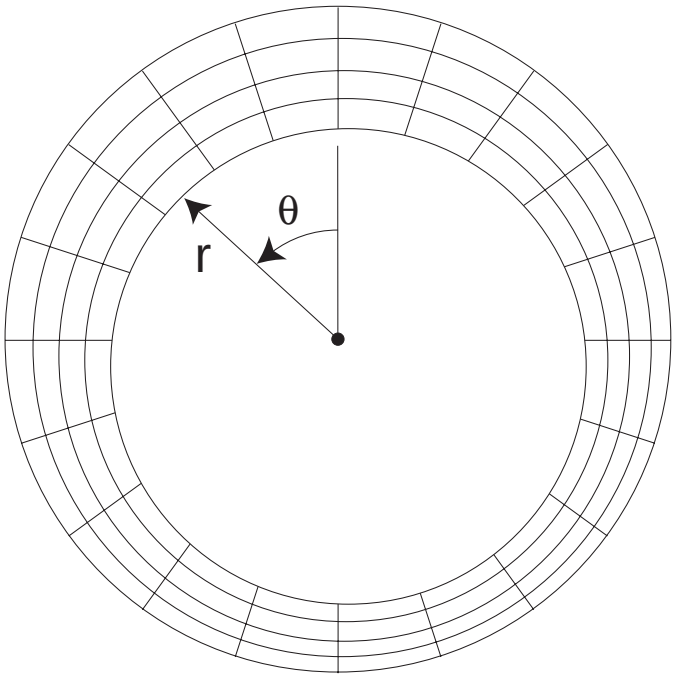

Figure 2.1: Example BASICS grid for an eccentric journal. Note that one set of gridlines is purely radial and distributed equally in θ while the other varies in both θ and r when the journal is eccentric.

is the surface's radius of curvature, taken as positive for concave surfaces.

Because a no-slip condition is assumed at solid surfaces, V is zero at the bearing. Furthermore, because the grid was constructed with lines of constant θ, the normal direction at the bearing surface is always aligned with one of the grid directions. The above boundary condition is thus straightforward to implement: a one-sided difference for the pressure was written at the surface and set to zero. The resulting equation was then simply solved for the pressure at the wall.

At the journal surface, the situation is considerably more complicated. First, the velocity's magnitude is known to be $V = R_j\omega$ but its direction is not aligned with the grid if the journal is eccentric. Second, the convenience of a grid line corresponding to a normal direction is lost. A coordinate transformation is therefore necessary to calculate surface normal quantities from gradients taken from nodal data.

The key advantage of the pressure boundary condition is that it does not admit sawtooth modes. Its application at the final state vector update therefore obviates the need for artificial viscosity in the radial direction. In addition, the periodic boundary conditions applied in the circumferential direction destroy sawtooth modes if an odd number of nodes are employed. Artificial viscosity is thus unnecessary in BASICS.

Because the bearing is a closed system, an additional constraint was necessary on its mass content. The mass content must be set to establish a connection with the ambient density used in the nondimensionalizations of Eqs. 2.1. The subtleties of this issue were

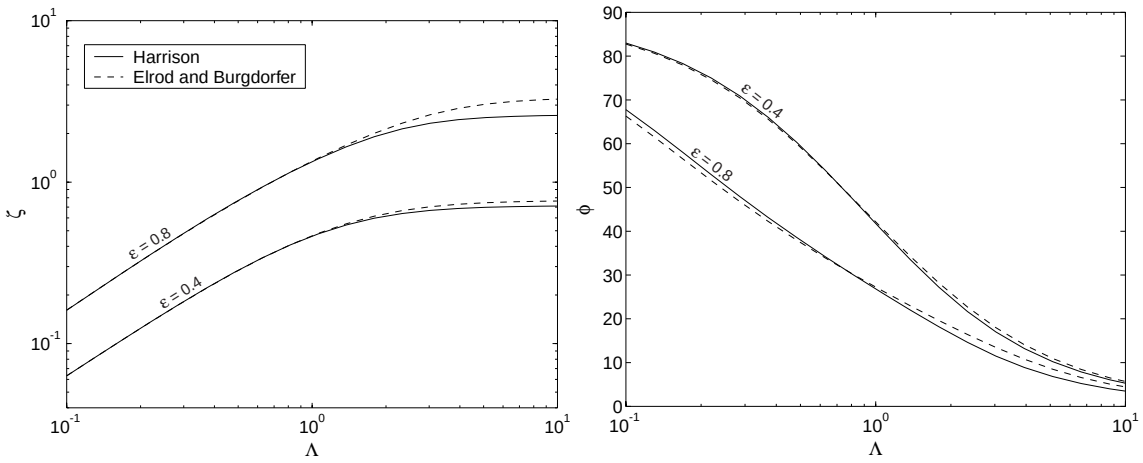

(a) Load Parameter **(b)** Attitude Angle

Figure 2.2: Effect of mass-content rule choice on the computed operating parameters of long bearings.

discussed in a paper by Elrod and Burgdorfer [44] who developed a closed-form solution for the mass content of a bearing in terms of its eccentricity via a clever manipulation of the Reynolds equation. Because, BASICS was written to investigate the effect of assumptions made in the Reynolds equation, however, using a mass content rule derived from it was deemed inconsistent. Instead, the simple mass content rule of Harrison [45] was implemented, whereby the total mass of fluid in the bearing is held at its level if it were stationary and in communication with ambient conditions. This implies that the bearing is truly infinite or the ends are perfectly sealed. The ramifications of this arrangement are discussed by Ausman in the appendix of Elrod and Burgdorfer's paper. Most notably, the difference is small except at very large bearing numbers. For reference, load parameter and attitude angle traces produced from finite difference solutions of the lubrication equations with either constraint are compared in Fig. 2.2 for the bearing numbers and eccentricities treated in this document. It is immediately evident that the differences are slight except at high eccentricities and bearing numbers.

In addition to setting an initial mass content, it was necessary to occasionally correct it during the course of the calculation. This was necessary because numerical errors can accumulate due to the closed nature of the flowfield and change the reference condition. The implementation of the centripetal acceleration boundary condition worsens this problem because it produces changes in the density independent of the continuity equation. The correction was accomplished by measuring the total mass content during the final state-vector update and comparing it to the desired value. The density on the entire grid is then multiplied by the ratio of the current total mass to the starting value.

2.1.3 Validation

Two cases were used to validate BASICS: Taylor-Couette flow and journal bearing flow.

Taylor-Couette flow takes place in the annulus of concentric cylinders. Unlike lubrication flow, there is no restriction on the clearance ratio so this test case was selected to activate at least a few terms involving κ in the governing equations. The compressible Taylor-Couette problem was chosen for generality, though it must be solved numerically. Analytical solutions have been published only for the incompressible case (see, for example, White, Chap. 3 [46]).

The results of a zero eccentricity computation in BASICS are shown in Figure 2.3 for $M = 0.5$ and $Re = 100$ on a 41×25 grid. These results are compared to finite difference solutions of the compressible Taylor-Couette problem with 250 nodes in the radial direction. Agreement is excellent for all three clearance ratios presented, $\kappa = 1/2, 1/8$ and $1/100$.

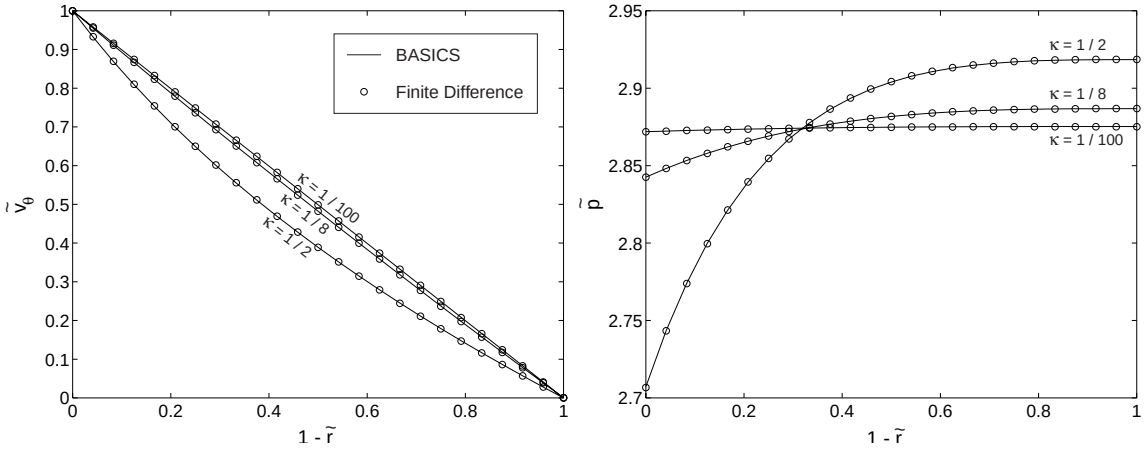

(a) Tangential Speed **(b)** Pressure

Figure 2.3: Comparison of BASICS results with finite difference Taylor-Couette flow solutions at various clearance ratios.

The second test case, journal bearing flow, may be described as Taylor-Couette flow with an eccentric inner cylinder and with κ vanishingly small.

A sample bearing pressure distribution is shown in Fig. 2.4. In the depicted calculation, ϵ=0.6, Λ=3.5, M=1.09, Re=577, κ=0.005, and χ=2.9. The gap is greatly exaggerated for visibility. The figure is oriented such that the load points vertically downward.

The figure shows a feature typical of journal bearing flows: cross-channel pressure gradients are insignificant when compared to circumferential gradients. The evolution toward this condition as the inner and outer cylinder radii approach each other may be observed by noting the trend of Fig. 2.3(b) as κ decreases.

For easy comparison to Reynolds equation solutions, a series of calculations were performed and the resulting load capacity and attitude angle were measured. In these cases,

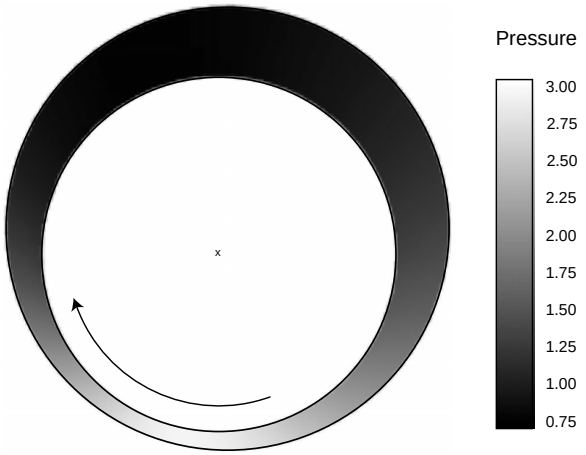

Figure 2.4: Pressure distribution for a journal bearing at 60% eccentricity. The journal is rotating clockwise.

κ was held at 1/1000 and Re was held at 100. The bearing number was varied by changing the Mach number. A finite difference solution of the Reynolds equation for an infinitely-long bearing with Harrison's mass content constraint (discussed in the previous section) provided the comparative data. This comparison is presented in Fig. 2.5. Agreement is excellent over the entire bearing number range at both high and low eccentricities.

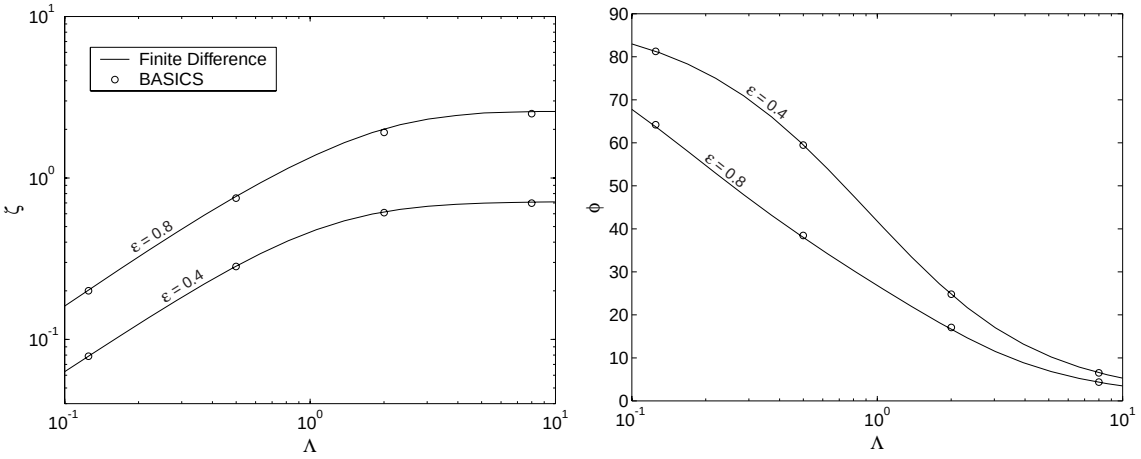

(a) Load Parameter **(b)** Attitude Angle

Figure 2.5: Comparison of BASICS results with finite difference lubrication equation solutions.

2.2 SPECTRES

BASICS was written to investigate issues brought about by the high Mach number and nonvanishing inertial parameter of the MIT microengine bearing. Once it appeared that

these issues were not of primary significance, as discussed in App. B, the large number of remaining unknowns regarding the behavior of microfabricated bearings demanded a less expensive computational tool. In response, a new tool, SPECTRES, was built with the Reynolds equation, rather than the Navier-Stokes equations, as its fluid model.

2.2.1 Equations and Nondimensionalizations

The Reynolds equation, as discussed in Sec. 1.2.3, is a very convenient fluid model because it collapses all the conservation equations of Eq. 2.2 into a single expression. Furthermore, the only dependent variables are height and pressure and its domain is only two-dimensional for 3-D bearings. This formulation is especially convenient for dynamic bearing computations because the force on the journal, or the integrated pressure, is the output quantity of interest. These features reduce the computation time considerably, speeding the calculation and allowing a greater number of effects to be investigated in a given time period.

For unsteady calculations, Newton's second law is also included to describe the journal motion under the influence of the applied forces. To enable imbalance and external damping to be simulated in SPECTRES, the nondimensional form of Newton's second law presented in Sec. 1.2.3 is augmented with additional terms:

$$\frac{1}{\bar{M}\Lambda^2}\left(\vec{\zeta} - \Lambda\eta\vec{v}\right) + \delta_u\vec{n} = \frac{\partial\vec{v}}{\partial\tau} \tag{2.4}$$

where $\vec{\zeta}$ includes applied loads and pressure forces developed from the fluid. As described in detail by Castelli and Elrod [41], forces due to tangential viscous stress are a factor C/R smaller than those due to pressure, so they are neglected to maintain consistency with similar arguments made elsewhere in SPECTRES' formulation.

The $\Lambda\eta\vec{v}$ term can be used to include the effects of external damping contributions, such as translational drag in thrust bearings or aerodynamic effects in the compressor or turbine. The non-dimensional damping coefficient, η, is defined as:

$$\eta = \frac{D}{12L\mu}\left(\frac{C}{R}\right)^3, \tag{2.5}$$

which is the ratio of the damping force to the drag produced in a gap of height C by a journal moving with linear speed $C\omega$.

The $delta_u\vec{n}$ term in Eq. 2.4 can be used to include imbalance, where δ_u is the distance between the geometric and mass centers normalized by the clearance and $\vec{n}$ is a unit vector rotating at synchronous speed in the same direction as the journal. If a large number of balanced cases are to be run in SPECTRES, this term may be eliminated from the motion equation by setting a preprocessor flag to avoid the costly calculation of sines and cosines (to establish the direction of $\vec{n}$) every iteration only to multiply them by a zero imbalance

distance.

2.2.2 Algorithm

Preliminary investigation for the MIT microengine using Jacobson's 4x1 mode Galerkin code [40] indicated that, due to the design constraints outlined in Sec. 1.3, the bearing's operating eccentricity at low speed would be nearly 98%. Throughout the operating range, in fact, the required eccentricity was predicted to be above 90%. This finding implied that further work was required because, as discussed in Sec. 1.4.1, the 4x1 Galerkin code's accuracy is called into question at high eccentricity by its small number of modes. Unfortunately, for reasons detailed by Orr [34], extension to a significantly greater number of modes was not feasible with the techniques in use at the time.

Because fixed-point operation appeared unlikely at this point, it was deemed necessary to investigate the feasibility of deliberate operation in a whirling mode, at least at low speed [47]. Furthermore, it was recognized that significant imbalance could be imparted by the complex manufacturing process, noncircular bearings might be adopted to improve stability, and circumferentially-nonuniform pressures would almost certainly be used to provide loading.

With these issues in mind, the requirements for a new design tool were defined. First, its accuracy must be acceptable at high eccentricity. Second, the accuracy should be easily adjustable to decrease the computational cost of lower-eccentricity calculations in order to enable the exploration of a large design space. Third, the tool should be capable of handling nonlinear orbits, such as whirls and imbalance orbits, preferably without *a priori* assumptions about the orbit shape. Finally, the tool should be flexible to enable the rapid addition of new models as new possibilities are suggested.

Orbit Method

Of all the bearing analysis techniques currently in the literature, only the orbit method is suitable for analyzing the stability of journals about a static point as well as those in motion without *a priori* assumptions about the shape of their motion or its period. First applied by Castelli and Elrod [41], this method is perhaps the most intuitive of the many techniques for bearing stability evaluation. It consists of coupling the fluid and motion equations and marching them together in time. In effect, the computation functions as a well-controlled experimental rig. The orbit method is thus inherently flexible because no *a priori* assumptions about the journal's steady-state position or its orbit are required. It is also relatively straightforward to add models of physical phenomena such as imbalance, external damping, or non-circular geometries. Not surprisingly, this generality is accompanied by an increased computational expense. Choosing an efficient solution method is therefore imperative to creating a practical tool.

Spectral Methods

Spectral methods are very attractive means for solving the Reynolds equation for self-acting journal bearings due to their periodic and smooth pressure distributions. These methods involve computing the transform of a function and performing derivatives in transform space using well-known coefficient manipulations [48]. Because the transform represents a global approximating function for the nodal data, spectral methods achieve greater accuracy than typical finite difference schemes on a given grid because derivatives involve information from all nodes in the derivative direction. An additional advantage is gained for journal bearing computations: instead of integration of discrete pressures to calculate the net fluid force on the journal, spectral methods allow the pressure to be integrated as a smooth function in transformed space. A computational price is paid for these advantages, however, in time spent performing the transforms.

In "non-interpolating" methods, such as Galerkin's method, the expansion coefficients are chosen by requiring that the residual be orthogonal to the truncated series [48]. While this results in an efficient estimate in terms of the number of required coefficients, it requires integration over the transform direction.

Cheng and Pan [16] and Orr [34] performed this integral analytically, taking advantage of trigonometric cancellations. Because they performed the integral by hand, Cheng and Pan were limited to two modes in the circumferential direction and one mode in the axial direction. Orr took advantage of pattern-recognition capabilities of MATHEMATICA [49] to produce 24 modes in the circumferential direction. In either case, it is not possible to adjust the number of modes at run-time to suit the needs of the problem. In addition, many of the trigonometric cancellations in the expansion are a result of assuming a circular bearing, which produces a sinusoidally-varying height. Expansion to noncircular bearings is therefore nontrivial.

In "interpolating" methods, including the current pseudospectral method, the expansion coefficients are chosen by requiring that the truncated series match the input function exactly at a set of nodes. The key feature of this formulation is its ability to employ fast Fourier transforms (FFTs) for determining the expansion coefficients. The number of modes in each direction can then be easily adjusted at run-time to tailor the truncation error to the problem and the computational cost of the expansion scales only as order $N \log_2 N$, where N is the number of modes. The drawback of this method is the efficiency of its coefficient choice: the requirement of an exact match at the nodes is not as stringent as non-interpolating methods' orthogonality requirement.

Because interpolating methods perform expansions on a grid without regard to the governing equation, nonlinearities are trivial to treat: derivatives are computed in frequency space from the expansion coefficients, then transformed back to physical space and simply multiplied together. The resulting method, a combination of global functions and derivative calculation in frequency space with a grid and governing equation in physical

space is often referred to as "pseudospectral."

In view of the requirements placed on SPECTRES from the outset, the pseudospectral method's flexibility outweighs its lower mode efficiency. Furthermore, the gap in efficiency is regained somewhat in terms of the FFT's rapid coefficient calculation.

The efficiency issue may be demonstrated by comparing SPECTRES and Galerkin results over a range of grids. For this comparison, the calculation of journal stability about a static point, such as that performed by Cheng and Pan [16], was chosen because it is quite sensitive to the correct calculation of the steady eccentricity and attitude angle, as well as the unsteady stiffness and damping. This comparison is presented in Fig. 2.6 in terms of the "speed parameter" employed by Cheng and Pan. The 4x1 Galerkin results were obtained from Jacobson's extension of their work [40]. The 32x8 SPECTRES result is grid-converged and will be considered the "correct" answer for the purposes of this comparison.

It can be observed in Fig. 2.6 that the 4x2 pseudospectral results underpredict the critical speed parameter at all eccentricities studied. At 8x2, the pseudospectral results compare reasonably with the high-order solution at low eccentricity. More importantly for the purposes of this comparison, the 8x2 SPECTRES and 2x1 Galerkin results are roughly equivalent throughout the studied eccentricity range, supporting the above efficiency arguments. This 4:1 mode ratio does not hold for the 4x1 Galerkin, however. This solution breaks away from the high-order result at high eccentricity while the 16x4 SPECTRES solution retains its agreement.

Another significant observation can be made from Fig. 2.6: the eccentricity at which a given resolution begins to fail is relatively insensitive to speed. Both the 2x1 Galerkin and the 8x2 SPECTRES solutions disagree noticeably from the high-order solution for $\epsilon > 0.6$ at all three bearing numbers. The extension of the Galerkin method to 4x1 modes moves this boundary to $\epsilon > 0.7$. In this case, the solution becomes indistinguishable from the high-order solution at $\Lambda = 10$ because the trace "curl up" occurs prior to $\epsilon = 0.7$. This finding implies that the low-order schemes may be applied with confidence for bearings whose stability boundaries occur at low eccentricity, defined roughly as $\epsilon < 0.5$. If the result predicts a high eccentricity, a higher-order scheme should be used to verify the solution.

Equation Selection

Because the greatest computational effort in the pseudospectral method is expended performing the transforms, selecting a Reynolds equation formulation that minimizes their number is crucial to obtaining an efficient algorithm. Toward this end, following Ausman [36], Ψ is defined as the pressure, p, times the channel height h. The Reynolds equa-

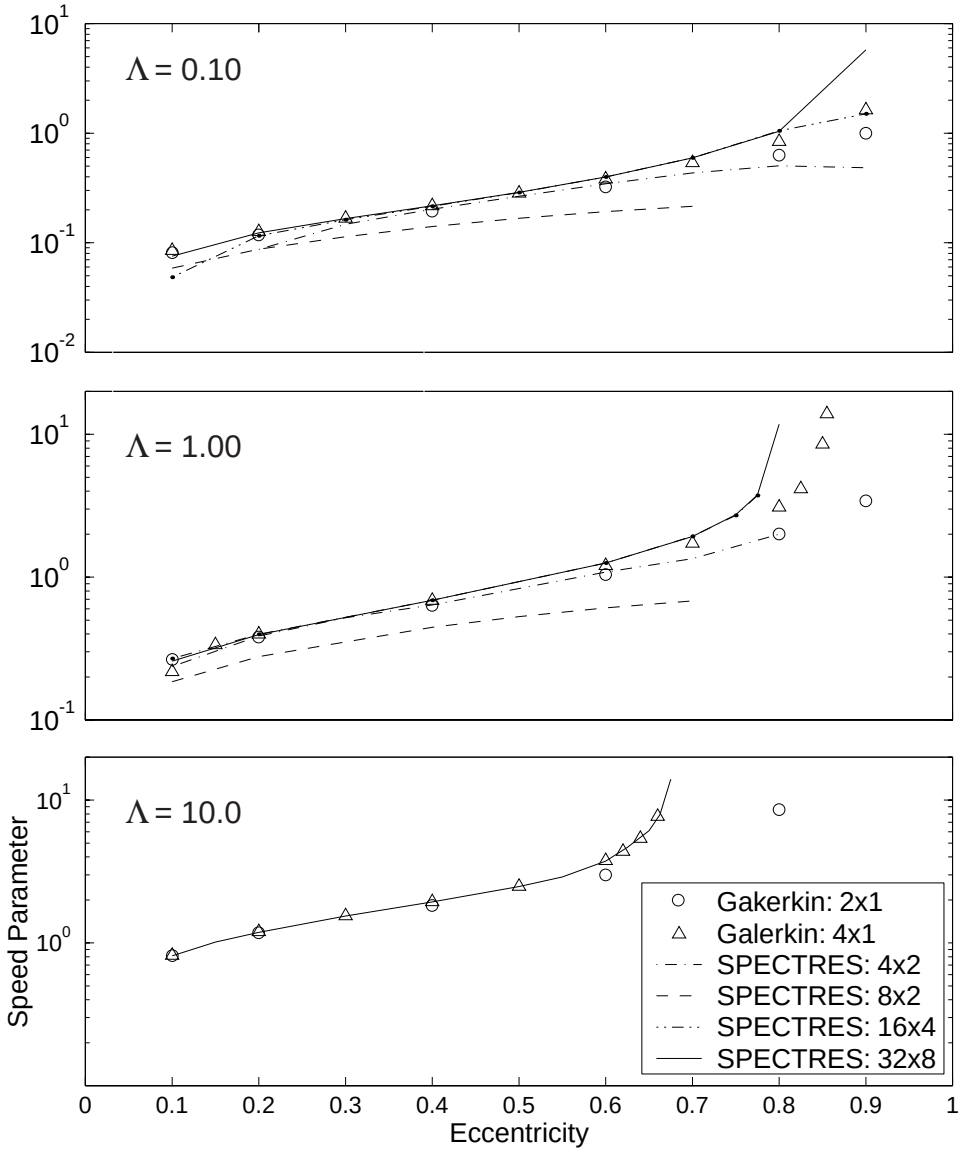

Figure 2.6: Comparison Galerkin and SPECTRES stability predictions for an $L/D = 0.25$ bearing. The 2x1 Galerkin method produces reasonable results at load eccentricity while the SPECTRES requires 8x2 modes for comparable accuracy. Furthermore, the breakdown of a given resolution appears to occur at an eccentricity that is independent of speed.

tion, presented in Sec. 1.2.3, may then be expressed as:

$$\begin{aligned} 2\Lambda\frac{\partial\Psi}{\partial\tilde{t}} &= h\Psi\left(\frac{\partial^2\Psi}{\partial\theta^2}+\frac{\partial^2\Psi}{\partial\xi^2}\right)-\Psi^2\left(\frac{\partial^2 h}{\partial\theta^2}+\frac{\partial^2 h}{\partial\xi^2}\right)-\Lambda\frac{\partial\Psi}{\partial\theta} \\ &\quad -\Psi\left(\frac{\partial h}{\partial\theta}\frac{\partial\Psi}{\partial\theta}+\frac{\partial h}{\partial\xi}\frac{\partial\Psi}{\partial\xi}\right)+h\left(\left(\frac{\partial\Psi}{\partial\theta}\right)^2+\left(\frac{\partial\Psi}{\partial\xi}\right)^2\right), \end{aligned} \tag{2.6}$$

This equation differs from that employed by Cheng and Pan only in the absence of a grid rotation term and the inclusion of axial height variation. It is very convenient for a spectral method because it is devoid of cross-derivatives and, in total, only four spatial derivatives of Ψ must be computed. Just two forward transforms and four backward transforms are therefore required per timestep. Derivatives of h are performed analytically.

Basis Function Selection

For maximum efficiency in a spectral method, it is also important to choose a transformation that requires the minimum number of modes to reach the target accuracy. In the circumferential direction, full Fourier modes are a logical choice due to the periodic boundary conditions and the lack of symmetry about the coordinate axes. These were also chosen by Cheng and Pan. In the axial direction, a single sine mode is often employed; for this work, Chebyshev polynomials were chosen.

Using polynomials rather than trigonometric functions in the axial direction is an important step toward creating a flexible and efficient pseudospectral Reynolds equation solver for low L/D bearings. Flexibility improvement is gained from the ability to enforce different boundary conditions at the each end, the application of which will be demonstrated in Sec. 5.1. Efficiency improvement is related to the fact that an incompressible short bearing has a parabolic axial pressure distribution [50]. It may therefore be argued that the pressure distribution remains at least somewhat parabolic for reasonable bearing numbers. A large number of trigonometric modes are necessary to accurately represent a parabola due to its inherent non-periodicity: patterning a parabola into a full-wave function yields discontinuous first derivatives and patterning it into a half-wave function yields discontinuous second derivatives.

To demonstrate this phenomenon, the coefficient magnitudes as a function of wavenumber k and polynomial order n for sine and Chebyshev expansions, respectively, are shown in Fig. 2.7 for an axial pressure distribution at the minimum passage height. The depicted case is an L/D=0.075 bearing at Λ=1 and ϵ=0.8 but the trend is typical (the same trend is reported at $L/D=0.5$ in [51], for example). Because the second derivative appears discontinuous to the sine series, the coefficients decay as $\mathcal{O}(1/N^3)$. In contrast, the Chebyshev expansion exhibits “exponential convergence”, where the coefficients shrink faster than $1/N^q$ for any finite q, with N representing the number of terms in the expansion. Noting that the sum of the absolute values of the neglected coefficients forms the upper bound on

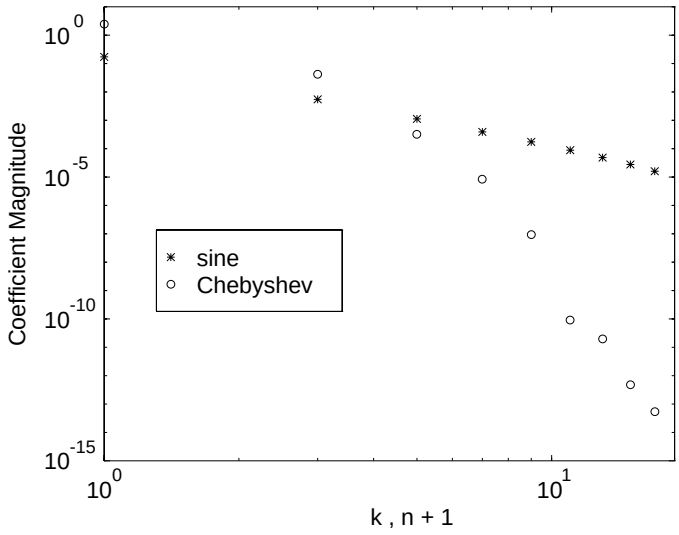

Figure 2.7: Power spectrum for sine and Chebyshev expansions of the axial pressure distribution for an L/D=0.075 bearing at ϵ=0.8, Λ=1.

the truncation error [48], it can be seen that more terms must generally be used in a sine series to drive the error below a given level.

Time Integration

A third-order Adams-Bashforth scheme was chosen for time integration to prevent phase errors in the numerical method from affecting the bearing dynamics. This issue was investigated by Coleman [52]. For most cases, this choice is over-cautious because stability constraints imposed by the Reynolds equation integration restrict the time step to a small fraction of the rotational period. Fortunately, due to the small number of nodes, storing information from step to step brings little increased cost.

Through an empirical investigation, a good estimate of the appropriate timestep for most of the L/D's and grids used in this document may be obtained through:

$$\Delta t = 21.6 \frac{\Lambda}{N_z^4} \left(\frac{L}{D} \right)^2 \tag{2.7}$$

Fixed-Point Stability Determination

For bearings without imbalance, the ability of a journal to return to a fixed operating point may be determined automatically in SPECTRES. This is accomplished by converging the steady-state flowfield, increasing the eccentricity and decreasing the attitude angle by 0.001%, releasing the journal, and observing the eccentricity over time. Example orbits from stable and unstable cases are shown in Fig. 2.8. In this presentation, the solid line represents the journal center. The dashed line represents positions where the journal surface would first make wall contact. The initial perturbation is increased by several orders

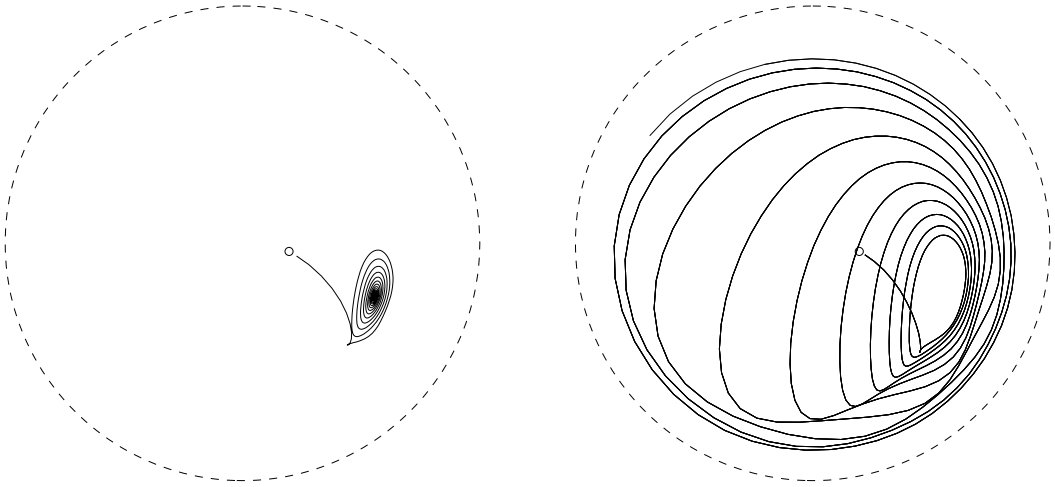

(a) Stable **(b)** Unstable

Figure 2.8: Sample orbits for stable and unstable cases, with "stability" defined in terms of the journal's ability to regain fixed point operation following a perturbation. The starting point is indicated by '$\circ$' and the dashed line denotes positions involving wall-contact. For visibility, the initial perturbation is several orders of magnitude larger than those used in SPECTRES.

of magnitude to make the stable case visible.

The magnitudes of the waveform extrema are monitored to judge the orbit either convergent or divergent. If the most recent maximum is larger than its predecessor and the most recent minimum is smaller than its predecessor, then the case is ruled unstable. Cases exhibiting the opposite behavior are ruled stable and cases which satisfy neither criteria are marched forward in time until a decision can be made. As an additional check, the amplitude of the oscillation, or the maximum minus the minimum, must also increase or decrease for an orbit to be ruled stable or unstable, respectively.

The choice of eccentricity or attitude angle monitoring may be indicated by a preprocessor switch. In this work, it was found that attitude angle monitoring was generally a better choice because the eccentricity waveform at high bearing numbers often exhibited a stable high frequency transient that took many rotations to decay. While this mode was also visible in the attitude angle, it was generally weaker. This finding supports Jacobson's observation [40] that the unstable eigenvalue, when approaching the boundary from below, is associated with the attitude angle. Orr [34] later showed that the high frequency mode, primarily associated with the eccentricity, can also become unstable at very high eccentricities. This issue will be discussed in Sec. 3.2.3.

The variable under search is increased or decreased in a bisection method until the step decreases to the desired uncertainty, expressed in terms of a fraction of the search variable. Searching may be performed for either critical ζ, ϵ, $\bar{M}$, or Λ. Ranges of non-

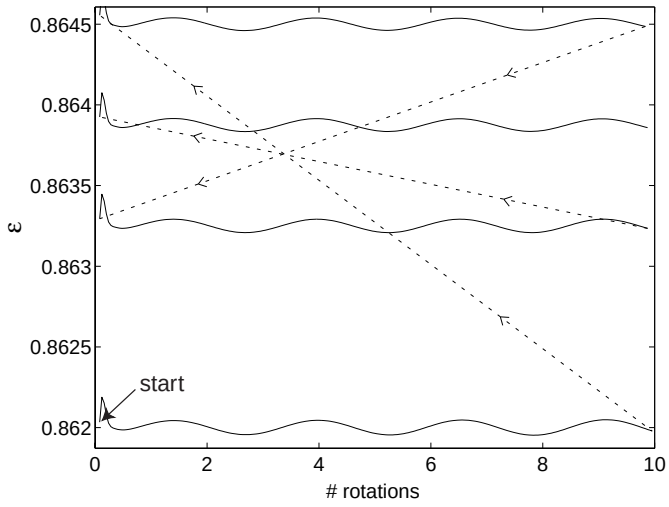

Figure 2.9: Eccentricity progression in a fixed point stability search on ϵ.

search parameters may be swept automatically to construct stability boundaries.

A sample eccentricity search is shown in Fig. 2.9. In this case, the initial eccentricity proves to be unstable, so it is increased by the initial stepsize and the calculation is repeated. The second case proves to be stable, so the stepsize is halved and subtracted from the initial eccentricity and the calculation is repeated. The third case is then unstable, so the stepsize is again halved and added to the previous eccentricity and the calculation is repeated. The fourth case is stable. Another halving of the stepsize brings it below the stopping criterion so the calculation ceases and the fourth case eccentricity, minus the final stepsize, is reported as the stability boundary.

Side-Pressurization Modeling

Bearing loading through application of a circumferentially-nonuniform pressure at one end (see Sec. 5.1 for a description and motivation) is modeled through a simple change of boundary condition. Nodes that fall within the boundaries of a side-pressurization plenum are set to that plenum's pressure. To avoid discontinuous first derivatives at the plena edges, nodes that fall between plena are set according to a half-wave cosine distribution with endpoints at the surrounding plena pressures.

Noncircular Bearing Modeling

To incorporate the effects of noncircular bearings (see Sec. 4.1 for description) with maximum generality, SPECTRES accepts geometries in the form of equally-spaced points around the bearing circumference. To speed the calculation, as well as to separate noncircular geometries from the intrinsic part of the code and maintain a clear definition of the clearance, input points measure the desired shape's departure from circularity, rather than its profile.

With this arrangement, the channel height at an angular location θ is given by:

$$h = 1 + \epsilon \cos(\theta - \phi) + \delta_r(\theta) \tag{2.8}$$

δ_r is the difference between the geometry's radius at a given point and that of a circle with the same mean clearance, normalized by the mean clearance.

Because ϕ is the only time-dependent term in Eq. 2.8, this formulation allows the channel height increments and derivatives associated with noncircularity to be calculated at startup and used throughout the calculation without regard to journal position.

To calculate the derivatives, and to estimate height changes at the nodes if the input file contains a different number of points, the data are Fourier expanded. The radius variation is forced to a zero mean by eliminating the zeroth-order coefficients of the expansion. Derivatives are then performed in transform space and transformed back, along with the function δ_r, to physical space and sent to the SPECTRES kernel.

Axial Height Variation Modeling

The method chosen for axial height variation modeling (see Sec. 4.2 for description) is similar to that described above for noncircular geometries. In this case, two additional terms are required in the Reynolds equation to account for nonzero height derivatives in the axial direction. For the remaining terms, the channel height increment as a function of axial position is simply added to the h from the cylindrical case wherever it appears outside a derivative.

As in the noncircular case, introducing axial variation opens a question as to where to measure the clearance. In order to maintain the interpretation of $\epsilon = 1$ as a wall-strike, the clearance is measured at the axial location with the smallest average height. In this case, however, a wall-strike takes place at a single axial location rather than along the entire bearing length.

Two axial height distributions are implemented: linear and hyperbolic. At run time, SPECTRES prompts for the type of variation to be modeled (linear, hyperbolic, or none) and the amplitude of the axial clearance variation, normalized by C. The derivatives and height increments as a function of axial location are then calculated from analytical expressions for use in the calculation. As with noncircular geometries, this data need only be calculated once because the circular component absorbs the geometry's time dependence.

2.2.3 Validation

Because SPECTRES contains a variety of models, many test cases were required to gain confidence in the code before it was applied to new problems. Where possible, SPECTRES results were compared against those of other authors. Where such data was not available,

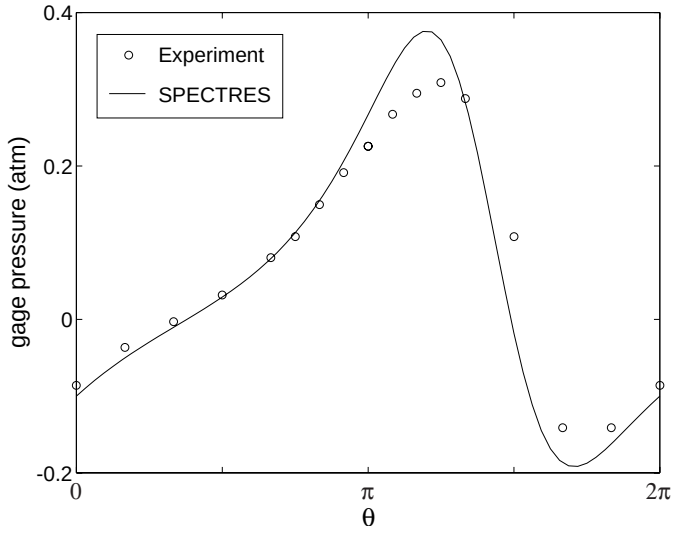

Figure 2.10: Computed and experimental pressure distributions for a plain journal bearing running at 15,000 RPM with a 69 N load.

"sanity checks" were performed to ensure the model produced results that were within bounds established by intuition.

Plain Journal Bearings

Steady State

Validation for the plain bearing case was begun by comparison of a SPECTRES pressure distribution with an experimental measurement by Dimofte, Addy, and Walker [1]. This data was obtained (in both SPECTRES and the experiment) by loading the bearing to the prescribed level at a given speed and allowing it to move to its steady-state position. The resulting pressure distributions are shown in Fig. 2.10 for a bearing running at 15,000 RPM loaded with a force of 69 N. Good agreement is obtained, though it appears that SPECTRES predicts a larger pressure peak and a lower attitude angle. One possible explanation of the error trend is shaft / bearing misalignment, which is common in bearing experiments and tends to reduce the pressure extrema. The data are also consistent with a lower bearing number for a fixed load parameter, or a lower load parameter for a fixed bearing number, so uncertainty in calculating these parameters from the published information on the geometry and running condition can also cause error of the type shown in Fig. 2.10.

To verify the proper operation of SPECTRES' basic Reynolds equation solver over a range of parameters, a series of steady-state cases were run. In these cases, the journal was held in place at a given eccentricity and the amplitude and direction of the fluid force was measured. This exercises all terms in the equation except the axial height derivatives, and, of course, the time derivatives, both of which will be investigated in subsequent sections.

The comparison data for this study was obtained from work by Raimondi [11] in which

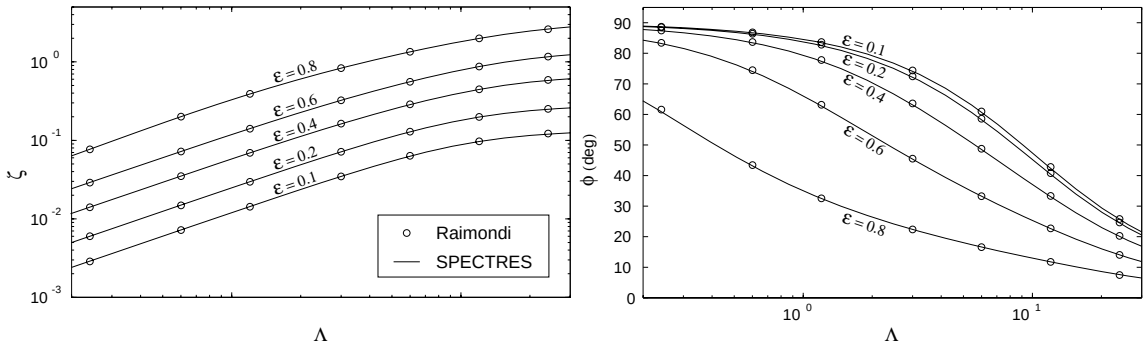

(a) Load Parameter **(b)** Attitude Angle

Figure 2.11: Comparison of steady-state load parameter and attitude angle results for an $L/D = 0.5$ bearing. SPECTRES was run with half the nodes in each direction used in Raimondi's finite difference scheme.

he computed finite difference solutions for journal bearings with various L/D's. Due to the care with which Raimondi prepared this data, his has become the de-facto standard for validation of steady-state results.

The comparison of Raimondi's data with SPECTRES' output is presented in Fig. 2.11. The agreement is excellent for both load parameter and attitude angle over the entire range of bearing number and eccentricity presented. In addition, in a demonstration of the efficiency of spectral methods, this agreement was obtained with SPECTRES running half as many nodes in each direction as Raimondi's finite difference scheme.

Stability

To test the time derivative term in the Reynolds equation, as well as the basic motion equation, the stability of plain cylindrical journal bearings was computed and compared to experimental data obtained by Sternlicht and Winn [53]. Their experimental setup consisted of a rotor supported by two journal bearings and driven with an air impulse turbine. This assembly was mounted on a rotating fixture to enable the bearing load to vary between zero and the shaft weight. Their experiments involved holding the load at a constant value and increasing the speed until an onset of whirl was observed. This speed was then labeled a "threshold speed" and the operation was repeated for a range of loads and three different bearings. A comparison of their data to SPECTRES' results is presented in Fig. 2.12.

Good agreement between these results is obtained across the two orders of magnitude in $\bar{M}$ and Λ and one order of magnitude in ζ. The maximum error in the data presented is 18% and occurs for low $\bar{M}$ and high ζ. In general, the agreement appears to worsen as $\bar{M}$ decreases. One source of this disagreement may be the existence of an orifice in the bearing surface on the experimental rig, which was used to prevent rubbing during starting and

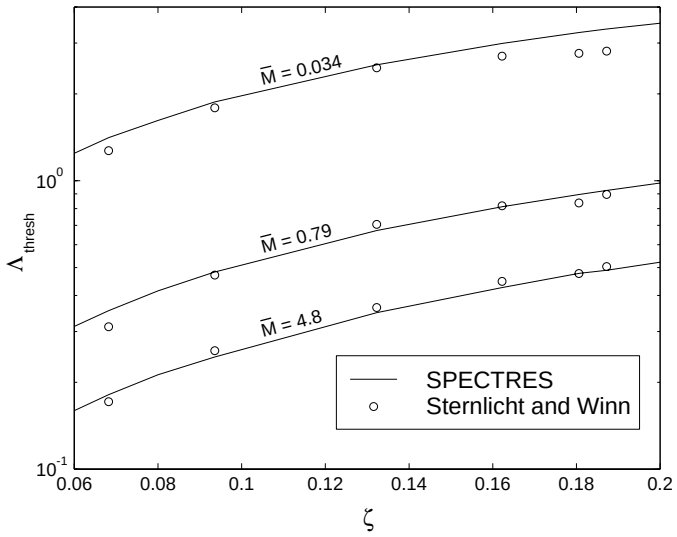

Figure 2.12: Comparison of SPECTRES results with experimental data for the whirl threshold speed of bearings with $L/D=1$ and three values of $\bar{M}$.

stopping and to control whirl amplitude. For the data presented, the orifice was plugged and rotated to a position opposite the resting journal location under load. This arrangement should produce the minimum orifice effect, though the authors note sensitivity of the stability boundary to orifice location even for the plugged case. The sensitivity to orifice location was also noted to increase with decreasing clearance, though for the open orifice case. In terms of the nondimensional parameters of Fig. 2.12, decreasing clearance implies a smaller $\bar{M}$, thus their finding is consistent with the increasing error with decreasing $\bar{M}$ trend observed with SPECTRES' output because the orifice was not modeled.

Imbalance

To validate the imbalance term in the equation of motion, as well as verify the unsteady terms in the Reynolds equation for large amplitude motion, a series of calculations with imbalance were performed and compared to experimental data collected by Sternlicht and Elwell [54]. In this experiment, a 2" diameter rotor was mounted vertically and run with varying levels of imbalance imparted via bolt-on weights. The rotor was spun using an electric motor attached with a flexible quill and the position of the rotor was monitored with four capacitance probes. Because the static load is negligible, the observed orbits under imbalance will be centered and their radii will be the maximum eccentricities measured by the capacitance probes.

The eccentricity data for a number of speed-imbalance combinations are provided in Fig. 2.13 for $L/D=1$ and $L/D=2$ bearings. The raw data show significant disagreement at higher speeds, with the disagreement increasing for the higher imbalance level and higher L/D. The trends, however, match very well. Most notably, the SPECTRES traces exhibit

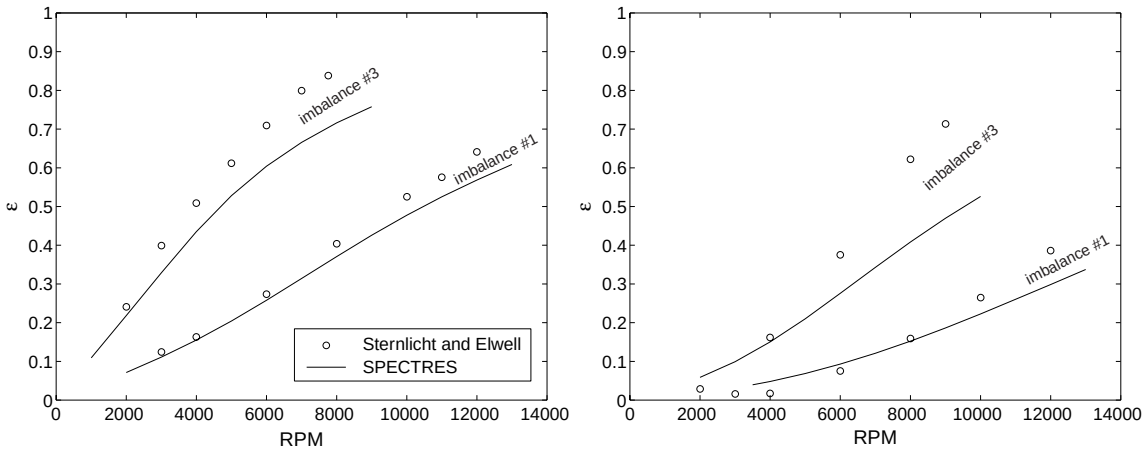

(a) $L/D = 1$ **(b)** $L/D = 2$

Figure 2.13: Comparison of SPECTRES results with experimental imbalance response measured by Sternlicht and Elwell [54].

the change in concavity observed in Ref. 54 when the L/D is doubled.

Centrifugal growth of the rotor presents one possible explanation for the quantitative disagreement. As shown in Fig. 3 in Ref. 54, a hollow rotor (11/32" wall thickness on a 2" rotor) was utilized in the experiments. Because the clearance was less than $13\mu m$, it can decrease significantly at higher speeds due to small radial strains. Such a decrease would increase the running bearing number, measured eccentricity, and imbalance ratio. These effects push the data toward better agreement. Unfortunately, decreasing the clearance will also decrease $\bar{M}$, which pushes the data toward poorer agreement.

To evaluate this possibility, the bearing numbers for the experimental data were recalculated from the reported rotation rates assuming that the clearance varied according to the following relationship [55]:

$$c = c_o + \frac{\rho_s R^3}{E}\omega^2 \tag{2.9}$$

c_o is the reported clearance at zero speed and ρ_s and E are the density and Young's modulus of steel and the rotor is assumed to be a hollow cylinder. The actual rotor has a solid section at its midspan so Eq. 2.9 represents the largest likely clearance shrinkage.

When the imbalance response was recalculated using the above expression, little difference was visible in the solution. While Λ and δ_u increased due to clearance shrinkage, which reached as high as 18% and 9% at 12,000 RPM, the effect was almost perfectly canceled by the decrease in $\bar{M}$, which reached 34% at 12,000RPM. Furthermore, the decrease in Sternlicht and Elwell's reported eccentricity after clearance adjustment was not sufficient to close the gap between traces in Fig. 2.13.

Because the journal motion in this case is circular and concentric with the bearing, the Reynolds equations may be solved in a rotating coordinate system to find the appropri-

ate load and attitude angle (rather than solving the Reynolds equations in tandem with the motion equations with an imbalance forcing term, as is done is SPECTRES). In this case, the attitude angle refers to the phase difference between the imbalance forcing and the journal position. Sternlicht and Elwell performed such an analysis and observed error of the same type shown Fig. 2.13, *i.e.* a reduced load capacity at a given speed, leading to higher eccentricity for a given rotating load. Also, as observed with SPECTRES' results, their error increases as the speed increases, reaching as high as 35% for $L/D = 2$ at 12,000 RPM.

Sternlicht and Elwell offer a number of explanations for the disagreement between their computation and experiment, including non-circularity and taper of the test bearings and journal and misalignment due to skewing of the shaft centerline during testing. As will be shown in Sec. 4.2, taper significantly reduces load capacity. This is also true for misalignment, as has been shown by several authors. Both of these explanations are supported by the fact that the error appears greater for the larger L/D bearing.

In conclusion, the trends computed using SPECTRES agree quite well with Sternlicht and Elwell's experimental data, including the concavity change when L/D is increased. The quantitative difference between the data, while significant, have several physical explanations noted by the authors, who found a similar difference in their own calculations. This fact, combined with the simple, uncontroversial nature of the imbalance model and the good agreement between SPECTRES and Sternlicht and Winn's unsteady data, implies that SPECTRES' imbalance formulation is indeed correct.

Noncircular Geometries

Steady State

Steady-state validation for the noncircular bearing was accomplished in a similar manner to the circular case. Example cases were drawn from recent publications on a bearing with a sinusoidally-varying clearance known as a "wave bearing" [30] (see Fig. 4.1). First, the computed pressure distribution was compared to an experimental measurement made by Dimofte, Addy, and Walker [1] on a bearing whose shape is described by three sinusoidal cycles. This comparison is shown in Fig. 2.14 for a bearing with a wave amplitude normalized by the mean clearance, a_{nc}, of 0.547.

Overall, the data agree quite well. The maximum error between the experimental data and SPECTRES' results at the tallest pressure peak is 15%. An even better match is obtained between Dimofte's computations and SPECTRES' results, with a maximum error of only 4% at the primary peak, though the disagreement at the upstream peak increases.

As an additional validation measure, the dependence of load parameter on the wave shape's phase for a fixed speed was checked against calculations performed by Dimofte [30] in Fig. 2.15. In this case, $L/D = 1$, $\Lambda = 1$, and $a_{nc} = 0.4$. (Note that the wave phase

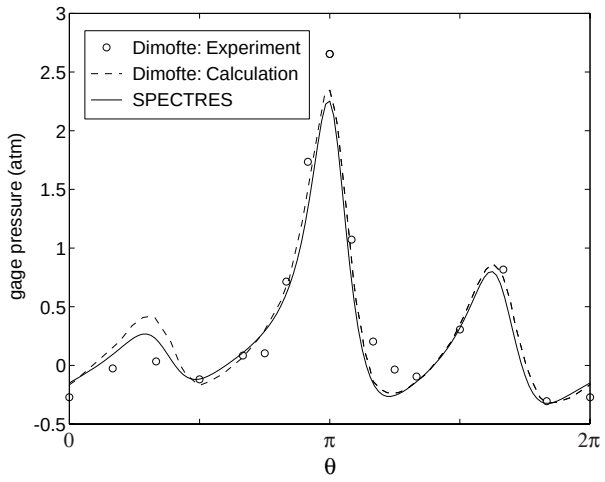

Figure 2.14: Computed and experimental pressure distributions for a three-wave bearing with $a_{nc} = 0.547$ running at 15,069 RPM with a 141 N load. A computational result reported in [1] for this case is also included for reference.

angle in Dimofte's work is measured in a direction opposite that used in Sec. 4.1.)

In this case, the two computations are virtually indistinguishable. A major reason for the improved agreement is the decrease in uncertainty about the running conditions for the published data effected by its provision in nondimensional form.

Stability

Dimofte's calculations [30] were also employed to evaluate SPECTRES stability predictions for noncircular bearings. In this case, the quantity reported by Dimofte as the "dimensionless critical mass", which is $\Lambda^2 \bar{M}$, was calculated as a function of wave position angle for an $L/D = 1$ bearing with wave amplitude 0.2 at $\Lambda = 1$.

The resulting comparison is presented in Fig. 2.16. Once again, the agreement is excellent for all wave position angles. This observation provides further evidence for the fidelity of SPECTRES' noncircular formulation, as well as its unsteady model in the context of small amplitude motion.

2.3 Chapter Summary

In this chapter, the two numerical tools developed for this work were described: BASICS, for *B*earing *A*nalysis *S*uite for *I*nvestigating *C*ommon *S*implifications, and SPECTRES, for *SPEC*tral *R*eynolds *E*quation *S*olver.

BASICS employs the Navier-Stokes equations for fluid modeling and is intended for investigation of effects neglected in common lubrication analyses such as inertia and heat transfer. It is a 2-D formulation, treating the radial and circumferential directions, thus it models flows in very long bearings. The computation is steady-state and therefore gen-

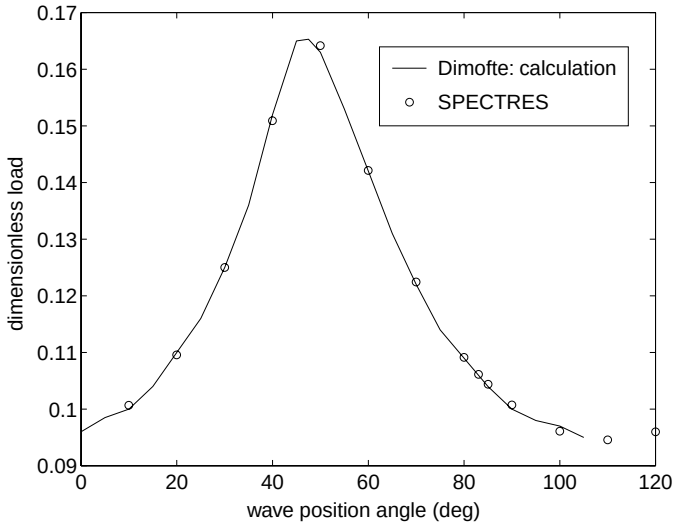

Figure 2.15: Comparison between SPECTRES and Dimofte steady-state results for a 40% wave bearing at $\Lambda = 1$ and a range of phase angles.

erates load capacity, attitude angle, and drag data, as well as flowfield features such as temperature and pressure distributions.

SPECTRES employs the Reynolds equation for fluid modeling and therefore functions under the lubrication assumptions. It employs a pseudospectral technique for solving the Reynolds equation and can treat bearings of arbitrary length. The "orbit method" formulation, where the code serves as a numerical experiment by fully coupling the fluid and motion equations, allows general motions to be investigated without *a priori* assumptions about their shape. The combination of pseudospectral Reynolds equation treatment and orbit method also makes inclusion of additional models straightforward. Current features include imbalance, noncircular geometries, side-pressurization loading, and axially-varying clearance modeling.

The validation measures used to gain confidence in the proper formulation and construction of both these tools were also presented. In all cases, comparison between the current results and the experiments or computations of other researchers was within the uncertainties in the reported data or conditions.

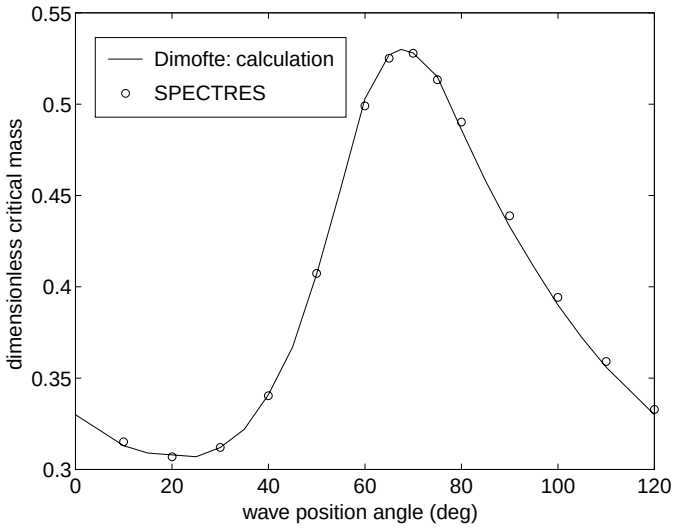

Figure 2.16: Comparison between SPECTRES and Dimofte stability results for a 20% wave bearing at $\Lambda = 1$ and a range of position angles.

Chapter 3

Plain Bearings

This chapter details the effect of various design parameters on the performance of plain journal bearings. In this context, "plain" implies that both the journal and the bearing are circular, cylindrical, complete, and without additional features such as tilting pads [56], grooves [28], or foils [10]. The meaning of the term "performance" itself will also be explored as various metrics are discussed.

3.1 Steady-State Behavior

As outlined in Sec. 2.2, SPECTRES may be run in a "steady mode", where the journal is held at a desired position and the pressure field is calculated around it. The load capacity, attitude angle, and bearing drag may then be easily computed for a given running state. It must be kept in mind, however, that this state may not be attainable by a particular bearing because the calculation is done without regard to its dimensionless mass, $\bar{M}$, or other time-dependent effects such as imbalance. These considerations will be treated in subsequent sections.

3.1.1 Load Capacity and Running Position

The load parameter and attitude angle from a steady-state calculation are presented in Fig. 3.1 for an $L/D = 0.075$ bearing. This L/D corresponds to a $4mm$ diameter rotor etched from a $300\mu m$ wafer. A set of charts for $L/D = 0.5$, which is more typical of a macro-scale bearing, is also included for comparison.

Comparing Figures 3.1 and 3.2, it is immediately evident that reducing L/D has a drastic effect on the load parameter. For instance, a 6.7x reduction in L/D produces nearly a two-order-of-magnitude reduction in ζ at a given eccentricity at low Λ. Across the entire depicted speed range, the load parameter at $\epsilon = 0.8$ for $L/D = 0.075$ is comparable to that of $\epsilon = 0.1$ for $L/D = 0.5$. A smaller L/D therefore implies a much greater eccentricity if a given load parameter is required.

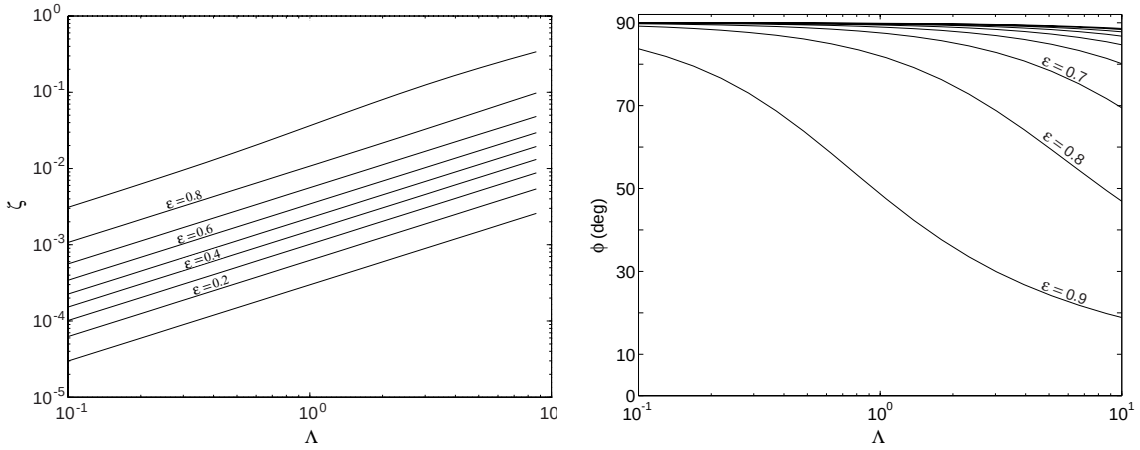

(a) Load Parameter **(b)** Attitude Angle

Figure 3.1: Steady design charts for a journal bearing with $L/D = 0.075$

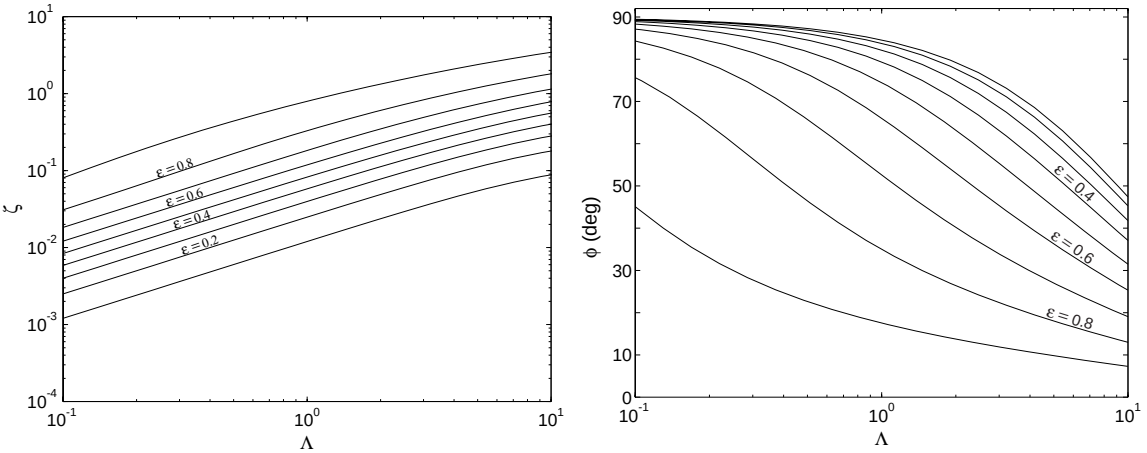

(a) Load Parameter **(b)** Attitude Angle

Figure 3.2: Steady design charts for a journal bearing with $L/D = 0.5$

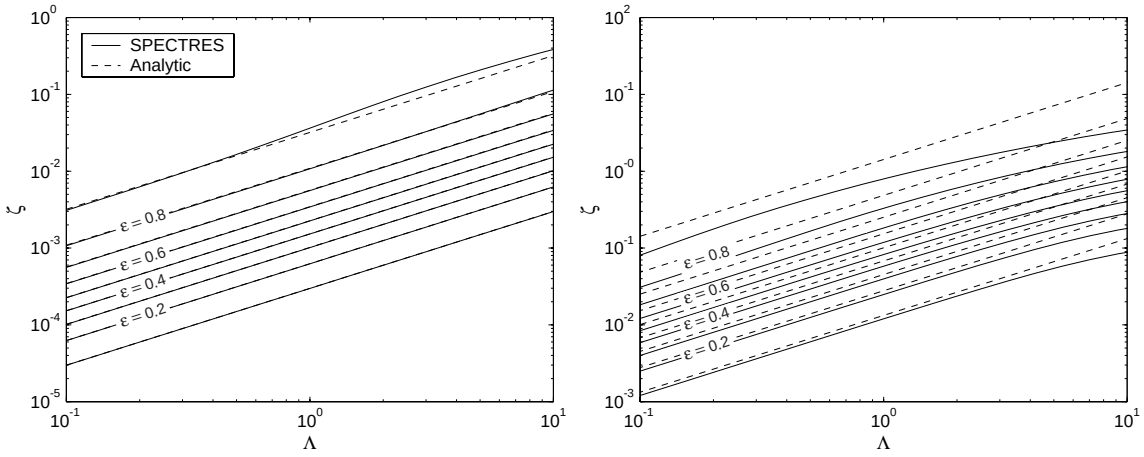

(a) $L/D = 0.075$ **(b)** $L/D = 0.5$

Figure 3.3: Comparison of computed load parameters with an incompressible short bearing solution.

In many machines, the bearings are designed to carry a given dimensional load, W. In this case, the effect of L/D on the required eccentricity is not easily obtained in the format of the previous figures because ζ has an L and a D in its denominator. Further complications arise if changes in the diameter are studied because D also appears in Λ.

For short bearings, insight into tradeoffs may be gained through examination of the analytic solution for an incompressible short bearing. Generally considered valid for bearings with $L/D \leq 0.5$ running at low speeds and eccentricities, this solution yields an expression for load capacity given by [12]:

$$W = \frac{\mu R \omega L^3}{2C^2} \frac{\pi \epsilon}{(1-\epsilon^2)^{3/2}} \tag{3.1}$$

or, nondimensionally:

$$\zeta = \frac{\Lambda}{6} \left(\frac{L}{D}\right)^2 \frac{\pi \epsilon}{(1-\epsilon^2)^{3/2}} \tag{3.2}$$

The results of Eq. 3.2 are compared to the calculated load parameters of the previous figures in Fig. 3.3. The agreement is remarkable for the $L/D = 0.075$ case. Poorer agreement is obtained in the $L/D = 0.5$ case because it is on the boundary of the accepted L/D range for the short bearing approximation. The agreement is sufficient, however, to use the above expressions to study the trends in load capacity.

Pushing forward with this study, a number of observations are possible. First, the strong variation of ζ with L/D is explained by Eq. 3.2, which shows a square dependence. Second, the dimensional load capacity, W, is insensitive to the diameter if the linear speed at the bearing's edge, $R\omega$, is held constant. This is a realistic constraint for tradeoffs in

turbomachines with journal bearings on the compressor rim because, as mentioned previously, a centrifugal compressor's pressure ratio increases strongly with tip Mach number [31]. It is thus desirable to hold the rim speed constant to maintain the power level and efficiency of the overall engine through the study.

Further inspection of Eq. 3.1 reveals a cubic dependence on the length. Shortening a bearing therefore dramatically decreases its load capacity at a given speed and eccentricity under this approximation. In addition, the clearance appears as a squared term in the denominator of Eq. 3.1. Increased clearances therefore result in significant decreases in dimensional load capacity. Combined, these observations are particularly troublesome for microfabricated bearings because etching become more difficult and expensive as the etch aspect ratio, in this case C/L, decreases. The dimensional load capacity is therefore proportional to the inverse of C/L, or the expense of the etch, squared.

A bright note on this finding is that the reduced load capacity of the short bearing is an advantage when it is necessary to load a bearing to a given eccentricity via side-pressurization. As discussed in Sec. 1.3.3, this is almost always the case for microturbomachines due to their low load parameters due to weight and their high speeds. Smaller load requirements imply smaller pressure differences acting across the rotor's projected area. Reduced loading pressures are desirable for self-contained machine because 1) they are more easily produced in the system and 2) they result in smaller bleed air mass flows.

The departure from linearity of the higher ϵ traces, particularly at the larger L/D, on the steady-state load parameter charts is also explainable via the incompressible solution. This departure occurs at lower Λ as the eccentricity is increased and at lower Λ and lower ϵ as L/D is increased. Noting that, as shown by Eq. 3.2 and Fig. 3.3, incompressible solutions predict a linear distribution everywhere, Raimondi [11] points out that the departure from linearity of the load parameter traces may be used as an indication of the importance of compressibility. In this context, the above observations make intuitive sense because compressibility is likely to become more important as the rotation speed or eccentricity increases. The increase in compressibility effect with length may also be understood physically in terms of the difficulty a particular fluid element encounters in escaping the bearing via axial leakage if it encounters compressive stress in the circumferential direction. The onset of compressibility may also be assessed via the attitude angle traces because the incompressible short-bearing analysis predicts a 90° attitude angle for all conditions. Again, the higher L/D bearing shows an earlier departure from the incompressible solution.

In general, compressibility effects reduce the load capacity at a given eccentricity and speed, thus the constant-ϵ lines curve downward and become constant in Λ (see, for example, the charts in Raimondi [11]). In Fig. 3.3, however, the $\epsilon = 0.8$ and $\epsilon = 0.9$ traces for both L/D break upward from the linear case before curving downward. Thus, for a range of Λ that appears to increase with decreasing L/D compressibility effects improve the load capacity.

Compressibility effects can therefore lessen the leakage-related load capacity disadvantage of short bearings operating at high bearing number and / or eccentricity through two mechanisms. First, due to its earlier onset of compressibility, the longer bearing will suffer greater losses at a given operating point. Second, the increase in load capacity at the onset of compressibility is likely to be larger and survive over a greater Λ range for the shorter bearing. Unfortunately, late onset of compressibility may be problematic for stability because it can be shown analytically that a truly incompressible gas bearing, if it existed, would be unconditionally unstable [57].

3.1.2 Drag

Another design chart commonly constructed from steady-state analyses depicts the nondimensional bearing drag. This is an important factor because, for microturbomachines in particular, bearing power consumption may determine the machine's viability.

In nondimensional terms, the bearing drag is expressed by the "friction variable," $\mathcal{F}$, defined as:

$$\mathcal{F} = \frac{F_v C}{2\pi\mu R^2 \omega L} \tag{3.3}$$

where F_v is the total viscous drag on the journal surface. Physically, this parameter is simply the ratio of the actual drag to that experienced in the concentric position.

The bearing drag is calculated by integrating the shear stresses over the journal surface. It may be observed, however, that the solution of the Reynolds equation (see Sec. 2.2.1) yields only a pressure distribution while shear stress is computed from the tangential flow speed derivative. To close this gap, it is noted that the Reynolds equations are developed by solving the momentum equations for what amounts to a combined Couette-Poiseuille flow after the terms involving C/R are neglected. Recovering flow speed from pressure in this context, it becomes clear that the drag has two components: a Couette contribution that is related to surface motion, and a Poiseuille contribution that is related to pressure gradients.

Through direct integration of the Couette term and integration by parts of the Poiseuille term in the Reynolds equation (see, for example, [11]), the following expression is obtained:

$$\mathcal{F} = \frac{1}{\sqrt{1-\epsilon^2}} + \frac{3\epsilon}{\pi\Lambda}\,\zeta \sin\phi. \tag{3.4}$$

This is a useful result for two reasons: first, the nondimensional bearing drag may be calculated via a closed-form expression from data already in hand, thus it does not add significantly to the computational workload; second, the first term in the drag may be computed without running a steady-state computation at all if the running eccentricity is known from other sources.

Inspecting the load parameter plots in the previous section, it is clear that ζ will be much less than unity for most microbearings. Furthermore, operating points with large

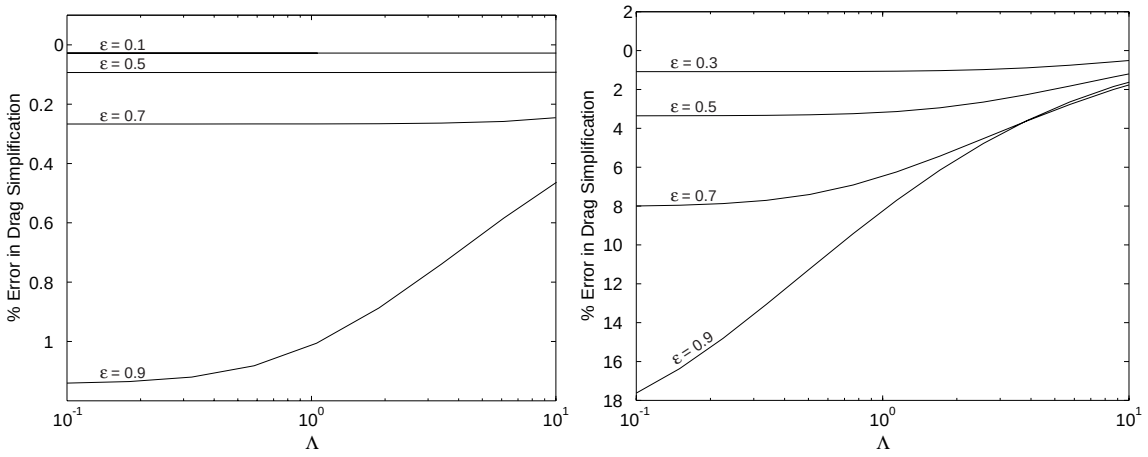

(a) $L/D = 0.075$ **(b)** $L/D = 0.5$

Figure 3.4: Error incurred in neglecting the Poiseuille contribution to bearing drag. The error is less than 2% for the $L/D = 0.075$ bearing at all bearing numbers and eccentricities shown. This error increases by more than an order of magnitude for the $L/D = 0.5$ bearing due to its much larger load capacity.

load parameters tend to have small attitude angles so the sine function will be small. Combined, these considerations tend to reduce the Poiseuille term's importance over the entire operating range. The possibility therefore exists of calculating good drag estimates from the Couette term alone.

The error incurred in calculating $\mathcal{F}$ without the Poiseuille term for both $L/D = 0.075$ and $L/D = 0.5$ bearings is shown in Fig. 3.4. From this figure, it can be concluded that, for most purposes, the drag for the $L/D = 0.075$ bearing may indeed be estimated from only the Couette term. This finding is a boon for designers because this term involves only the eccentricity, greatly simplifying tradeoff studies. For the longer bearing, however, this simplification must be made with caution because the error grows to nearly 20% at high eccentricity and low Λ.

3.2 Unsteady Behavior

In this section, the journal is allowed to move freely under the applied and developed forces, leading to the introduction of time-dependent effects in the fluid equations. The most important of these effects is fractional frequency whirl, which is treated in the first two sections. A second important unsteady phenomenon is imbalance, which is treated in the second section. The final section provides methods for estimating shock tolerance from steady-state data, followed by unsteady simulations of impulsive loads to assess the utility of these estimates and provide insight into the dominant mechanisms.

3.2.1 Fixed-Point Stability

As described from a physical perspective in Sec. 1.2.2, journal bearings suffer from a phenomenon known as "fractional frequency whirl." In this section, susceptibility to fractional frequency whirl will be investigated in the context of "fixed-point stability," implying that a bearing ruled "stable" will return to a static point following a disturbance. The distinction must be made because some bearings will depart from a fixed point when disturbed but the resulting orbit does not end in wall contact. This phenomenon will be investigated in the next section.

Many different journal bearing stability maps appear in the literature using vastly dissimilar parameter spaces. These spaces tend to evolve for convenience, historical, and application-specific reasons. In this document, an effort is made to use a set of reasonably independent parameters (see Sec. 1.2.3) to construct maps that enable straightforward exploration of design tradeoffs. It should be noted, however, that these parameters and their associated maps tend to reflect the demands of a micromachined bearing design environment and may therefore not be the most convenient set for every application.

Even if universal agreement existed on a parameter space, choices may still be made that affect the ease with which the data may be used. Most notably, the gas bearing fixed-point stability boundary is four-dimensional, with one fluid condition (Λ), two geometric conditions ($L/D, \bar{M}$), and one loading condition (ζ or ϵ). Expressing a four-dimensional object on a two-dimensional medium presents a number of difficulties. Various solutions to this problem will be presented in this section, with a focus on investigating the effect of various design decisions on the stability of microfabricated bearings.

Minimum Eccentricity Chart

In many bearings, L/D is fixed by external constraints. This ratio is also constant when determining the running characteristics of existing bearings. In these cases, the stability boundary is reduced to three dimensions ($\Lambda, \bar{M}$, and either ζ or ϵ). Selecting eccentricity to fix the loading condition, the resulting 3-D stability surface may be expressed as a contour plot of minimum eccentricity for a given geometry and fluid condition. Such a plot will be referred to as a "minimum eccentricity chart." An example of such a chart is shown in Fig. 3.5 for an $L/D = 0.075$ bearing.

On the minimum eccentricity chart, the contour intersected by a given Λ and $\bar{M}$ represents the minimum ϵ that must be maintained for stability. Static points with eccentricities smaller than this minimum value will expand into a whirl after a slight perturbation while those with eccentricities greater than this minimum will return to the static point. (It will be shown in Sec. 3.2.2, however, that large perturbations may still result in a whirl for these cases.)

As an example of the minimum eccentricity chart's interpretation for a micro-turbo-

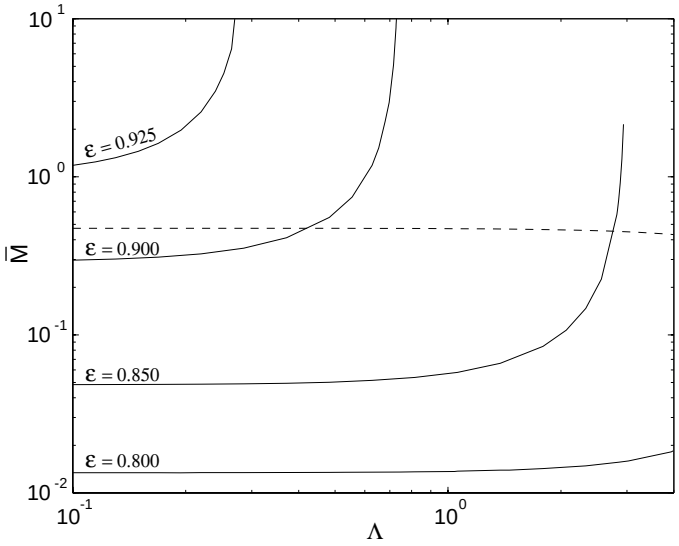

Figure 3.5: Minimum eccentricity chart for an L/D=0.075 bearing. The contour intersected by a given Λ and $\bar{M}$ represents the minimum ϵ that must be maintained for stability. A sample operating line (- - -) for an air-driven microturbine (Fig. 3.6) is included for reference.

machine, an operating line for a silicon turbine driven by compressed air is included in Fig. 3.5 as a dashed line. For this device, shown in Fig. 3.6, $\bar{M}$ is not constant because centrifugal stresses cause the rotor to expand slightly with speed. This has little impact on R but it can significantly decrease C. The ambient pressure term in the denominator of $\bar{M}$ also causes it to decrease slightly with speed because, as shown in Fig. 3.6, the bearing end is located between the stators and the turbine blades. The bearing ambient pressure therefore increases with rotor speed.

For this device, noting that the constant-ϵ contours have a constant-$\bar{M}$ asymptote at low Λ, the minimum eccentricity is slightly greater than 90% for all bearing numbers up to approximately 0.2. After this point, the contours begin to curve upward, crossing the operating line. The example device's minimum eccentricity therefore decreases with speed to less than 85% at its operating point, $\Lambda = 3$.

The minimum eccentricity chart format makes it clear that $\bar{M}$ variation has a relatively weak effect on minimum eccentricity. Furthermore, ϵ_{min} is independent of speed near the chart's left side and a weak function of speed on its right. As a result, the minimum eccentricity chart of Fig. 3.5 covers three orders of magnitude in $\bar{M}$ and 1.5 orders of magnitude in Λ, but only 15% in ϵ. Noting Fig. 3.1, the corresponding span in ζ is about three orders of magnitude due to the large stiffness at high eccentricity and the wide speed range. Thus, ϵ_{min} gleaned from the minimum eccentricity chart varies very little with moderate changes in the geometric parameters, and even relatively large changes in operating speed, whereas ζ_{min} varies considerably. Minimum eccentricity is therefore a more convenient parameter to use as an input to downstream calculations in the early design stages because a good estimate can be made from loosely-established geometric and operational parameters.

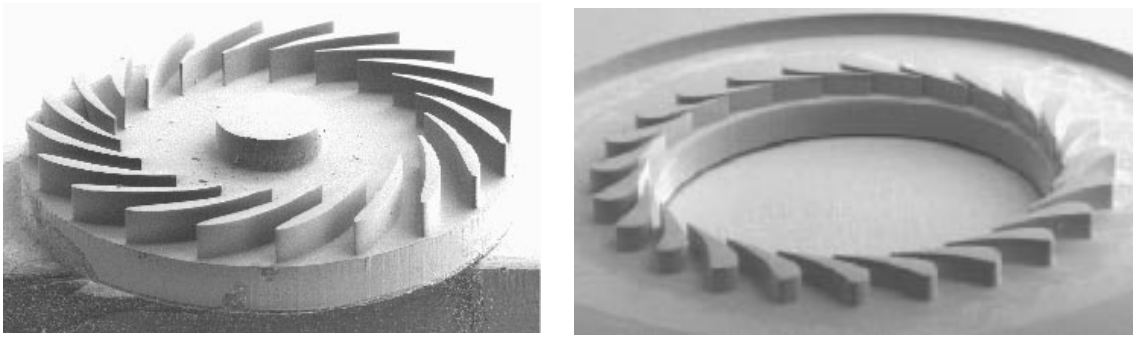

(a) Rotor **(b)** Stator

Figure 3.6: Sample microturbine geometry, shown disassembled and without plena. A cross-section of the assembled device is shown in Fig. 1.2. Airflow is inward through stators to rotor blades and out at the rotor center. $R = 2\,mm, L = 300\,\mu m, c = 10\,\mu m, m = 8.8\,mg$. Figure courtesy C.C. Lin.

As noted previously, the microbearing designer is primarily tasked with determination of a loading condition to enable a bearing of a tightly-constrained geometry to run at a given speed. Knowledge of the running eccentricity, independent of the required load, is useful in the early design stages because ϵ determines the closest approach to the wall. This information may be used to determine a tolerance to surface roughness and rotor noncircularity. In addition, referring to the results of Sec. 3.1.2, a very good estimate of the drag for very short bearings may be calculated from eccentricity information alone.

In addition to its utility as a preliminary design tool, the minimum eccentricity chart may be used to explain the large-scale trends behind several unexplained experimental observations of previous researchers.

First, the concept of a "threshold speed" is a result of the bearing's increasing load capacity with Λ at a given ϵ (see Fig. 3.1). For a fixed load, a common situation in experiments due to the convenience of loading by rotor weight, ϵ will therefore decrease with speed. At some Λ, the ϵ_{min} contour for the given $\bar{M}$ is crossed, at which point the bearing becomes unstable. This Λ is then reported as Λ_{thresh}.

Second, varying the load for each run by tilting their apparatus, Sternlicht and Winn [53] observed that "the eccentricity ratio at the whirl onset [threshold speed] remained virtually constant even though the bearing load is varied." This behavior can also be explained through use of a minimum eccentricity chart. A chart drawn for Sternlicht and Winn's L/D ($= 1$) is shown in Fig. 3.7 with the experimental range of Λ_{thresh} indicated by dashed lines for each $\bar{M}$ they studied. From this chart, it can be seen that the ϵ_{min} contours are nearly horizontal for the reported range of Λ_{thresh} at the two largest $\bar{M}$. The bearing would thus become unstable at the same eccentricity in all experiments, though increasing the load would increase Λ_{thresh}. Furthermore, though the range of Λ_{thresh} for $\bar{M} = 0.039$ is in the region where the constant-ϵ lines begin to descend, the total span in variation across

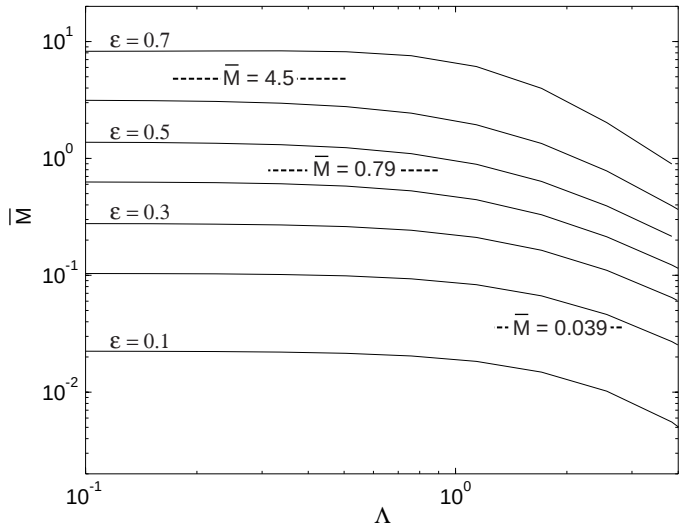

Figure 3.7: Minimum eccentricity chart for Sternlicht and Winn's experiment at $L/D = 1$. The Λ ranges for each tested $\bar{M}$ are denoted by dashed lines.

the range is still less than 5%.

Reynolds and Gross [26] also observed a constant eccentricity at the stability boundary in their experiments by noting that the threshold speed versus applied load had a linear relationship. Referring to Fig. 3.2, for example, this finding is indicative of constant eccentricity at a sufficiently low Λ and ϵ that compressibility has not caused a slope reduction. Reynolds and Gross then carried the observation one step further and plotted a "threshold eccentricity ratio" for each of their bearings.

Finally, Sternlicht and Winn's data also show that decreasing the journal mass raised the threshold speed for a given load. This phenomenon is also predicted by Fig. 3.7. Reducing the journal mass decreases $\bar{M}$ which moves the operating line down the vertical axis, resulting in a decreased minimum eccentricity at all bearing numbers. A higher Λ is therefore reached before the bearing stiffens sufficiently to reduce ϵ below this lowered ϵ_{min}.

Reynolds and Gross made the opposite observation: they did not observe a change in threshold speed for their lighter rotor. This finding may also be explained on the minimum eccentricity chart if their bearing falls in the region where the eccentricity contours "curl" up or down and approach the vertical. In this region, the minimum eccentricity is very weakly dependent on $\bar{M}$ over a large range. Changes in the rotor mass will therefore have little effect on ϵ_{min} and, thus, Λ_{thresh}.

In a design situation, the minimum eccentricity chart can be used for a rapid assessment of the running eccentricity changes brought about by varying the operating point or geometry for a bearing with a fixed L/D. To investigate L/D effects in the general case, multiple charts are necessary. For illustration, a chart drawn for $L/D = 0.25$ is provided in Fig. 3.8. The operating line for the microturbine is again included, which does not change

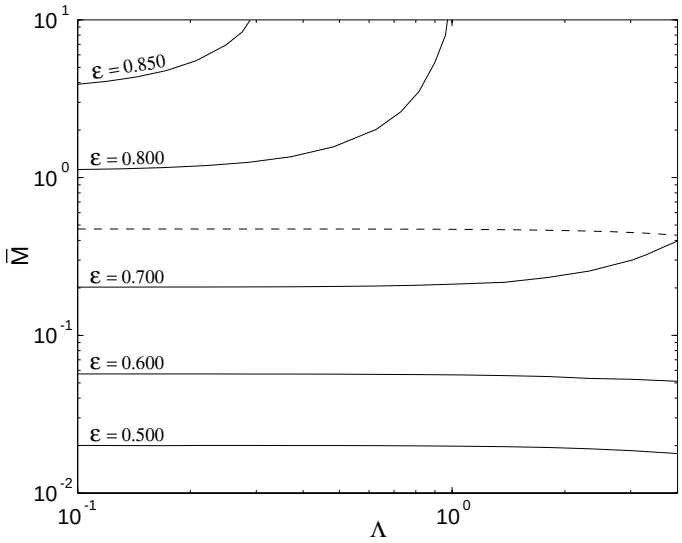

Figure 3.8: Minimum eccentricity chart for an $L/D = 0.25$ bearing with the same sample operating line (- - -) shown in Fig. 3.5. Increasing L/D causes a shift of the minimum eccentricity surface toward the upper left-hand corner, resulting in lower ϵ_{min} for a fixed $\bar{M}$.

because, for solid rotors, the rotor mass is proportional to its length and these quantities appear as a quotient in $\bar{M}$

Comparing these figures, it may be seen that increasing the L/D causes the eccentricity contours to shift toward the upper left-hand (low Λ - high $\bar{M}$) corner of the chart. This means that, for a given $\bar{M}$, increasing L/D strongly decreases the minimum stable eccentricity for bearings in the depicted region. This trend is also visible in Figure 8 in Reynolds and Gross [26].

An interesting consequence of the curling up of the constant ϵ lines in high-ϵ regions of Figs.3.5 and Fig. 3.8 is that a bearing in this region is actually somewhat *more* stable at high speed than at low speed in the sense that it can run at a lower eccentricity. The difficulty at high speed therefore lies in providing sufficient load to force the journal to the proper ϵ. Though the decrease in ϵ_{min} at high speed relaxes the requirement somewhat, the load can be considerable if the target Λ is large. The opposite situation occurs where the lines curl downward, as shown in the Fig. 3.7 and the lowest ϵ trace in Fig. 3.8. In this case, a higher eccentricity is required as the speed increases.

The curvature change in the constant-ϵ contours on the minimum eccentricity surface can be visualized by considering the two eccentricity extremes.

At the high end, a bearing at $\epsilon = 1$ is expected to be stable at all speeds for all $\bar{M}$. Its contour on the minimum eccentricity chart is therefore a single point at $\bar{M} = \infty$, $\Lambda = 0$. Just below this eccentricity, the contour is expected to be horizontal at extremely low Λ and high $\bar{M}$, but then become vertical at some Λ. As ϵ decreases, the low speed asymptote moves to a lower $\bar{M}$ and the transition to a vertical line moves to a higher Λ, thus the nested, upward-curling shape of the minimum eccentricity chart's upper portion.

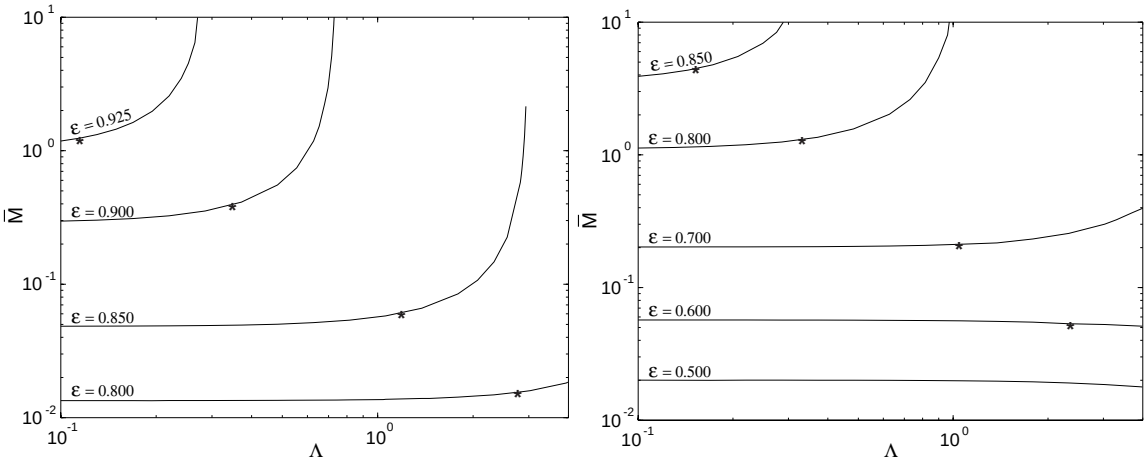

(a) $L/D = 0.075$ **(b)** $L/D = 0.25$

Figure 3.9: Minimum eccentricity charts with $\phi < 70^\circ$ point indicated with an asterisk (*). This point appears to give a good estimate for where the constant-ϵ_{min} contours depart from their low-Λ asymptote.

At the low end, a bearing at $\epsilon = 0$ is expected to be unstable at all speeds for all nonzero $\bar{M}$ [58]. The $\epsilon = 0$ contour is therefore a single point at $\bar{M} = 0$, $\Lambda = 0$. At a very small eccentricity, a stability margin opens so the contour is expected to be horizontal at a small $\bar{M}$and Λ and curve downward to unconditional instability around at some Λ.

Toward explanation of the minimum eccentricity surface's shape, a comment is noted in Reynolds and Gross that the linear load-speed relation they used to experimentally discover the fixed ϵ_{min} region does not hold once compressibility becomes significant. Furthermore, they note that compressibility may be a stabilizing factor because it lowers the attitude angle. The latter observation indeed appears to be the case because the minimum eccentricity lines for high eccentricity curve upward as Λ increases. The fact that this curling, for a given Λ, occurs at lower eccentricity for the $L/D = 0.25$ bearing than for the $L/D = 0.075$ bearing also supports the stabilizing effect of compressibility because compressibility becomes significant earlier as the bearing length increases.

Toward a prediction method for where this curling up occurs, the minimum eccentricity contours of Fig. 3.5 are compared to the load lines of Fig. 3.1(a). Unfortunately, it can be seen that the minimum eccentricity contours curl up long before the constant-ϵ load lines in depart visibly from linearity. Trying another measure of compressibility, the departure of the attitude angle from the incompressible value of 90°, the comparison is repeated using the attitude angle of Fig. 3.1(b). In this case, it appears that a good rule of thumb for when the constant ϵ_{min} lines depart from their low-Λ asymptote is when the attitude angle drops below 70°. This point is indicated with an asterisk (*) on minimum eccentricity charts for $L/D = 0.075$ and $L/D = 0.25$ in Fig. 3.9 with good results.

The mechanism behind the curling down of the low eccentricity contours at $L/D = 0.25$ and all the plotted contours at $L/D = 1$ remains unexplained. Because it appears as speed increases, it is tempting to blame a compressibility effect. One argument against this conclusion, however, is the fact that the ϕ rule used above to measure compressibility onset must fail for the curling down of the low eccentricity cases because ϕ at a given Λ decreases with ϵ. In other words, compressibility onset, by this measure, occurs later for smaller eccentricity. The above prediction method applied to the curling down of the ϵ_{min} contours would therefore predict their crossing, which is not the case.

Loading Schedule

If the loading condition is converted from ϵ to ζ, a different type of chart may be drawn. Further changing the presentation, the stability surface is rotated such that ζ and Λ are on the axes and the contours are lines of constant $\bar{M}$. This type of chart will be referred to as a "loading schedule" because it depicts the required load for stability as a function of Λ for a bearing with a given $\bar{M}$. This formulation reflects the microbearing designer's task, discussed in Sec. 1.3.3, of determining an appropriate load for a tightly-constrained geometry (*i.e.* a more or less fixed $\bar{M}$). In a macro-scale bearing, where the load is often fixed by the shaft weight and greater opportunities exist for varying the clearance or the radius, the axes would be reversed, yielding a threshold speed chart.

A sample loading schedule is presented in Fig. 3.10. This type of chart contains more information than the minimum eccentricity chart because ϵ contours can be included, enabling both the minimum load *and* eccentricity to be determined for a given $\bar{M}$-L/D-Λ point. It is thus a sort of operating map, containing most of the relevant data for a bearing anywhere in its operating envelope. The data can be completed, in fact, by adding attitude angle contours. These contours have been removed from the current chart for readability.

Interpreting the loading schedule is straightforward: the Λ-ζ point of interest is located and the bearing is ruled stable if it lies above the proper $\bar{M}$ line and unstable otherwise. The minimum eccentricity chart can be interpreted in this fashion only when the bearing eccentricity is specified *a priori* and $\bar{M}$ is varied to meet this requirement.

This chart provides another graphical representation of the mechanism behind the constant-load "threshold speed" reported by many researchers. In this case, the threshold Λ occurs when the (horizontal) applied load line intersects the bearing's $\bar{M}$ curve. The experimental observations of Sternlicht and Winn and Reynolds and Gross are also visible. Behavior consistent with Sternlicht and Winn's observation of an increased threshold speed with decreased mass occurs on the left half of the chart where the curves are distinct and larger $\bar{M}$'s correspond to larger minimum loads at every speed. The behavior observed by Reynolds and Gross, where the threshold speed is insensitive to $\bar{M}$, occurs on the right half of the chart where the $\bar{M}$ lines coalesce.

In addition, this chart provides a graphical representation of the insufficient weight

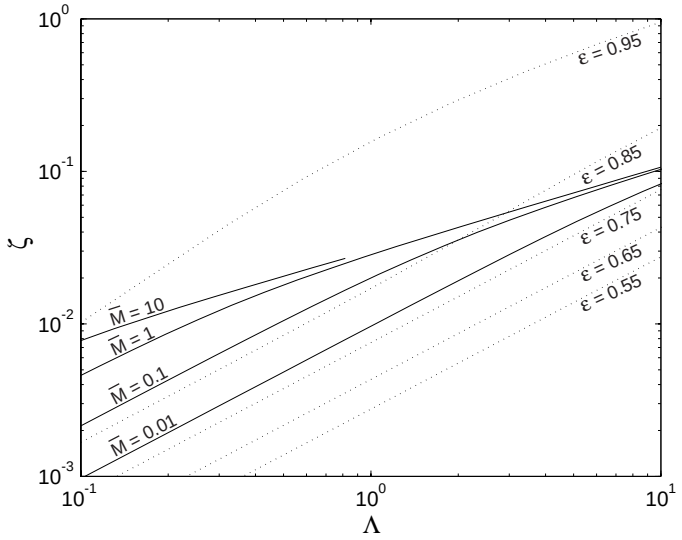

Figure 3.10: Loading schedule for an $L/D = 0.075$ bearing. A given Λ-ζ point is stable if it lies above the proper $\bar{M}$ line and unstable otherwise.

loading issue discussed in Sec. 1.3.3. For example, the microrotor of Fig. 3.6 has a load parameter due to weight of approximately 7×10^{-4} but an $\bar{M}$ of almost 0.5 when P_a is at atmospheric pressure. Referring to Fig. 3.10, its threshold speed under gravity loading is off the figure's low end, at approximately $\Lambda = 0.02$. In dimensional terms, this translates to a threshold speed of less than 5000 RPM, well short of the 2.4 MRPM design speed.

Finally, to demonstrate L/D effects in the load schedule format, a chart is provided in Fig. 3.11 for an $L/D = 0.25$ bearing. Noting the upward shift in the constant-$\bar{M}$ lines, it is evident that that higher ζ is required to maintain stability in the longer bearing. For example, comparing the $\bar{M} = 1$ lines in Figs. 3.10 and 3.11, it can be seen that at $\Lambda = 0.1$, the $L/D = 0.25$ bearing requires $\zeta = 0.01$ while the $L/D = 0.075$ bearing requires half this load. From the eccentricity contours, however, it can be seen that the associated eccentricities are lower, in agreement with the previous section. This apparent contradiction is resolved by recalling the key finding of Sec. 3.1: increasing bearing length increases load capacity for a given speed and eccentricity.

Worst-Case Eccentricity Chart

Due to etching limitations on etch aspect ratio (C/L), increasing L in a microfabricated bearing often enlarges C . This leads to a trade-off between L/D and C/R. To study this trade-off, it would be advantageous to incorporate L/D effects on stability into a single plot. Unfortunately, simply overlaying minimum eccentricity charts for various L/D's results in an impenetrable presentation. The key problem is that such a figure is once again four-dimensional ($\bar{M}, L/D, \Lambda, \epsilon$).

To reduce the number of dimensions, it is noted that the minimum eccentricity con-

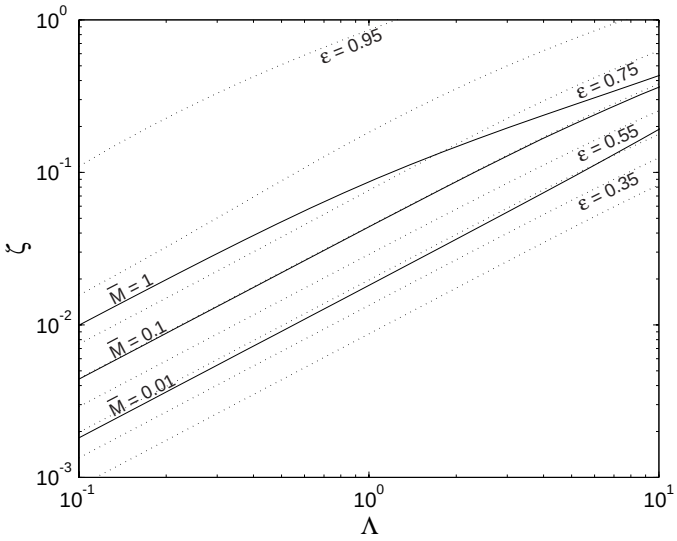

Figure 3.11: Loading schedule for an $L/D = 0.25$ bearing

tours of Figs. 3.5 and 3.8 become horizontal toward the left side of the chart, *i.e.* the function $\epsilon_{min}(\Lambda)$ approaches a constant at low speed. Furthermore, for an upper range of eccentricities, the extent of which increases with decreasing L/D the ϵ_{min} contours curl upward as Λ increases. Consequently, in this region, ϵ_{min} decreases as the bearing number increases for a fixed $\bar{M}$. Thus, the "worst-case" eccentricity may be determined from the low-speed asymptote. The associated running clearance represents the smallest distance between the journal and bearing anywhere in the operating envelope. This distance may then be used to set tolerances to surface roughness and, to some extent, journal noncircularity.

An example of such a "worst-case eccentricity" chart is presented in Fig. 3.12. To use this chart, $\bar{M}$ is calculated for a given bearing and the worst-case eccentricity for the appropriate L/D trace is read from the vertical scale. For reference, several points illustrating a design tradeoff are included on the chart. In this example, the baseline bearing is from the microturbine of Fig. 3.6 and the rotor is assumed solid.

Once again, it is apparent that even relatively large changes in $\bar{M}$ do not drastically alter the minimum eccentricity from the baseline case. The worst-case eccentricity chart clarifies the trend behind this observation: the slope of the stability boundary decreases as ϵ_{min} approaches unity. Designs that require large ϵ_{min} will therefore be relatively insensitive to changes in $\bar{M}$ and L/D. In a design situation, this implies that the gain obtained by varying first-order terms, such as the bearing pressure or rotor mass, is not likely to justify even minimal increases in complexity for devices in this region.

Notably, doubling or halving the clearance has little effect on the dimensional distance between surfaces, d. This observation is explained by noting that larger clearances produce larger $\bar{M}$s, which imply greater minimum eccentricities. The reverse is true for smaller clearances. Bearing stability requirements therefore act to cancel attempts to change the

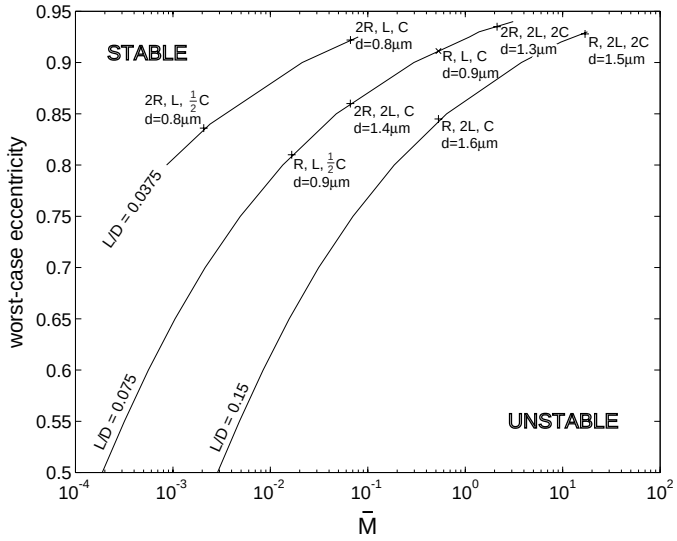

Figure 3.12: Worst-case eccentricity chart for L/D's of interest to the μengine. Example points corresponding to various design options are indicated and the resultant minimum distance from the wall is given by d. For the example points, $R = 2mm$, $L = 300\mu m$, and $C = 10\mu m$.

running distance via clearance modification alone.

Tradeoffs with a Fixed Etch Aspect Ratio

Further exploiting the low-speed $\epsilon_{min}(\Lambda)$ asymptote, a tradeoff may be constructed that is more appropriate for a microfabricated bearing. In this case, the bearing etch aspect ratio, C/L, is held constant as the tradeoffs are studied. Again assuming the bearing is a solid disk and fixing the conditions at sea-level pressure and room temperature, only two variables may be chosen in this case: R and L. An example of a tradeoff between these parameters for a 1:30 etch aspect ratio are shown in Fig. 3.13.

Two major trends of interest are visible in this figure. To understand these trends, it is helpful to note that, under the constraints set forth for this series of calculations:

$$\bar{M} \propto \frac{L^5}{r^3}.$$

First, for fixed diameters, shorter lengths produce smaller eccentricities because $\bar{M}$ is fifth-power dependent on L while L/D is only linearly dependent. As L decreases, the eccentricity reduction associated with the decrease in $\bar{M}$ outweighs the ϵ increase associated with the shrinking L/D.

Second, for fixed lengths, smaller diameters produce smaller eccentricities for shorter bearings while the trend is reversed for longer bearings. This behavior may be explained by noting from Fig. 3.12 that the ϵ_{min} decrease associated with a given increase in L/D shrinks as $\bar{M}$ increases. Also, the above expression for $\bar{M}$ has a cubic dependence on the

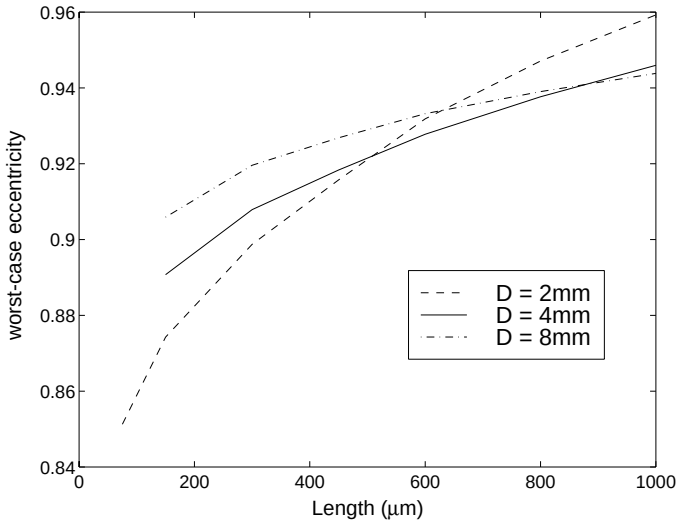

Figure 3.13: Low-Speed eccentricity tradeoff for silicon rotors of various diameters and lengths assuming an etch aspect ratio (C/L) of 1:30.

radius in the denominator. It is therefore reasonable to expect that, at some length, the eccentricity benefit brought about by the decreased $\bar{M}$ from a given ΔR will exceed the detriment associated with the decreased L/D.

Recasting the data of Fig. 3.13 in terms of dimensional minimum distance from the wall, (Fig. 3.14), significant differences are visible. First, the trend is upward with increasing L but, in this case, the ordinate represents physical distance from the wall so, contrary to the eccentricity case, an upward trend is desirable. The increase in physical distance between the journal and bearing with L therefore outweighs the increase in minimum eccentricity visible on the previous plot. Second, the difference between the various curves is small until the $D=2mm$ curve breaks downward at $L=500\mu m$. At small lengths, the bearing is therefore insensitive to changes in diameter. Finally, the overall design trend remains the same as on the previous chart; a smaller diameter brings larger d at short lengths, but the trend is reversed as the bearing becomes longer.

Finally, it may be noted that C/R reaches 1/30 for the largest L-D combination in this series of calculations. The model's validity may therefore be questioned near the right side of Figs. 3.13 and 3.14 because, as noted in Sec. 2.2.1, SPECTRES' formulation assumes terms of involving C/R are insignificant. Looking back at the order-of-magnitude analysis of Sec. 1.2.3, however, the first-order C/R terms are multiplied by the Reynolds number. Noting that the diagrams in this section were drawn at the stability boundary's low-speed asymptote, it may be argued that the Reynolds number can be taken as arbitrarily small in these results. The assumption of negligible inertia is therefore justifiable in this context, despite the not-so-small C/R.

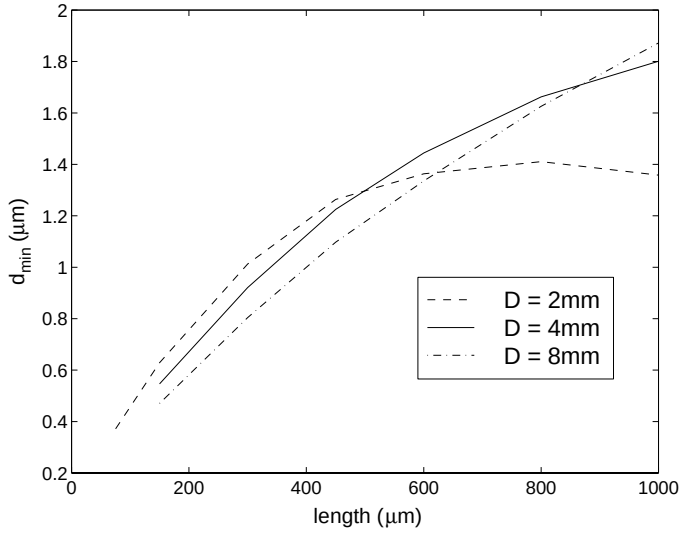

Figure 3.14: Low speed running clearance tradeoff for silicon rotors of various diameters and lengths assuming an etch aspect ratio (C/L) of 1:30.

3.2.2 Whirling Operation

Bearings labeled "unstable" in the previous section depart from their static point to enter a whirl. No information was given, however, as to whether or not the resultant whirl ends in wall contact. This issue will be treated in the current section.

It has been shown analytically for liquid-film bearings that a region exists where a finite-amplitude whirl is stable [59]. This behavior has also been observed experimentally by Reynolds and Gross [26] and Wilson [60] for gas bearings. In both experiments, the authors applied a constant load and gradually increased the rotation speed until the journal began to whirl. Labeling this speed the "threshold speed," Reynolds and Gross were able to increase the speed and run their bearing in a stable whirling mode. The extent to which the threshold speed could be exceeded varied with applied load, L/D, and clearance ratio.

To investigate this phenomenon, the experiment of Reynolds and Gross was performed numerically with SPECTRES. The results of a series of such calculations are shown in Fig. 3.15 for an $L/D = 0.075$ bearing with $\bar{M} = 0.1$ loaded to $\zeta = 0.05$. At each data point, the change in speed from the previous data point caused the rotor to oscillate. At low bearing numbers, these oscillations decreased in amplitude as the journal settled into the static operating point appropriate for the new speed. The resultant collection of fixed-point runs are denoted by a solid line in Fig. 3.15. The left-hand figure contains the maximum eccentricity of the orbit, which is simply the running eccentricity for fixed points, and the right-hand figure contains the frequency of ϵ oscillation normalized by the rotational frequency.

At Λ_{thresh}, the oscillations caused by the speed change become neutrally-stable. If the speed is increased beyond this point, the oscillations begin to grow, corresponding to an

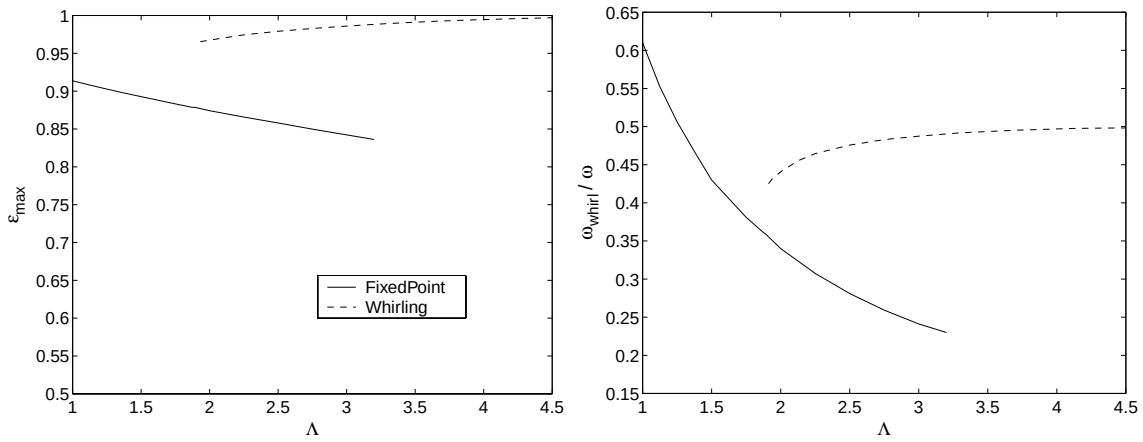

(a) Maximum Eccentricity **(b)** Whirl Frequency

Figure 3.15: Stable running modes for an $L/D = 0.075$ bearing with $\bar{M} = 0.1$ and $\zeta = 0.05$.

increasing-radius spiral orbit. As reported by Reynolds and Gross, however, the growth of this orbit ceases before wall contact is made. Examples of the resulting periodic whirling orbits for the case shown in Fig. 3.15 at three bearing numbers are presented in Fig. 3.16. The maximum and minimum eccentricity of the orbit as a function of Λ are also presented. It can be seen that the orbit is asymmetric at first due to the applied load (pointing downward in the figure). As the whirl speed increases, however, the applied load becomes less significant compared to the centripetal acceleration and the whirl approaches a circle. As a result, the maximum and minimum eccentricities converge, as shown by Fig. 3.16(b). It may be noted, however, that a discernible difference remains between ϵ_{max} and ϵ_{min} due to a slight orbit eccentricity caused by the load. This eccentricity is visible (barely) in Fig. 3.16(a).

The maximum eccentricity and whirl speed of the steady-state orbits exhibited by the first example case are presented as dashed (- -) lines in Fig. 3.15. For this bearing, stable whirls above the threshold speed have very high maximum eccentricities ($\epsilon > 0.99$). Because eccentricities of this magnitude are unattractive in a real bearing due to film rupture, load-control, roundness, surface roughness, and drag issues, the threshold speed is effectively an operational stability boundary. It should be noted, however, that external damping mechanisms, perhaps from electrostatic or viscous sources, can be used to continue the solution along the fixed point line past Λ_{thresh}.

Another important observation made by Reynolds and Gross is that, when decreasing the rotor speed to defeat a whirl, the speed at which fixed-point operation was regained was always lower that the speed at which it was lost. This effect is also visible in Fig. 3.15: the whirling solutions (dotted line) extend to speeds where fixed-point solutions also exist. In this case, the “overlap region” spans more than 40% of the fixed-point operating range.

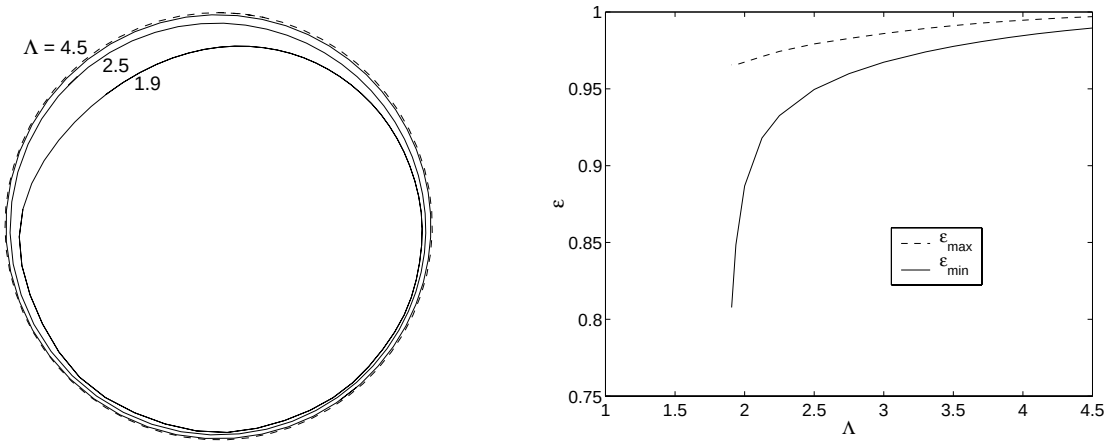

(a) Orbits **(b)** Max / Min Eccentricity

Figure 3.16: Whirl mode progression of an $L/D = 0.075$ bearing with $\bar{M} = 0.1$ and $\zeta = 0.05$.

In the overlap region, the bearing may operate stably in either mode. Experimentally, Reynolds and Gross found that the bearing could be switched between modes by jolting their apparatus.

Crooijimans *et al.* [61] also investigated this issue for liquid-film bearings by assuming a periodic solution exists. Using the analytical Ocvirk short bearing solution [62], the motion equations are discretized in time over an unknown period. The orbit shape and period are then determined by solving the resulting system of algebraic equations using a multidimensional Newton-Raphson method. An initial solution for starting the Newton-Raphson is obtained via Hopf bifurcation theory [59]. From this work, the authors concluded that periodic solutions exist before and after the fixed-point stability threshold, in agreement with the above observation of stable whirls and an overlap region.

To demonstrate the effect of $\bar{M}$ on these phenomena, a second SPECTRES simulation was performed with an order-of-magnitude reduction in $\bar{M}$. The results of this calculation are presented in Fig. 3.17. Two changes are immediately evident: reduced overlap range and reduced whirling mode ϵ_{max}.

For the $\bar{M} = 0.01$ bearing, the overlap region spans less than 16% of the fixed-point operating range; more than a factor of two smaller than the range exhibited by the larger $\bar{M}$ bearing. This agrees with Reynolds' and Gross' experimental observation that "the extent of the hysteresis region decreased and the resistance to jolts increased with decreasing clearance ratio." In fact, when $\bar{M}$ is decreased by decreasing the clearance, the overlap region's contraction is somewhat understated graphically in the preceding figures due to the rotation rate multiplier in Λ's inverse-square dependence on C.

At Λ_{thresh}, the whirling mode for the smaller $\bar{M}$ involves a maximum eccentricity of less than 95%, down from more than 99% for the previous case. Because the nondimen-

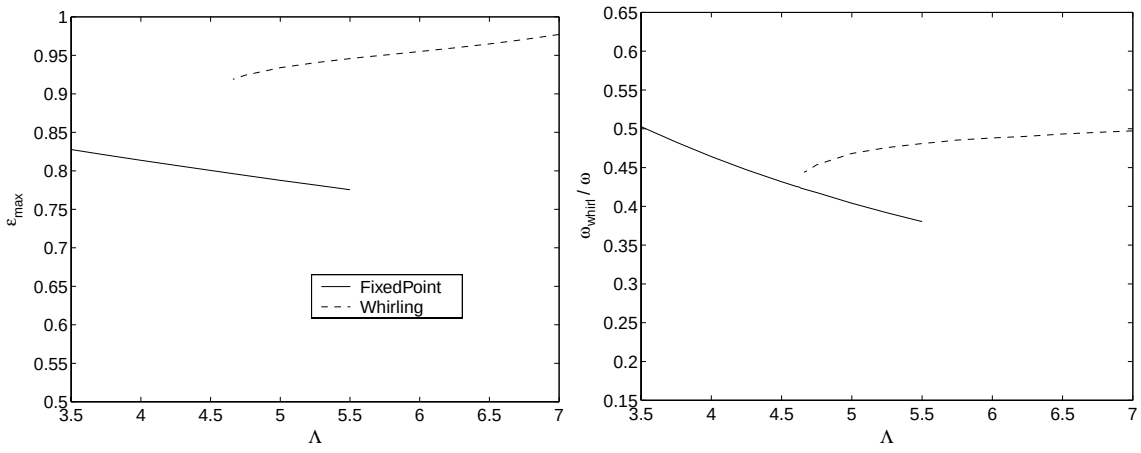

(a) Maximum Eccentricity

(b) Whirl Frequency

Figure 3.17: Stable running modes for an $L/D = 0.075$ bearing with $\bar{M} = 0.01$ and $\zeta = 0.05$.

sional parameters involve a number of variables, the orbit size reduction with $\bar{M}$ may be explained from more than one viewpoint.

Viewing $\bar{M}$ as a mass variable, this behavior is expected because the more massive bearing will experience greater centripetal acceleration in the whirling mode, leading to a larger orbit for a given bearing shape and speed (and hence hydrodynamic load capacity). It may be suggested, however, that this interpretation is clouded somewhat by the fact that Λ_{thresh} is more than 40% larger for the smaller $\bar{M}$ case but Λ is independent of m. This issue is resolved by noting that centripetal acceleration is dependent on the speed squared. The speed contribution to the centripetal acceleration therefore increases by almost a factor of two between Figs. 3.15 and 3.17, but $\bar{M}$ was increased by an order of magnitude so the centripetal acceleration's overall magnitude decreases by a factor of five.

Viewing $\bar{M}$ in terms of the clearance, the smaller orbit for decreasing $\bar{M}$ may be understood in terms of the squeeze-film force's inverse dependence on clearance cubed [12]. Tightening the clearance therefore strongly increases the squeeze-film effects, reducing the whirling orbit for a given mass and speed.

In both Fig. 3.15 and Fig. 3.17, the whirl speed approaches $\omega/2$ as the eccentricity approaches unity. To understand this asymptote, it is first noted that a centered circular orbit at 0.5ω can be shown [58] to have zero load capacity and, therefore, unity eccentricity.

For a loaded bearing in a whirl, the orbit is initially eccentric but it expands and the whirl frequency rises as the rotation rate increases. This progression is visible in Fig. 3.16. The bearing therefore approaches a zero load capacity condition as its speed increases. In physical terms, the approach to a centered, circular orbit, regardless of its frequency, defeats the squeeze-film mechanism that helps keep the journal and bearing apart while whirling. Furthermore, the load capacity due to viscous pumping disappears for half-

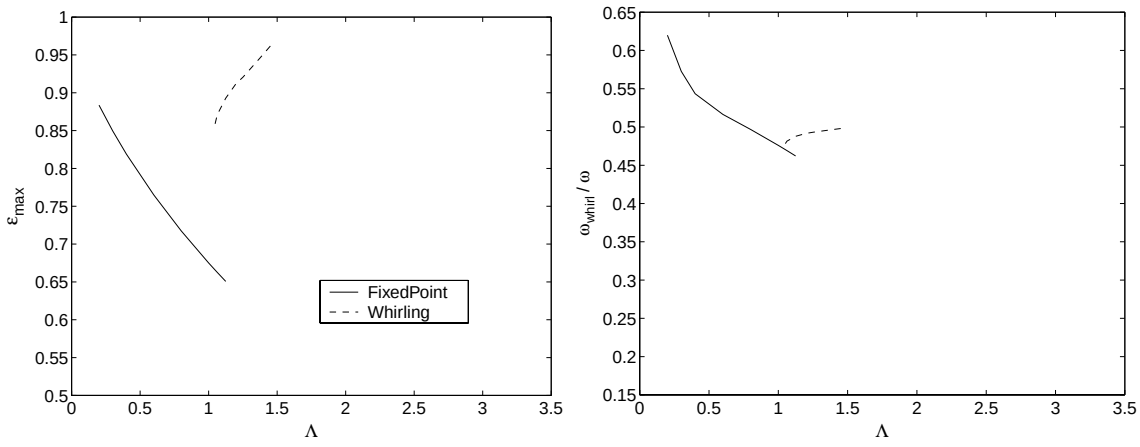

(a) Maximum Eccentricity **(b)** Whirl Frequency

Figure 3.18: Stable running modes for an $L/D = 0.25$ bearing with $\bar{M} = 0.1$ and $\zeta = 0.05$.

speed whirl because the converging / diverging section responsible for the load-carrying pressure distribution moves away from the lubricant at its average flow speed.

To demonstrate the effect of L/D on these phenomena, a third SPECTRES simulation was performed at $L/D = 0.25$. The results of this calculation are presented in Fig. 3.18.

In this case, the overlap region is very narrow, covering less than 8% of the fixed-point operating range. Furthermore, the whirl mode maximum eccentricity increases extremely rapidly with speed. The fixed-point (solid) line therefore provides a very good indication of the operating range and characteristics for this particular bearing because the whirl mode starts very near the boundary and wall contact is made soon after.

The very rapid increase in whirl eccentricity for the higher L/D bearing may be related to the fact that the whirl mode's *lowest* frequency is 0.475ω. Because the load capacity due to viscous pumping action diminishes very quickly as a circular orbit at $\omega/2$ is approached, entry of this bearing into a whirl mode causes a very rapid transfer of load capacity to squeeze film action, which quickly diminishes as the orbit becomes circular.

To generalize the observations made thus far in this section, we first note that overlap region is larger for bearings with lower response frequencies in the fixed point mode at Λ_{thresh}. Due to the large increase in stiffness with eccentricity experienced by a journal in fixed-point operation (see Fig. 3.1(a)), it is possible to observe oscillations higher in frequency than $\omega/2$ when below Λ_{thresh} (see, for example, Figs. 3.15 and 3.18). At Λ_{thresh}, however, balanced plain bearings have response frequencies below $\omega/2$. A sampling of response frequencies for various values of $\bar{M}$ and Λ_{thresh} are plotted for $L/D = 0.075$ and 0.25 bearings in Fig. 3.19.

Noting from the previous figures that the whirling mode's frequency is higher than that of the fixed-point mode, a defined corridor in frequency space can be seen. This corridor is

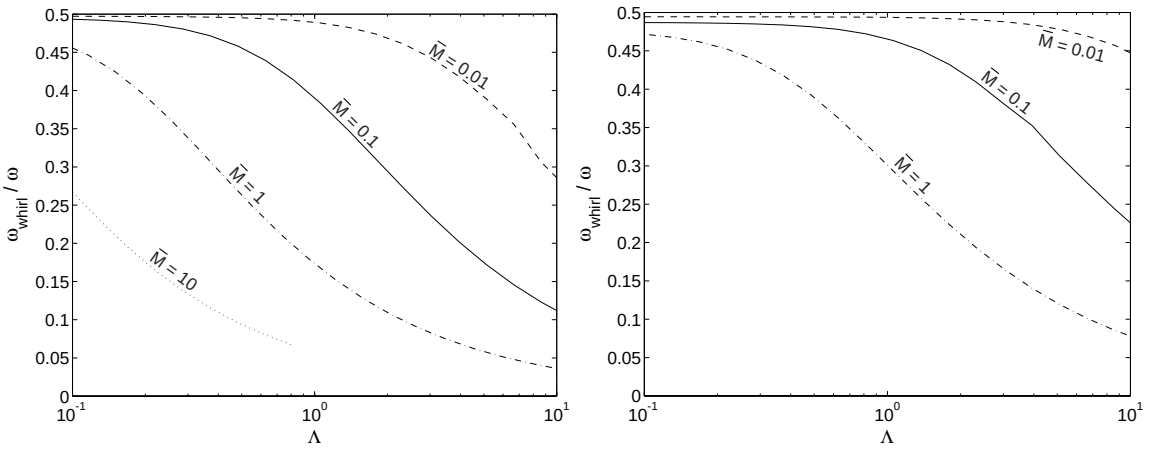

(a) $L/D = 0.075$ **(b)** $L/D = 0.25$

Figure 3.19: Response frequency at loss of fixed-point stability.

bounded above by $\omega/2$ and below by the fixed-mode's response frequency at Λ_{thresh}. If the fixed-mode frequency is close to $\omega/2$, little corridor is available for the whirling solution to exist so the mode will not be significant. On the contrary, if the fixed-point solution dips below $\omega/2$ long before Λ_{thresh}, a considerable corridor exists for the whirling solution and a large overlap region is likely.

Viewing the response frequency curves with respect to the minimum eccentricity charts (Figs. 3.5 and 3.8) and loading schedules (Figs. 3.10 and 3.11) presented in previous sections, it can be concluded that the response frequency begins to differ significantly from $\omega/2$ when the minimum eccentricity departs from its low speed asymptote. On the minimum eccentricity chart, this is where the constant ϵ lines curve upward. On the load schedule, it is where the constant $\bar{M}$ lines become nonlinear and begin to cross eccentricity contours. Physically, as shown in Sec. 3.2.1, this behavior indicates the emergence of compressibility effects.

With this framework in place, previous qualitative observations about the overlap region's extent can be predicted from the static charts presented in previous sections. First, larger $\bar{M}$ curves depart from linearity at lower ζ on the loading schedule. The fixed-point response frequency at Λ_{thresh} will therefore decrease with increasing $\bar{M}$ for fixed ζ, supporting the increase in overlap region length observed in this section. Second, the increasing departure from linearity, and thus decreasing response frequency, with increasing ζ for constant $\bar{M}$ supports the result of an increasing overlap region with applied load for a given bearing reported in Fig. 11 in Reynolds and Gross [26]. Finally, comparing Figs. 3.10 and 3.11, it can be seen that increasing L/D decreases Λ_{thresh} for fixed load. In addition, the departure from linearity for a given $\bar{M}$ occurs at a larger Λ. The overlap region will therefore decrease with increasing L/D for fixed load, as observed above. Furthermore, if

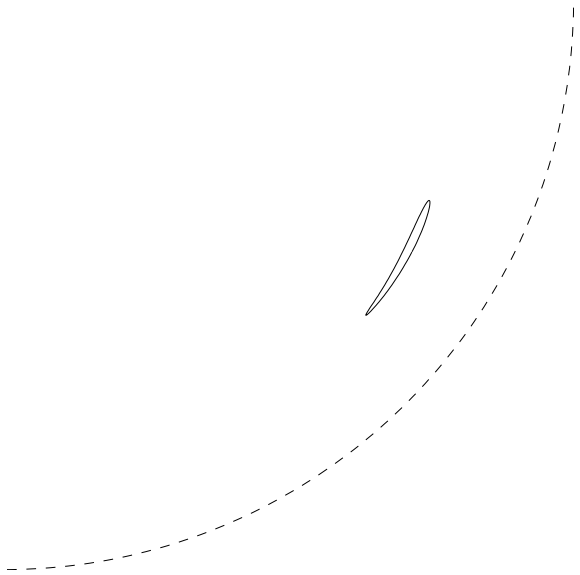

Figure 3.20: "Small-Whirl" solution for an $L/D = 0.075$ bearing with $\bar{M} = .1$ and $\zeta = 0.05$ at $\Lambda = 3.22$. This solution is extremely sensitive and easily decays into large whirl mode. It is therefore unlikely to be observed experimentally.

the loading is increased to produce the same Λ_{thresh}, the larger L/D bearing will still tend to have a smaller overlap region.

Finally, it should be mentioned that a second whirl mode was observed in the course of this work. This whirl is very small amplitude and occurs very near the fixed point in terms of frequency. It appears despite grid and timestep changes so it is likely to be a physical, rather than numerical, phenomenon. Figure 3.20 shows an orbit plot of this "small-whirl" mode found in the $L/D = 0.075$ bearing with $\bar{M} = 0.1$ and $\zeta = 0.05$. This case has a bearing number of 3.22 and was started from the $\Lambda = 3.2$ fixed-point solution. Due to its close proximity to the fixed-point stability boundary, the oscillations grew very slowly, requiring nearly 5000 revolutions to establish the stable whirl shown in Fig. 3.20. It is this small growth rate that made the observation of this mode possible because it was found that the slightest perturbation caused a decay to the large whirl solution. This sensitivity makes the mode unlikely to be observed experimentally. It therefore has little practical importance.

3.2.3 Radial Instability

It was noted in Sec. 2.2.2 that a high-frequency mode was observed at the startup of fixed-point stability calculations. Furthermore, it was observed that this mode was more visible when plotting eccentricity than when plotting attitude angle. These observations were explained by Jacobson [40] through an eigenvalue analysis. He showed that the unstable eigenvalue when approaching the fixed-point stability boundary from below is associated

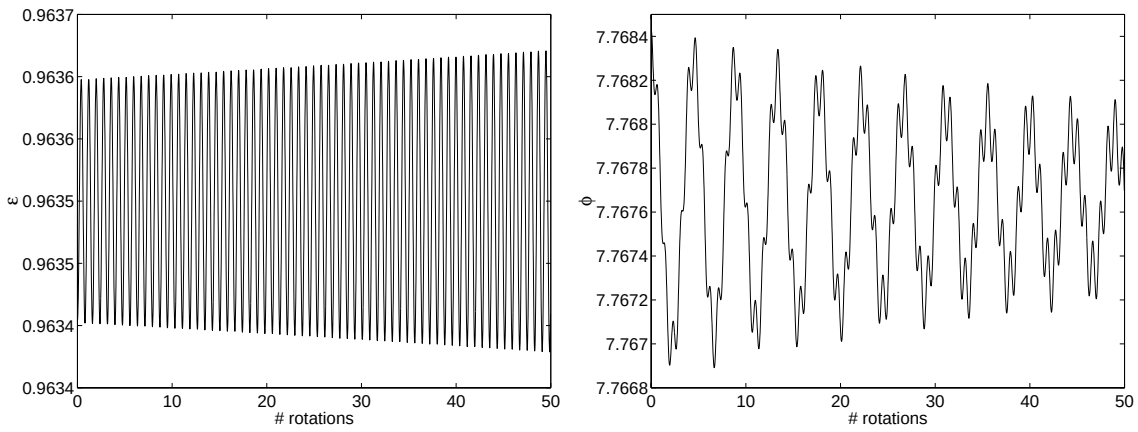

(a) Eccentricity

(b) Attitude Angle

Figure 3.21: Initial revolutions of a bearing exhibiting radial instability at $\Lambda = 4, \bar{M} = 0.01, \epsilon = 0.9635$. The observed frequencies agree very well with the predictions of Orr [34]

with the attitude angle. He also showed, however, that a high frequency mode associated with eccentricity was lightly damped and had the potential to cross the imaginary axis. With a higher-order model, Orr [34] later showed that the high frequency mode, did, in fact, become unstable at very high eccentricities. The stability boundaries presented in Sec. 3.2.1 are therefore not thresholds, but lower boundaries on a stability corridor.

Orr has presented detailed stability maps for this mode at $L/D = 0.075$. The objective of this section is to demonstrate the existence of this mode through an independent means and to observe the orbit in order to gain physical insight into the relevant mechanism.

Choosing the case of Fig. 4-27 in [34]: $\Lambda = 4$ and $\bar{M} = 0.948$, a simulation was run in SPECTRES at $\epsilon = 0.9635$. Orr's calculation places this point just past the stability boundary so it expected to be weakly unstable. The resulting eccentricity and attitude angle progressions for the first few revolutions are shown in Fig. 3.21.

From Fig. 3.21, it can be seen that the predicted behavior indeed occurs. First, the eccentricity oscillations are growing slightly with time. Second, the oscillation frequency is 1.26ω, which compares well with Orr's prediction of 1.21ω. Third, the attitude angle trace, though contaminated by the eccentricity oscillation, shows a convergent oscillation at approximately 0.23ω, which compares well with Orr's prediction of approximately 0.22ω.

At this point, the orbit appears as narrow interlinked ellipses slowly expanding in the radial direction. The position of these orbits oscillates in the circumferential direction and the envelope of these oscillations decreases. As the calculation evolves, these orbits converge on top of one another and continue expanding in the radial direction. At this point, an expansion is evident in the attitude angle variation as well because the orbit ceases moving back and forth and begins grow and tilt from the radial direction. The corresponding

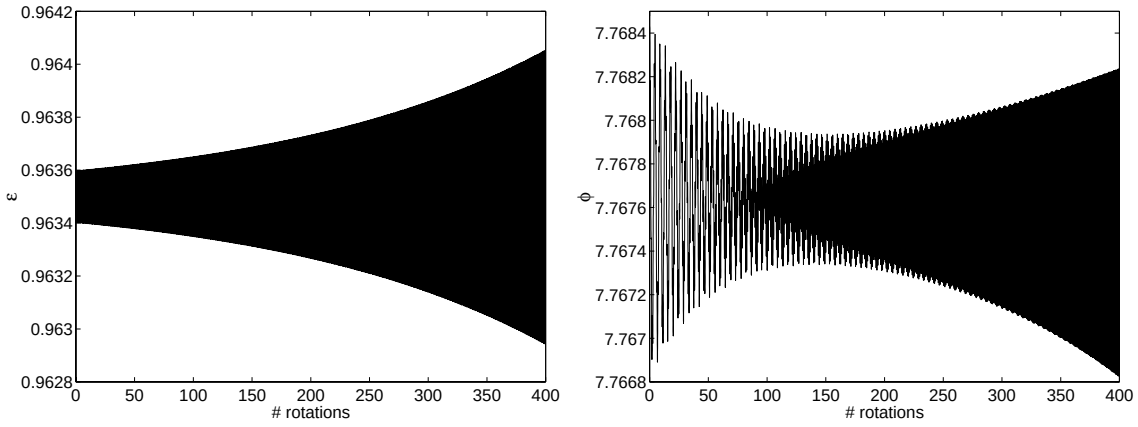

(a) Eccentricity **(b)** Attitude Angle

Figure 3.22: Later revolutions of a bearing exhibiting radial instability at $\Lambda = 4, \bar{M} = 0.01, \epsilon = 0.9635$. The convergent, low frequency attitude angle oscillations have given way to growing oscillations at the radial mode frequency.

eccentricity and attitude angle progressions are shown in Fig. 3.22.

Thanks to the slow growth of this orbit, it establishes a stable whirl. Very slight increases in Λ result in crashes, however. This behavior is due to the very high loading, which results in a highly skewed, largely radial orbit, with extremely large eccentricities at its bottom that eventually reach unity. The bifurcation predicted by the eigenvalue analysis therefore does not generally lead to a stable nonlinear orbit and the instability traces reported by Orr [34] represent operational boundaries.

Physically, the behavior of this orbit is consistent with a "bouncing" action against the extremely high stiffness near the wall. Each rebound produces a trajectory toward the center which acts against the applied load but no significant stiffness. When the bounce peaks, the journal falls back toward the wall under the action of the applied load. It then penetrates the large stiffness area slightly further, gaining energy and bouncing up slightly further, and so on until failure. Due to the extremely high stiffness at the wall, squeeze film damping is largely unable to restrict the orbit's energy and it usually makes wall contact.

3.2.4 Imbalance Effects

In real machines, the rotor geometric and mass centers are inevitably separated by some distance, d_u, due to asymmetries in the manufactured geometry or irregularities in the material. This separation is referred to as an "imbalance". In this document, in common with much of the bearing literature, the distance will be normalized by the clearance and reported as an "imbalance distance," δ_u. This normalization provides the convenient interpretation of δ_u as the eccentricity at which the journal whirls when rotating about its mass

center in an otherwise unloaded state.

From a bearing perspective, imbalance results in a load proportional to the rotor weight, the imbalance distance, and the rotor frequency squared. The direction of this load varies sinusoidally at the rotor (synchronous) frequency and is thus often referred to as a "rotating load." This load can have a beneficial or detrimental effect on bearing operation depending on geometry and operating point. If, for example, the journal is operating at very high eccentricity, as is often the case for microbearings, a sufficiently large imbalance can produce destructive wall contact. Conversely, if the static load on the journal load is insufficient to guarantee fixed-point stability, the rotating load contributed by imbalance can defeat a tendency to whirl.

Reynolds and Gross [26] support the rotating load argument experimentally with their finding that an unloaded rotor became stable to self-excited whirl when the speed was sufficient to produce an imbalance orbit at an eccentricity approximately equal to the minimum value required for fixed-point stability. Sternlicht and Elwell [54] also observed a stabilizing influence while performing a series of experiments with variable imbalance. Notably, these authors stated their finding as "synchronous whirl tends to suppress half frequency whirl." This viewpoint is a common alternative to the rotating load argument.

An example SPECTRES imbalance response is presented in Fig. 3.23. In this case ($L/D = 0.1$, $\Lambda = 4.6$, $\bar{M} = 0.7$), the minimum eccentricity for fixed point stability is 80%. To represent a running case with a "safety factor", the eccentricity was set to 85%, corresponding to $\zeta = 1.6\zeta_{min}$. The calculation was begun from a zero imbalance which was slowly increased. While this progression appears to be nonphysical, the calculation is actually a numerical analog of Sternlicht and Elwell's experiment, which was performed with a series of bolt-on imbalance weights.

One key difference between the earlier experiment and the current work is the presence of a sideload. Because a sideload is applied in the current work, the resulting orbits will be nonconcentric with the bearing. Consequently, it was necessary to generalize Sternlicht and Elwell's presentation in terms of whirl eccentricity to include the orbit's maximum and minimum eccentricity at each imbalance level. For a centered, circular orbit, $\epsilon_{max} = \epsilon_{min}$ and the two presentations are identical. Three sample orbits are also included.

The results presented in Fig. 3.23 begin as intuitively expected: a small circular orbit, centered on the static point forms and expands as the imbalance distance grows. As δ_u passes 5%, however, a discernible asymmetry is visible between ϵ_{min} and ϵ_{max} with respect to the zero-imbalance eccentricity. This asymmetry implies that the orbit's radial motion is no longer centered on the static point.

To investigate this issue, the pertinent orbits are expanded in Fig. 3.24. From this figure, it is immediately evident that the median eccentricity is indeed decreasing with increasing imbalance, indicating a departure of the orbit's center from the static point. Furthermore, the orbit shape is elliptical, rather than circular. The minor axis of the ellipses is oriented

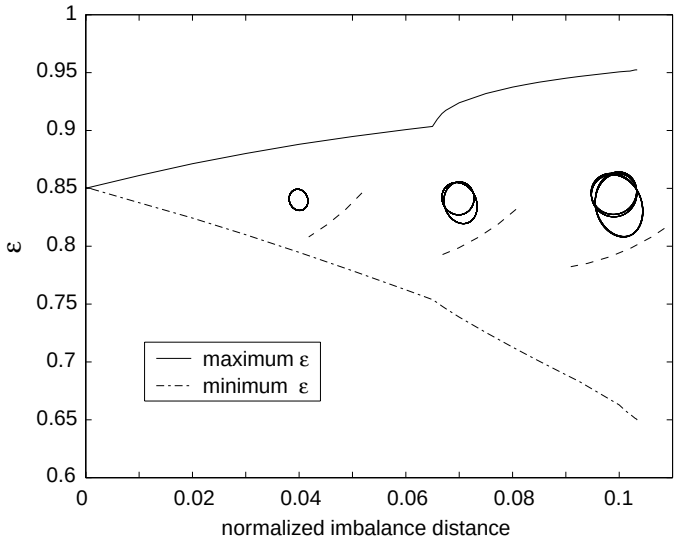

Figure 3.23: Rotor response to imbalance at 160% of loading required for fixed-point stability. Three example orbits are included, where the dashed line corresponds to positions associated with wall-contact. A bifurcation from a single to a double loop orbit is clearly visible. A second, though less obvious, bifurcation also occurs just before the maximum imbalance.

in the circumferential direction and has length equal to twice the imbalance radius. The major axis is radial and is larger than expected from the imbalance distance. The median attitude angle decreases with increasing imbalance level.

The inverse relationship between median eccentricity and imbalance distance is a consequence of the increasing stiffness with eccentricity that is characteristic of self-acting bearings (see, for example, Fig. 3.30). When attempting to whirl around the static point, the journal therefore experiences greater resistance to its motion in the direction of increasing ϵ than in the opposite direction (where it is resisted only by a weak squeeze film effect). As a result, the orbit's minimum eccentricity shrinks faster than its maximum grows, decreasing the median eccentricity as the imbalance distance increases.

The elliptic orbits of Fig. 3.24 were predicted analytically by Ausman [18], though his analysis indicated that the center would rest on the static point. This shape is another consequence of the anisotropic stiffness around the orbit.

Finally, the decrease in attitude angle with increasing imbalance distance mirrors the effect of increasing load in a plain bearing (see Fig. 3.1), lending support to the view of imbalance as a load source. From this point of view, the experimental observation of imbalance as a stabilizing mechanism is not surprising because, as shown in Sec. 3.2.1, increasing the load generally improves fixed-point stability. The fact that this effect occurs despite the decreasing median eccentricity with δ_u implies that the former quantity may not be a good choice for expressing imbalance behavior.

Returning to Fig. 3.23, a bifurcation occurs at $\delta \sim 0.066$ that results in a sudden increase in the maximum eccentricity and the minimum eccentricity slope with respect to δ_u. In-

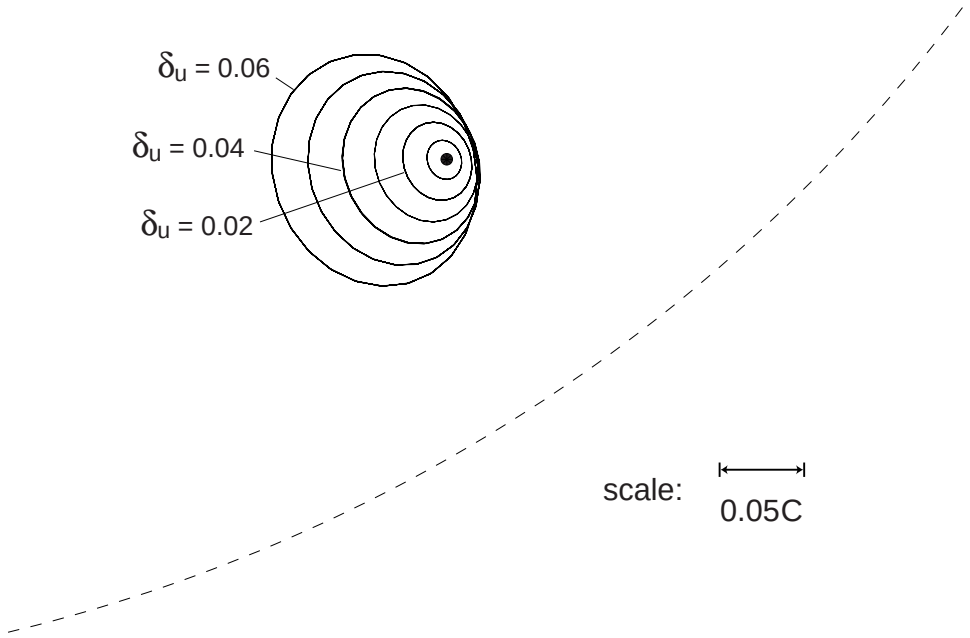

Figure 3.24: Journal orbits for increasing levels of imbalance. The zero-imbalance position is indicated with a solid circle and the locus of positions corresponding to wall contact are denoted by '--'. Noting the scale, it can be seen that the elliptic orbits have a minor axis equal in length to twice the imbalance radius, but a larger major axis due to a rebound effect from the increasing stiffness in the inward wall-normal direction.

specting the orbit at this point, the jump in maximum eccentricity is a result of a second loop forming in the orbit that extends beyond the circular path. At this point, the depicted orbit represents two revolutions and is indicative of a second-order subharmonic response. This orbit shape is maintained and increases in size with δ_u until $\delta \sim 0.1$, where the orbit shape remains the same but the paths split in two, indicating a $\frac{1}{4}\omega$ component is asserting itself. Shortly thereafter, a $\frac{1}{16}\omega$ component appears and the paths divide into fours, with two of them separating at one point to form a third loop. These orbits, along with their associated frequency spectra, are presented in Fig. 3.25.

It may be noted from the power spectra in Fig. 3.25 that frequency components appear in addition to the expected peaks at the synchronous frequency plus the appropriate number of subsynchronous peaks for the path divisions. These peaks occur at sums and differences of the expected frequencies and are indicative of a nonlinear system. In this case, the nonlinearity is provided by the strong increase in stiffness with eccentricity characteristic of a self-acting bearing.

The pattern of sum and difference modes may be calculated via an empirical formula promulgated by Ehrich [63] for rotating machinery. This idea was applied to hybrid bearings by Orr [34], who employed the Cauchy product to extend Ehrich's method and reproduce an extremely complex spectrogram. In this case, the key point to note is that the modes in Fig. 3.25 show only whole multiples of $1/2\omega$. The zero imbalance case, however,

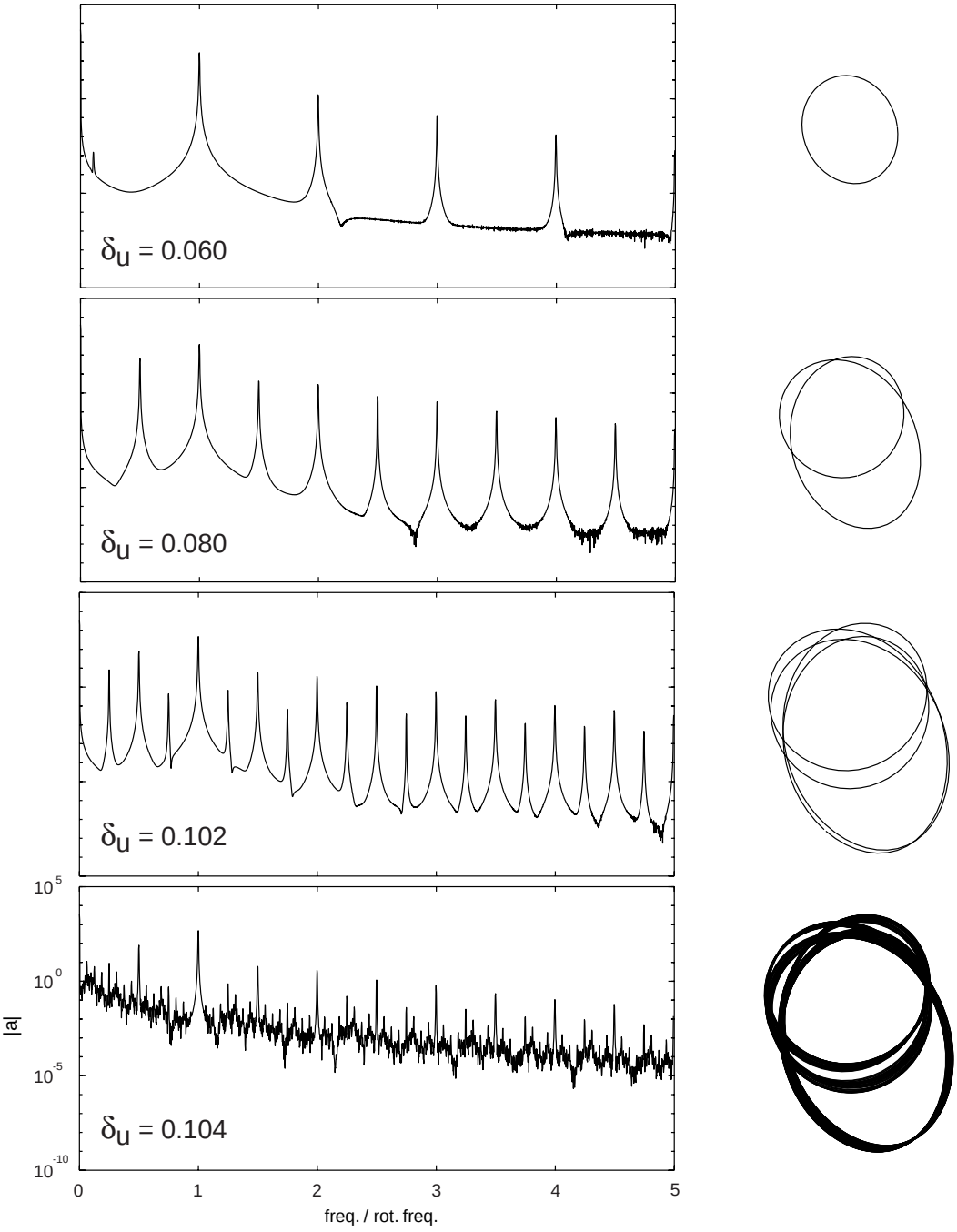

Figure 3.25: Frequency spectra and orbits for increasing levels of imbalance as limit is approached. As imbalance increases, each path splits so the lowest frequency is divided by a power of two *i.e.* first a $1/2\omega$ mode appears, then $1/4\omega$, then $1/16\omega$.

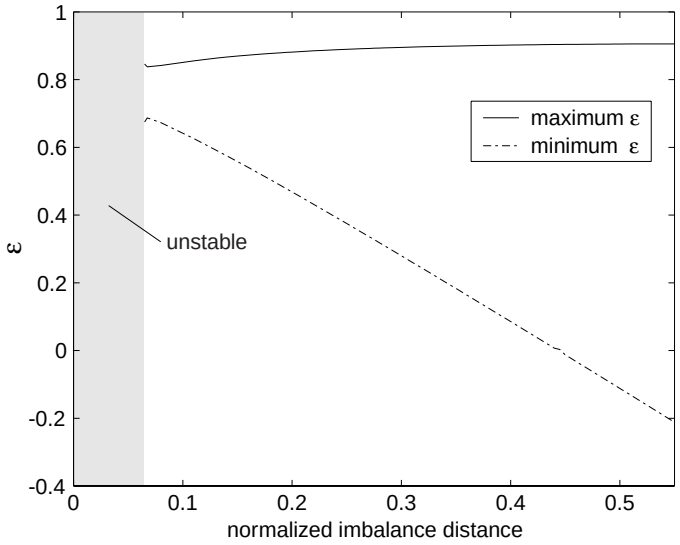

Figure 3.26: Rotor response to imbalance at 80% of loading required for fixed-point stability. Because $\zeta < \zeta_{min}$, a stable orbit cannot be maintained if $\delta_u < 0.065$. The maximum δ_u is, however, increased significantly to $\delta_u > 0.55$. The orbits are all nearly circular.

has a natural frequency of 0.09ω, which is weakly visible on the power spectrum for the elliptical orbit at $\delta_u = 0.06$. The imbalance has therefore suppressed the natural whirl frequency and the orbit bifurcations are entirely due to an intermittent interaction between the rotating journal and the large stiffness at the wall.

For the bearing / load combination of Fig. 3.23, further increases of δ_u beyond approximately 10% resulted in crashes. This imbalance level was therefore ruled the operational limit for this case. A possible explanation of this limit is that a bifurcation involving a step-increase in maximum eccentricity, such as that observed near $\delta = 0.066$, would form after that point but was prevented from doing so by the already-high eccentricity.

In this case, imbalance can have a destructive effect on an otherwise stable bearing. A demonstration of the opposite situation is presented in Fig. 3.26. This case is identical to that of Fig. 3.23 except the load is set below the minimum for fixed-point stability, instead of above it. In this series of calculations, $\zeta = 0.8\zeta_{min}$, corresponding to an eccentricity of 78%. The fixed point is thus expected to be unstable for some range of imbalance including zero. For the current bearing / loading combination, this range is $0 < \delta_u < 0.065$, which is shaded gray in Fig. 3.26. At greater imbalances, as observed by previous experimenters, the orbit stabilizes into a nearly circular shape.

Two key differences between Figs. 3.23 and 3.26 can be seen. First, the eccentricity limits do not undergo the sudden slope changes associated with orbit bifurcations in the previous case. Indeed, the orbits over the entire imbalance range were nearly circular. Second, the range of tolerable imbalances is much greater in the current series: while the overloaded case could not tolerate imbalances much greater than 10%, the underloaded case's tolerance extends above 55%. In fact, the simulation was simply stopped at this

point; a limit was never encountered.

This finding implies that "under-loading" the journal can increase its tolerance to imbalance. A pitfall exists for this approach, however: if the imbalance is smaller than planned, the journal could be subject to a whirl instability. In cases where the imbalance can be measured after manufacture, this situation can be avoided; the load schedule is simply tuned for the known imbalance. For a microdevice, however, it is generally difficult to estimate the imbalance of a given unit. It is therefore desirable to have a method for tuning the load schedule experimentally.

A key issue with the experimental approach is that the number of observables in a microdevice tends to be quite low. Toward a solution of this problem, Orr [34] showed that significant information can be gleaned from the frequency content of the rotor motion. This is a significant finding because the necessary data may be obtained from a sensor of marginal spatial accuracy, provided it is responsive in time.

Exploring this possibility for determining the proper loading in the presence of imbalance, the power spectra and orbits for a series of calculations of increasing load are presented in Fig. 3.27. In this figure, the calculation was started at the load and imbalance of the last case in Fig. 3.23 ($\zeta = 0.155$, $\delta_u = 0.103375$), and the load was slowly reduced until the orbit began to break up, indicating a whirl instability. This break-up point was found to be $\zeta = 0.0645$, which is less than half of the starting load.

Comparing Figs. 3.25 and 3.27, it is immediately evident that increasing load and increasing imbalance have very similar effects. The most notable difference between these two figures is that the orbits in the current case, due to the constant imbalance level, are of roughly the same size, while they grow with δ_u in the variable-imbalance case.

In terms of the power spectra, the imbalance orbits have components at frequencies that are multiples of $1/2\omega$ when they become very close to the wall. In the interim region, where the bearing is in a roughly circular orbit, the spectrum is very clean, showing only multiples of the synchronous frequency. In the lowest stable load case, the spectrum again becomes rich, but this time the strongest frequency, not counting the synchronous, is roughly the whirl frequency yielded by the fixed point stability analysis for this case: 0.088ω.

This suggests that the ideal load for a given geometry, running point, and imbalance may indeed be found from spectral information. If the spectrum shows power at multiples of $1/2\omega$, the load is lowered until only synchronous forcing and its multiples appear. If, however, these modes are absent but the significant power appears at the bearing's fixed-point whirl frequency, then the load should be increased to establish a clean synchronous spectrum. This technique may be difficult, however, for very small $\bar{M}$, low speeds, and large L/D, where, as shown in Fig. 3.19, the self-excited whirl frequencies tend to be very near $1/2\omega$.

Finally, even when the load was decreased slightly below the minimum found for whirl

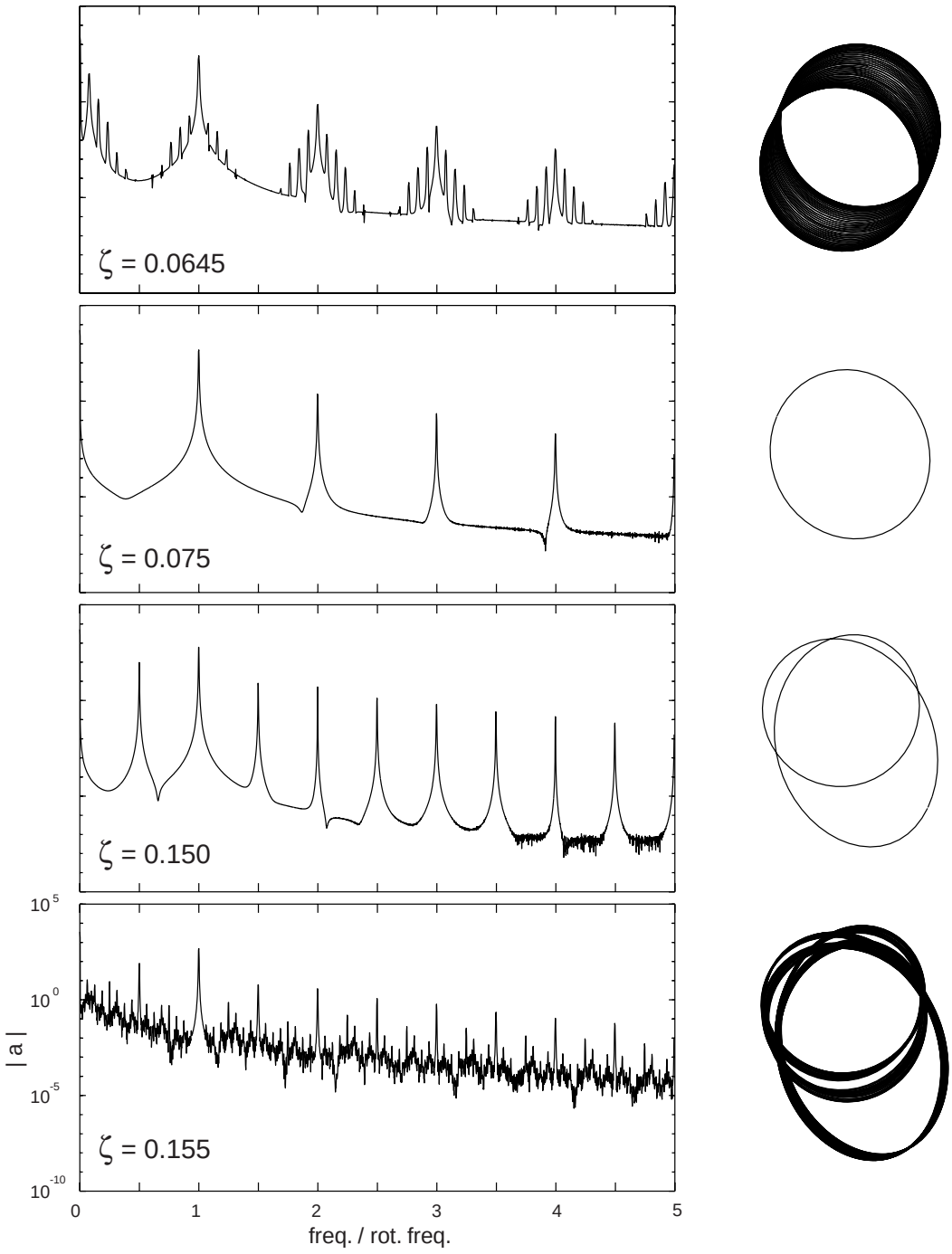

Figure 3.27: Frequency spectra and orbits for various loading levels between whirl stability and imbalance limits. The behavior is very similar to that shown in Fig. 3.25, supporting the tradeoff between load and imbalance levels in terms of bearing operation. Crashes resulting from applying too much or too little static load are differentiated by the dominance or absence of strong $1/2\omega$ multiples in the frequency spectrum.

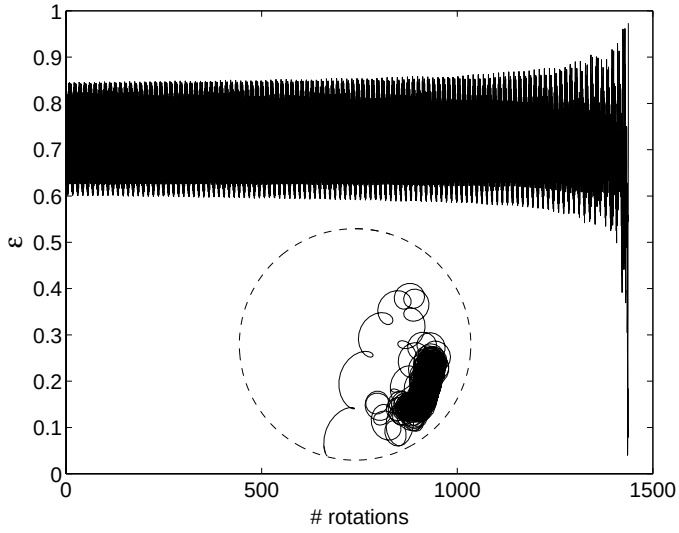

Figure 3.28: Example of a failed attempt to establish a stable whirl in a bearing with neither sufficient load nor imbalance to maintain fixed-point stability. In this case, the eccentricity oscillations grow very slowly and the orbit is relatively stationary for nearly 1500 revolutions before the journal breaks out and crashes.

stability and the orbit grew very slowly, which tended to produce a stable whirl mode in even the most sensitive zero-imbalance cases, the journal would suddenly spiral out and crash. This behavior is shown in Fig. 3.28 for the previous case run at $\zeta = 0.06375$. In this case, the bearing makes nearly 1500 revolutions before coming to an abrupt end.

From experiences such as these, the conclusion may be made that establishing a stable whirl in the presence of imbalance is difficult. This result is not surprising when the high eccentricities typically associated with whirling modes are considered. The synchronous frequency imbalance orbit cannot coexist with the nearly half-frequency, large-radius, self-excited whirl orbit except, perhaps, when their radii are comparable. In this case, an orbit of two linked and nearly concentric circles can satisfy both frequencies without causing the "wobbling" motion that resulted in the crash of Fig. 3.28.

3.2.5 Shock Tolerance

Another performance parameter of interest to designers is a device's tolerance to shock loading. Such loading may be imposed by dropping (most likely the worst case), aerodynamic buffeting and maneuvering loads in flight vehicles, or vibration from external sources.

Two failure modes may be envisioned as a result of an impulsive load. In the first, the shock load simply exceeds the bearing's capacity and forces the journal into the wall. In the second, the shock load reduces the eccentricity below the minimum required for stability and the resulting whirl results in wall contact. Due to the short duration of most shocks and the multiple rotations required for hydrodynamic whirls to grow to failure, the latter

mode is unlikely to be of concern. This intuitive contention is supported by experimental observations of Reynolds and Gross [26], who conclude that "both synchronous and self-excited whirl are uniformly asymptotically stable to excitations which are not large enough to cause initial metal-to-metal contact." Consequently, shock tolerances reported in this section will refer to the first failure mode.

In this section, three methods are presented for determining shock tolerance. The first two techniques will be referred to as "quasi-static" estimation methods because they rely entirely on a bearing's steady-state performance charts. The final method is a full dynamic simulation of a running bearing subjected to a step increase in load. The chief difference between these methods is the dynamic calculation's inclusion of squeeze-film and history effects versus the static calculation's assumption of a quasi-equilibrium at each eccentricity during the journal reaction. Additionally, the journal is allowed to follow a general path in the dynamic simulation, rather than a strictly radial motion, as assumed in the static analysis.

Quasi-Static Estimation

To estimate the shock magnitude necessary to force the bearing to wall contact from static data, the total work done by the shock load may be equated to the work done by the fluid against its motion. The eccentricity at which this equation balances will be the maximum eccentricity under the shock, assuming that its duration is sufficient to reach this eccentricity. The maximum shock will therefore be the case where the final eccentricity is nearly unity.

Assuming the shock acts in the direction of the bearing's static load, the resulting equation for its shock tolerance in multiples of the gravitational acceleration (g's) is:

$$a_s = \frac{1}{\epsilon_f - \epsilon_o} \int_{\epsilon_o}^{\epsilon_f} \frac{\zeta}{\zeta_g} d\epsilon - \frac{\zeta_o}{\zeta_g} \tag{3.5}$$

where ϵ_o is initial eccentricity, ϵ_f is the final eccentricity, ζ_o is the static applied load parameter, and ζ_g is the load parameter calculated from the journal weight.

There are a number of ways to handle this integral. The most direct, and most accurate within the constraints of the quasi-static method, is to numerically integrate a steady-state dataset taken at closely-spaced eccentricities. A more convenient option is to freeze the stiffness at its initial value so that:

$$\zeta = \zeta_o + \left(\frac{d\zeta}{d\epsilon}\right)_o (\epsilon - \epsilon_o),$$

in which case Eq. 3.5 becomes simply:

$$a_s = \frac{\epsilon_f - \epsilon_o}{2\zeta_g} \left(\frac{d\zeta}{d\epsilon}\right)_o \tag{3.6}$$

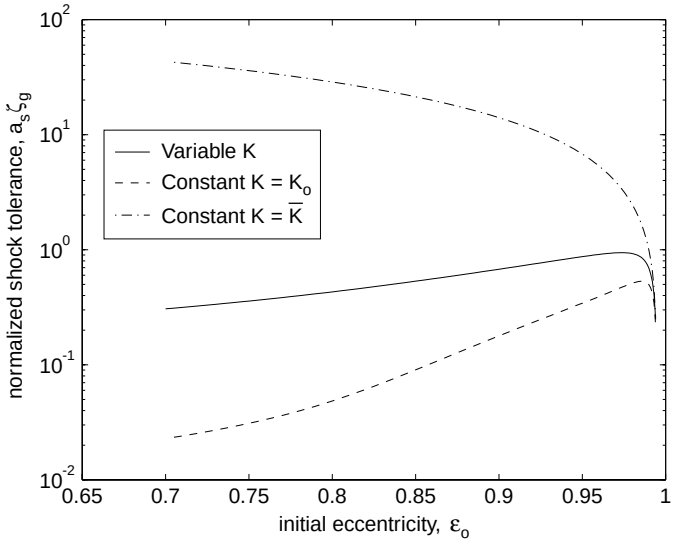

Figure 3.29: Comparison of shock tolerance for L/D=0.075 bearings at $\Lambda = 5$ computed with variable and constant stiffness. The variable stiffness model can over or underpredict the shock tolerance at low eccentricity, with respect to the variable stiffness model, by more than an order of magnitude depending on whether the starting or average stiffness is employed.

To compare the results of the variable and constant stiffness techniques, the shock tolerance for an $L/D = 0.075$ bearing at $\Lambda = 5$ is shown in Fig. 3.29 for $\epsilon_f = 0.995$. To generalize the chart to bearings with different masses, a normalized shock tolerance, $a_s\zeta_g$, is plotted.

It is clear from this figure that the frozen-stiffness model consistently underpredicts the shock tolerance computed with the variable stiffness model. This result is not surprising because the former model neglects the considerable stiffness increase found near the wall shown in Fig. 3.30. As a result, one would expect the greatest difference between the constant and variable stiffness estimates to be found at low eccentricity. An inspection of Fig. 3.29 shows that this is indeed the case, with the difference exceeding an order of magnitude near $\epsilon_o = 0.7$.

It may be suggested that a means of reducing this error may be to use an average of initial and final stiffnesses in Eq. 3.6. In this case, due to the exceptionally large stiffnesses at high ϵ shown in Fig. 3.30, the shock tolerance is drastically larger than predicted by the variable stiffness model at all but the largest eccentricities.

Due to the orders-of-magnitude error of the frozen-stiffness model, and the uncomplicated nature of generating and numerically integrating the steady-state data, the latter model is recommended for all but the roughest estimates of shock tolerance.

Dimensionalizing the variable-stiffness result for a microdevice: solid, millimeter-scale silicon rotors were shown in Sec. 1.3.3 to have ζ_g of order 10^{-4}. From Fig. 3.29, the normalized shock tolerance predicted by the variable stiffness model is of order unity, thus the estimated shock tolerance for the microdevice at this operating point is of order 10^4 g's. Conversely, a macrodevice with order unity mass at the same operating point would tolerate only order unity g's. As noted previously, this is a key feature of microdevices

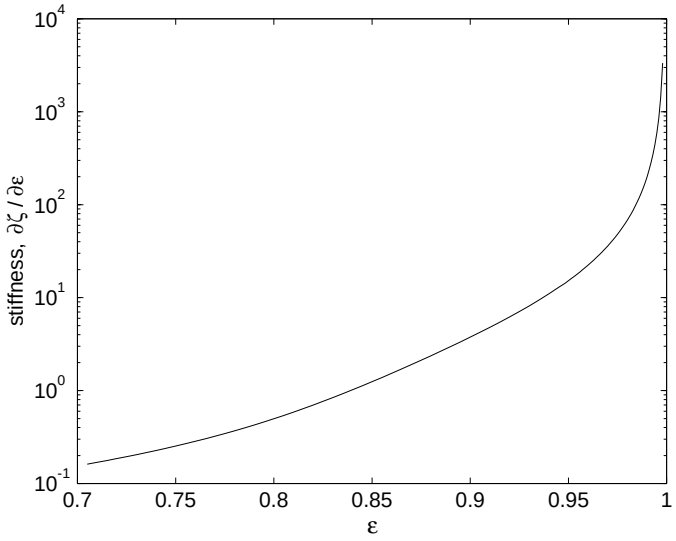

Figure 3.30: Nondimensional stiffness ($\frac{\partial\zeta}{\partial\epsilon}$) for an L/D=0.075 bearing at $\Lambda = 5$. Note the extremely rapid stiffness increase as the eccentricity approaches unity.

in general: their low inertia implies that sudden accelerations produce little stress on the surrounding structure compared to macrodevices at the same conditions.

The effect of L/D on the variable stiffness shock tolerance estimate is shown in Fig. 3.31. Due to the longer bearing's greater load capacity (compare Figs. 3.1 and 3.2), it is more tolerant to shocks. This conclusion also holds true for changes in rotation speed, *i.e.* slower running speeds imply lesser shock tolerance than faster speeds.

Dynamic Simulation

To investigate the importance of unsteady effects, which are very likely to be significant in a sudden-load situation, a dynamic simulation of shock loading was performed at the same conditions used in the previous section. Before the calculation even begins, however, a complication appears: in the quasi-static calculation, the journal mass can be eliminated by reporting the shock tolerance in terms of the load parameter due to weight, ζ_g. In the dynamic case, however, $\bar{M}$ remains as a parameter. This observation highlights $\bar{M}$'s role as a dynamic variable involving the unsteady film properties in addition to the journal mass.

A further complication in comparing these results is presented by the fact that the journal does not react to the shock with a simple monotonic approach to the wall; it may rebound several times. If, as may be intuitively assumed, the first approach produces the maximum eccentricity, this fact is not an issue. It was found in the course of this investigation, however, that a shock loading may be found for many configurations where the journal survives the initial wall approach but crashes on a subsequent approach. This behavior is shown in Fig. 3.32 for an $L/D = 0.075$ bearing with $\bar{M} = 0.1$, running at $\Lambda = 5$ and an initial eccentricity of 83%, subjected to an order-of-magnitude step increase of the

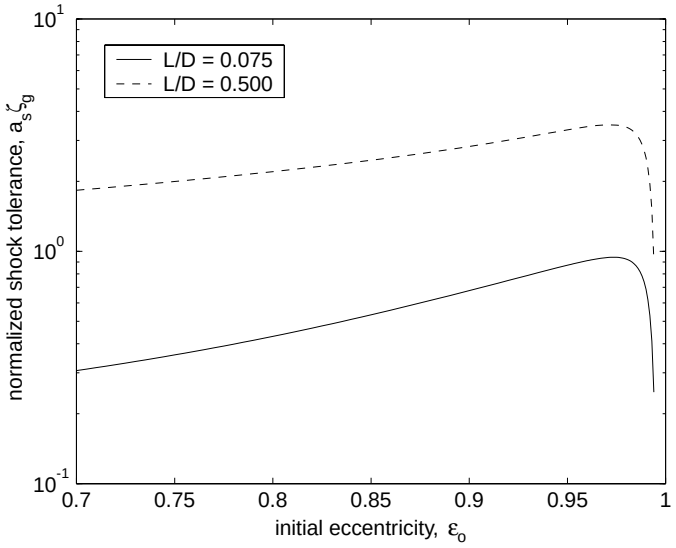

Figure 3.31: Comparison of shock tolerances at $\Lambda = 5$ for bearings with $L/D = 0.075$ and $L/D = 0.5$. Owing to its larger load capacity, the longer bearings have a greater tolerance to shocks at a given running speed and eccentricity.

applied load. In this case, the second bounce occurs at higher eccentricity (99.4%) than the first (99%) and the bearing crashes on the fourth bounce after a relatively weak third bounce to 98.8% eccentricity.

For the purpose of comparison with the static results, we will take the maximum shock as that which pushes the journal's first bounce to 99.5% eccentricity. These calculations will therefore yield the true tolerance to shocks with duration greater than or equal to the time required to reach the first eccentricity peak, but shorter than that needed to reach a subsequent higher peak, if such a peak exists. This time tends to decrease with $\bar{M}$ and initial eccentricity, ϵ_o. Its variation for an $L/D = 0.075$ bearing at $\Lambda = 5$ moving to an eccentricity of 99.5% after a step input from various ϵ_o is shown in Fig. 3.33 in units of journal revolutions. Dimensionalizing this example for a microturbomachine: a journal with $\bar{M} = 0.1$ revolving at 2 million RPM at a steady-state eccentricity of 80% will require approximately 8 microseconds to reach its first eccentricity peak.

With the above provisos in place, the shock tolerance for an $L/D = 0.075$ bearing at $\lambda = 5$ may be compared to the statically-derived results of the previous section. As before, the shock is applied along the direction of the steady-state load holding the bearing at the initial eccentricity. In this case, it was necessary to perform the calculation for a range of $\bar{M}$s. The numerically-integrated static estimate is included for comparison.

From a design standpoint, a key trend of Fig. 3.34 is that the static calculation underestimates the shock tolerance for all $\bar{M}$s, except at very high initial eccentricities ($\epsilon_o > 0.95$). The shock tolerance calculated from the static data therefore represents a "worst case" for most bearings. The difference between the dynamic and static results tends to increase with decreasing $\bar{M}$ except near the cross-over of the constant-$\bar{M}$ lines above $\epsilon_o \simeq 0.92$.

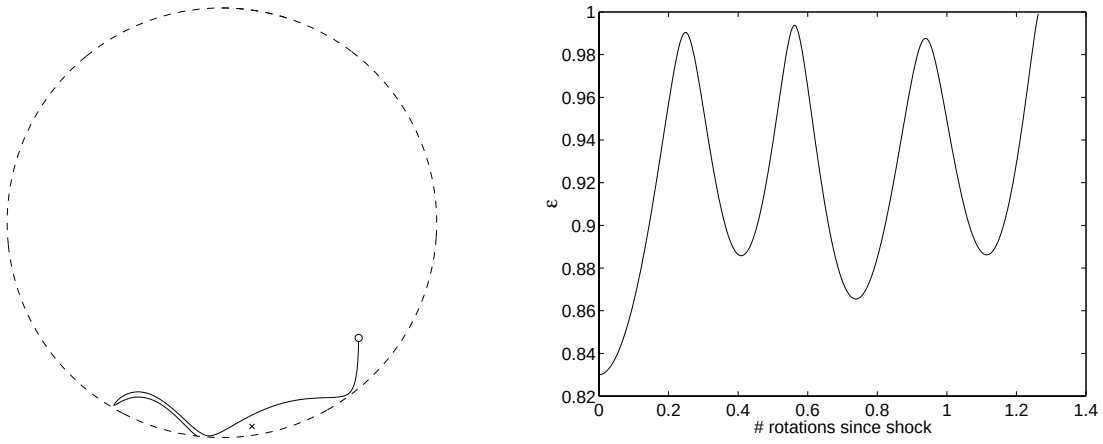

(a) journal path **(b)** eccentricity history

Figure 3.32: Response of an $L/D = 0.075$ bearing with $\bar{M} = 0.1$ running at $\Lambda = 5$ and an initial eccentricity of 83% to an order-of-magnitude step increase in applied load. The 'o' in (a) indicates the starting position and the 'x' indicates the static position associated with the increased load.

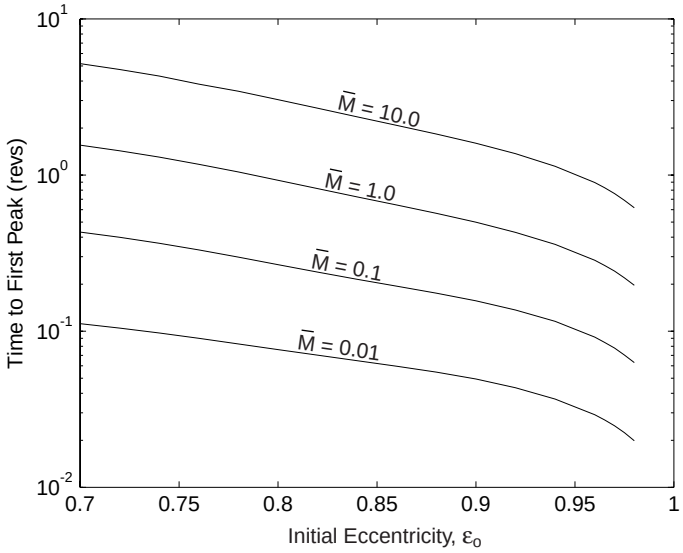

Figure 3.33: Time required to reach an initial eccentricity peak of 99.5% for $L/D = 0.075$ bearings at $\Lambda = 5$ of various $\bar{M}$s subjected to step loading from a range of initial eccentricities.

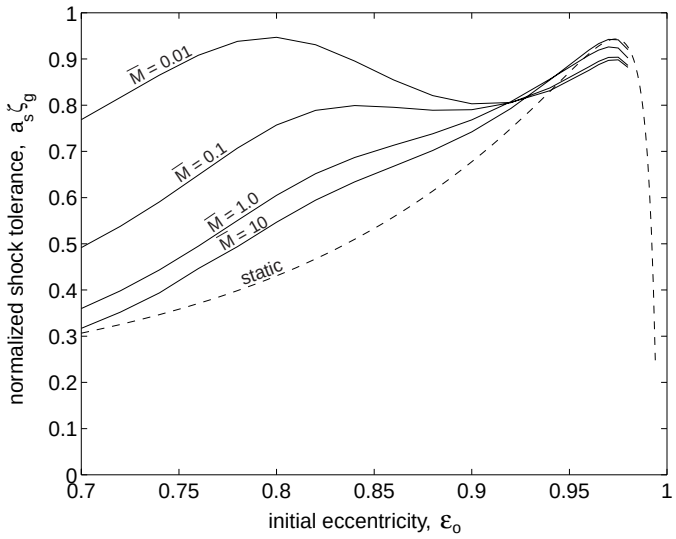

Figure 3.34: Shock tolerance at $\Lambda = 5$ for $L/D = 0.075$ bearings of various $\bar{M}$ compared to an estimate computed from steady-state data.

Bearings with small $\bar{M}$ may thus be considerably more tolerant to shocks than predicted from static data.

Furthermore, in place of the uniform concave up shape of the static estimate (except near the limiting eccentricity), the dynamic results show a varying curvature that becomes concave-down in the neighborhood of $\epsilon = 0.8$. This transition occurs at lower eccentricity and becomes more pronounced as $\bar{M}$ decreases. In the lower $\bar{M}$ curves, this behavior produces a maximum in the shock tolerance versus initial eccentricity. For the smallest $\bar{M}$, this is also a global maximum. For these bearings, the shock tolerance may be maximized without incurring the drag penalty associated with very high eccentricity operation.

The results of Fig. 3.34 may be understood in terms of a tradeoff between two unsteady effects that have competing influence on shock tolerance. Hamrock [12] refers to these effects as as "squeeze" and "local expansion." Both of these effects necessarily spring from the unsteady term in the continuity equation because all unsteady terms in the fluid momentum equations vanish when inertia is dropped during the Reynolds equation's development.

Squeeze appears as a $p\,\partial h/\partial t$ term. Its position in the Reynolds equation with respect to the Poiseuille term implies that a negative value brings increased load capacity. When a sudden load is applied, $\partial h/\partial t$ is negative on the journal side opposite the loading direction, thus the squeeze effect acts to counter the shock loading. In addition, as the journal moves under its new load, this region also becomes the minimum gap location where both squeeze and viscous pumping effects act to increase the pressure. The presence of a pressure multiplier on the squeeze term increases the importance of $\partial h/\partial t$ as the eccentricity (and hence the peak pressure) increases.

Physically, squeeze produces load capacity via the local increase in pressure required

to force fluid out of a decreasing volume against viscous retardation. On the leeward side, it has the reverse effect, causing a decrease in pressure to draw fluid into the increasing volume. This effect is present in incompressible bearings, as evidenced by the existence of oil-filled squeeze-film dampers.

Local expansion appears as an $h\,\partial p/\partial t$ term. In the impulsive loading case, this term could be referred to as "local compression" because the time derivative of pressure is positive under the journal. This term's position in the Reynolds equation is similar to that of the squeeze term. The positive derivative therefore implies that local compression acts to weaken opposition to the journal motion.

Physically, the local compression effect is related to the coupling between pressure and density changes in an isothermal film. Unlike an incompressible fluid, upon a sudden change of its boundary conditions, a compressible fluid may undergo a density change instead of immediately redistributing itself in the new volume. The time rate of change of density in the compressible continuity equation thus produces a "history effect," whereby the pressure field can differ from that predicted by the instantaneous conditions at the solid walls. For example, the steady-state analysis can predict a higher pressure in a given region than currently exists, thus mass must be moved into the area. As in the squeeze mechanism, moving fluid against viscosity requires a pressure distribution. In this case, however, the distribution is counter to the load-carrying distribution because fluid can only be moved into its characteristic high pressure area by a higher pressure elsewhere. In the shock case, this implies that the integrated work is lower than predicted by the static analysis because the force at each eccentricity is lower than predicted by the static analysis, thus this effect reduces shock tolerance.

Competition between these effects produces the cross-over in constant $\bar{M}$ lines at $\epsilon \simeq 0.92$ on Fig. 3.34. Journals operating at lower eccentricities when the shock load is applied reach higher translational speeds because the initial bearing stiffness is smaller. The combination of large translational speed and small stiffness implies that squeeze effects provide a large share of the unsteady reaction for these bearings. Furthermore, because the mean translational speed has an inverse relationship with $\bar{M}$ (see Fig. 3.33), this effect increases with decreasing $\bar{M}$. In Fig. 3.34, this situation produces the increasing agreement with the static estimate at low ϵ_o as $\bar{M}$ increases.

Conversely, journals operating at larger initial eccentricities experience larger stiffnesses along their entire path so the maximum journal speed is lower. Viscous pumping, as predicted by the static analysis, therefore provides a larger share of the reaction. The higher load capacity at these eccentricities, however, implies large peak pressures and therefore large $\partial p/\partial t$, even with small translation speeds. Local compression effects therefore cause a net decrease in the shock tolerance over the statically-calculated value for high ϵ_o. This decrease worsens as $\bar{M}$ shrinks because the increase in journal speed results in an increase in $\partial p/\partial t$. The trend of increasing agreement between static and dynamic

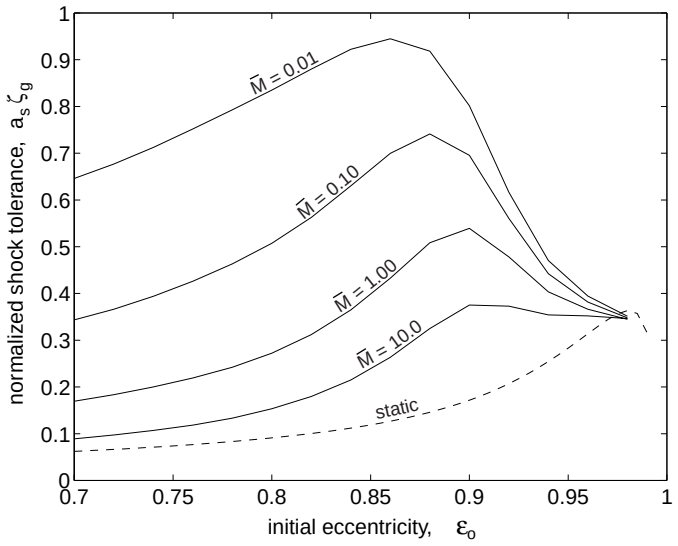

Figure 3.35: Shock tolerance at $\Lambda = 0.5$ for $L/D = 0.075$ bearings of various $\bar{M}$ compared to an estimate computed from steady-state data.

cases with decreasing $\bar{M}$ is therefore reversed at high eccentricity when local compression dominates.

The tradeoff between these unsteady effects may be altered by changing the bearing number. Squeeze is independent of bearing number because it is created by journal translation, rather than rotation. Local compression, however, is a function of $\partial p/\partial t$. For a given change in journal position, the change in pressure is dependent on Λ, thus local compression in the shock loading context should also be dependent on Λ. The result of this rebalancing of unsteady effects via Λ change is shown in Fig. 3.35.

Several observations can be made on this figure. First, the statically-estimated shock tolerance is sharply reduced by decreasing Λ. This reduction is a consequence of the steady-state load capacity's dependence on Λ (see Sec. 3.1.1). Second, once again, the unsteady results show a shock tolerance greater than the static estimate, with the improvement increasing with decreasing $\bar{M}$. Notably, however, the peak shock tolerance for $\bar{M} = 0.01$ changes very little between Figs. 3.34 and 3.35, despite the order-of-magnitude reduction in Λ. This observation implies that squeeze dominates the shock tolerance of low $\bar{M}$ bearings running at moderate eccentricities for the range of bearing numbers studied. This conclusion is further supported by the larger peak differences from the static estimate for all $\bar{M}$ traces at the lower Λ. Finally, the crossover of traces is absent from Fig. 3.35. Because the lower speed case reaches a much lower peak pressure at all eccentricities, the eccentricity at which local compression becomes important increases, thus the handoff of dominance from squeeze to local compression will occur later. In the $\Lambda = 0.5$ case of Fig. 3.35, the crossover point shifts out of the depicted eccentricity range.

Additional insight into the tradeoff between squeeze and local compression effects may

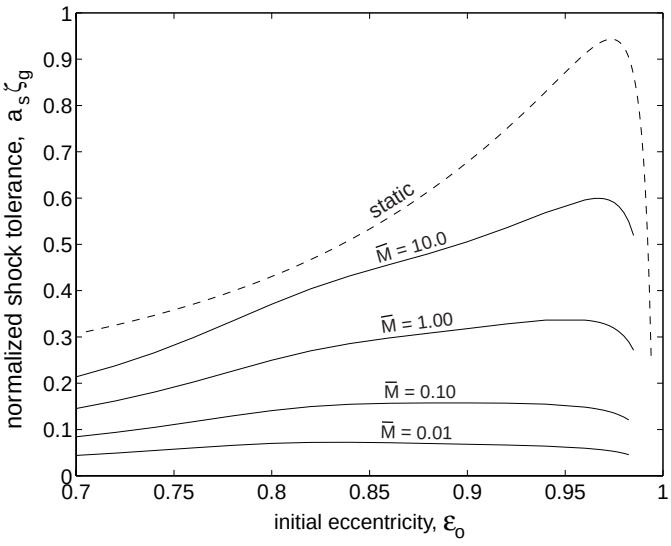

Figure 3.36: Shock tolerance at $\Lambda = 5$ for $L/D = 0.075$ bearings of various $\bar{M}$s calculated with time derivative of height deleted.

be obtained by performing a series of calculations with one of them removed. In Fig. 3.36, the calculations of Fig. 3.34 were performed with the $\frac{\partial h}{\partial t}$ set to zero, eliminating the squeeze mechanism.

In this case, all the $\bar{M}$ traces fall below the static estimate. In addition, their ordering is inverted, *i.e.* larger $\bar{M}$s now imply greater shock tolerance. This finding supports the above hypothesis that local compression has a uniformly deleterious effect on shock tolerance, with the level of degradation increasing with journal translational speed.

3.3 Chapter Summary

In this chapter, the behavior of plain journal bearings was investigated. Due to the small lengths found in most micromachines, a focus was held on the effect of very small L/D on the treated phenomena.

Load Capacity

The steady-state load parameter at low speed was shown to decrease significantly as the bearing L/D was reduced. This trend was explained via the analytical solution for an incompressible short bearing. The remarkable fit of this solution to the $L/D = 0.075$ bearing throughout the depicted speed and eccentricity range led to the conclusion of a later onset of compressibility effects as L/D decreases. Because compressibility tends to decrease load capacity, this observation implies that a portion of the short bearing's load capacity disadvantage may be recovered at high speed.

Drag

It was shown that calculation of drag may be considerably simplified for the short bearing because its low load capacity and large attitude angles deemphasize the Poiseuille term involving these quantities compared to the Couette term involving only the eccentricity. Due to the relative insensitivity to design permutations of the stability boundaries in terms of eccentricity shown in Sec. 3.2.1, this finding implies that a reasonable estimate of the bearing drag can be obtained very early in the design process.

Fixed-Point Stability

The tendency of a journal to return to fixed-point (*i.e.* non-orbiting) operation following a small perturbation was presented in a number of formats. The experimental observations of other researchers were explained via trends illuminated on these charts. In general, it was found that decreasing L/D increases the running eccentricity but, due to the associated loss of load capacity to side-leakage, it may also reduce the required load. For a self-contained machine, this situation implies that the short bearing may have lower bleed air requirements when loading is provided via a pressure differential. Furthermore, when designing bearings under the fixed C/L constraint imposed by microfabrication, it was found that greater improvement is generally obtained by increasing L than by decreasing D.

Whirling Operation

A stable whirling mode was shown to exist for journals with negligible imbalance, in agreement with previous researchers' experimental and numerical observations. This solution was demonstrated in regions with a fixed point solution as well as those where no such solution exists. The extent of the whirling solution into both regions was shown to be a function of applied L/D and $\bar{M}$. A method for estimating this extent from fixed-point stability solutions was suggested. For microbearings, whirling solutions were shown to exist at very high eccentricities and were difficult to establish in the presence of significant imbalance. They are therefore unlikely to be of operational importance.

Imbalance

A striking similarity was shown between applied load and imbalance in terms of bearing operation. In both cases, too little produces self-excited whirl and too much implies a direct wall strike. Applying the two quantities in tandem, tradeoffs may be made between them. If sufficient load is applied to guarantee fixed-point stability, a limit to the allowable imbalance is implied. Reducing this load implies a tolerance to greater imbalance levels, but the journal is liable to whirl if some minimum imbalance is not maintained. A method

for determining the load boundaries experimentally for a journal with unknown imbalance based on a power spectrum of its motion was suggested.

Shock Tolerance

By comparing unsteady simulations of step-input loading to quasi-static estimation results, it was shown that the shock tolerance estimated by numerically integrating steady-state data is a "worst-case" value except at very high initial eccentricities and high speeds. It was noted that the difference between these solutions increases as $\bar{M}$ decreases because squeeze film effects become more important. These results indicate that the shock tolerance will typically be thousands of g's for millimeter-scale devices made of silicon.

Chapter 4

Geometric Variations

This chapter explores the effect of variations in geometry from the plain, cylindrical journal bearing case. These deviations may be deliberate, eg. Dimofte's "wave bearing" [30], or an undesirable consequence of the manufacturing method, eg. axially-tapering clearance in etched bearings [64]. In either case, geometric effects can significantly alter the bearing's performance so it is important to consider them early in the design process.

4.1 Noncircular Bearing

As noted in Sec. 3.2, the plain journal bearing has a limited envelope within which operation is possible. For machines that cannot tolerate the vibration associated with a high-eccentricity whirling mode examined in Sec. 3.2.2, the envelope is reduced further to the fixed-point mode boundaries examined in Sec. 3.2.1. In an effort to expand this envelope, many researchers have suggested that the journal's tendency to whirl may be reduced by breaking the bearing's rotational symmetry. In effect, this changes the distribution of convergence / divergence in the fluid passage. Because the Reynolds equation relates pressure gradients to passage height gradients in time and space, a shape change can greatly alter a bearing's steady-state and dynamic performance.

Comparisons between various noncircular shapes appear in the literature [65, 66]. For example cases, this section will employ a relatively recent geometry: the wave bearing [30]. This bearing, introduced in 1995 by Dimofte, has a sinusoidally-varying clearance. Three parameters must therefore be chosen to define the noncircularity of wave bearings: the wave amplitude, A_{nc}, normalized by the mean clearance, C_{nc}, to yield a_{nc}, the wave phase, α, and the number of wave cycles, n_w. The influence of wave amplitude and phase are treated in [30]. The influence of the number of waves is treated in [67]. Results on the influence of these parameters on microfabricated wave bearings will be presented in the current section.

4.1.1 Considerations for Microfabricated Machines

The microfabrication environment's unique characteristics affect the design tradeoffs of noncircular bearings. First, because many devices are made from a single photolithographic mask, an increase in shape complexity has no effect on the per-unit manufacturing difficulty in the ideal case. [1] Second, because the minimum clearance is set by etching considerations discussed in Sec. 1.3, any departure from circularity must be accomplished solely by increasing the clearance around the bearing in various locations. A microfabricated noncircular bearing will therefore always have a larger mean clearance than its plain counterpart. This consideration is illustrated in Fig. 4.1, which contains a sketch of the wave bearing and its controlling parameters as well as its equivalent circular bearing.

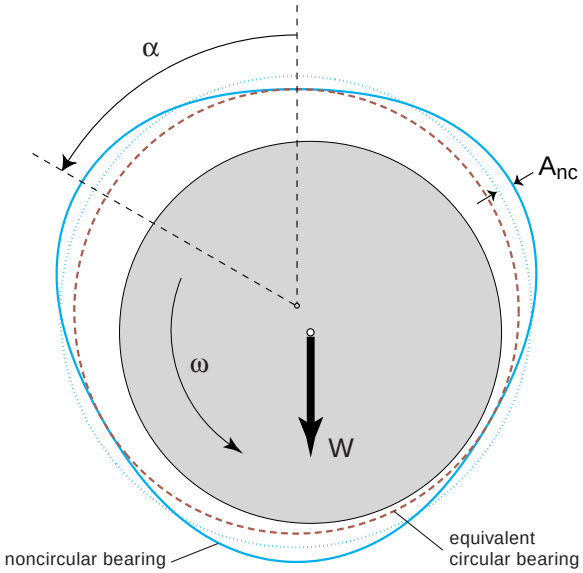

Figure 4.1: Schematic of a three-wave ($n_w = 3$) bearing showing the definition of the wave phase and the wave amplitude with respect to the equivalent microfabricated circular bearing (dashed line). The noncircular bearing's mean clearance (dotted line) is always greater than that of the equivalent circular bearing due to the fixed minimum clearance constraint.

From a physical standpoint, it can be understood that increasing the mean clearance generally reduces the steady-state load capacity of a bearing because its rotating surface area decreases with respect to the total fluid volume. Unsteady operation is also affected by increasing the clearance due to a reduction in the ratio of journal to bearing projected areas. This reduction tends to weaken squeeze film effects because a given displacement produces a smaller volume change relative to the area over which the fluid can escape. This, in addition to the reduced static load capacity, makes it more difficult for a large-clearance bearing to defeat a whirl.

These physical arguments can be supported by examining the nondimensional param-

[1] In the real case, aspect ratio-dependent etching (ARDE) [64] can be a serious concern if the clearance varies appreciably around the bearing.

eters. As noted in Sec. 2.2.2, the parameters used in this work are based on the mean clearance. These quantities will therefore reflect the increase in mean clearance associated with adding noncircularity to microfabricated bearings.

The minimum clearance for a noncircular bearing is:

$$C_{min} = C_{nc} - A_{nc} = C_{nc}(1 - a_{nc}) \tag{4.1}$$

Because the C_{min} is held constant as the geometry is varied, it is also the clearance of the equivalent circular bearing, C_c. The mean clearance of a noncircular case may be therefore be related to an equivalent circular case by:

$$\frac{C_{nc}}{C_c} = \frac{1}{1 - a_{nc}} \tag{4.2}$$

With Eq. 4.2, the nondimensional parameters of noncircular bearings may be related to those of comparable circular bearings running at the same conditions:

$$\epsilon_{nc} = \epsilon_c(1 - a_{nc}) \tag{4.3}$$

$$\Lambda_{nc} = \Lambda_c(1 - a_{nc})^2 \tag{4.4}$$

$$\bar{M}_{nc} = \frac{\bar{M}_c}{(1 - a_{nc})^5} \tag{4.5}$$

where the first expression assumes equal dimensional deflection of the journal from its concentric position between the circular and noncircular cases, as shown in Fig. 4.1. A convenient trait of this formulation is that, while the noncircular bearing can crash with $\epsilon_{nc} < 1$, ϵ_c is always at least unity at crash, though it can be greater than unity as well. Unfortunately, it is not possible to define an eccentricity that is always unity at crash without including details of the shape and the journal position.

Inspecting Eqs. 4.3 - 4.5, the physical arguments regarding the effect of clearance increases on bearing operation become clear in nondimensional space. Under otherwise identical conditions, a noncircular bearing runs at a smaller eccentricity, a lower bearing number, and a larger dimensionless mass than comparable circular bearing. It was shown in Chap. 3 that each of these changes results in lower load capacity and, in general, poorer stability.

In view of this finding, the decision to adopt noncircular bearings in a microfabricated machine must be justified by performance gains large enough to offset any losses associated with the concomitant increase in mean clearance. The current section is constructed with this tradeoff in mind.

4.1.2 Steady-State Behavior

To demonstrate the effect of the microfabrication constraints on the steady-state performance of a wave bearing, a series of calculations were performed for an $L/D = 0.075$ bearing at $\epsilon = 0.3$ with varying wave phase angles. A sample result of this series at a fixed Λ is included in Fig. 4.2.

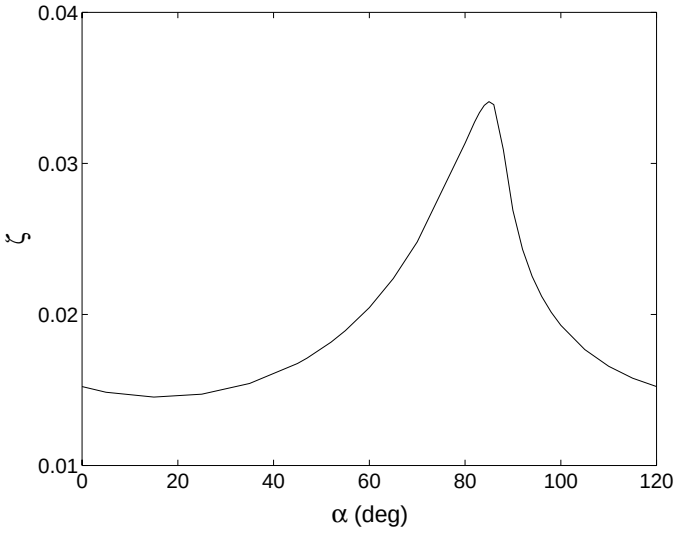

Figure 4.2: Dependence of load capacity on wave position angle, α, for a 3-wave bearing with $a_{nc} = 0.4$. In this case, $L/D = 0.075$, $\Lambda = 10$, and $\epsilon = 0.3$

Following Dimofte [30], the maximum load parameter obtained from the series of calculations performed at each Λ is plotted in Fig. 4.3 for bearings of various wave amplitudes with equal mean clearances. As observed by Dimofte, the maximum load capacity of a wave bearing is generally greater than that of a circular bearing. In Fig. 4.3, ζ increases by more than an order of magnitude when the wave amplitude reaches 60% of the clearance (*i.e.* $a_{nc} = 0.6$).

Two features distinguish Fig. 4.3 from Dimofte's result at $L/D = 1$ (see [30], Fig. 3). First, the overall load level is two orders of magnitude smaller. This effect is a consequence of increased side leakage suffered by the much shorter bearing treated here. Second, and more importantly, the difference between the circular and noncircular results is much greater for the shorter bearing. This observation implies that a greater benefit may be obtained by adopting noncircular geometries as the L/D shrinks.

The comparison presented in Fig. 4.3 changes considerably under fixed minimum clearance constraint imposed on microfabricated bearings. Under this constraint, the bearing number is reduced in the calculation using Eq. 4.4, but the data is plotted with respect to the equivalent circular case bearing number, Λ_c. Furthermore, the running eccentricity is reduced using Eq. 4.3 to provide a fixed dimensional running distance between the journal and bearing centers.

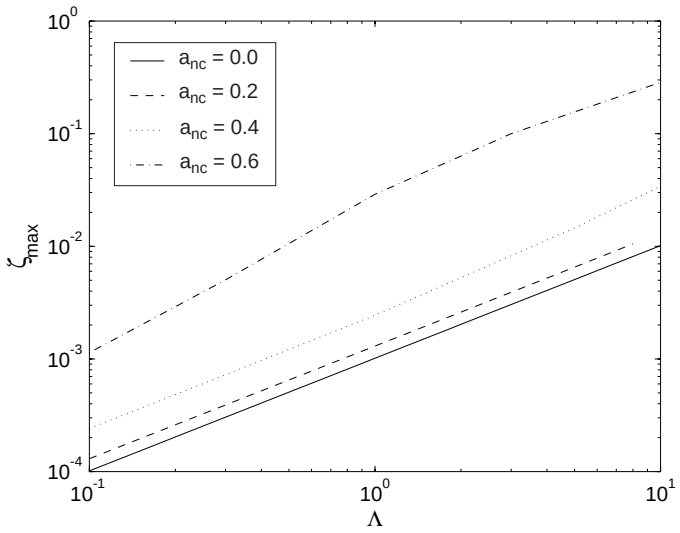

Figure 4.3: Maximum load parameter of $L/D = 0.075$ three-wave bearings of various amplitude at $\epsilon = 0.3$ for a range of bearing numbers. In this case, as in much of the bearing literature, the mean clearance is held constant, so the minimum clearance decreases with increasing wave amplitude

Repeating the calculations with these factors in mind, a new chart is presented in Fig. 4.4. Notably, the trend of Fig. 4.3 is reversed: now the load capacity at a given running point *decreases* as the wave amplitude increases. This finding demonstrates that the increase in mean clearance brought by noncircularity under the minimum clearance constraint can consume the advantage in steady-state load capacity reported by other researchers.

For a turbomachine with self-acting bearings, the decreased load capacity may be an advantage because it reduces the bleed air flow required to force the bearing to a sufficient eccentricity to guarantee stability. The associated disadvantage is realized in terms of a reduced tolerance to transient loading from vibration, dropping, or unplanned pressure imbalances.

Before proceeding with comparisons involving noncircular bearings, an important feature regarding the load capacity in terms of eccentricity should be noted: these parameters do not necessarily have a one-to-one relationship. This behavior is demonstrated in Fig. 4.5, where the load on two 40% three-wave bearings with differing phase angles was slowly increased at $\Lambda = 1$ and the corresponding eccentricity measured. The results for a circular bearing running at the same nondimensional conditions (*i.e.* without adjustment for the minimum-clearance constraint) are also shown for reference.

Unlike the circular bearing, whose eccentricity always increases with applied load, Fig. 4.5 shows that wave bearings have regions in which increasing the load decreases the eccentricity. Moreover, the extent and amplitude of the decreasing-ϵ region is a strong function of the wave phase angle.

An additional peculiarity of wave bearings is presented in Fig. 4.6, which shows the at-

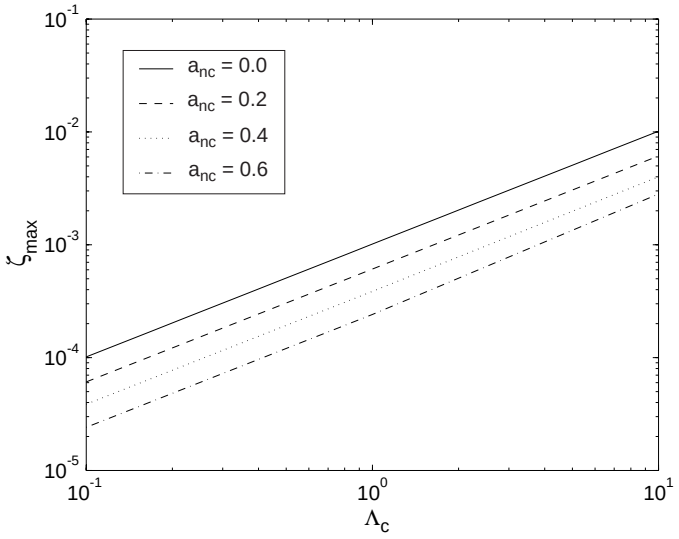

Figure 4.4: Maximum load parameter of $L/D = 0.075$ three-wave bearings of various amplitude at a range of bearing numbers. In this case, the running eccentricity was adjusted to reflect a fixed dimensional running distance under the fixed minimum clearance constraint. The bearing number is also renormalized to match the circular case at the same running condition.

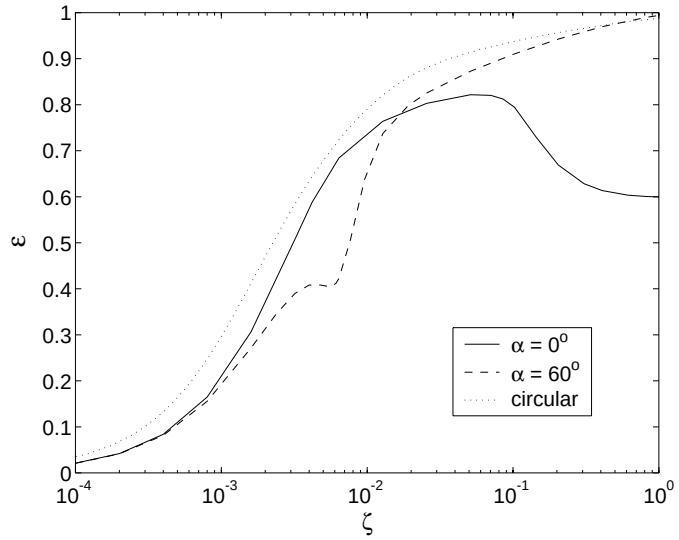

Figure 4.5: Eccentricity variation with applied load for $L/D = 0.075$, $a_{nc} = 0.4$ three-wave bearings with $\alpha = 0°$ and $\alpha = 60°$ at $\Lambda = 1$. A given eccentricity does not imply a unique load, as it does in the circular case run at the same nondimensional conditions.

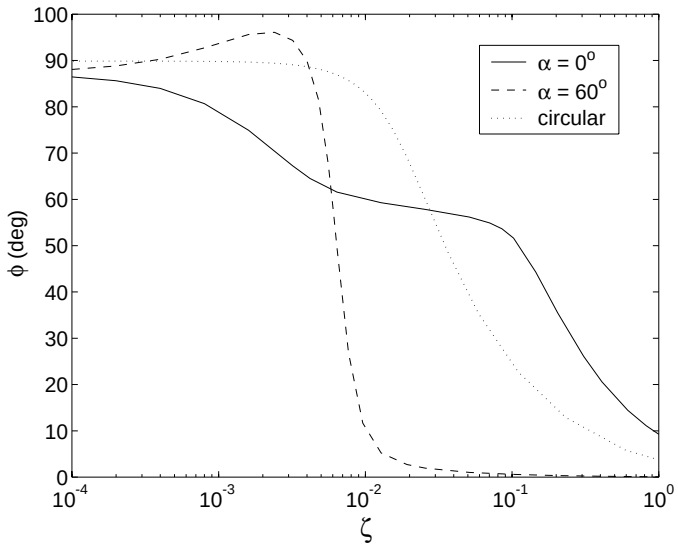

Figure 4.6: Attitude angle variation with applied load for $L/D = 0.075$ 40% three-wave bearings with $\alpha = 0°$ and $\alpha = 60°$ at $\Lambda = 1$. The $\alpha = 60°$ trace exhibits unusual features of increasing ϕ with load and $\phi > 90°$ in the low-ζ region.

titude angles associated with the load points in the previous figure. Once again, the traces show a strong dependence on α. In a stark contrast to typical circular bearing behavior, the $\alpha = 60°$ trace shows an increasing attitude angle with load for small loads. Furthermore, ϕ exceeds 90 degrees, which is not possible in circular bearings.

The physical mechanism behind the behavior shown in Figs. 4.5 and 4.6 can be understood with the help of Fig. 4.7. This figure shows the journal path with respect to the wave geometry, which has been greatly exaggerated for visibility. In the $\alpha = 0°$ case, a clearance minimum occurs at $\theta = 180°$ and another at $\theta = 300°$. In this case, the journal assumes smaller attitude angles than the circular case for small loads because it tracks down the wave peak centered at $\theta = 300°$ as eccentricity increases. When the attitude angle reaches $60°$ (*i.e.* h_{min} is at $\theta = 240°$), however, it begins to track up the $\theta = 180°$ peak and the rate of ϕ decrease, as well as the rate of ϵ increase, with ζ slows. At very large loads, the journal approaches the $\theta = 180°$ peak and the measured eccentricity begins to decrease strongly.

In the $\alpha = 60°$ case, the bearing geometry has clearance minimum at $\theta = 240°$. The attitude angle trace of Fig. 4.6 therefore implies that the increasing attitude angle for low ζ corresponds to the journal moving to higher eccentricity by tracking down the geometry peak *in the direction of rotation*, thus the unusual result of increasing attitude angle with load. As ζ increases past 10^{-3}, the journal's attitude angle progression with load reverses and it moves to the upstream side of the peak. In the course of this movement, the eccentricity decreases briefly as it passes the peak, hence the turndown in Fig. 4.5 corresponds to the area where ϕ is near $60°$ in Fig. 4.6. From this point forward, the behavior is more familiar because the increasing eccentricity causes the journal to track down the lobe in a direction opposite its rotation, as it would in the circular case.

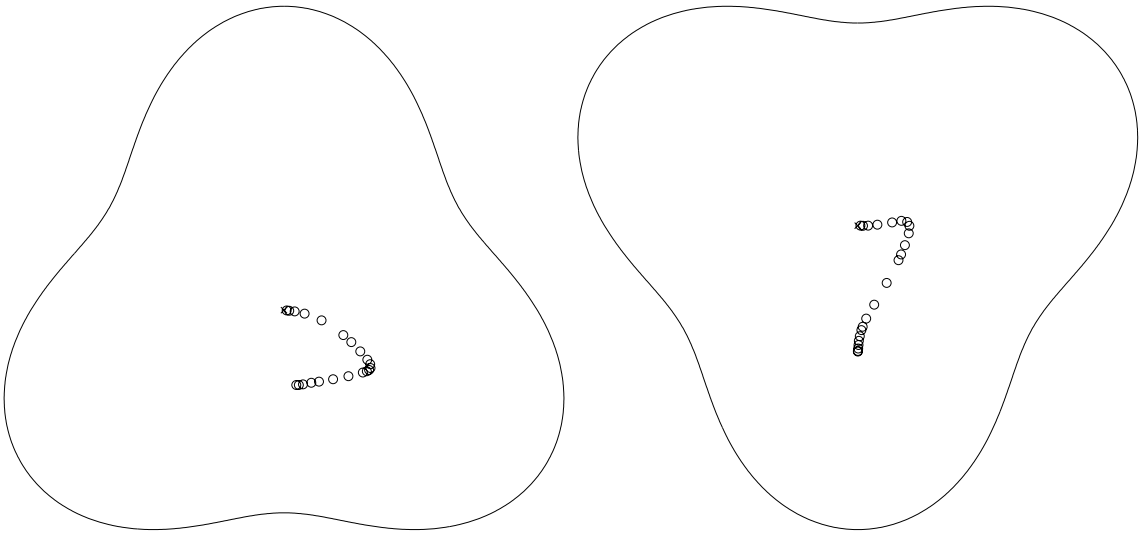

(a) $\alpha = 0^\circ$ **(b)** $\alpha = 60^\circ$

Figure 4.7: Demonstration of the effect of wave phase angle on the journal path under increasing load. The positions shown correspond to the data in Figs. 4.5 and 4.6 and the wave shape is greatly exaggerated for visibility.

Thus, the aberrant behavior of the wave bearing with respect to the circular bearing stems from a varying relationship between journal position and wave shape as the attitude angle decreases under increasing load. From this argument, one would also expect similar behavior from bearings run under fixed load over a range of speeds because the attitude angle is dependent on speed.

The apparently complex behavior of noncircular bearings under increasing load shown in the preceding figures may be simplified by replacing eccentricity with the minimum distance between solid surfaces normalized by the clearance, a quantity to be referred to as δ. For the circular case, δ is simply $1-\epsilon$. For the noncircular case, δ also depends on ϕ and the three wave bearing parameters, n_w, a_{nc}, and α. As shown in Fig. 4.8, however, the additional effort involved in computing δ is rewarded by a vastly simplified presentation.

In this coordinate space, the noncircular bearing data fall closer to the behavior expected from circular cases. First, the relationship between δ and ζ becomes one-to-one and monotonic. Second, the traces for differing α collapse almost perfectly. The key to understanding steady noncircular bearing behavior therefore lies in examining the journal's position with respect to nearby features in the bearing shape instead of its position with respect to the bearing center.

Figure 4.8 exhibits another important feature to keep in mind when comparing noncircular bearing data found in the literature: the circular case δ has a zero-load asymptote of unity while the noncircular case's asymptote occurs at 0.6. In other words, the noncircu-

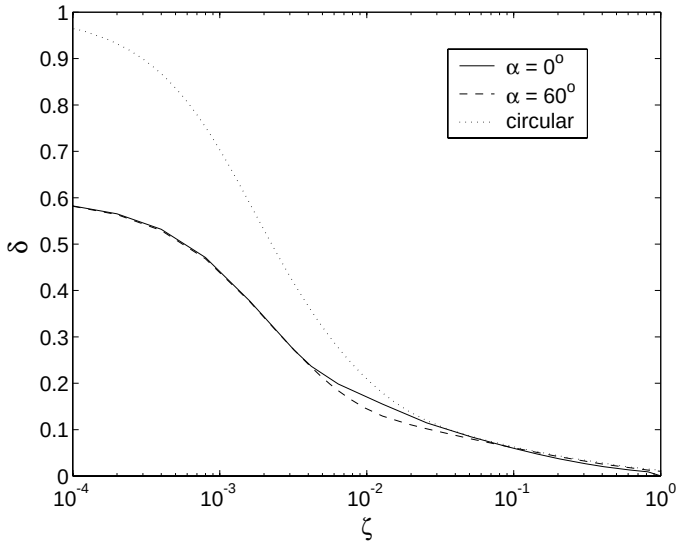

Figure 4.8: Data of Fig. 4.5 replotted versus the minimum distance between journal and bearing, δ. In this case, the curves for differing wave phase angles collapse and a one-to-one relationship is shown.

lar bearing may have a much smaller minimum running clearance for a given eccentricity due to the incursion of the bearing surface into the mean circle. The fixed minimum clearance constraint eliminates the incursion issue, but it also implies a larger mean clearance and, hence, a different normalizing factor in the definition of ϵ. The relationship between dimensional minimum heights for various bearings is therefore unclear when examining δ. This issue is addressed in the current document by reporting δ in terms of δ_c, which is δ renormalized by the clearance of the equivalent circular bearing under the minimum clearance constraint using Eq. 4.2. With this normalization, the nondimensional minimum height will vary between zero and one for all cases.

4.1.3 Unsteady Behavior

Repeating the progression followed in Chap. 3, this section will expand upon its predecessor by adding time-dependent effects to the calculation. As noted in the previous chapter, the operating positions reported in the previous section are only realizable by bearings within a given range of dimensionless mass. Other bearings will depart from their static equilibrium position to enter a whirl that may or may not end in wall contact.

Fixed-Point Stability

In this section, as in Sec. 3.2.1, journal stability will be assessed with respect to the tendency to return to a fixed position after a small perturbation. Noncircular bearings complicate this investigation and the presentation of its results for two primary reasons. First, the already-large parameter space expands to include constants describing the bearing shape.

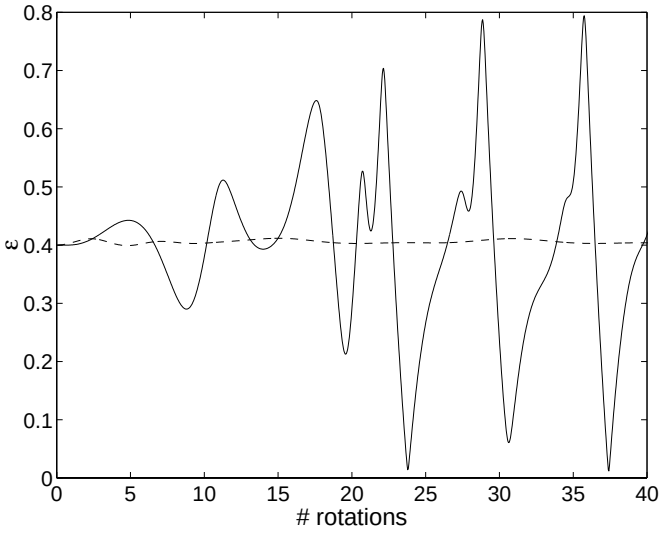

Figure 4.9: Demonstration of stable and unstable bearings with the same equilibrium eccentricity ($\epsilon = 0.4$). Both cases are $L/D = 0.075$, 40% three-wave bearings with $\alpha = 60°$. The unstable case is $\zeta = 0.0037$ and the stable case is $\zeta = 0.0055$.

For the wave bearing, this description adds three variables (a_{nc}, n_w, α). Second, the charts used in Sec. 3.2.1 in terms of eccentricity are not appropriate for noncircular bearings because, as pointed out in the previous section, the relationship between ϵ and ζ is not always one-to-one. From a physical standpoint, however, one expects the stability boundary to be one-to-one in terms of a loading condition. The load parameter and δ will be investigated in this section as a more appropriate variables for this role.

To underscore this point, a demonstration of a stability boundary lying between two load parameters corresponding to the same eccentricity is presented in Fig. 4.9. The bearing is a $L/D = 0.075$, 40% three-wave bearing with $\bar{M} = 1$ and $\Lambda = 1$. Supporting the concept of a loading condition, the bearing under higher ζ (0.0055) is stable and that under lower ζ (0.0037) is not, despite the fact that both correspond to an equilibrium position of $\epsilon = 0.4$.

It should be noted that, while the static equilibrium points for the two cases depicted in Fig. 4.9 have the same eccentricity, their attitude angles are different: $69.5°$ and $91.8°$ for the high and low ζ cases, respectively. This observation supports the intuitive expectation that a given load corresponds to a unique running position at fixed Λ. The varying geometry simply introduces multiple points along the load line that correspond to the same eccentricity.

In addition, the higher and lower ζ traces in Fig. 4.9 correspond to $\delta = 0.20$ and $\delta = 0.25$, respectively. The minimum running distance is therefore a good candidate for use as a loading condition in the same way ϵ was used in the previous chapter.

As a demonstration of bearing stability dependence on various wave parameters in the coordinate space used in this document, Fig. 4.10 contains the minimum load required

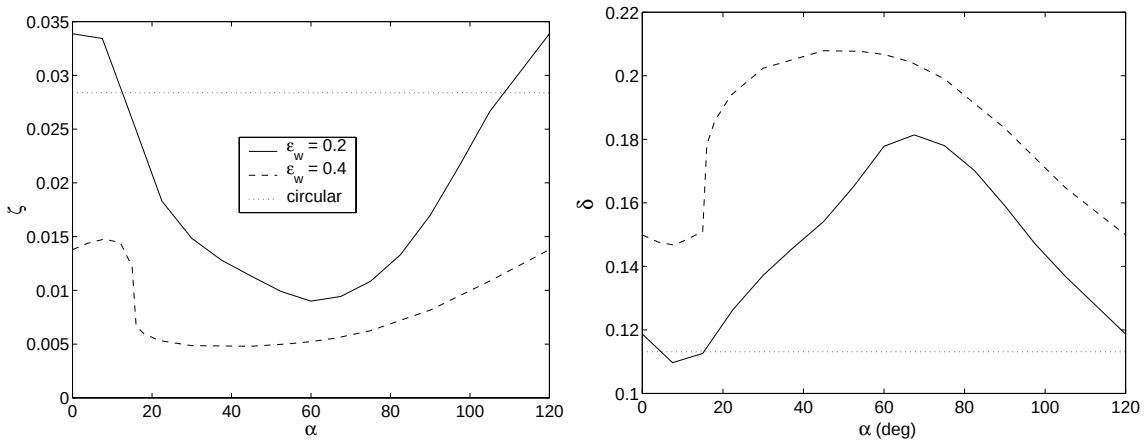

(a) Load **(b)** Minimum Running Distance

Figure 4.10: Minimum stable ζ and δ for 20 and 40% amplitude three-wave bearings as a function of wave phase angle. The circular result at the same nondimensional condition ($L/D=0.075$ $\Lambda=1$, $\bar{M}=1$) is included for reference.

for stability at $\Lambda = 1$ for three-wave bearings of amplitude 0.2 and 0.4 with $\bar{M} = 1$ at a range of wave phase angles. The results for a circular bearing at the same nondimensional condition are included for reference.

As noted by Dimofte [67] for the $L/D=1$ steady-state case, the 20% wave bearing trace crosses the circular bearing result. This finding implies that α must be chosen carefully when adopting small amplitude three wave bearings to avoid a performance degradation, both in steady state load capacity and stability margin. Because the optimal α is likely to depend on Λ (see [30], Fig. 5), these bearings may not be a good choice for machines that operate at a wide range of speeds. In the context of this result, Dimofte [67] points out that manufacturing tolerances on a circular bearing can make it appear to be a small amplitude, small wavenumber, noncircular bearing so its performance can be worse than the intended circular bearing. In this case, Dimofte recommends increasing the manufacturing tolerances to ensure that the variation is greater than 20% of the clearance (which has the beneficial side-effect of reducing cost in a conventionally-machined bearing).

Another feature of Fig. 4.10 worth noting is that the variation of both ζ and δ decreases slightly with increasing wave amplitude. In this case, the variation of ζ and δ from the median value is 63% and 25% for the $a_{nc} = 0.2$ bearing and 51% and 17% for the $a_{nc} = 0.4$ bearing.

To reinforce the difference between ϵ and δ in noncircular bearings discussed in the previous section, the minimum eccentricities corresponding to Fig. 4.10 is shown in Fig. 4.11. It is immediately evident that the variation of ϵ with α is much greater than that of δ. Furthermore, significant differences can be seen in the curve shapes. For instance, the eccentricity plot for the 40% bearing shows a sharp minimum near $\alpha = 60^{\circ}$ whereas the δ

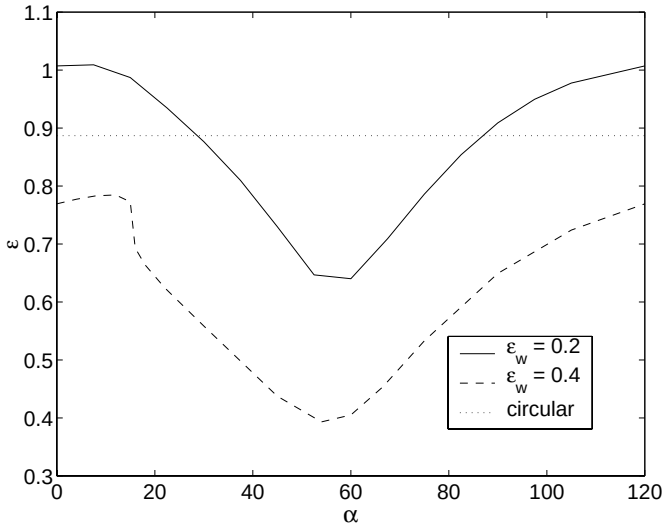

Figure 4.11: Data of Fig. 4.10 replotted versus eccentricity. Note that variation of ϵ with α is much greater than that of δ and the curve shapes are not related in a simple manner.

chart shows a much broader maximum. This is also true, although to a lesser extent, for the 20% bearing. In both cases, the peak in δ occurs at a smaller phase angle than predicted by the eccentricity plot.

Finally, Fig. 4.11 implies that larger wave amplitudes are generally better in terms of lower required load and larger running clearance. Under the minimum clearance constraint often imposed by microfabrication concerns, this may not be the case because larger amplitudes imply larger mean clearances.

Before applying the minimum clearance constraint to the noncircular bearing results, the effect of wavenumber on stability in the parameter space employed in this document will be investigated. For a fixed wave amplitude, changing the wavenumber does not affect the clearance. These results will therefore be independent of the minimum clearance constraint. As mentioned previously, increasing bearing shape complexity has little effect on the manufacturing difficulty of each unit in a microfabrication environment. Most of the increased difficulty is absorbed in the construction of the mask, which is then used to define to geometry of many units. In addition, Dimofte [67] reported that increasing the wavenumber decreases the performance variation with phase angle. If these findings apply to the current bearings and parameter space, subsequent tradeoff investigations can be greatly simplified.

For this study, 40% wave bearings of wavenumber 3, 6, and 9 were run at the conditions of the previous figure. The resulting data are presented in Fig. 4.12.

The most immediately evident trend in Fig. 4.12 supports the findings of Dimofte [67]: the performance data variation with α weakens considerably as wavenumber increases. In the depicted case, the span of ζ changes from a factor of three for the 3-wave bearing to almost imperceptible for the 9-wave bearing. The collapse of the δ variation is also

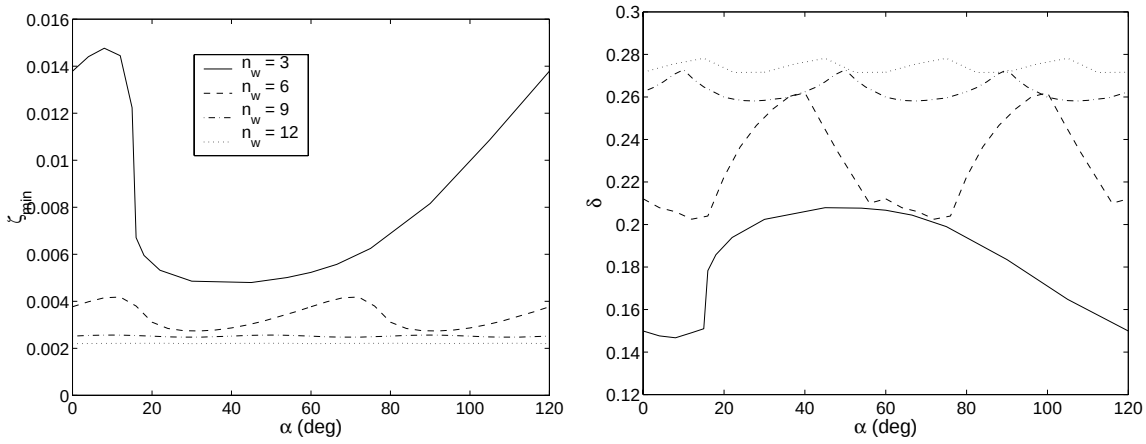

(a) Load **(b)** Minimum Running Distance

Figure 4.12: Minimum stable ζ and δ for 40% amplitude wave bearings as a function of wave phase angle and wavenumber at the same nondimensional condition ($L/D = 0.075\ \Lambda = 1, \bar{M} = 1$).

dramatic: the ratio of maximum to minimum δ drops from a factor of 1.42 in the 3-wave case to 1.06 in the 9-wave case.

Dimofte also reported a decreasing load capacity with increasing wave number. Support for this finding may be found in Fig. 4.12. For instance, the 3 and 6-wave bearings have similar δ in the interval $50 < \alpha < 70$. Referring to Fig. 4.12(a), however, ζ is significantly higher in this interval for the 3-wave bearing. Similarly, the 6 and 9-wave bearings have virtually indistinguishable δ near $\alpha = 40$, but the 6-wave bearings shows a greater ζ in this area in Fig. 4.12(a).

As mentioned previously, reduced load capacity is an advantage for turbomachines loaded with self-generated pressures in terms of bleed air requirements but a disadvantage in terms of shock tolerance. Fortunately, the reduced load required for stability with increasing wavenumber shown in Fig. 4.12(a) is much larger than can be explained by lost load capacity; it is also a result of the increased δ realized at most α as the bearing wavenumber increases. Furthermore, the increased δ also implies reduced running drag and that the journal will not be riding between wave peaks, which could be a problematic situation in the presence of imbalance.

An intuitive attempt to explain this finding may be made by considering the infinite wavenumber limit. Approaching this limit, the waves become so tightly packed that the bearing begins to appear circular to the journal, but with clearance equal to C_{min}. This thought experiment explains the decreased dependence on α, because α is irrelevant to a circular bearing, as well as the increased stability, because decreasing clearance generally improves stability.

The above argument does not, however, explain the reduced load capacity reported by

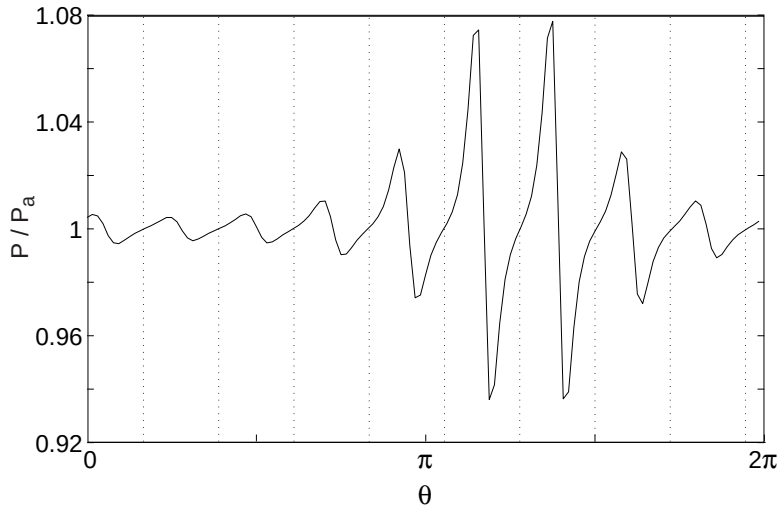

Figure 4.13: Mid-length pressure distribution for a 40% 9-wave bearing at $\Lambda = 1$, $\epsilon = 0.35$. The wave shape's clearance maxima are indicated by dotted lines. It can be seen that, even at the pressure peak, the pressure is fixed at its ambient value at the lobes, supporting the axial groove argument of wave bearing behavior under the minimum clearance constraint.

Dimofte. Furthermore, for the circular case with $C = C_{min}$, the nondimensional condition represented in Fig. 4.12(a) is: $\Lambda = 2.8$ and $\bar{M} = 0.078$. From the previous chapter, this implies $\delta = 0.16$ and $\zeta = 0.04$; a much higher load and lower δ asymptote than the data suggest. The discrepancy can be explained by considering the effect of the wave valleys: they appear as axial grooves of depth much greater than their width. Particularly for a short bearing, these grooves will function as restricted vents to atmospheric pressure. They will therefore bleed down high pressure areas, reducing the load capacity, but they will also break the pressure film into several somewhat independent segments, which typically improves stability [29].

Far from the infinite-wavenumber limit, this effect is visible in the pressure distribution of a 9-wave bearing, such as that presented in Fig. 4.13. In this case, a 40% bearing with $\alpha = 10^\circ$ at $\Lambda = 1$ is shown at $\epsilon = 0.35$, $\phi = 50.58^\circ$. As suspected, the pressure is fixed at its ambient value at each of the wave valleys, whose positions are indicated by dotted lines.

In this case, the attitude angle places the journal between two wave peaks. Consequently, two major pressure peaks occur upstream of the geometric peaks, divided by a sub-ambient region. The appearance of this sub-ambient region amidst the high-pressure peak indicates that the fixing of pressures at the ambient value in the wave valleys is more of a leeward-facing step effect than an axial leakage phenomenon. This contention is also supported by the appearance of significant sub-ambient pressures opposite the journal position, where the pressure is indistinguishable from ambient in the circular case.

To demonstrate the effect of α dependence on bearings operating over a range of speeds, 40% wave bearings of wavenumbers three and nine with $\bar{M} = 1$ were run over a two order of magnitude range of Λ. The 3-wave bearing was run with $\alpha = 0^\circ$ and $\alpha = 60^\circ$, which correspond to placing a wave peak at $\phi = 0^0$ and $\phi = 60^0$, respectively (as shown in Fig. 4.7).

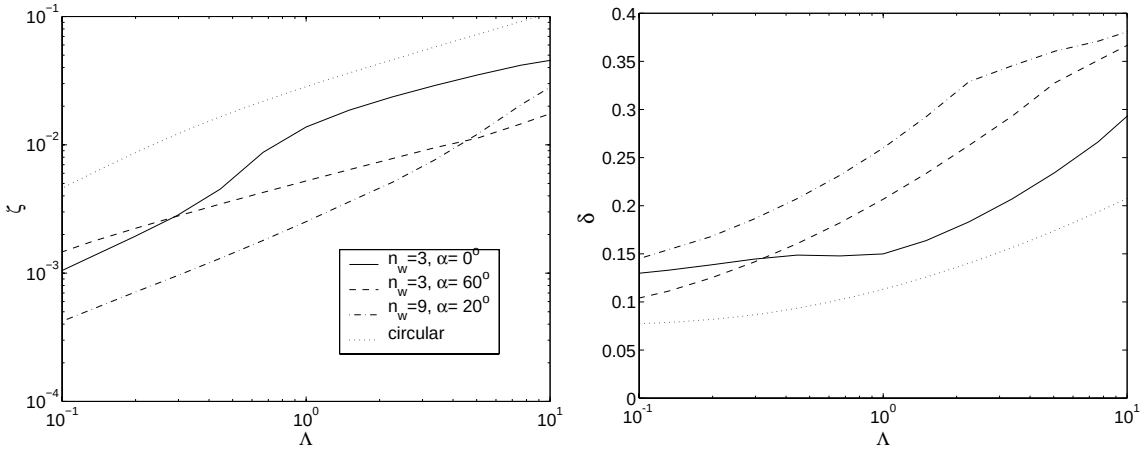

(a) Load **(b)** Minimum Running Distance

Figure 4.14: Minimum stable ζ and δ for 40% amplitude three and nine wave bearings as a function of speed. For reference, a circular bearing at the same nondimensional condition ($L/D = 0.075$ $\bar{M} = 1$) is included.

The results of these calculations are presented in Fig. 4.14. As before, the circular case at the same nondimensional condition is included for reference.

From this figure, it may be seen that the 0°, 3-wave bearing has an advantage at low Λ over the 60° case, in terms of both the required load and its associated minimum running distance. As Λ increases, however, this advantage is lost and the 0° case has significantly higher required load and lower running clearance. It is therefore necessary to make a choice between low and high speed performance when employing a three-wave bearing in the depicted conditions.

In contrast, the 9-wave bearing retains its stability advantage in terms of required load over both 3-wave bearings and the unnormalized circular bearing except near $\Lambda = 10$, where the 60° 3-wave bearing requires a smaller load. In terms of δ the 9-wave bearing's advantage holds throughout the depicted range. It is notable that, because the 9-wave bearing still has a larger δ when the ζ curves cross over, the 9-wave bearing's load capacity exceeds that of the 3-wave bearing near this point, in contrast to the result reported at $\Lambda = 1$ in Fig. 4.10.

With the 9-wave bearing's insensitivity to α and its improved ζ and δ for most Λ, a reasonably fair comparison may finally be made between wave and circular bearings under the minimum clearance constraint simply in terms of wave amplitude. Such a comparison is presented in Fig. 4.15. In this case, the bearing number and minimum running clearance is reported in terms of the equivalent circular bearing, Λ_c and δ_c, so the wave bearing cases were actually run at lower bearing numbers according to Eq. 4.4.

In contrast to the steady-state load capacity findings of the previous section, where the

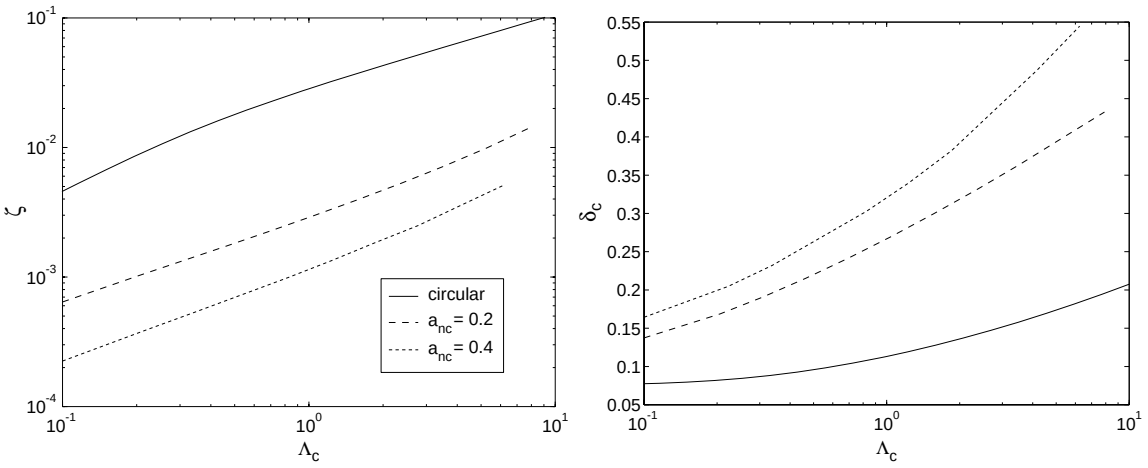

(a) Load **(b)** Minimum Running Distance

Figure 4.15: Comparison of minimum stable ζ and δ_c for circular and two 9-wave bearings as a function of speed under the minimum clearance constraint. Despite the fact that the wave bearings run at a lower bearing number and higher $\bar{M}$ than the circular case under this constraint, their advantage holds. $L/D = 0.075$ for all cases. $\bar{M} = 1$, 3, and 13 for the circular, $a_{nc} = 0.2$, and $a_{nc} = 0.4$ cases, respectively.

minimum clearance constraint reversed the trend of increasing load capacity with wave amplitude, Fig. 4.15 indicates that the wave bearing's improvement to the stability boundary, in terms of both presented metrics, survives the constraint. In terms of required load, this result is not surprising in light of the previous findings of a decreased load capacity because the wave bearing will have a lower required load even if the minimum running clearance is smaller. The finding of an increased δ_c with increasing wave amplitude was not expected because $\bar{M}$ increases by more than an order of magnitude and Λ is reduced by a factor of three for the 40% bearing under the minimum clearance constraint. Despite these adjustments, even the unnormalized δ for the wave bearing was larger than that of the circular case. This advantage is amplified even further by the adjustment of the nondimensionalizing factor in δ to the circular bearing's clearance.

Whirl Stability

In a similar manner used in Sec. 3.2.2 for plain bearings, the current section will explore the behavior of noncircular bearings when they depart from fixed point operation and enter a whirling motion. This mode change may be brought about by either a violation of the stability criteria outlined in the previous section or a jolt, as shown experimentally by Reynolds and Gross [26]. In either case, it is important to understand the conditions under which this whirl is stable and those under which it ends in potentially destructive wall contact.

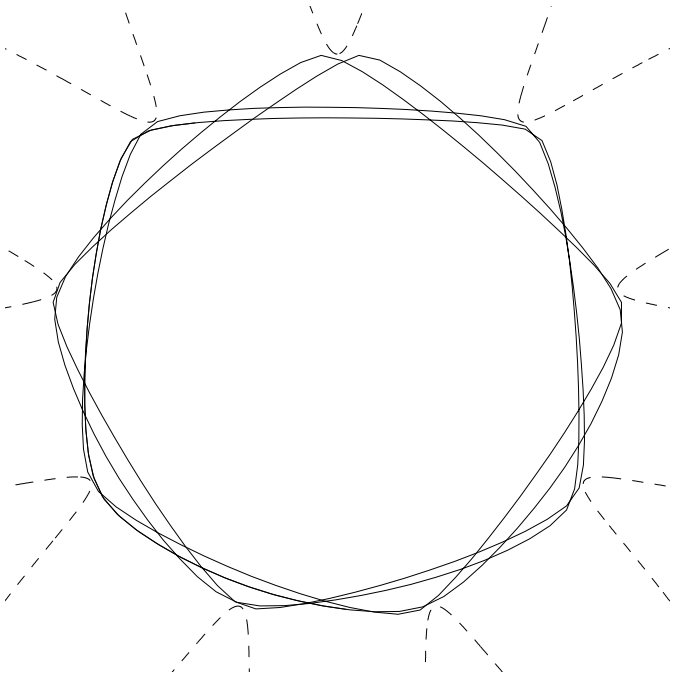

Figure 4.16: Whirl mode at fixed point for 40% 9-wave equivalent to the bearing of Fig. 3.15. As in previous figures, the contact with the dashed line denotes a wall strike. The extent of the noncircularity is greatly exaggerated in this presentation and the shape is cropped.

The line of inquiry in the current section will follow that of its predecessor for plain bearings. Numerical experiments will be conducted in which the load is fixed and the speed is increased past the threshold of fixed point stability. Once a whirl is entered, the speed will be increased until operation can no longer be sustained. A parallel series of computations will also be performed in which the speed is reduced once a whirl is established to examine the "overlap region" detailed in Sec. 3.2.2, where the whirling mode persists despite the fact that the speed has dropped below its threshold value for fixed point stability.

In order to facilitate comparison between the results of this section and those of Sec. 3.2.2, the first case to be presented is the 40% 9-wave analogue of the condition shown in Fig. 3.15. In this case, under the minimum clearance constraint, $\bar{M} = 0.1/(1 - 0.4)^5 = 1.29$. Also, the load parameter was set to 0.0028 so that the loss of fixed point stability occurred at a circular equivalent bearing number of approximately 3.5.

The whirl mode at the threshold speed for this bearing is shown in Fig. 4.16. Two features of this orbit are immediately evident. First, the shape is decidedly noncircular due to the interaction between the wave peaks and the whirling journal. Second, despite the fact that this orbit is at the whirl threshold, the journal and bearing surfaces approach each other to within 2.5% of the clearance. In terms of an eccentricity-like measure, $1-\delta$, this orbit reaches 97.5%.

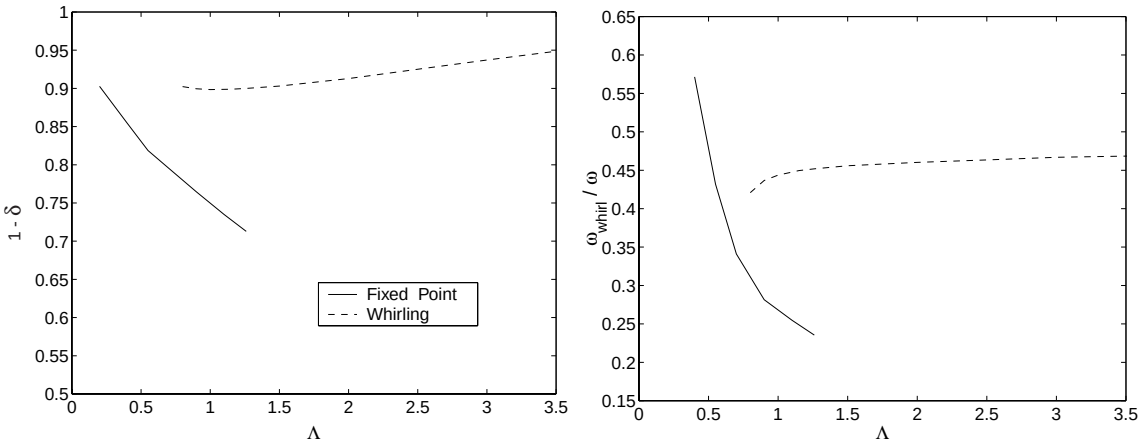

(a) Modified Eccentricity **(b)** Whirl Frequency

Figure 4.17: Stable running modes for an $L/D = 0.075$ 40% 9-Wave Bearing with $\bar{M} = 0.13$ and $\zeta = 0.0028$. Under the minimum clearance constraint, this $\bar{M}$ corresponds to a circular bearing with $\bar{M} = 0.01$

The orbit shown in Fig. 4.16 was established gradually by choosing a fixed-point with a very small growth rate. Attempts to increase or decrease the speed to gather data of the form presented in Sec. 3.2.2 caused the journal to crash. The extreme sensitivity of this orbit makes it unlikely to be observed in a physical system, thus the fixed point stability boundary for this case is, in effect, an operational boundary.

Following the progression of Sec. 3.2.2 the $\bar{M}$ of this bearing was reduced by an order of magnitude and the simulation repeated. The resulting behavior is shown in Fig. 4.17 in a format similar to that used in Sec. 3.2.2. Again, the eccentricity was replaced by $1-\delta$ to ease comparison between the current figure and Fig. 3.17.

In this case, a stable whirl was established at sufficiently small eccentricity that the orbit was circular. Also in contrast to the previous case, it was possible to increase the speed significantly from the fixed-point threshold and maintain a stable whirl. At approximately $\Lambda = 5.25$, however, further increases caused the journal to crash. At this bearing number, the whirl orbit was still almost perfectly circular. The difficulty in increasing Λ at this point may therefore be caused by an attempted transition to an orbit of the type shown in Fig. 4.16 where the journal "hops" from peak to peak. Because this trajectory results in situations where the journal eccentricity is increasing as the bearing surface is closing in (at the orbit "corners" in Fig. 4.16) the minimum height dips to a very small value. As a result, a small disturbance, such as a speed increase, can easily cause a crash, hence the sensitivity of the $\bar{M} = 1.29$ case.

As observed for the circular bearing in Sec. 3.2.2, the whirling mode also persisted below the fixed-point threshold speed if the bearing was started from a whirling condition and Λ was slowly decreased. This finding implies that, as observed experimentally by

Reynolds and Gross [26] for circular bearings, a jolt can cause a bearing operating below its threshold speed to whirl while another jolt can return it to fixed-point operation. In this case, unlike the $\bar{M} = 1.29$ case, the running distance between the journal and bearing in the whirl mode is sufficiently large to make it tolerant to disturbances.

4.2 Axially-Varying Clearance

In all previous (and following) sections of this document, the clearance is assumed constant in the axial direction. This assumption implies strictly translatory journal motion in addition to the geometric requirement of journal surface normals everywhere perpendicular to the rotation axis. In this section, the kinematic constraint will be held, but the geometric constraint will be released.

4.2.1 Description

In a conventional fabrication environment, unintended clearance variations in the axial direction are typically negligible because the parts are turned, ground, and/or lapped. Axial clearance variation would therefore be produced only through misalignment of the machine tool's axes. On commercial tools, this misalignment is typically very small compared to the clearance of most macro-bearings.

In the microfabrication environment, however, the parts are created by etching or deposition; generally starting at one axial end and proceeding to the other. As a result, many factors can cause the local clearance to change as the members are defined. Examples include varying chamber conditions during the process, erosion of (or buildup on) the resist, redeposition of etch products, device charging, and uneven erosion of the protective layer on the sidewalls [68]. Because the clearances required to create viable bearings in the micro scale are on the order of tens of microns, these effects have produced clearance variations as high as 40% in some of the early MIT micromachines.

Two general classes of axial clearance variation have been observed in the MIT microengine bearings and will be explored in this section: taper and bow. SEMs showing cross-sections of bearings with each type of variation are provided in Fig. 4.18. In taper, the clearance varies linearly from the maximum to the minimum value. In bow, the clearance reaches a maximum at the bearing center and has minima at both ends. For modeling purposes, this variation is taken to be hyperbolic.

Because the local clearance appears as only a total channel height in the Reynolds equation, there is no difference between clearance variation on both the journal and the bearing, as shown in Fig. 4.18, or the same total variation on one or the other member.

The inclusion of height variation adds terms to the Reynolds equation (Eq. 2.6) that are absent in all other sections of this document. Both taper and bow add a term involving the

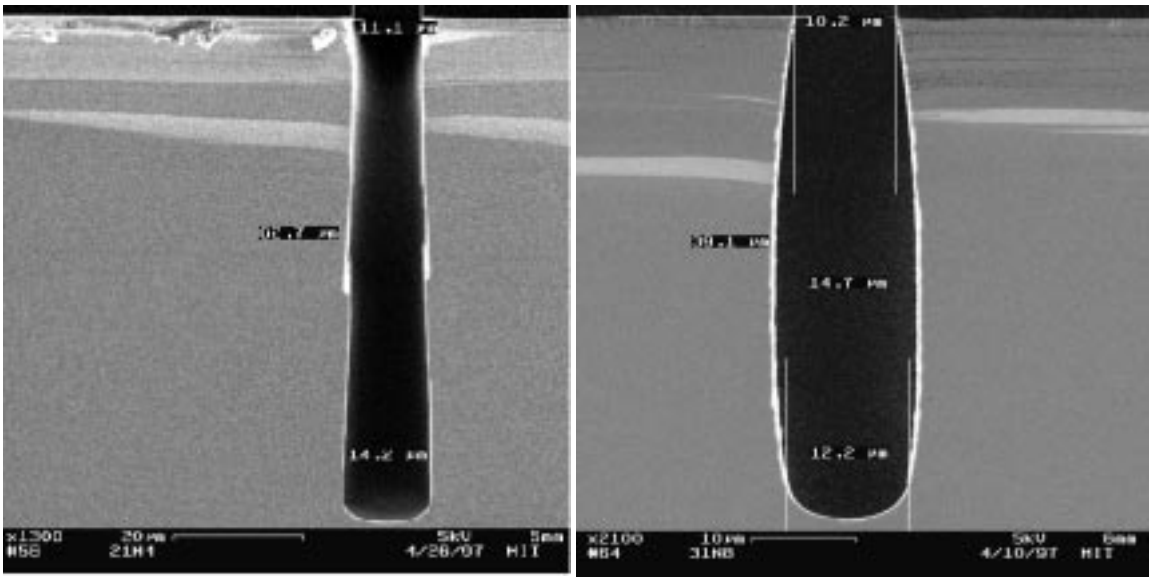

(a) Taper **(b)** Bow

Figure 4.18: SEMs showing taper and bow in etched channels [64]. Figure courtesy A. Ayón.

first derivative of height in the axial direction. Bow adds an additional term involving the second derivative.

Because the clearance is a function of axial location in this section, a choice must be made regarding the definition of C for nondimensional parameters such as eccentricity and bearing number. For convenience in the code, C was chosen to be the minimum clearance. With this choice, $\epsilon = 1$ denotes wall contact, as it does in the cylindrical case, but contact does not take place along the entire bearing length.

4.2.2 Steady-State Effects

From the outset, both taper and bow are expected to have a deleterious effect on load capacity when compared to an axially-uniform case at the minimum clearance. From a physical point of view, this expectation springs from observing that part of the bearing will be operating further from the wall and at a larger clearance ratio. The reduced area ratio in the converging region will reduce the pressure rise developed by rotation and, consequently, the load capacity. From a nondimensional point of view, the portions with larger clearance, $\tilde{C}$, are effectively running at lower eccentricities and bearing numbers, $\tilde{\epsilon}$ and $\tilde{\Lambda}$, given by:

$$\tilde{\epsilon} = \epsilon \left(\frac{C_{min}}{\tilde{C}} \right) \tag{4.6}$$

$$\tilde{\Lambda} = \Lambda \left(\frac{C_{min}}{\tilde{C}} \right)^2 \tag{4.7}$$

As shown in Sec. 3.1, reduction of either Λ or ϵ results in reduced load capacity and increased attitude angles, supporting the intuitive expectation of performance degradation due to axial clearance variation.

The effects of taper will be investigated first. This process will then be repeated for bow. Besides the changes in distribution of clearance, taper and bow differ in the slope and curvature of the channel height, h, in the axial direction. In particular, $\frac{\partial^2 h}{\partial z^2} = 0$ for taper while it is nonzero for bow.

Taper

The pressure distribution of a bearing with 25% taper (*i.e.* $\Delta C/C_{min} = 0.25$) is compared to that of an untapered bearing with $C = C_{min}$ in Fig. 4.19. Not surprisingly, the increased clearance of the tapered case weakens the pressure variation, reducing the load capacity from $\zeta = 0.096$ to $\zeta = 0.033$, a loss of 66%. In addition, the pressure peak in the tapered case shifts from the axial center toward the end with smaller clearance (bottom of figure).

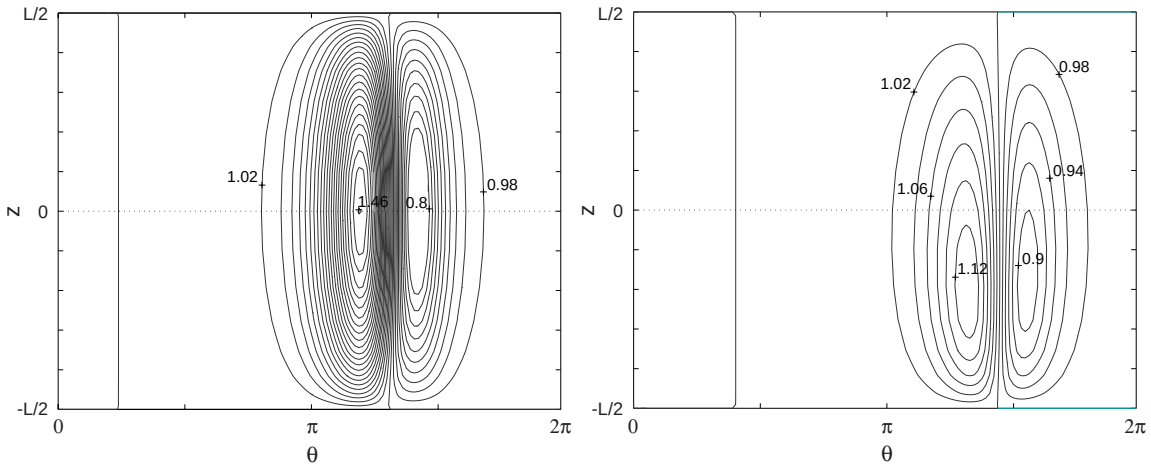

(a) Constant-Clearance **(b)** 25% Taper

Figure 4.19: Pressure distributions for constant-clearance and tapered bearings. In both cases, $L/D = 0.075$, $\Lambda = 5$, and $\epsilon = 0.85$. In the tapered case, the maximum and minimum pressures relax and shift toward the minimum clearance end (bottom of figure).

It may be intuitively expected that the performance of a tapered bearing will fall somewhere between that of a bearing with clearance C_{min} and one with clearance C_{max} running at a lower eccentricity, $\tilde{\epsilon}$, and bearing number, $\tilde{\Lambda}$, given by Eqs. 4.6 - 4.7. As shown in Fig. 4.20, this expectation proves to be correct.

This result, at the very least, suggests that untapered bearing calculations at the clearance extremes can be used to establish bounds for the operating characteristics of tapered bearings. Because these bounds are quite coarse (they are an order of magnitude apart

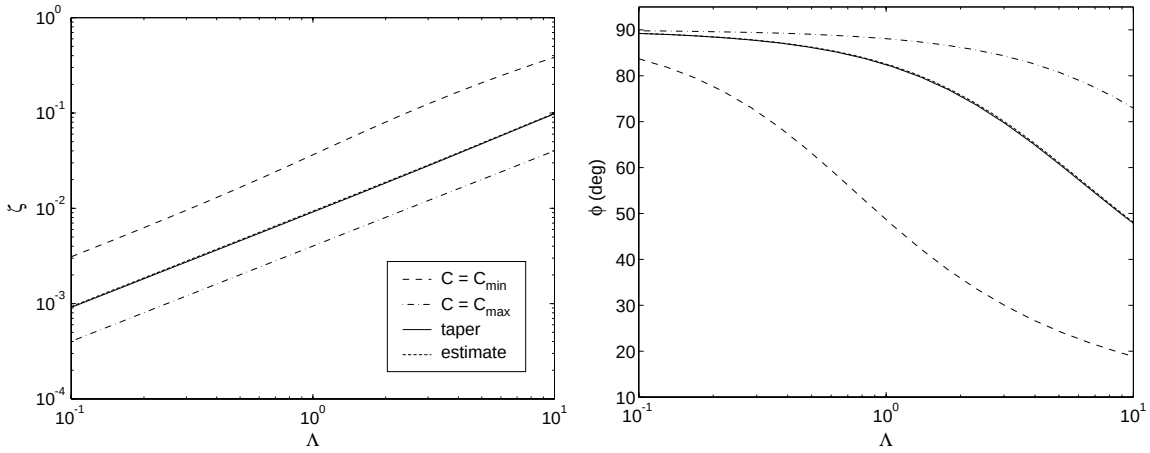

(a) Load Parameter **(b)** Attitude Angle

Figure 4.20: Comparison of tapered result with untapered bearings at clearance extrema. Bearing has $L/D = 0.075$ and 25% taper and is running at $\epsilon = 0.9$. For comparison purposes, C_{max} results computed at $\tilde{\Lambda}$ are reported at Λ. An estimate computed from a constant-clearance bearing with $C = C_{min} + 0.45\Delta C$, calculated at the appropriate $\tilde{\Lambda}$ and reported at Λ, is also included. This estimate shows excellent agreement with the tapered calculation at all Λ.

in ζ for the case of Fig. 4.20), it is desirable to refine this estimate. Possibilities are therefore investigated for estimating tapered bearing performance from untapered results. The primary goal of this effort is to construct a general purpose scheme that obviates numerical solutions for tapered bearing so codes without taper models, or existing cylindrical bearing design charts, can be used. One step below this ideal, a scheme that reduces the number of tapered bearing calculations would still provide a significant savings.

Noting that the tapered load parameter trace is nearly parallel to the C_{max} trace, a simple scheme is proposed in which the tapered load parameter is estimated as multiple of the C_{max} load parameter. For the case shown in Fig. 4.20, the multiplier proves to be approximately 2.3. This multiplier also provides a good estimate if the L/D is doubled. Unfortunately, the load multiplier drops to 1.8 if the taper level is halved and it becomes 1.5 if ϵ is halved (at 25% taper). Consequently, it is not possible to to eliminate taper calculations entirely under this scheme, but they can be reduced to a single case per eccentricity or taper level if only ζ is required. Furthermore, the attitude angle curves are not parallel, so this scheme is ineffective for estimating ϕ.

In an attempt to remedy these shortfalls, an alternative scheme suggested by Jacobson [40] is investigated. In this case, the estimate is constructed from data for an untapered bearing with a clearance between C_{min} and C_{max}. For the example case of Fig. 4.20, good estimates of both ζ and ϕ are obtained from a bearing with:

$$C = C_{min} + 0.45\Delta C. \tag{4.8}$$

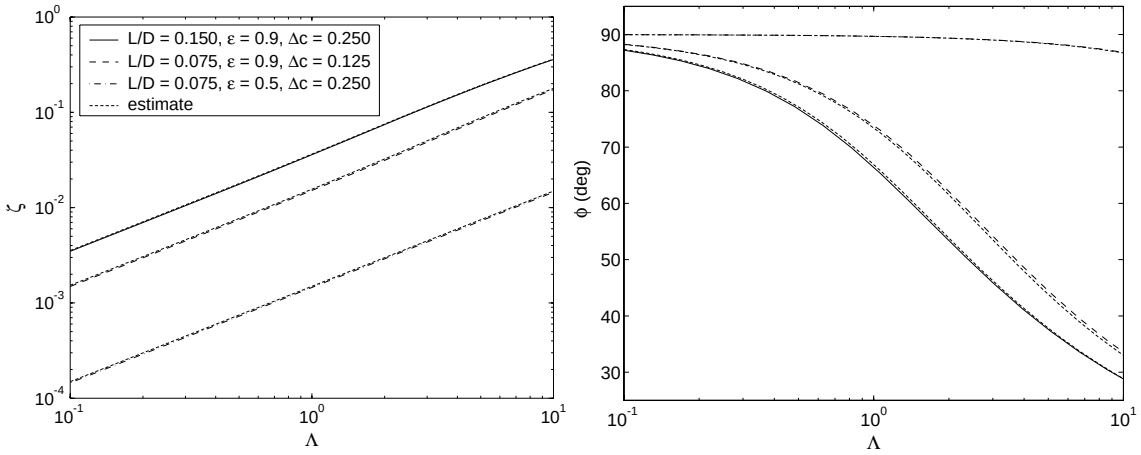

(a) Load Parameter **(b)** Attitude Angle

Figure 4.21: Comparison of tapered results for bearings with various L/D, ϵ, and Δc with an estimate computed from a comparable untapered bearing with $C = C_{min} + 0.45\Delta C$.

These estimates are shown in Fig. 4.20.

To assess the generality of this method, the calculation was repeated for cases with different L/D taper level, and eccentricity. The results are shown in Fig. 4.21. In all cases, data from an untapered bearing with $C = C_{min} + 0.45\Delta C$ provides an excellent estimate of the load parameter and attitude angle at all studied bearing numbers. The method is therefore shown to be general, at least for the MIT microengine class of bearings.

The effect of taper on both ζ and ϕ for a wide range of eccentricities and bearing numbers is presented in Fig. 4.22 in the form of a percent change from the untapered case. Two major trends are visible in this figure: the taper effect increases with increasing eccentricity and it varies with bearing number; decreasing at high Λ after passing through a maximum at an intermediate Λ. The Λ variation increases with eccentricity and results from compressibility-related curvature in the load lines (see Fig. 3.1(a)).

To investigate the relative importance of ΔC and slope on taper losses, the above calculation was repeated with $L/D = 0.15$ and the results presented in Fig. 4.23. Examination of this figure reveals that doubling the L/D (hence halving the taper slope, while holding C_{max} and C_{min} constant) does not have a strong effect on the magnitude of change induced by taper. The curves remain almost exactly the same shape, though they shift toward lower Λ. This shift is a result of compressibility effects occurring earlier in the longer bearing, forcing an earlier departure from linearity in the load, and from $\phi = 90°$ in the attitude angle, versus Λ trace.

The similarity between Figs. 4.22 and 4.23 implies that the effect of taper is primarily due to portions of the bearing running at higher clearance, rather than the introduction of an axial slope to the bearing walls. This conclusion is supported by the clearance-based

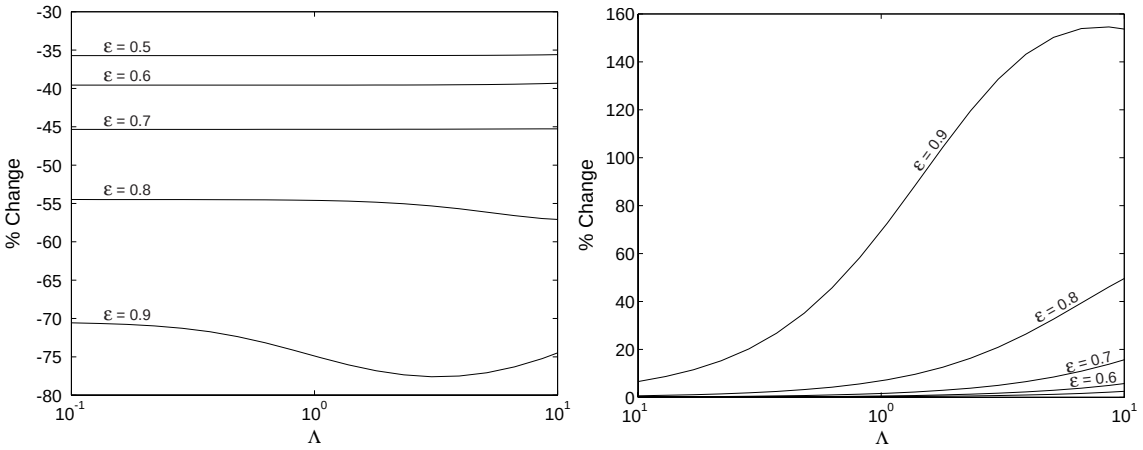

(a) Load Parameter **(b)** Attitude Angle

Figure 4.22: Percent change in steady-state parameters when 25% taper is added to an $L/D = 0.075$ journal bearing. The taper-induced performance change increases with eccentricity, with the load capacity loss reaching 78% at $\epsilon = 0.9$.

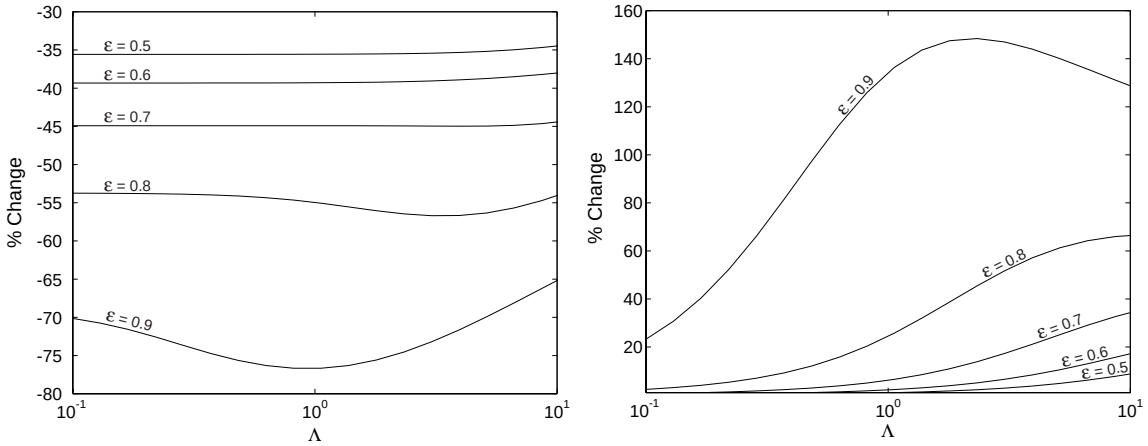

(a) Load Parameter **(b)** Attitude Angle

Figure 4.23: Percent change in steady-state parameters when 25% taper is added to a $L/D = 0.15$ journal bearing. The performance change is very similar to that obtained at $L/D = 0.075$, implying that taper effects are more closely related to the clearance change than to the wall slope.

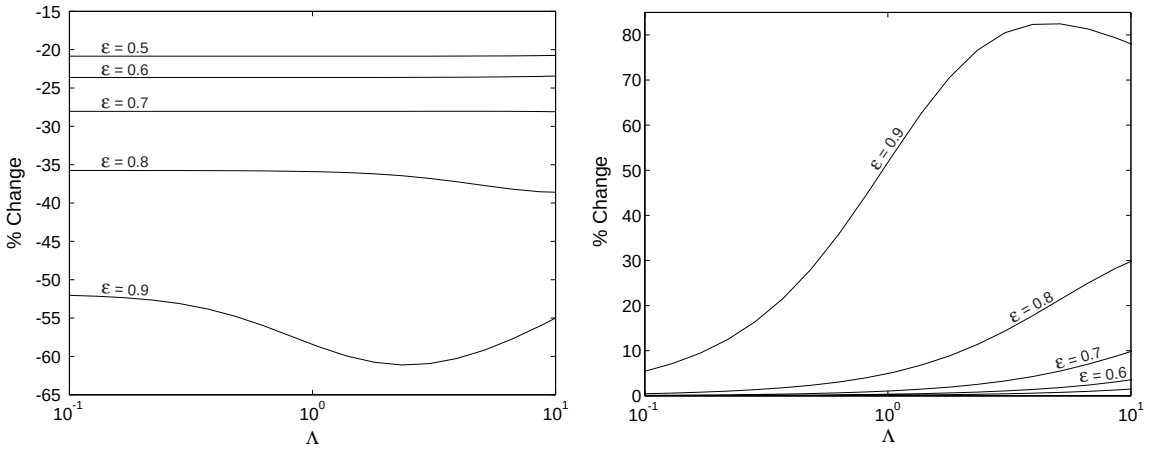

(a) Load Parameter **(b)** Attitude Angle

Figure 4.24: Percent change in steady-state parameters when 12.5% taper is added to a $L/D = 0.075$ journal bearing.

estimator's (Eq. 4.8) effectiveness. Furthermore, it is intuitively reasonable considering that the slope for a 25% taper on 300μm bearing with a 12μm clearance, for example, is only approximately 0.01 radians, yet it results in a loss of as much as 80% in the load capacity at $\epsilon = 0.9$.

Finally, to demonstrate the effect of taper level on a given bearing, Fig. 4.24 presents the results of a series of calculations in which the L/D was held at 0.075 but the taper was halved, corresponding to a 10% decrease in C_{max} over the previous case (but a 50% decrease in Δc). Not surprisingly, the load capacity loss weakens as the taper level decreases. In addition, noting that the constant ϵ lines are closer together in Fig. 4.24(a), it can be seen that the rate of load capacity degradation with increasing eccentricity also decreases, particularly at low eccentricity. Reducing taper therefore brings a greater performance benefit as eccentricity increases. Also, in both ζ and ϕ, curve shape is similar to the baseline case and the point of maximum taper effect is relatively stationary, shifting only slightly toward lower speed. These observations support the previous contention that the shift is a product of compressibility because the constant-clearance bearing at C_{min} is equivalent for Figs. 4.22 and 4.24, thus compressibility will appear at the same Λ. The slight shift in the smaller taper case is a consequence of is closer proximity to the $C = C_{min}$ case, which exhibits compressibility effects earlier than the larger clearance cases.

Bow

The above analysis will now be repeated for bearings with bowed clearances of the form shown in Fig. 4.18(b). Looking at the geometries, it is tempting to conclude that the bow will induce milder performance degradation than taper bearing because the clearance

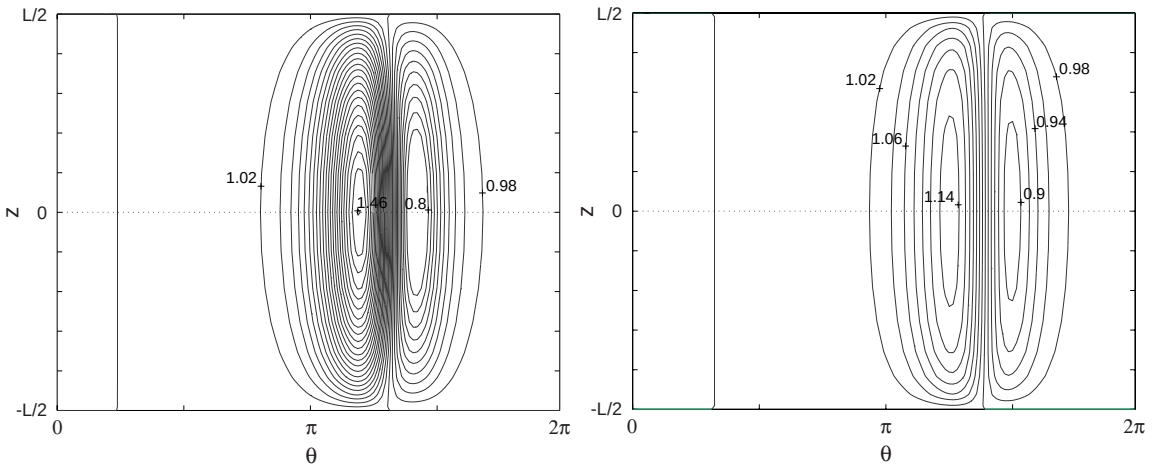

(a) Constant-Clearance **(b)** 25% Bow

Figure 4.25: Pressure distributions constant-clearance and bowed bearings. In both cases, $L/D = 0.075$, $\Lambda = 5$, and $\epsilon = 0.85$

maximum's appearance at the axial center, rather than at one end, may decrease leakage. On the other hand, the results of the previous section point to a dependence on total clearance variation, rather than slope.

In a similar fashion to Fig. 4.19, the pressure distributions of a bowed and an unbowed bearing with $C = C_{min}$ are compared in Fig. 4.25. Again the increased clearance in the unbowed case weakens pressure variation, reducing the load capacity. The reduction is less severe than in the tapered case, however. This observation is reflected in the load capacity, with $\zeta = 0.044$ for this case; 54% of the unbowed ζ under the same conditions and 33% higher than with equivalent taper. Also, as might also be expected from symmetry, the pressure peak in this case remains in the axial center for the bowed cases, in contrast to the eccentric pressure peak observed in tapered cases.

The scheme for estimating steady-state performance from constant-clearance bearing data, shown in the previous section to be successful for taper, is applied to a $L/D = 0.075$ bearing with 25% bow at $\epsilon = 0.9$ in Fig. 4.26.

Two differences between bowed and tapered bearings are evident in Fig. 4.26. First, as noted previously, the performance degradation due to bow is less severe than that of taper. In Fig. 4.26, this conclusion is evidenced by the smaller coefficients on ΔC of the unbowed bearings yielding estimates comparable to the bowed result. The bowed bearing's performance is therefore nearer to that of the unbowed bearing. Second, unlike the taper case, a single ΔC coefficient does not exist that produces a good estimate for both ζ and ϕ. In Fig. 4.26, a coefficient of 0.30 yields a good result for ζ, while ϕ appears to require a coefficient between 0.15 and 0.20 to yield the best estimate.

To assess the generality of this result, the estimate is repeated for an $L/D = 0.15$ bearing

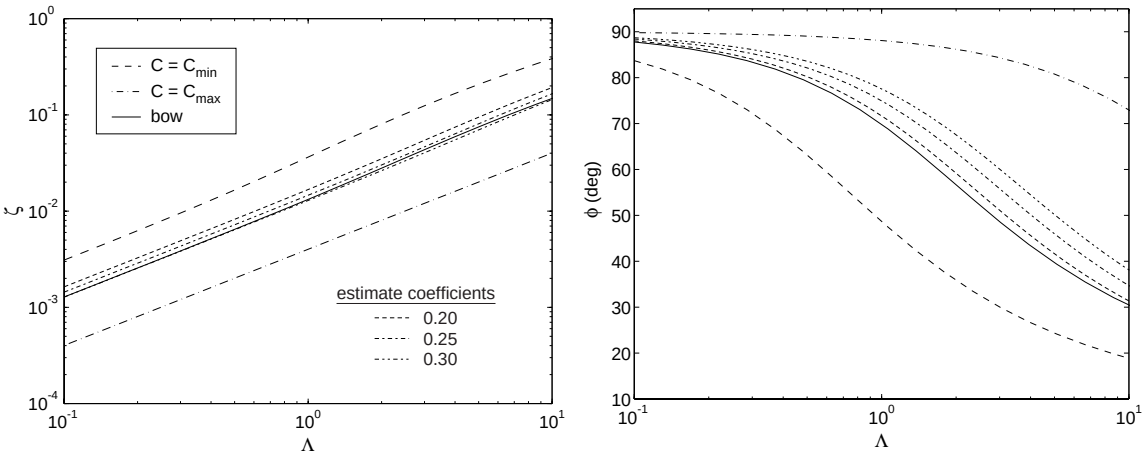

(a) Load Parameter **(b)** Attitude Angle

Figure 4.26: Comparison of bowed result with unbowed bearings at clearance extrema and an estimate calculated from them. Bearings have $L/D = 0.075$ and 25% bow and are running at $\epsilon = 0.9$.

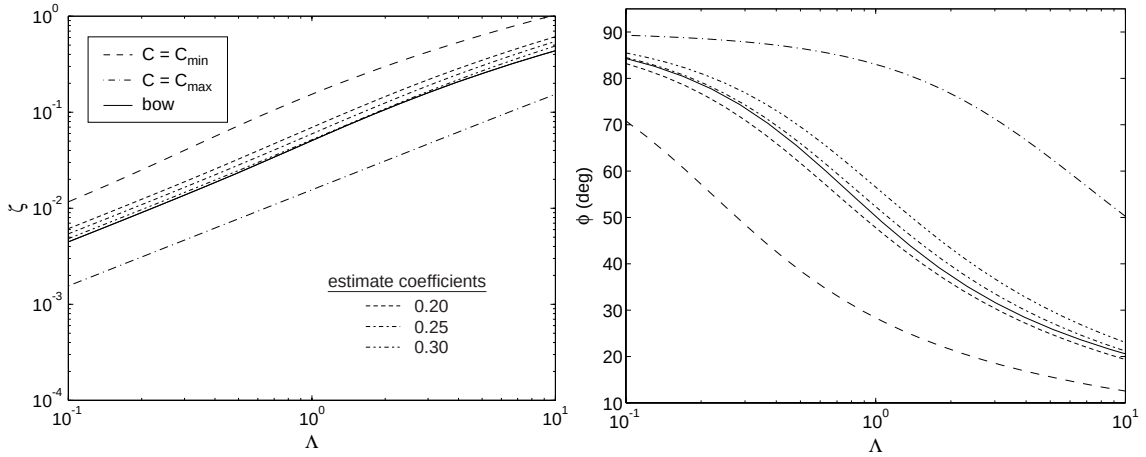

(a) Load Parameter **(b)** Attitude Angle

Figure 4.27: Comparison of bowed result with unbowed bearings at clearance extrema and an estimate calculated from them. Bearings have $L/D = 0.15$ and 25% bow and are running at $\epsilon = 0.9$.

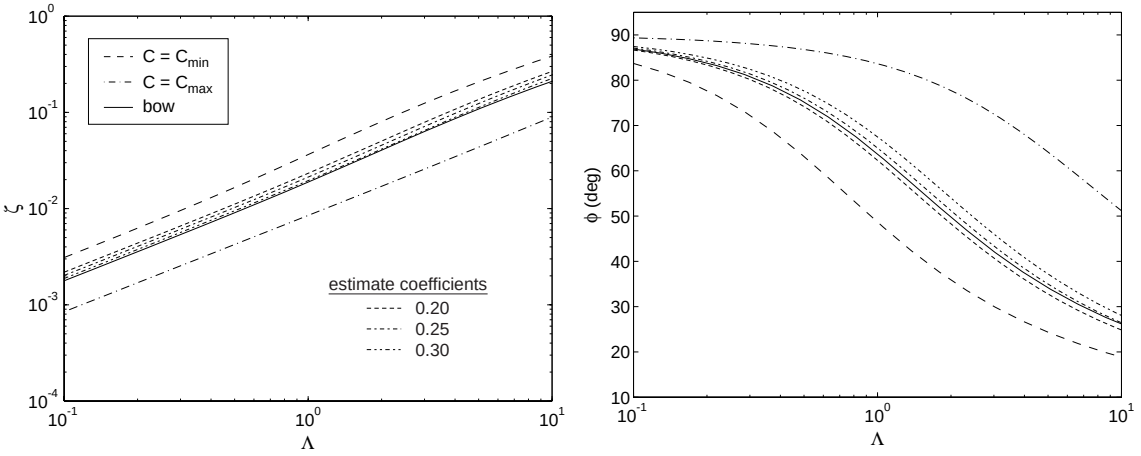

(a) Load Parameter **(b)** Attitude Angle

Figure 4.28: Comparison of bowed result with unbowed bearings at clearance extrema and an estimate calculated from them. Bearings have $L/D = 0.075$ and 12.5% bow and are running at $\epsilon = 0.9$.

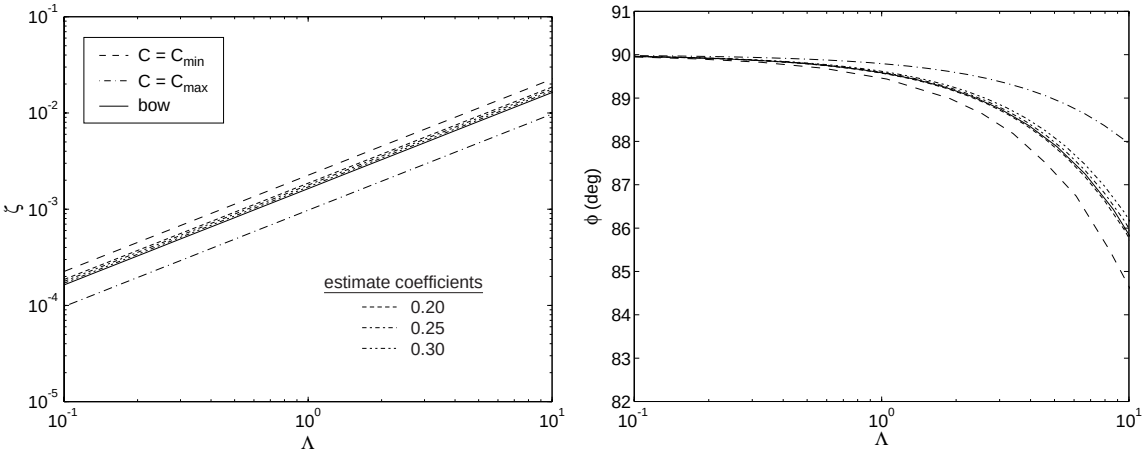

(a) Load Parameter **(b)** Attitude Angle

Figure 4.29: Comparison of bowed result with unbowed bearings at clearance extrema and an estimate calculated from them. Bearings have $L/D = 0.075$ and 25% bow and are running at $\epsilon = 0.5$.

at otherwise identical conditions. The results of this calculation are presented in Fig. 4.27. Comparing this figure to its predecessor, it can be seen that, unlike in tapered bearings, the error of a given estimate changes with L/D. The larger coefficient and, thus, a larger "effective clearance" in both ζ and ϕ indicates a trend of increasing performance degradation with L/D at a given level of bow. Fortunately, the ΔC coefficient changes very little for ζ, which is typically more important to designers than ϕ. A useful load estimate can still be constructed with a coefficient of 0.30.

The effect of $\Delta C/C$ on the estimate's error is demonstrated in Fig. 4.28. Comparing with the previous figure, a striking similarity is evident. Again, the 0.30 coefficient provides a reasonable estimate of for ζ and the ideal coefficient for ϕ lies between 0.20 and 0.25.

Finally, the effect of eccentricity on the relative positions of the traces is shown in Fig. 4.29 by repeating the baseline case at $\epsilon = 0.5$. Several observations may be made from the result. First, due to the lower eccentricity, the ζ traces are almost perfectly straight and parallel. Second, the estimate derived from a 0.30 coefficient on ΔC overpredicts the load capacity throughout. Performing calculations with a coefficient of 0.35 yields an estimate that is almost indistinguishable from the bowed calculation. The bowed calculation for attitude angle once again falls between the 0.20 and 0.25 traces.

Overall, estimating bearing performance from constant-clearance calculations for bowed bearings involves additional considerations not important in tapered bearings. First, the optimum coefficients differ for load and attitude angle. Separate calculations are therefore required for each quantity. Second, the optimum coefficients vary slightly with L/D, eccentricity, and bow level. The coefficients must therefore be adjusted on a case-by-case basis to achieve estimation accuracy for bowed bearings comparable to that shown for tapered bearings. This consideration reduces the method's flexibility because a tool with nonconstant clearance capability is required to provide comparison cases for coefficient calculation.

Fortunately, these considerations may be neglected in many situations. For example, the error in constructing a load estimate using a coefficient of 0.30 is no greater than 10% for the cases in Figs. 4.26 - 4.29, except for the $L/D = 0.15$ case at $\Lambda > 8$. This is an acceptable error under many operating circumstances because the running eccentricity is relatively insensitive to changes in applied load at the high eccentricities studied. Similarly, a coefficient of 0.20 provides a reasonable estimate for ϕ in all treated cases.

The effect of bow on both ζ and ϕ for a wide range of eccentricities and bearing numbers is presented in Fig. 4.30 in the form of a percent change from the unbowed case. From this figure, it is apparent that, throughout the studied space, bow causes milder load capacity depression than taper (maximum of 65% vs. 78% for $\epsilon = 0.9$). In addition, bow causes much weaker attitude angle increase than taper (maximum 63% vs. 155% for $\epsilon = 0.9$). In addition, the peak change occurs at slightly lower speed.

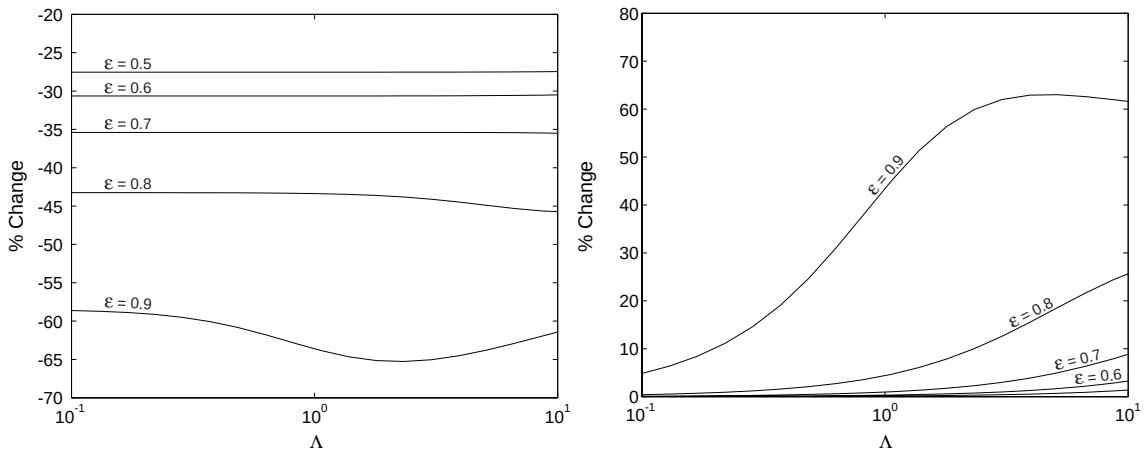

(a) Load Parameter **(b)** Attitude Angle

Figure 4.30: Percent change in steady-state parameters when 25% bow is added to an $L/D = 0.075$ journal bearing

In common with the shift associated with reducing taper, the leftward shift observed when comparing tapered and bow results is caused by the closer relationship between the bowed case to its associated $C = C_{min}$ case. This closer relationship is also visible in the optimum estimator coefficients for the two cases, which are approximately 0.30 and 0.45 for bow and taper, respectively. The bowed case therefore runs at a smaller effective clearance and will, consequently, begin to exhibit compressibility effects at a lower Λ.

Investigating the dependence of bow effect on L/D, a similar presentation for an $L/D = 0.15$ bearing is provided in Fig. 4.31. As noted from Fig. 4.31, and unlike the taper case, it is evident that increasing L/D *increases* the effect of bow. The maximum load capacity loss at $\epsilon = 0.9$ increases slightly, from 65% to 68%, but the attitude angle growth increases sharply, from 63% to 77%. In addition, while the curves in the taper case hold their shape and simply shift to lower speed when L/D increases, the peaks in the bow case become sharper, in addition to shifting to the left.

It is not possible to explain this behavior based on mean clearance arguments. While the expression for the mean clearance of the bowed case is considerably more complex than for the tapered case, it is not a function of L/D.

To establish the dependence on the amplitude of clearance variation, the change in steady-state parameters for 12.5% bow is shown in Fig. 4.32. In this case, the behavior mirrors that observed in the taper case: the loss of load capacity is reduced by about 15%, the increase in attitude angle is cut almost in half, and the curves shift only slightly to lower speed, maintaining their overall shape.

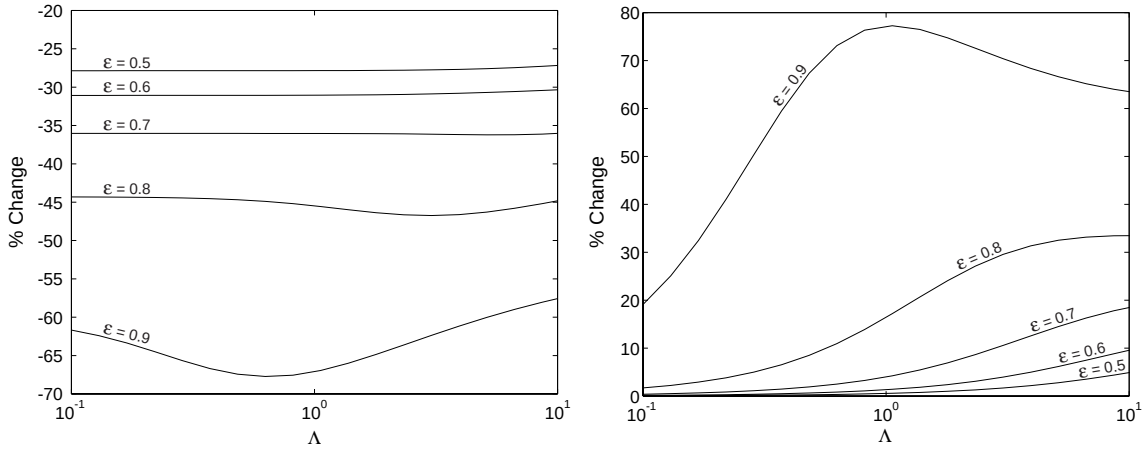

(a) Load Parameter **(b)** Attitude Angle

Figure 4.31: Percent change in steady-state parameters when 25% bow is added to an $L/D = 0.15$ journal bearing

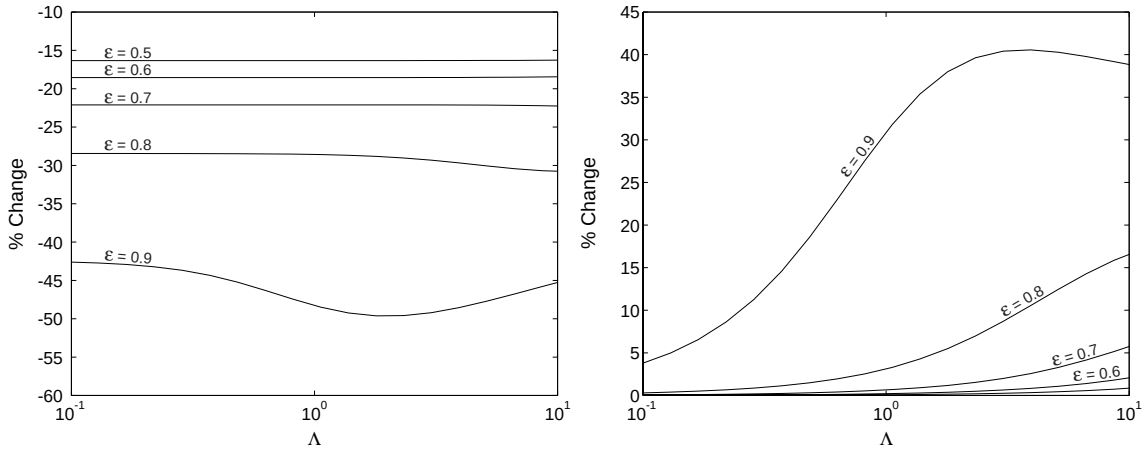

(a) Load Parameter **(b)** Attitude Angle

Figure 4.32: Percent change in steady-state parameters when 12.5% bow is added to an $L/D = 0.075$ journal bearing

4.2.3 Unsteady Effects

The increased attitude angles observed in the previous section for both the bow and taper cases arouse suspicion that these shapes also degrade the bearing stability. To investigate this suspicion, stability boundaries were computed for $L/D = 0.075$ bearings with $\bar{M} = 0.5$ and various levels of taper and bow. The results are presented in Fig. 4.33.

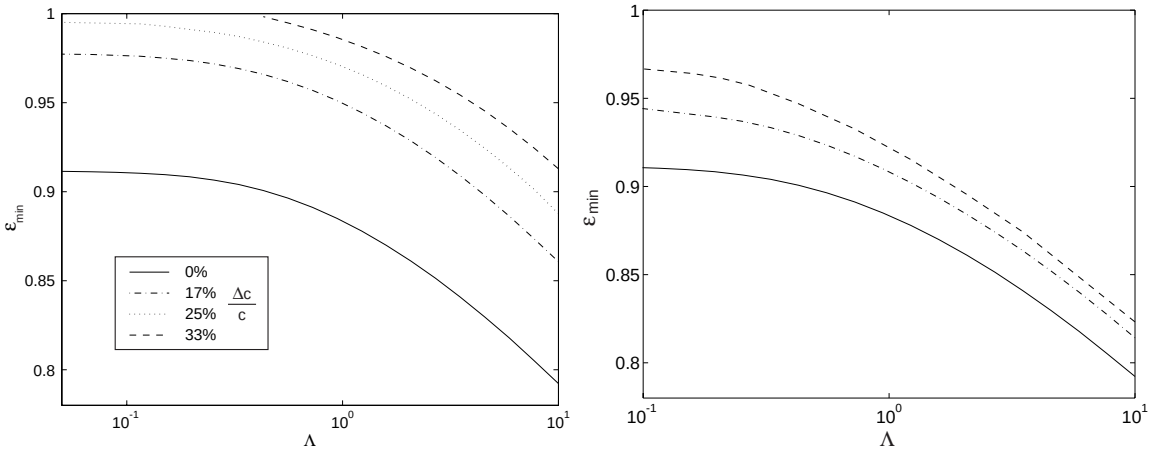

(a) Tapered Clearance **(b)** Bowed Clearance

Figure 4.33: Effect of clearance taper and bow on stability boundaries for $L/D = 0.075$ bearings with $\bar{M} = 0.5$.

As suspected, tapered and bowed bearings have higher minimum eccentricities throughout the presented Λ range. This has serious implications for low L/D bearings because their stability boundaries are already close to $\epsilon = 1$ before the addition of clearance variation. For example: at 33% taper, the minimum eccentricity reaches unity at approximately $\Lambda = 0.38$. Such a bearing will therefore be unable to operate hydrodynamically below this bearing number. Even at 25% and 17% taper, the stable eccentricity range is extremely narrow, with minimum eccentricities peaking above 99% and 97%, respectively, at low Λ.

Bowed bearings have a less serious effect on the stability boundaries. The stability boundary for the 33% bow roughly corresponds to that of 17% taper at low Λ. At high Λ, the 17% bow case is significantly better than the 33% taper case. Most importantly, even for the 33% bow case, the bearing still has a physically-attainable, though not terribly attractive, minimum eccentricity at low Λ.

It can be observed in Fig. 4.33(a) that the traces for varying levels of taper are quite nearly parallel throughout the depicted bearing number range. At large Λ, the traces for varying levels of bow also become parallel. This observation raises the possibility of estimating axial clearance variation effects on the minimum stable eccentricity over a range of Λ by performing calculations at a single Λ and drawing a trace parallel to the constant-clearance trace through the resulting data point.

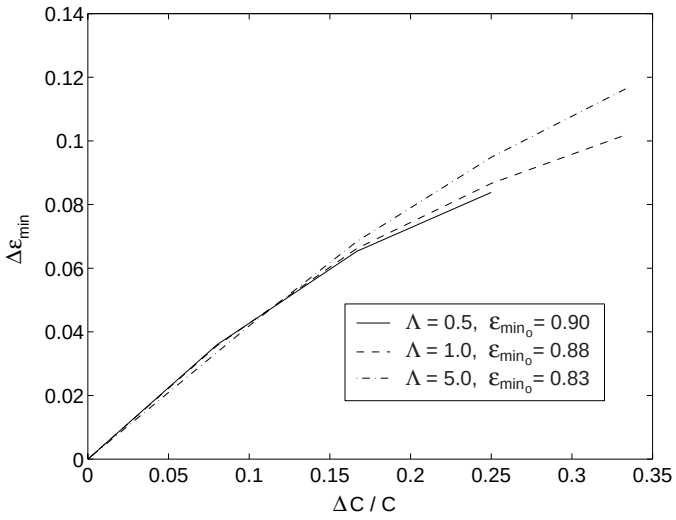

Figure 4.34: Effect of increasing levels of taper on ϵ_{min} at three values of Λ for an $L/D = 0.075$ bearing with $\bar{M} = 0.5$.

As a first step toward investigating this possibility, Fig. 4.34 presents the increase in minimum eccentricity associated with various levels of taper at $\Lambda = 0.5, 1,$ and 5. As suspected, the curves are nearly coincident for taper magnitudes less than approximately 15%. Furthermore, the maximum difference in $\Delta\epsilon_{min}$ between traces anywhere on the chart is approximately 0.02.

Noting that the zero-taper minimum eccentricities, ϵ_{min_o}, are nearly 90% and increase with decreasing Λ, it may be surmised that the divergence of the constant-Λ traces in Fig. 4.34 at high levels of taper may be caused by the extremely rapid change in bearing behavior when approaching unity eccentricity. Remembering from Chap. 3 that increasing L/D generally decreases ϵ_{min}, and from Sec. 4.2.2 that the effect of taper on steady-state parameters is a weak function of L/D, this theory may be tested by repeating the calculation at a larger L/D. The results of such a calculation at $L/D = 0.15$ are presented in Fig. 4.35.

The closer proximity of the higher L/D, and hence lower ϵ_{min_o}, traces of Fig. 4.35 at high $\Delta\epsilon_{min}$ supports the near-wall effect theory. In addition, the similarity between Figs. 4.34 and 4.35 demonstrates that the effect of taper on unsteady parameters is a weak function of L/D, as observed previously for steady parameters. These observations may be used to simplify design analyses. In fact, the straightforward linear estimate of:

$$\Delta\epsilon_{min} = 0.4\,\frac{\Delta C}{C}, \tag{4.9}$$

which describes a corner-to-corner diagonal line in Fig. 4.35, departs by no more than 0.01 from any computed trace in Fig. 4.35. This accuracy is also obtained in Fig. 4.34 for taper ratios lower than 20%.

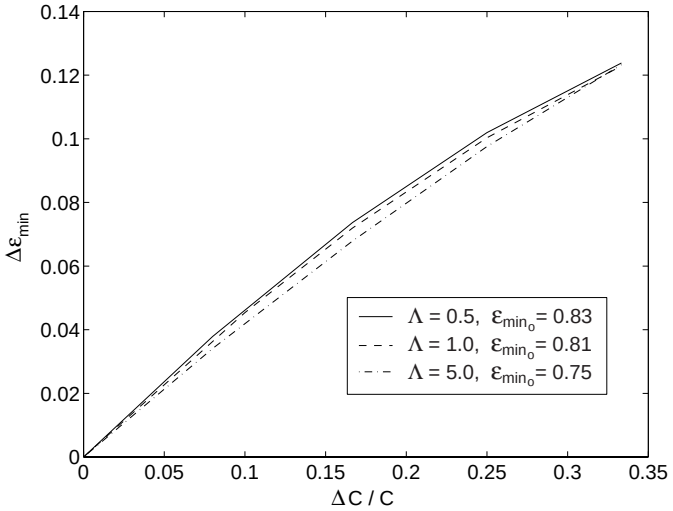

Figure 4.35: Effect of increasing levels of taper on ϵ_{min} at three values of Λ for an $L/D = 0.15$ bearing with $\bar{M} = 0.5$.

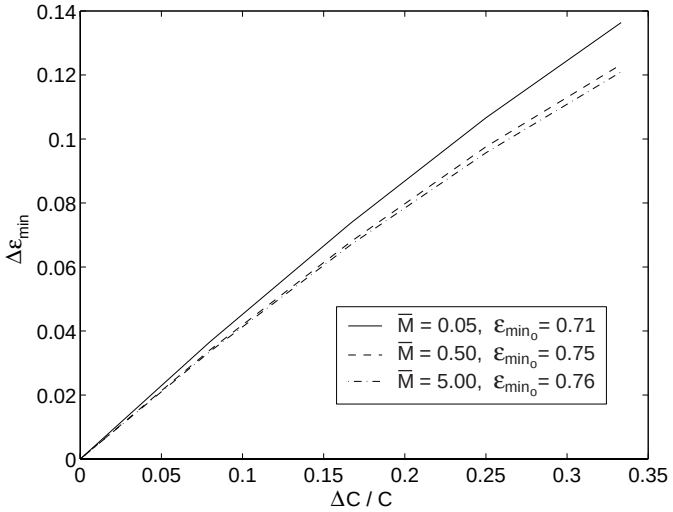

Figure 4.36: Effect of increasing levels of taper on ϵ_{min} in an $L/D = 0.15$ bearing at $\Lambda = 5$ for three values of $\bar{M}$.

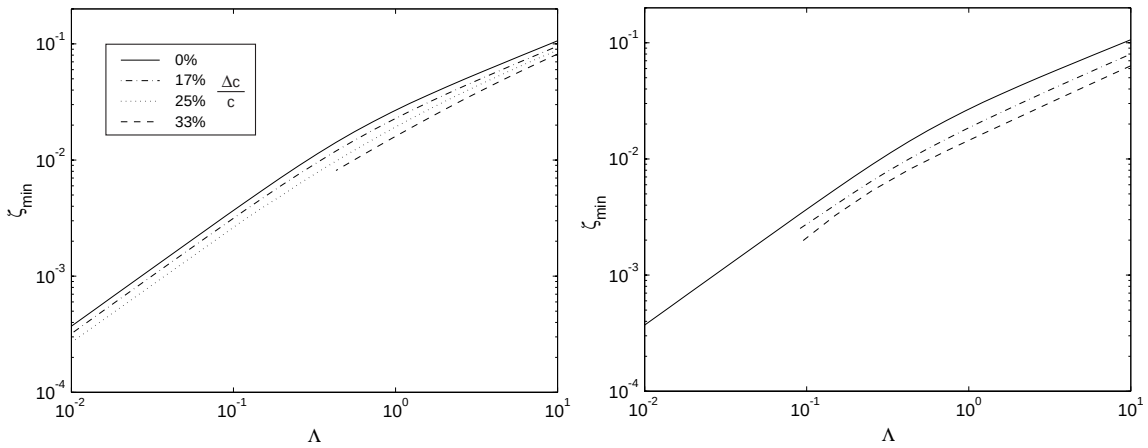

(a) Tapered Clearance **(b)** Bowed Clearance

Figure 4.37: Effect of clearance taper and bow on required load for $L/D = 0.075$ bearings with $\bar{M} = 0.5$.

It may be noted that Figs. 4.35 and 4.34 are both drawn for $\bar{M} = 0.5$. Thus, while Eq. 4.9 is useful for design studies at fixed $\bar{M}$, such as varying the length of a solid rotor, its applicability to studies involving variable $\bar{M}$, such as varying the clearance, is unclear. The above observations simply imply that $\Delta\epsilon_{min}$ for a range of taper ratios may be calculated at a single Λ for each $\bar{M}$. While this finding provides a considerable time savings over repeating the calculations over a range of Λ, the convenience of Eq. 4.9 warrants an investigation of its applicability for varying $\bar{M}$. Such an investigation is presented in Fig. 4.36.

In the calculations for Fig. 4.36, an $L/D = 0.15$ bearing was run at $\Lambda = 5$ and various levels of taper with three values of $\bar{M}$ covering two orders of magnitude. Once again, Eq. 4.9 provides an estimate of $\Delta\epsilon_{min}$ that departs from the computed value by no more than 0.01. It therefore proves to be a convenient estimator for taper effects on minimum eccentricity in short bearings, provided the net minimum eccentricity is not sufficiently large (greater than roughly 95%) for near-wall effects to become prominent.

Finally, for applications that depend on a fixed load, such as the shaft weight, to maintain stability, there may be a bright note to axial clearance variation: the diminished load capacity may reduce the required load at a given speed, despite the larger associated eccentricity. This effect is presented in Fig. 4.37 for the conditions of Fig. 4.33. As suspected, the required load decreases as the clearance variation increases throughout the depicted Λ range. The threshold speed for a fixed load therefore increases with $\Delta C/C$. Similarly, the applied load required for a fixed speed is lower, reducing side-pressurization requirements. Taper and bow may therefore be a desirable features if the circularity, surface roughness, etc. allow operation at high eccentricity.

4.3 Chapter Summary

In this chapter, bearings with circumferential and axial clearance variation were investigated. It was shown that this variation has beneficial as well as harmful effects so it must be carefully adopted, in the case of deliberate variation, or controlled, in the case of manufacturing limitations.

Circumferential Clearance Variation

With circumferential clearance variation, it was noted that the results reported in the literature must be reinterpreted for microfabricated bearings due to their etching-imposed constraint of fixed minimum clearance. Noncircularity must therefore be obtained by increasing the clearance in various circumferential locations, causing an increase in its mean value.

For the wave bearing, the reported increase in load capacity with wave amplitude was indeed reversed by the minimum clearance constraint. This was not the case for stability, which showed improvement in terms of minimum separation between journal and bearing despite the increased mean clearance. Combining these results, the wave bearing was shown to have a much lower load requirement for stability than the equivalent circular bearing. Furthermore, high-wavenumber bearings were shown to be preferable to low-wavenumber bearings because they were less sensitive to orientation variation and had generally better performance.

Many attempts to obtain stable whirls over speed ranges, such as those obtained in Sec. 3.2.2 were unsuccessful. It was observed that very near-wall operation in the wave bearing made it sensitive to perturbations because the orbit was not circular, dipping between wave peaks and becoming very susceptible to crashing into one. Whirls at lower $\bar{M}$ with their associated greater minimum running distances, were circular and were maintainable over ranges of Λ comparable to those found for circular bearings.

Axial Clearance Variation

Two types of axial clearance variation observed in microfabricated bearings were investigated: taper and bow.

Taper was modeled as a linear variation that creates a bearing with a clearance maximum at one end and a minimum at the other. It was shown that this variation caused a significant decrease in load capacity, as great as an order of magnitude, at a given eccentricity. Furthermore, the minimum eccentricity for fixed point stability exceeded unity at low speed for the 33% taper case, implying that this bearing was inoperative below a certain Λ.

Bow was modeled as a hyperbolic clearance variation with a maximum in the axial center. This type of variation was shown to have a less deleterious effect on bearing per-

formance, both in terms of the load capacity and the minimum eccentricity required for stability.

For both cases, an attempt was made to derive an estimate for the varying clearance case from bearings running at an intermediate clearance. It was shown that this method is quite effective for taper but slightly less satisfactory for bow. In both cases, a good load estimate is available.

Finally, because axial clearance variation effects scale as the ratio of $\Delta C \,/\, C$, increasing the nominal clearance can improve performance. First, increasing C is likely to decrease ΔC. Even if it does not, however, the overall ratio will still decrease due to the larger denominator. Particularly in the case of taper, where the performance degradation is strong, this improvement may outweigh the loss (in terms of reduced ζ and increased ϵ_{min}) normally suffered by increasing C.

Chapter 5

Considerations of Operation

This chapter presents information regarding issues that emerge when considering the details of operating journal bearings. These issues are general, but they are most significant in the somewhat unique operating regime of microbearings.

5.1 Side-Pressurization Loading

It was shown in Sec. 1.3.2, via the cube-square law, that microbearings tend to have a much smaller load parameters due to weight than their macro-scale counterparts. While a low ζ_g presents advantages in terms of shock tolerance, for example, it can be problematic in terms of providing sufficient side-load to guarantee stability. In Sec. 3.2.1, for instance, it was calculated that the silicon microturbine of Fig. 3.6 becomes unstable at only 5000 RPM when loaded by its weight alone.

To quantify the load deficit, we first recall from Sec. 1.3.3 that millimeter-scale silicon machines have load parameters due to weight of order 10^{-4}. Assuming the millions of RPM ($10^5\ rad/s$) required by the MIT microengine and clearances in tens of microns, a similar order-of-magnitude analysis for the bearing number yields:

$$\Lambda = \frac{6\mu\omega}{P_a}\left(\frac{r}{c}\right)^2 = \frac{(10)(10^{-5})(10^5)}{(10^5)}\left(\frac{(10^{-3})}{(10^{-5})}\right)^2 = (1) \tag{5.1}$$

Referring to Figs. 3.10 and 3.11, this Λ implies a load parameter of order 10^{-2} will be necessary at the design speed for the range of L/D currently likely to be found in these devices. It can therefore be concluded that the required load is two orders of magnitude greater than that available from rotor weight for many microturbomachines.

This finding has a positive implication: weight loading will be insignificant to the bearing's operation, thus the machine will be insensitive to orientation with respect to gravity. This is a key feature because microdevices are, in general, intended to be portable. The negative implication is that an external load source must be found. This section explores

the possibility of providing this load via a noncircumferentially-uniform pressure on the journal, supplied from plena at one of its axial ends.

5.1.1 Description

Although the responsible mechanism was not understood at the time, it was observed long ago that a bearing's threshold speed could be significantly increased by the provision of a high pressure source on one side. The technique was patented in 1952 by Brewster [69], who supplied high pressure air through a single port located at the bearing's axial center.

This technique is particularly attractive in turbomachines due to the availability of a range of pressures via tapping different locations in the device. The 2-D extrusion constraint on the geometry implied by microfabrication, however, makes it difficult to impose pressures through ports in the bearing midplane. In fact, only one method is currently deemed feasible for the MIT micromachines: etching into a wafer surface then bonding this surface to another wafer to yield a centerline channel between two wafers. The bearing is then defined on the two-wafer stack.

This method, while demonstrated to be possible [68], entails either etching trenches that are twice as deep to define the bearing, which will generally at least double the clearance, or handling wafers half as thick, which tend to be fragile and subject to warping. Furthermore, this technique adds another wafer bonding step to an already-complex fabrication process. This is an unattractive addition when striving for a robust process because contaminants and gases can create voids between the wafers, resulting in poor bonds and subsequent rejection of devices.

An alternative means of supplying side-pressure that is entirely compatible with current microfabrication techniques is to apply the nonuniform circumferential pressure from plena at one of the bearing ends. This opportunity exists in the MIT microturbomachines because the rotors are held in a "sandwich" of wafers, as shown in Fig. 1.2. A schematic of a proposed plenum geometry is presented in Fig. 5.1.

The arrangement of Fig. 5.1 is similar to that used in the macro-scale experiments for the MIT microengine bearings [34]. In this device, as in the early microbearing experiments [70], the "high" pressure P_H was applied to two plena and the "low" pressure, P_L was applied to one. The thin circumferential extensions of the two high-pressure plena visible on Fig. 5.1 were included to reduce torque caused by pressure differences under the rotor.

5.1.2 Steady-State Effects

A comparative demonstration of side-loading options is presented in Fig. 5.2. In this figure, pressure distributions from weight loading and three side-pressurization combinations are presented for $L/D = 0.075$ bearings running at $\Lambda = 5$ displaced to $\epsilon = 0.8$. In all cases, the axis of rotation is assumed aligned with the bearing's symmetry axis. In practice,

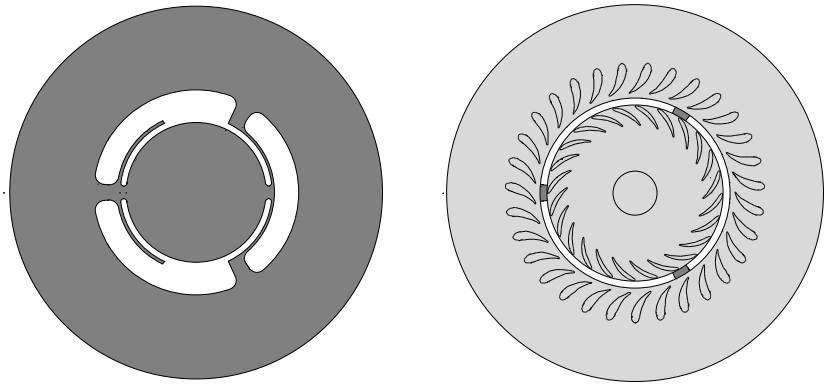

(a) Plenum Plate

(b) Plenum Plate + Rotor Plate

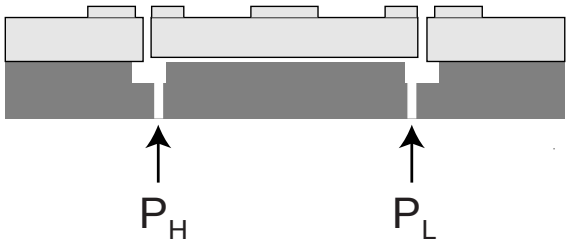

(c) Side View

Figure 5.1: Schematic of three-plenum, axially-imposed side-pressurization arrangement. The thin circumferential extension of the two high-pressure plena around the plenum plate was included to reduce torque caused by pressure differences under the rotor.

nonuniform pressures below the rotor associated with side-pressurization will produce an out-of-plane torque that will cause a misalignment inversely proportional to the restoring moment provided by the thrust and journal bearings.

In the first case of Fig. 5.2, load was applied directly to the journal, simulating, for example, weight loading (though it could also represent electrostatic or magnetic loading). In the second case, the low pressure sump was held at ambient conditions and P_H was increased. In the third case, a combination of increased P_H and lowered P_L was applied. In the final case, P_H was held at ambient conditions and P_L was lowered. Color bars above and below each case indicate the relative local pressure at each axial end. On these bars, white, gray, and black represent sub-ambient, ambient, and super-ambient pressures, respectively.

In the side-pressure cases, the imposed pressure departs little from the ambient to produce the required eccentricity, despite the appreciable bearing number. For the high pressure alone, $P_H/P_a = 1.121$; for high + low pressure, $P_H/P_a = 1.062$ and $P_L/P_a = 0.938$ and, finally, for the low pressure alone, $P_L/P_a = 0.874$. The modest pressure requirements are a consequence of the low load capacity of the $L/D = 0.075$ bearing. As mentioned previously, low pressure requirements are desirable in a self-contained machine because they imply that less air must be bled from the cycle to run the bearings, improving overall efficiency.

Not surprisingly, the imposed pressures associated with this loading method affect the pressure distribution produced by rotation. Comparing Figs. 5.2(a) and 5.2(b), it may be observed that the pressure peak upstream of the channel convergence changes very little when high pressure is imposed, except for a slight adjustment where the distribution is near the active plenum. The the pressure valley downstream of the convergence, however, is reduced in magnitude by roughly 6% and its peak moves away from the plenum as the low pressure region is preferentially "filled-in" by fluid from the higher-pressure end. The situation in the low pressure case of Fig. 5.2(d) is almost its mirror image: the downstream pressure valley is virtually unaffected but the upstream pressure peak is reduced in magnitude and shifted away from the active plenum. In this case, the peak reduction and shift is caused by fluid being preferentially bled-off to the lower-pressure plenum. The result of applying high and low side-pressure simultaneously, shown in Fig. 5.2(c), is a combination of these effects. In this case, the magnitude of both pressure extrema are reduced and their position shifts away from the active plena.

To construct an estimate for the pressure level required for a given loading condition, we recall the Reynolds equation discussion of Sec. 1.2.3. Due to its assumption of negligible fluid inertia, Reynolds equation solutions for flow through a channel with different pressures imposed at each end is guaranteed to be "fully-developed," or of constant velocity distribution. Remembering the elementary Poiseuille flow solution for flows of this type [46], it is observed that the imposed pressures are connected by a linear distribution.

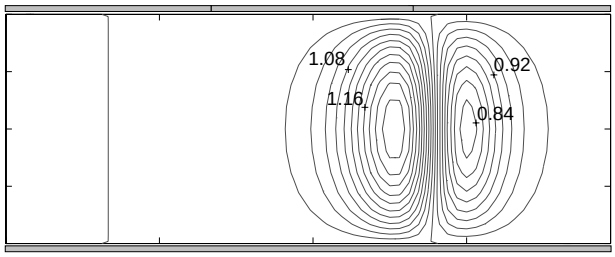

(a) Gravity

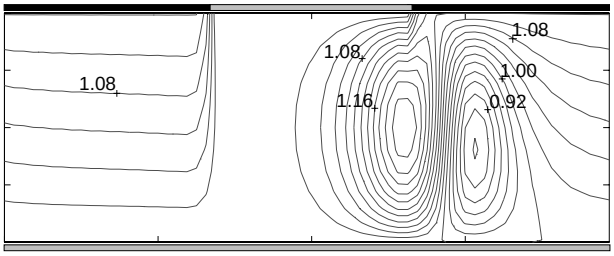

(b) High Pressure

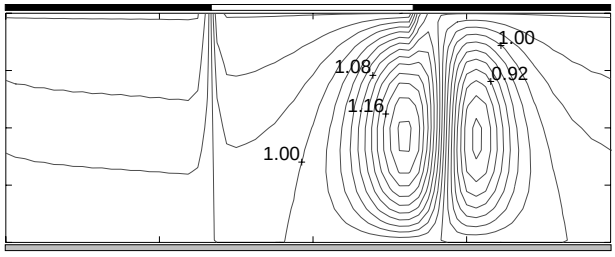

(c) High+Low Pressure

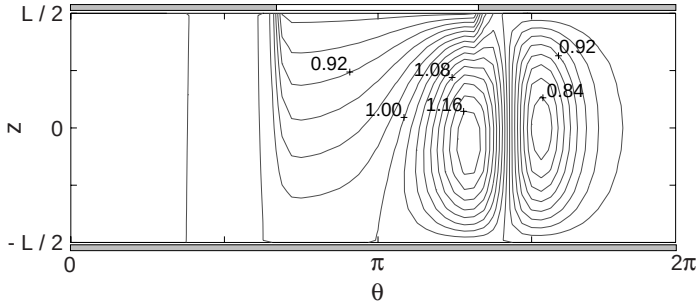

(d) Low Pressure

Figure 5.2: Pressure contours for four methods of achieving $\epsilon = 0.8$ at $\Lambda = 5$ in an $L/D = 0.075$ bearing. Color bars above and below each case indicate pressures applied at its axial ends. White, gray, and black indicate sub-ambient, ambient, and super-ambient pressure, respectively

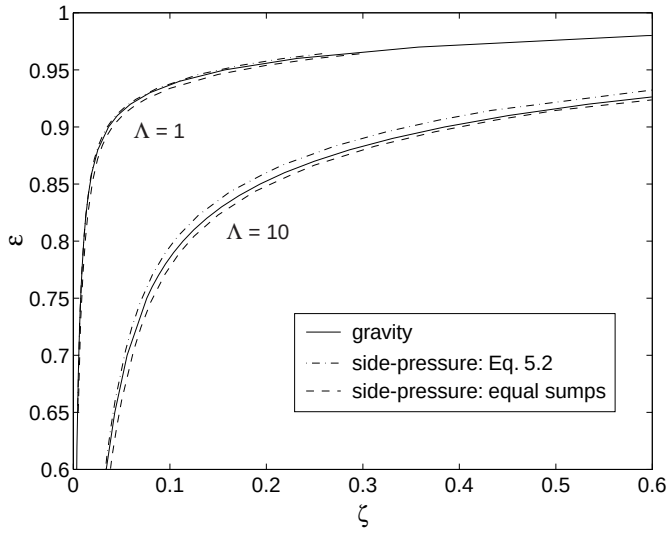

Figure 5.3: Comparison of eccentricities produced by loads from weight and from side pressure in the sump arrangement of Fig. 5.1 imposed according to Eq. 5.2. A trace calculated under the assumption of two equal sumps is also included.

Consequently, if the journal were not rotating, the axial pressure distribution would be linear throughout.

When the journal rotates, however, a moving surface-driven (Couette) flow produces a pressure distribution that can affect the linear axial distribution. For the current purpose, it is fortunate that this effect is generally weak at the bearing "top," or the circumferential position opposite the minimum channel height. This phenomenon may be observed as an absence of pressure contours at $\theta = 0$ in Fig. 5.2(a). It may also observed as a nearly linear axial distribution near this region in Fig. 5.2(b).

It is therefore expected that, if the two plena at the top (at the left in Fig. 5.1) are run with a high pressure and the plenum at the bottom (at the right in Fig. 5.1) is run at ambient pressure, a reasonable estimate may be derived for the load parameter due to side-pressurization through the assumption of a linear axial pressure profile. For the high pressure-only case of Fig. 5.2(b), the resulting expression is simply:

$$\zeta_{sp} = \frac{\frac{1}{2}(P_H - P_a)(L)(2r)}{2rLP_a} = \frac{\sqrt{3}}{4}\left(\frac{P_H}{P_a} - 1\right) \tag{5.2}$$

To test the applicability of Eq. 5.2, a series of calculations were performed by setting P_H and measuring the resulting eccentricity. The data was then plotted against the load parameter calculated from Eq. 5.2 and compared against a similar series generated using weight loading. This comparison is presented in Fig. 5.3 for $\Lambda = 1$ and $\Lambda = 10$.

From Fig. 5.3, it may be observed that, while the estimate of Eq. 5.2 agrees reasonably well with the conventionally-loaded case over the entire eccentricity range for both bearing numbers, it consistently overpredicts the eccentricity. This overprediction is likely caused

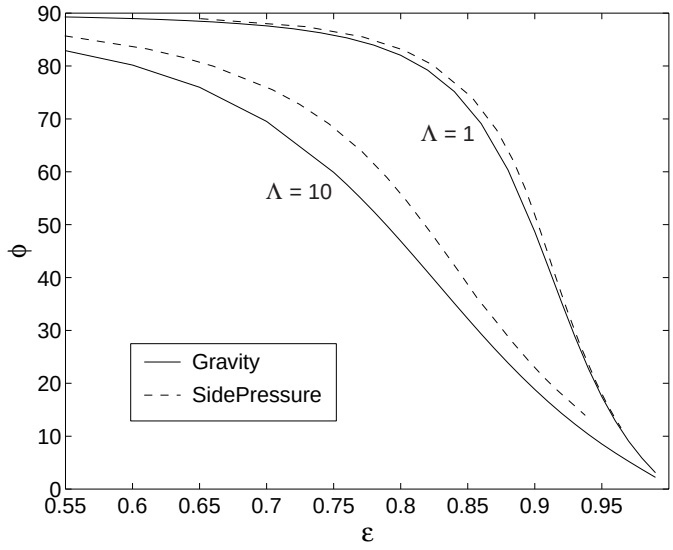

Figure 5.4: Comparison of attitude angles associated with eccentricities produced by gravity and side-pressure loading. From this information, it is clear that side-pressurization increases the attitude angle. This increase grows with speed and, for a fixed speed, is strongest at moderate eccentricity.

by interaction of the applied pressure distribution with the self-acting pressure distribution neglected when developing Eq. 5.2. This interaction is visible in Fig. 5.2(b) where the high pressure sump overlooks the low pressure region of the self-acting distribution near $\theta = 3\pi/2$.

Surmising that the high pressure sump's effect may be effectively canceled in this region, traces are included in Fig. 5.3 for two sumps of equal extent (via multiplying Eq. 5.2 by $2/\sqrt{3}$). In this case, the eccentricity is consistently under-predicted. Consistent bracketing of the calculated result by the two estimates implies that the arguments behind them are valid but that the physical situation is somewhere between the assumed effective geometries.

Further inspection of Fig. 5.2 reveals another effect of side pressurization: larger attitude angle for a given eccentricity. Qualitatively, this effect is visible as a slight variation in the sharpest circumferential gradient's θ location among the various loading schemes, despite the fact that they are all drawn for $\epsilon = 0.8$. Quantitatively, the attitude angles differ significantly, particularly between the gravity and side-pressurization cases, with $\phi = 59.8°$, $66.4°$, $64.4°$, and $66.1°$ for gravity, high, high+low, and low pressure loading, respectively.

Making use of the data generated for Fig. 5.3, the attitude angles produced by gravity and high-side loading are compared over a range of conditions in Fig. 5.4. From this presentation, it can be seen that achieving a given eccentricity via side-pressurization consistently produces a larger attitude angle than doing so via weight. Moreover, the ϕ difference increases with speed and, for a given speed, it is strongest at moderate eccentricities,

where ϕ begins to fall sharply from its low-speed asymptote of $90°$.

Recalling from Fig. 5.2b that the pressure valley, which is near the active plenum, is affected strongly by side-pressure while the peak is not, the physical mechanism behind these observations may be understood if three trends in gas bearing pressure distributions are noted: (1) the asymmetry in magnitude between the peak and valley increases with eccentricity at fixed speed until, at very high eccentricity, the valley is insignificant (2) the attitude angle decreases with eccentricity at fixed speed, thus the whole distribution shifts away from the high-side plenum with increasing ϵ (3) the pressure valley magnitude, compared with the peak, does not increase strongly with speed at fixed eccentricity (actually, a corollary of (1)).

Items 1 and 2 may be used to explain the decrease in attitude angle effect when the eccentricity is increased: not only does the pressure valley lose significance with respect to the overall flowfield (1), its position shifts away from the plenum (2). The overall impact of the plenum on the pressure field is thus reduced. Item 3 may be used to explain the increase in effect with speed by recalling from Fig. 3.1 that the load capacity increases approximately proportionally with speed. Combined with (3), this observation implies that the pressure in the high-side plenum is increasing proportionally with speed (for fixed ϵ) but the pressure valley is deepening much more slowly. More leakage into the valley is therefore expected at high speed, increasing the difference between the pressurized and non-pressurized cases observed on Fig. 5.4.

5.1.3 Unsteady Effects

The increased attitude angle observed for loading from the high-side plenum over the gravity-loaded case immediately raises suspicion of an effect on stability. In general, higher attitude angles imply larger cross stiffnesses and an increased tendency for a bearing to whirl when disturbed.

To test this suspicion, the critical $\bar{M}$ was computed for bearings moved to $\epsilon = 0.8$ and $\epsilon = 0.9$ via side-pressurization at a range of bearing numbers. This result is compared to its gravity-loaded counterpart in the minimum eccentricity chart shown in Fig. 5.5. In this case, it is helpful to read the chart in a slightly different manner than was discussed in relation to Fig. 3.5: bearings whose $\bar{M}$ is above the trace appropriate for their ϵ at a given Λ are unstable (in a fixed-point sense) and vice-versa.

From this figure, it may be observed that side pressurization reduces the maximum $\bar{M}$ ($\bar{M}_{crit}$) for stability at fixed eccentricity. Furthermore, in agreement with the attitude angle trend of Fig. 5.4, the degradation increases with speed. In this case, because $\bar{M}_{crit}$ is constant at low speed for the gravity-loaded case, this effect causes a local minimum to occur. This finding implies an operational difference in the sense that a gravity-loaded bearing will be stable at all speeds if it is stable at low speed, while its side-pressurized counterpart may become stable at an intermediate speed if $\bar{M}$ is sufficiently close to $\bar{M}_{crit}$.

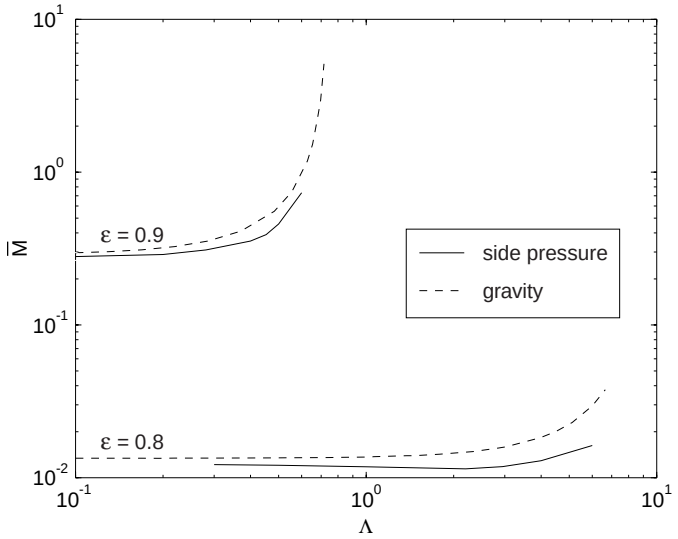

Figure 5.5: Comparison of minimum eccentricities for bearings loaded by gravity and side-pressurization over a range of bearing numbers.

Fortunately, due to the decrease in side-pressurization effect at high eccentricity, this degradation will not eliminate the stability corridor, as the taper effect, which showed increasing strength with ϵ, did in Fig. 4.33.

5.2 Stiffness Due to Axial Flow Inertia

In early journal bearing experiments for the MIT microengine, Orr [34] observed a translational natural frequency that was independent of rotor speed and gravity side-load. Because its stiffness is derived by a pumping action due to rotation and passage asymmetry, however, such a natural frequency is extremely unlikely in a self-acting bearing. Furthermore, Orr's bearing could operate stably at eccentricities much lower than the minimum predicted by SPECTRES or any other Reynolds equation-based tool, such as LUBEPACK [34].

From these observations, it was clear that the responsible mechanism was not represented in the Reynolds equation. After further observation by Orr that the frequency was a function of the axial pressure difference, the likely culprit was identified: inertial effects associated with axial flows produced by pressure gradients across the bearing length, such as those imposed by the side-pressurization scheme of the previous section.

In this section, a mechanism that produces stiffness from axial flow inertia is detailed, a general model and nondimensionalization is proposed, and results of including this model in SPECTRES simulations are presented.

5.2.1 Description

After trying several possible inertial models of various effects, a reasonable fit to the data was finally obtained by Orr [34] for an entry-length phenomenon suggested by Breuer [71]. This fit is presented in Fig. 5.6, which is a reproduction of Fig. 6-4 from Orr [34].

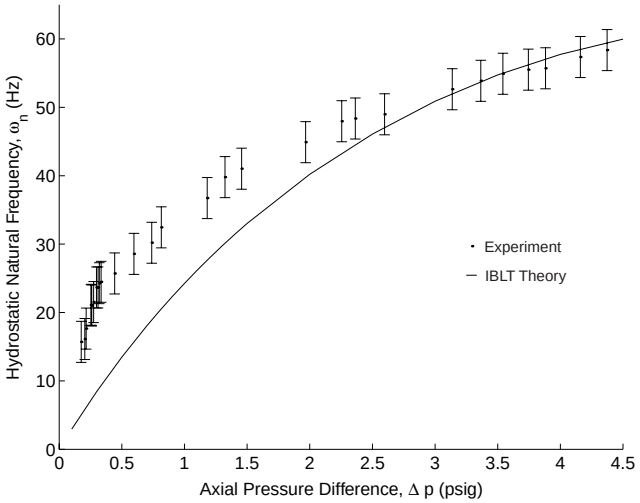

Figure 5.6: Comparison of Orr's interacting boundary layer theory model to the experimentally-observed natural frequency. Figure courtesy D.J. Orr [34].

To understand this phenomenon, two terms commonly used in channel flows must be introduced. First, the velocity profiles are identical at every lengthwise station in a pressure-driven flow of an inertialess fluid through a channel of constant area. This type of flow, and its associated parabolic velocity profile, is termed "fully-developed." Second, in a pressure-driven flow of a real fluid, the inlet velocity distribution evolves into the fully-developed profile over a finite distance. This distance, termed the "entry length," results from a need to overcome inertia when accelerating or decelerating fluid to change its velocity distribution.

For the current purpose, the important consequence of the entry region is its increased pressure drop over the linear rate predicted by fully-developed flow theory. Furthermore, the entry length and, thus, the departure of the pressure distribution from the linear case, is a strong function of channel height. An eccentric journal in a fluid with non-negligible inertia will therefore be surrounded by dissimilar axial pressure distributions, yielding a net force. Because the entrance region occupies a greater fraction of the channel length, and therefore causes a larger entry-region pressure drop, when the height is increased, the net force acts to restore the journal to a concentric position.

Because this mechanism provides stiffness even when the journal is not rotating, it will be referred to as a "hydrostatic," as opposed to a "hydrodynamic," effect, as described

in Sec. 1.2.2. Hydrostatic stiffness is not unusual in journal bearings. In the conventional implementation, however, the varying pressure in the film is established with the help of an upstream orifice, capillary tube, or valve known as a "restrictor" [12]. This restrictor provides an intermediary between the bearing and the supply pressure such that a greater pressure is communicated to the lubricating film when its height is reduced and vice-versa, generating a restoring force on a displaced bearing. Conversely, for the mechanism described in the current section, the supply pressure is always communicated directly to the film inlet. The film therefore provides its own restriction within the bearing gap itself, an arrangement known as "inherent restriction."

5.2.2 Model

In order to model the hydrostatic contribution to the forces on the journal, the pressure distribution must be computed for the entry length problem. Fortunately, due to its importance in heat exchangers, this problem has received a vast amount of attention, with many solutions published over a period of four decades.

In this work, incompressible flow will be assumed, which is reasonable if the flow rates remain moderate. The axial flow will also be assumed independent of the circumferential flow. Coney and El-Shaarawi [72] show that this is a reasonable assumption if the Reynolds number squared divided by the Taylor number is large (> 10). For a journal bearing, this parameter is given by:

$$\left(\frac{2\rho C U_{ax}}{\mu}\right)^2 \left(\frac{\mu^2}{\rho^2\omega^2 R C^3}\right) = \frac{4}{CR\omega^2} U_{ax}^2 \tag{5.3}$$

where U_{ax} is the axial flow speed. The final form is recognizable as $4R/C$ times the ratio of the axial flow kinetic energy to that of the rotating flow.

For the macro-rig, this number is of order 10^2 for flow-rates of order $10\,m/s$. The decoupling assumption may therefore be made with confidence. The MIT microengine has linear dimensions an order of magnitude smaller than the macro-rig's, however, but its rotation rate is two orders of magnitude larger. In this case, assuming comparable flow speeds, Coney and El-Shaarwi's parameter becomes order unity. Fortunately, these authors note that parameters of this size are associated with approximately a 3% change in pressure drop over the decoupled case, so the decoupling error is likely tolerable. If, however, comparable pressure drops are assumed instead of comparable flow rates, which is reasonable if thrust bearings at comparable supply pressures are used to cancel the axial force imbalance, the microdevice will have flow rates an order of magnitude smaller than the macro-rig. In this case, Coney and El-Shaarwi's ratio becomes of order 10^-2 and the error in decoupling axial and azimuthal flow may be significant. This factor must therefore be kept in mind when interpreting the results presented in the current section.

While Orr [34] employed interacting boundary layer theory (IBLT) to compute the en-

try length pressure distribution, an analytical solution is desired in the current work, both for reasons of computational efficiency and as a means to gain insight into scaling.

The most computationally convenient analytic solution was derived by Bhatti and Savery [73] by assuming a velocity profile in the entrance region and solving for the variable pressure gradient and the local boundary layer thickness via mass balance and mechanical energy relations. The resulting analytical expressions for the pressure distribution and centerline velocity evolution in a straight channel with uniform inlet are remarkably simple:

$$P = P_i - \frac{3}{280}\rho U_i^2 \left(22\hat{u}^2 - 10\hat{u} - 12 - 15\ln(3-2\hat{u})\right) \tag{5.4}$$

$$X = \frac{\rho U_i H^2}{4\mu}\frac{594\hat{u}^2 + 90\hat{u} - 684 - 15\hat{u}\ln(3-2\hat{u}) - 1308\hat{u}\ln(\hat{u})}{280\hat{u}} \tag{5.5}$$

where X is the dimensional distance from the entrance, U_i is the dimensional inlet speed, H is the channel height, and P_i is the pressure at the inlet. The nondimensional core flow speed, $\hat{u}$, is normalized by U_i and varies between unity at the entrance and $3/2$ where the flow becomes fully-developed.

Despite its simple appearance, particularly when viewed alongside many of the other solutions in the literature, Bhatti and Savery's solution has the correct asymptotic behavior for long channels and it matches experimental pressure drop measurements to within 3%. It is thus almost certainly sufficient for the current purpose.

To add hydrostatics to SPECTRES in the least disruptive manner, the linear pressure distribution of inertialess flow, which SPECTRES calculates, is subtracted from the entry-length correction to avoid double-counting it. This is a non-issue in uniformly pressurized cases because the linear pressure distribution integrates to zero. It is important in cases where side-pressurization is used, however, because the linear distribution's endpoints vary around the bearing.

The resulting hydrostatic force correction per unit circumferential depth may be expressed as:

$$F_{hs} = \int_0^{X_\ell} P dX + \frac{1}{2}(P_\ell + P_o)(L - X_\ell) - \frac{1}{2}(P_i + P_o)L \tag{5.6}$$

where X_ℓ is entry length, P_ℓ is the pressure at X_ℓ, and P_o is the outlet pressure. The integral is taken over the nonlinear pressure distribution in the entry region (first term) and a linear distribution is assumed for the remainder of the passage (second term). The third term represents subtraction of the inertialess distribution.

One complication in the above calculation is that the definition of X_ℓ is not precise. Strictly speaking, the velocity profile is never quite fully-developed, so X_ℓ is infinite. In common with the calculation of boundary layer thickness, convention places X_ℓ at a location where $\hat{u}$ reaches some percentage of its asymptotic value ($\hat{u}_\infty = 1.5$). Physically,

changing the definition of X_ℓ should not change the integrated pressure, but it can do so in Eq. 5.6 because the integration is stopped at X_ℓ and a linear distribution is assumed for the remaining length. The error in this approximation is small, however, if $\hat{u}_\ell$ is chosen to be very close to $\hat{u}_\infty$. In the majority of this work, $\hat{u}_\ell = 0.999\,\hat{u}_\infty = 1.4985$.

One more component is necessary to close the above system: a means for calculating the inlet velocity, U_i. If the flow becomes fully-developed somewhere in the channel, this means may be provided by rearranging the following expression, which appears in various forms in entry-length work [73]:

$$\frac{P_i - P}{\frac{1}{2}\rho U_i^2} = K_\infty + \frac{24\mu}{\rho U_i H^2} X \tag{5.7}$$

where K_∞ is a dimensionless excess pressure drop due to the entrance region. Various values for K_∞ appear in the literature, falling between 0.5 and 0.85. Bhatti and Savery's analysis yields $K_\infty = 0.5969$, which is in good agreement with the experimentally-measured value of $K_\infty = 0.5924$ published by Beavers *et al.* [74].

Writing Eq. 5.7 for the channel end, where $X = L$ and $P = P_o$, the resulting expression may be solved for U_i in terms of known quantities:

$$U_i = -\frac{12\mu L}{K_\infty \rho H^2} + \sqrt{\left(\frac{12\mu L}{K_\infty \rho H^2}\right)^2 + \frac{2(P_i - P_o)}{K_\infty \rho}} \tag{5.8}$$

If the flow does not become fully-developed, the calculation is more complex. First, U_i is eliminated between Eqs. 5.4 and 5.5. The resulting expression is then solved numerically at the channel exit for $\hat{u}$, given that $X = L$ and $P = P_o$ there. The value of U_i is then recovered by back-substitution into either expression.

All the terms in Eq. 5.6 may now be evaluated. Before doing so numerically, however, a significant savings may be realized through a bit more manipulation. Substituting Eq. 5.4 into the integral expression yields:

$$\int_0^{X_\ell} P dX = P_i X_\ell - \frac{3}{280}\rho U_i^2 \int_0^{X_\ell} \left(22\hat{u}^2 - 10\hat{u} - 12 - 15\ln(3 - 2\hat{u})\right) dX \tag{5.9}$$

Transferring the integration from X to $\hat{u}$ using Eq. 5.5, the integral becomes:

$$\frac{3}{280}\frac{\rho^2 U_i^3 H^2}{4\mu} \int_1^{u_\ell} \left(22\hat{u}^2 - 10\hat{u} - 12 - 15\ln(3 - 2\hat{u})\right) \left(\frac{(\hat{u} - 1)^2(513 - 297\hat{u})}{70\hat{u}^2(3 - 2\hat{u})}\right) d\hat{u} \tag{5.10}$$

Though this expression is considerably more complicated, it has a unique benefit: it need only be evaluated once as long as the defined speed ratio at the entry length, $\hat{u}_\ell$, does not change. The entire term may therefore be integrated offline and provided to the code as a constant, $\mathcal{I}$.

5.2.3 Nondimensionalization

For generality, and for integration into SPECTRES' operating space, the entry length expressions are nondimensionalized. This exercise also provides insight into the relevant scaling through development of appropriate nondimensional groups.

For normalizing the entry length, the factor chosen by Bhatti and Savery was employed:

$$X_\ell = \frac{\rho U_i H^2}{4\mu}\mathcal{L} \tag{5.11}$$

and similarly for the pressure at X_ℓ:

$$P_\ell = P_i - \frac{1}{2}\rho U_i^2 \mathcal{P} \tag{5.12}$$

The entry flow speed is normalized by the mean speed of a fully-developed flow through a channel of length L and height C:

$$U_i = \frac{C^2}{12\mu}\frac{P_i - P_o}{L}u_i, \tag{5.13}$$

the pressure drop across the channel is normalized by the outlet pressure:

$$\Delta P = P_i - P_o = P_o \Delta p, \tag{5.14}$$

and the force itself is normalized by LP_o to convert it to a normalized pressure per unit depth, $\hat{p}$:

$$F_{hs} = LP_o\hat{p}. \tag{5.15}$$

When these normalizations are inserted in Eq. 5.6, a new nondimensional group appears. Rearranging this group, it may be viewed as C/L times the Reynolds number based on the mean flow speed through a channel of length L and height C with P_o applied at the inlet and vacuum at the outlet. Because this form is similar to the inertial parameter, χ, introduced in Sec. 1.2.3, this parameter will be called the "axial inertial parameter" and represented by χ_{ax}:

$$\chi_{ax} = \left(\frac{\rho\, C}{\mu}\frac{C^2\, P_o}{12\mu\, L}\right)\left(\frac{C}{L}\right) = \frac{\rho\, C^4\, P_o}{12\mu^2 L^2} \tag{5.16}$$

With this framework in place, the absence of axial inertial effects in the gas bearing literature becomes clearer. First, and foremost, most bearings are run with their ends exhausted to ambient pressure. The pressure difference across the rotor, $P_i - P_o$, is thus small and the resulting axial flow has little discernible effect. Second, the macro-rig's $100\mu m$ clearance, chosen to maintain geometric similarity with the clearance-constrained silicon microdevice after appreciable growth is experienced in its steel rotor at high speed, is a factor of four larger than most other bearings in the literature. Similarly, the macro-rig's

$8\,mm$ length is short relative to most conventional bearings. Inspecting Eq. 5.16, χ_{ax} has a fourth-power dependence on clearance and a second-power dependence on the length. The macro-rig's $\chi_{ax} \sim 60$ is therefore much larger than that of most other conventionally-machined devices, which is of order:

$$\chi_{ax} = \frac{(10^0)(10^{-5})^4(10^5)}{(10^1)(10^{-5})^2(10^{-2})^2} = 10^{-2} \tag{5.17}$$

The macro-rig will tend to exhibit larger inertial effects for a given pressure difference than most conventional bearings.

Proceeding with the nondimensionalization, the parameters developed above are substituted into Eq. 5.6, yielding:

$$\hat{p} = \chi_{ax}\Delta p^2 u_i \left[\frac{h^2}{8}\left(\mathcal{L} - \frac{1}{12}\chi_{ax}\Delta p u_i \mathcal{I}\right) + \frac{u_i \mathcal{P}}{48}\left(\frac{1}{4}\chi_{ax}\mathcal{L}\Delta p u_i - 1\right)\right] \tag{5.18}$$

where $\mathcal{I}$ is calculated from Eq. 5.10 and h is the channel height, H, normalized by the bearing clearance, C. Expressions for $\mathcal{P}$ and $\mathcal{L}$ are nondimensional versions of Eqs. 5.4 and 5.5:

$$\mathcal{P} = \frac{3}{140}\left(22\hat{u}_\ell^2 - 10\hat{u}_\ell - 12 - 15\ln(3 - 2\hat{u}_\ell)\right) \tag{5.19}$$

$$\mathcal{L} = \frac{594\hat{u}_\ell^2 + 90\hat{u}_\ell - 684 - 15\hat{u}_\ell\ln(3 - 2\hat{u}_\ell) - 1308\hat{u}_\ell\ln(\hat{u}_\ell)}{280\hat{u}_\ell} \tag{5.20}$$

As with $\mathcal{I}$, $\mathcal{P}$ and $\mathcal{L}$ do not change once the entry length definition is fixed. For example, for $\hat{u}_\ell = 0.999\,\hat{u}_\infty$, $\mathcal{I} = 0.4149$, $\mathcal{P} = 2.3476$, $\mathcal{L} = 0.2920$. These values are provided to SPECTRES as constants. As a result, only the inlet speed u_i in Eq. 5.18 must be calculated at each timestep for each circumferential station using Eq. 5.8, which, under the above nondimensionalizations, becomes:

$$u_i = -\frac{12}{\chi_{ax}K_\infty\Delta p\,h^2} + \sqrt{\left(\frac{12}{\chi_{ax}K_\infty\Delta p\,h^2}\right)^2 + \frac{24}{\chi_{ax}K_\infty\Delta p}} \tag{5.21}$$

In Eq. 5.18, dividing through by Δp yields an expression where χ_{ax} and Δp always occur together. A generalized surface may therefore be constructed of $\hat{p}/\Delta p$ as a function of h and $\chi_{ax}\Delta p$. Because h is guaranteed to be between 0 and 2 on a journal bearing, the only decision to be made when constructing such a surface is the upper limit on $\chi_{ax}\Delta p$. This surface is presented in Fig. 5.7 for $\chi_{ax}\Delta p$ up to 25, which covers the entire reported operating range of Orr's frequency investigation. For a microdevice, which will usually have a smaller χ_{ax}, the Δp range covered in Fig. 5.7 is even greater.

A number of observations may be made from Fig. 5.7. First, as expected, the pressure correction for fixed Δp increases with increasing χ_{ax}. Particularly for large channel heights,

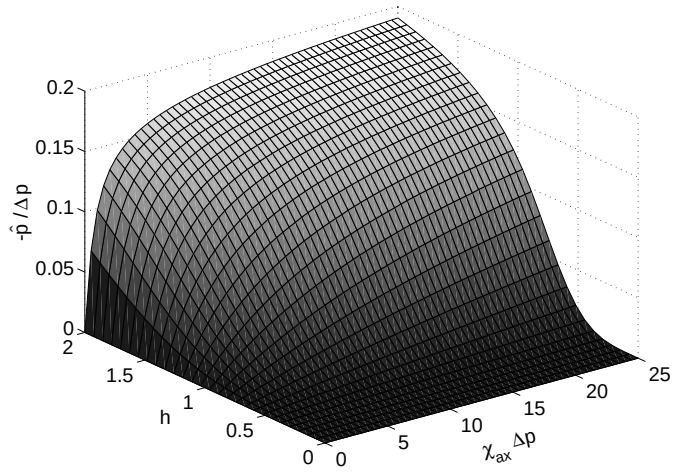

Figure 5.7: Generalized surface of hydrostatic correction pressure for channel heights found in journal bearings and a range of $\chi_{ax}\Delta p$.

this increase is very strong at small $\chi_{ax}\Delta p$ but flattens considerably at larger $\chi_{ax}\Delta p$. Also, because a centered journal is surrounded by a channel of uniform height $h=1$, the span of variation on the generalized $\hat{p}$ surface increases with ϵ. It may be noted, however, that the slope of $\hat{p}$ with respect to h decreases toward the two extremes except at very low $\chi_{ax}\Delta p$. Furthermore, the slope distribution around $h=1$ varies with $\chi_{ax}\Delta p$. These observations imply that the stiffness varies with eccentricity and the variation changes with $\chi_{ax}\Delta p$.

5.2.4 Natural Frequency Variation

Under the nondimensionalization of the previous chapter, only three parameters are required to calculate the hydrostatic restoring force on the journal: χ_{ax}, Δp, and ϵ, where ϵ is required simply to specify the height distribution around the journal. The attitude angle is not required because, unlike hydrodynamics, hydrostatics always produces only direct stiffness under the model outlined in this chapter. It should be noted, however, that finite flow rates in the plena cause leads and lags in the force magnitude and direction that, in some cases, can appear as a significant cross stiffness, as well as damping [75].

To calculate the natural frequency about zero eccentricity, the journal is displaced to $d\epsilon$, which was 0.0005 in this work, and the resulting $\hat{p}$ integrated around it to obtain a restoring force. Dividing by this $d\epsilon$ yields the nondimensional natural frequency squared.

$$\omega_n^{*2} = \frac{1}{d\epsilon}\int_0^{2\pi} \hat{p}(d\epsilon)d\theta \tag{5.22}$$

This frequency can then be dimensionalized by multiplying by the reference frequency, $\hat{\omega}$, where

$$\hat{\omega} = \sqrt{\frac{RLP_o}{Cm}} \tag{5.23}$$

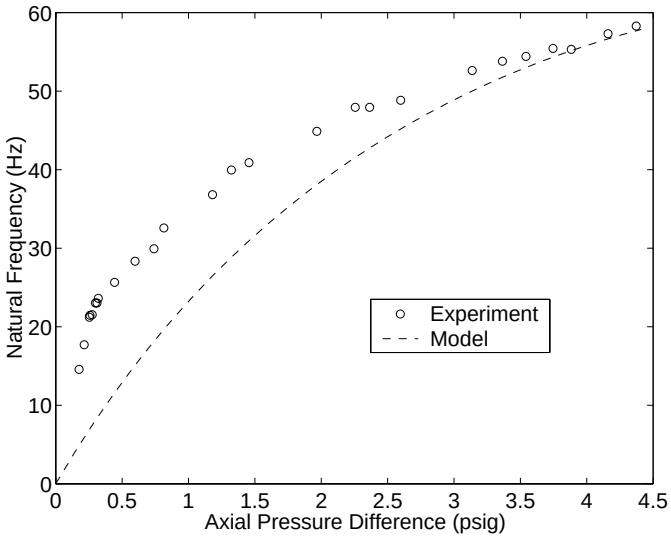

Figure 5.8: Comparison of zero-eccentricity hydrostatic natural frequency predicted by the current model and data from Orr [34]. The agreement between the two results is poor at low Δp but their asymptotic behavior at high pressure is comparable. The disagreement is similar to that found by Orr using an interacting boundary layer calculation.

or it can be expressed as a multiple of the rotational frequency through:

$$\frac{\omega_n}{\omega} = \frac{\omega_n^*}{\Lambda\sqrt{2\bar{M}}} \tag{5.24}$$

The natural frequency about a nonzero eccentricity is determined through a similar process. Integrals identical to that of Eq. 5.22 are calculated at $\epsilon + d\epsilon$ and $\epsilon - d\epsilon$ and their sum is divided by $2d\epsilon$.

Toward verification of the model, its results are compared to the experimental natural frequencies measured by Orr [34]. Assuming standard conditions and noting from [34] that $C = 101.6\,\mu m$, $m = 0.52\,kg$, $R = 5.2\,cm$ and $L = 7.8\,mm$, the inertial parameter is calculated to be $\chi_{ax} = 60$ and the reference frequency is $\hat{\omega} = 882\,rad/s$ for this device. The resulting natural frequency at zero eccentricity for the given range of pressures is shown in Fig. 5.8 along with Orr's data.

It may be noted that the current model and Orr's data show poor agreement at low Δp but their asymptotic behavior at high pressure is comparable. Because the disagreement between model and experiment at low Δp was also shown for Orr's IBLT calculations, this finding implies that the error is not one of execution, but of formulation.

The most obvious neglected phenomenon to check is compressibility. The current model, as well as that used by Orr, assume incompressible flow. In aerodynamics, the importance of compressibility is commonly assessed by computing the ratio between the flow speed and the sound speed, which is $347\,m/s$ at 300K. If this ratio, known as the Mach number, is greater than approximately 0.3, compressibility effects may be significant.

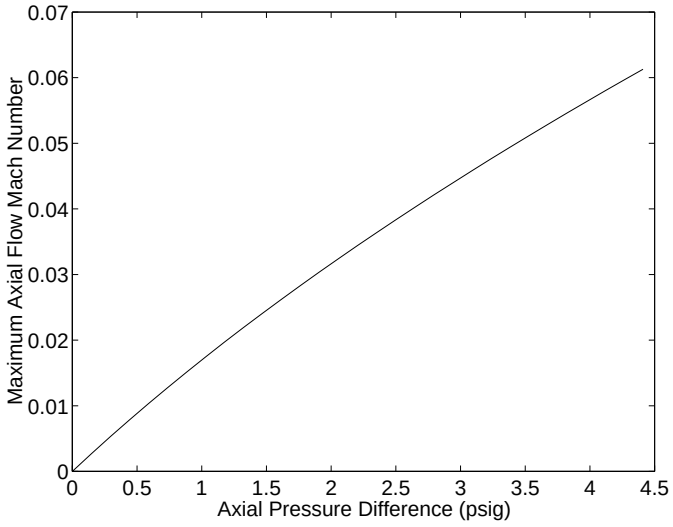

Figure 5.9: Mach number as a function of axial ΔP for the data of Orr [34]. While the Mach numbers are surprisingly large, they are not large enough to indicate that compressibility is a significant issue in this flowfield.

The Mach number at the channel centerline after the flow becomes fully-developed for the data of Fig. 5.8 is presented in Fig. 5.9. From this figure, it can be concluded that, while the Mach numbers are surprisingly large, they are not large enough to indicate that compressibility is a significant issue in this flowfield.

It should be noted, however, that this result indicates that the local density gradients are not significant but it does not provide information about the global density change. Assuming isothermal flow (worst case), this change is equal to $\Delta P/P_o$, which reaches 30% for Orr's data. The velocity integrated across the passage must therefore increase to conserve mass under the decreasing density, but the pressure distribution, which is the quantity of interest in the current section, will not be significantly affected.

The other key assumption of the current, as well as the IBLT, model is a uniform velocity profile at the entrance. For the experimental rig, this is a rather poor assumption because the entrance is a 90° corner, rather than a sharp leading edge. Separations will therefore form at the corners. Furthermore, the plena supplying the pressure are relatively shallow so the flow will likely experience a significant turning effect. Both effects will cause additional pressure drops in the passage. This effect is, in fact, similar to the orifice restriction used in many conventional hydrostatic bearings.

Recognizing that these effects may result in a greater "effective" axial inertial parameter than predicted by Eq. 5.16, Breuer [71] suggested an attempt to improve the agreement by varying χ_{ax}. The results of this effort are presented in Fig. 5.10.

Figure 5.10 shows that the model produces an excellent match to experimental data over the entire pressure range when χ_{ax} is increased by a factor of five. Under the above arguments regarding the inlet condition, this increase can be justified, if only heuristically.

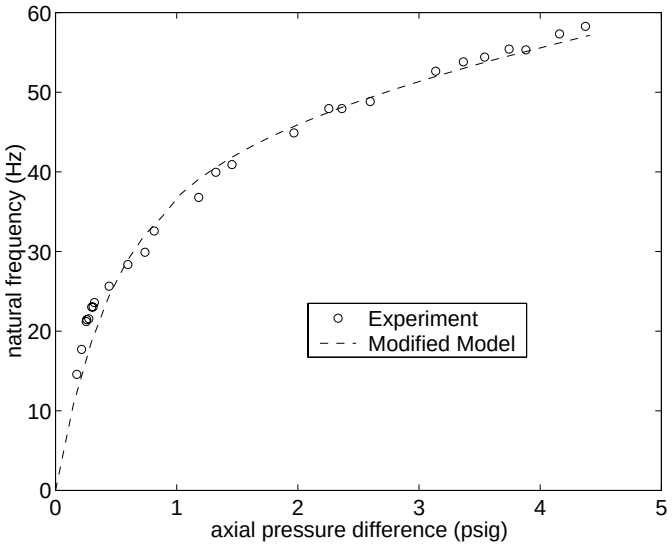

Figure 5.10: Comparison of model with $5 \times \chi_{ax}$ to experimental data. Excellent agreement is demonstrated. It was, however, also necessary to modify the normalization terms on the frequency as well, which is difficult to justify physically.

After modifying χ_{ax} however, it is also necessary to rescale the frequencies by increasing $\hat{\omega}$ by a factor of 1.3. This increase is more difficult to understand physically. It may be noted that the adjustment to both χ_{ax} and $\hat{\omega}$ only moves in the same direction if P_o is varied. Varying any of the other variables, such as c or L increases one of the parameters but decreases the other. Orr [34] suggested circumferential clearance variation as a possible explanation.

A number of features of the hydrostatic effect indicated by the generalized pressure correction surface in Fig. 5.7 can be clarified via study of the hydrostatic natural frequency, ω_n. Furthermore, this frequency is important experimentally because it provides a measure of the hydrostatic stiffness that can be easily observed from power spectra of relatively crude position sensor data. In addition, because the natural frequency will interact with the ever-present synchronous forcing due to imbalance, this frequency sets the location of "critical speeds" where strong journal responses may be seen. Because these responses may produce wall-contact, the associated ω may be an operational maximum. In these cases, ω_n must be increased to reach the design speed so it is important to understand its variation with χ_{ax} and Δp to avoid excessive axial massflow and force imbalance.

First, a family of normalized natural frequency curves at zero eccentricity are presented in Fig. 5.11 for a range of pressure ratios. The trend of hydrostatic effect versus χ_{ax} notable by comparing Figs. 5.8 and 5.10, continues: higher χ_{ax} implies a larger natural frequency for a given Δp at small Δp, but the trend reverses at large Δp.

The crossing of the constant-χ_{ax} lines in Fig. 5.11 may be explained by observing the slope reduction, or "knee point" that takes place on all curves as the pressure increases. This knee point becomes more pronounced and occurs at smaller Δp for bearings with

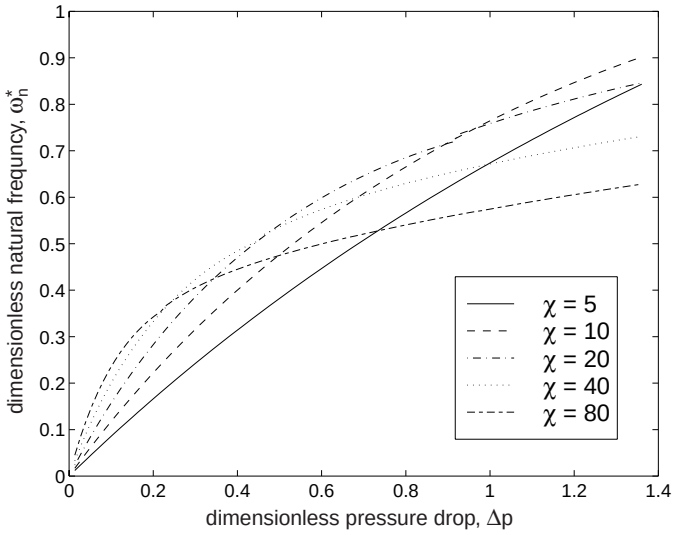

Figure 5.11: Effect of axial inertial parameter on the zero-eccentricity nondimensional natural frequency at a range of pressure ratios. A higher χ_{ax} implies a larger natural frequency for a given Δp at small Δp, but the trend reverses at large Δp due to earlier occurrence of the "knee" point.

larger χ_{ax}. This finding implies a tradeoff must be made between the maximum stiffness desired from the hydrostatic mechanism and its "efficiency" with respect to the increase in Δp needed to produce a given increase in ω_n. Bearings with large χ_{ax} show a very rapid increase in ω_n^* with Δp at low Δp, but the curve quickly flattens and crosses the lower χ_{ax} traces.

Toward explaining the knee points, the channel location at which the flow becomes fully-developed is plotted in Fig. 5.12 for the cases in Fig. 5.11. Comparing these figures, it can be concluded that the knee point in the natural frequency trace roughly corresponds to the Δp at which the flow reaches a fully-developed state at the channel exit. With further increases in Δp, the development point becomes virtual and moves outside the channel. As it moves further downstream, the boundary layers in the channel become thinner with respect to the channel height and, therefore, have diminished influence on the pressure distribution. The loss of slope on the ω_n-Δp curve is therefore related to a loss in sensitivity to channel height when the flow fails to become fully-developed.

A second characteristic of the entry-length hydrostatic stiffness is visible in Fig. 5.7, but most easily understood in terms of natural frequency: its dependence on eccentricity. This dependence is shown in Fig. 5.13 for two axial inertial parameters.

From this figure, it may be seen that the variation of ω_n^* with Δp has three regions. Furthermore, the extent of these regions in terms of Δp is an inverse function of χ_{ax}. In the low $\chi_{ax}\Delta p$ region, the natural frequency increases slightly with eccentricity. In the moderate $\chi_{ax}\Delta p$ region the natural frequency decreases noticeably with eccentricity, with the variation increasing with Δp. At high $\chi_{ax}\Delta p$, the curves begin to cross as the slope of ω_n^* with Δp decreases most strongly with decreasing eccentricity. This leads to a situation at very

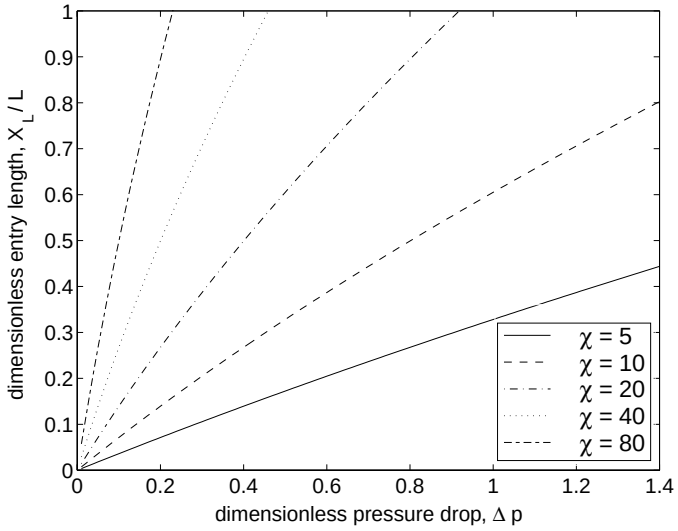

Figure 5.12: Entry length location with $u_\ell = 0.999 u_\infty$ for cases of Fig. 5.11. Comparing these figures, the knee point occurs as the point at which fully-developed flow is reached moves out of the channel.

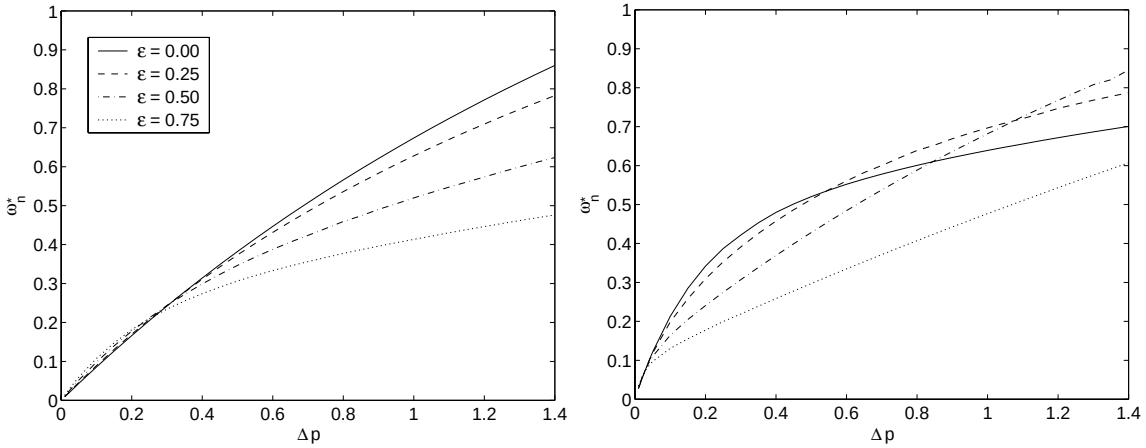

(a) $\chi_{ax} = 5$ **(b)** $\chi_{ax} = 50$

Figure 5.13: Dependence of normalized hydrostatic natural frequency on eccentricity for two values of χ_{ax}. At moderate values of $\chi_{ax}\Delta p$, an increase in eccentricity generally reduces ω_n^*. At very high $\chi_{ax}\Delta p$, this trend reverses.

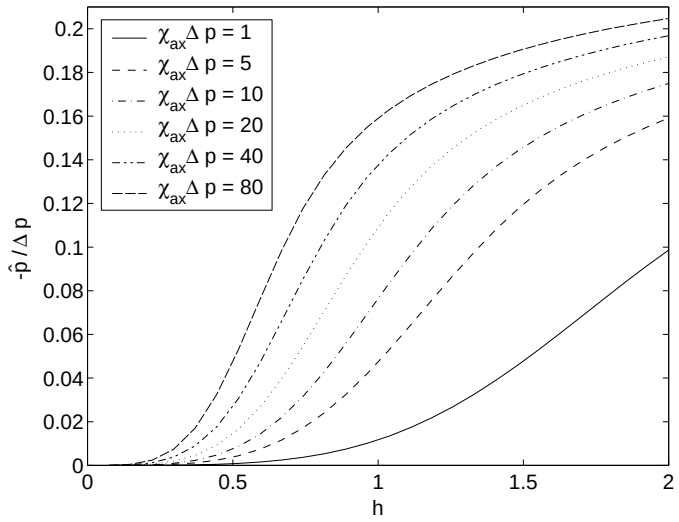

Figure 5.14: Normalized hydrostatic correction pressure as a function of channel height for various values of $\chi_{ax}\Delta p$. The non-constant slope over h is responsible for the eccentricity dependence of ω_n^* shown in the previous figure. The shift in maximum slope away from $h=1$ as $\chi_{ax}\Delta p$ increases is responsible for the re-ordering of the frequency versus eccentricity.

high $\chi_{ax}\Delta p$ where the trend is once again reversed and the natural frequency increases with eccentricity.

This behavior can be explained by inspecting the generalized hydrostatic correction pressure surface in Fig. 5.7. For convenience, several constant-$\chi_{ax}\Delta p$ traces from this figure are presented in Fig. 5.14. On each trace, the channel height is unity when $\epsilon = 0$. When ϵ is nonzero, the channel height varies between $(1-\epsilon) \leq h \leq (1+\epsilon)$ around the journal. For example, for $\epsilon = 0.5$, the channel height varies between $0.5 \leq h \leq 1.5$.

At low Δp, the increasing frequency with eccentricity may be explained by inspecting $\chi_{ax}\Delta p = 1$ trace in Fig. 5.14. On this line, a constant-slope region occurs from $1.25 \leq h \leq 2$. Furthermore, the maximum slope on the trace occurs in this region. Slight perturbations at zero eccentricity and small ΔP therefore do not penetrate the maximum slope region and the natural frequency is smaller than at larger eccentricity, where the span of h penetrates the high-slope region.

At moderate Δp, the constant-slope region encloses $h = 1$. The maximum stiffness is therefore found around $\epsilon = 0$ because the entire height distribution is within the maximum slope region. At a nonzero eccentricity, however, the height distribution extends into regions outside the maximum slope region. Slight perturbations about these points will therefore reveal decreased stiffness over the zero eccentricity case. Furthermore, because the slope decreases at both ends of the h range, increasing eccentricity further decreases the stiffness.

At very high Δp, the maximum slope region moves to the left of $h = 1$. The maximum stiffness is therefore no longer found at $\epsilon = 0$. In this case, increasing eccentricity once again causes the height distribution to move out into the maximum-slope region so it will

increase the stiffness.

In the areas between the three Δp regions, increasing eccentricity has a varying effect due to an interplay between penetrating the constant slope region and the reduced slope regions at the h extremes.

5.2.5 Interaction with Hydrodynamics

When the hydrostatic correction pressures are added to the dynamic simulation, a number of new effects are seen. First, of course, a frequency appears on the spectrum at ω_n that is independent of bearing number. Second, operating conditions that resulted in large whirls under solely hydrodynamic operation become stable under combined, or "hybrid" operation. Stability boundaries microbearings in this hybrid mode were calculated by Savoulides [76] using an eigenvalue analysis. This section will present examples of dynamic interactions between the operating modes in nonlinear orbits.

An example of a bearing operating in a primarily hydrostatic mode is presented in Fig. 5.15. In this case, the imbalance was set to 5% and all pressure plena were set to $P/P_a = 1.2$ and $\chi_{ax} = 5$. The bearing number was 0.17, placing the hydrostatic natural frequency at $\omega_n/\omega = 0.7$.

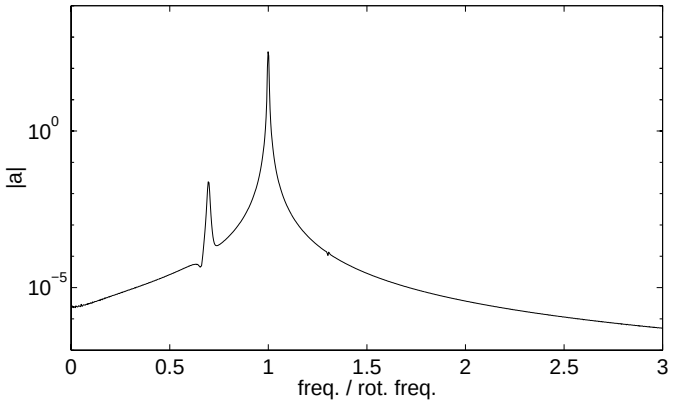

Figure 5.15: Frequency spectrum for a primarily hydrostatic case. The orbit is nearly circular and the spectrum consists of only the hydrostatic natural frequency and the synchronous frequency due to imbalance.

In this case, the orbit is centered and circular and the power spectrum shows a peak at the hydrostatic natural frequency and the synchronous frequency due to imbalance. Notably, the power spectrum is absent of the additional peaks due to sum and difference modes observed by Orr [34] for hybrid operation and also observable in Fig. 3.27 for purely hydrodynamic operation. This absence is a consequence of a very small hydrodynamic stiffness and the relatively constant hydrostatic stiffness found at small ϵ and Λ. Furthermore, the hydrostatic case was chosen such that the stiffness was nearly constant with ϵ.

Because ω_n is fixed and can be calculated in advance from the model, it is relatively easy to manipulate Λ to produce coherent orbits at rotation speeds that are fractions or multiples of ω_n. In these cases, it was also necessary to provide load to prevent the orbit from precessing in the perfectly circular bearing used in the numerical simulation. An example of a series of these orbits and their associated power spectra are shown in Fig. 5.16.

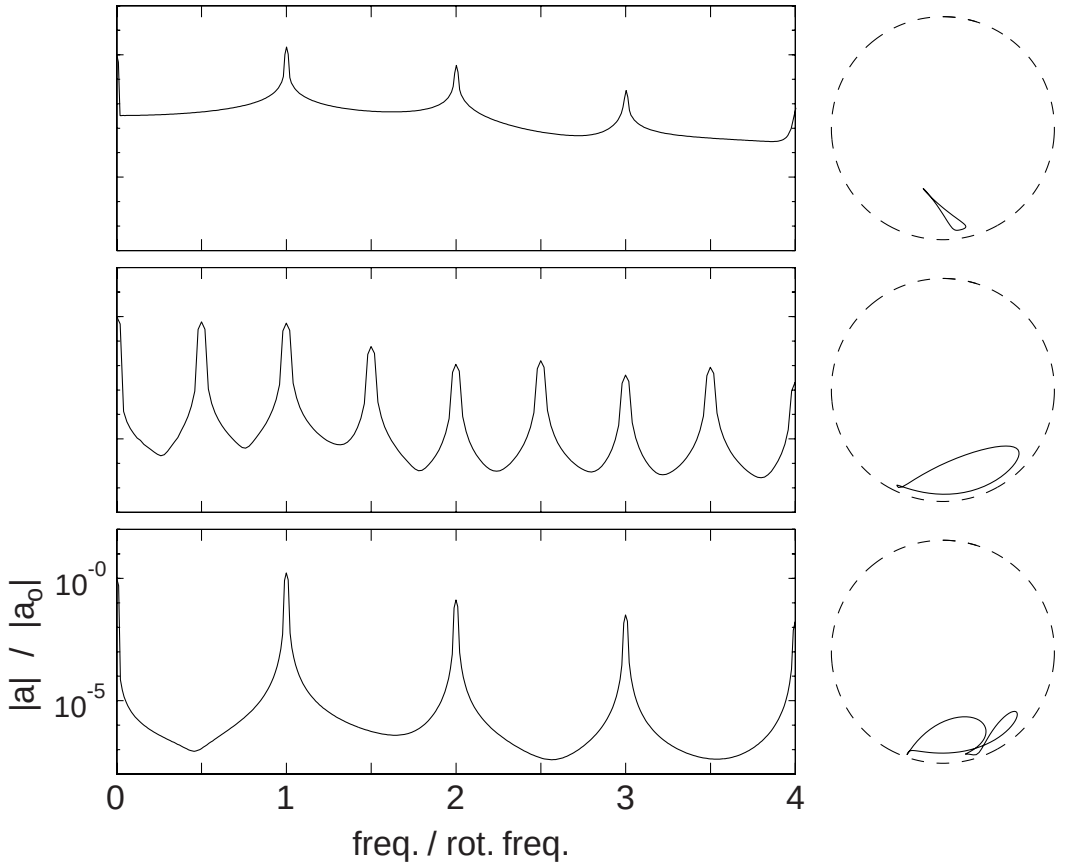

Figure 5.16: Frequency spectra and orbits for cases in which rotation frequency is a whole-number fraction or multiple of the hydrostatic natural frequency.

In these cases, the power spectrum contains sum and difference modes due to the large ϵ, which introduces nonlinearities due to hydrodynamics, and the large χ_{ax}, which introduces nonlinearity in the force characteristic.

The relative magnitude of hydrostatic and hydrodynamic forces during a beta orbit are shown in Fig. 5.17. As may be expected, the hydrodynamics provide a very strong repulsive force when the journal approaches the wall. In addition, a weaker attractive force is applied via the squeeze-film mechanism as the journal retreats from the wall after being repelled. For the remainder of the orbit, hydrostatic forces dominate.

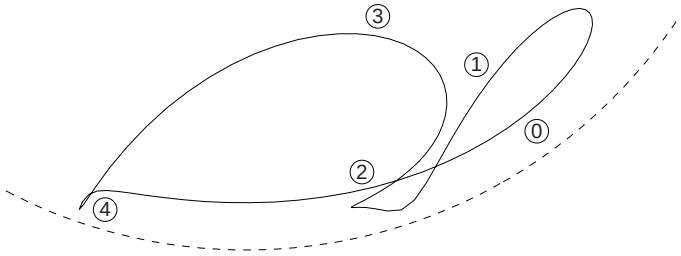

(a) Orbit

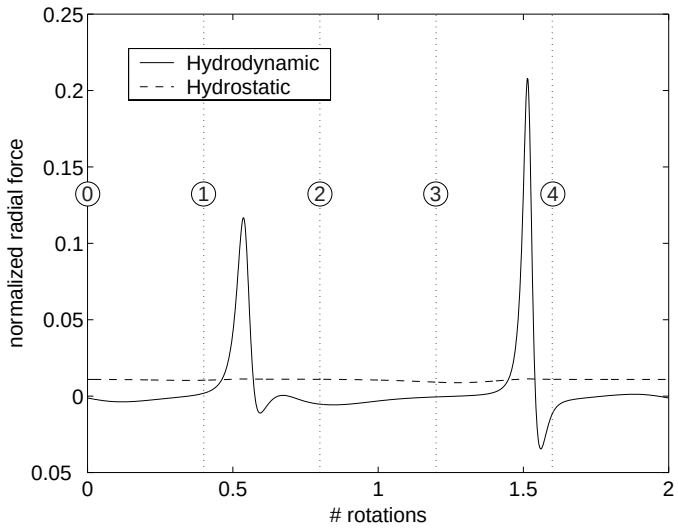

(b) Forces

Figure 5.17: Comparison of hydrostatic and hydrodynamic radial force levels during a beta orbit. A positive value denotes force away from the wall. Hydrodynamics provides a strong repelling force on wall approach and a weaker attractive force on retreat. Hydrostatics is dominant through the remainder of the orbit.

5.3 Chapter Summary

In this chapter, information was presented on two considerations for bearings in operation. The first consideration, the need to apply loads via side-pressurization, is a consequence of the very low weight of MEMS and the high eccentricities required for stable operation of short bearings. The second consideration, axial flow inertia, is a consequence of the first.

Side-Pressurization Loading

It was shown in Sec. 5.1 that imposing a non-circumferentially-uniform pressure at an axial end is an effective means of providing side load to a journal bearing. Furthermore, due to the low load capacity of the low L/D bearings likely to be found in microdevices, the required pressures are quite moderate.

An unfortunate consequence of this type of loading was discovered however: it tends to increase the attitude angle and decrease the critical $\bar{M}$ at a given eccentricity. This effect becomes stronger at higher speed but, fortunately, weakens with increasing eccentricity. This weakening is important for microbearings due to their typically large required eccentricity because it prevents the stability corridor from closing altogether, as it did for some tapered bearings.

Stiffness Due to Axial Flow Inertia

In Sec. 5.2, it was shown that pressure gradients in the axial direction of a short bearing, such as in side-pressurization loading of microbearings, can result in a flow with significant inertial effects. These inertial effects make the pressure distribution dependent on the local channel height, which results in a restoring force on a displaced journal. This restoring force is similar to that of a traditional externally-pressurized bearing with a flow restrictor but, in this case, the restrictor is built into the bearing itself.

A model was developed for these this stiffness and its controlling nondimensional parameter was shown to be very similar to the inertial parameter used in typical lubrication flows. The model was used to construct a generalized surface for determining the axial pressure distribution's departure from the inertialess case computed via the Reynolds equation. The variation of the stiffness with χ_{ax}, Δp, and ϵ was shown. This model was also incorporated into SPECTRES and several coherent orbits indicative of resonance with the new frequency observed in macro-scale bearing experiments were reproduced.

Finally, it should be noted that, while the axial flow hydrostatic mechanism originates from pressurization of the side-loading plena, it was experimentally detected when both plena were increased to large Δp, rather than one or the other, as would be the case if they were being used for their intended purpose. Due to the low load capacity of microbearings, significant hydrostatic effects are unlikely to be seen if one plenum is held at ambient pressure and the other is increased for the purpose of loading a hydrodynamic bearing.

For example, reading ζ from Fig. 5.3 and using Eq. 5.2 to recover Δp, it can be seen that producing a 90% eccentricity by side-pressurization at $\Lambda = 1$ will require $\Delta p \sim 0.1$. Noting that $\chi_{ax} \sim 5$ for the microturbine of Fig. 3.6, the hydrostatic correction pressure is, at maximum ($h = 1.9$), approximately -0.0058. Given that the input $\Delta p \sim 0.1$ and the maximum Δp produced hydrodynamically at this operating point is approximately 0.27, this correction pressure is unlikely to contribute significantly to the forces on the journal.

Chapter 6

Conclusions

6.1 Numerical Tools

Two distinct numerical tools were developed expressly for this work. This document is based almost entirely on their results. The large design space and wide variety of effects investigated are testament to the generality of their approach.

BASICS

BASICS was written to examine effects invisible to tools constructed via the standard assumptions of lubrication theory. Though it must be extended to 3-D, unsteady flows to provide direct solutions to problems of interest to (typically short) microbearings, its 2-D steady state results were useful for providing temperature data, inertia effects and insight into the flowfield that applies at least qualitatively to finite-length bearings.

SPECTRES

SPECTRES was written to be a flexible research tool and it has served this purpose well. First, it provided steady-state and stability data for the high eccentricities required by microbearings that was impossible with the low-order Galerkin methods and impractical with finite difference methods. Second, its "numerical experiment" framework allowed effects not necessarily expected or under study, such as the high frequency radial mode, to come to the fore. In addition, the flexibility of this approach allowed many models to be added in a modular fashion as new effects were identified in the course of the MIT microengine development. The wide variety of effects investigated is especially striking when it is noted that SPECTRES' source is only slightly over 2000 lines (not including the FFT routines).

A key enabler for SPECTRES is its pseudospectral formulation. This formulation strikes a balance between the run-time resolution flexibility of finite difference techniques and the grid efficiency of spectral techniques.

6.2 Design Methodology

In this work, a categorization of nondimensional variables is suggested consisting of three conditions: loading, geometry, and fluid. It is shown that one loading, two geometric, and one fluid condition are required to fully specify an unsteady problem in a finite bearing. It is also noted that the parameter sets that can be categorized into the above conditions tend to be complimented by other researchers while those that cannot, due to recurrence of variables logically associated with only one condition, such as ω, received complaints about their utility in a design environment. Framing the design process in terms of the suggested categorization should therefore be valuable in both micro and macro bearing design environments.

Stability boundaries in this work are expressed in terms of required load or eccentricity, rather than critical mass or threshold speed. This presentation highlights a difference in design philosophies for macro and micro bearings: a macro-bearing designer typically must choose a geometry to carry a given load whereas the micro-bearing designer must choose a load to stabilize a tightly-constrained geometry. It is asserted, however, that presenting the data in this format clarifies certain trends, so it is a worthwhile exercise even for macrobearing designers.

6.3 Microfabricated Journal Bearings

As concluded by Orr [34] on the basis of experiments, the extremely short bearings likely to appear in microdevices fabricated with current techniques are shown to be a viable means of supporting high-speed rotating members with gaseous lubricants. In addition, an exploration of the associated design space, enabled by the computational nature of the current investigation, suggests a number features that are typical of these bearings.

Low L / D

The L/D of the baseline MIT microengine bearing is nearly a factor of three smaller than the smallest value found in the literature. Low L/D is put forth as a characteristic feature of microbearings because, due to an interplay of constraints discussed primarily in Chap. 1, it is not likely to increase greatly in the near future.

It was shown in this work that the short bearing's substantial side-leakage causes it to behave very much like an incompressible bearing. Significant departure of the load capacity from the incompressible result, for example, was obtained only through a combination of high eccentricity and speed. Because (non-cavitating) incompressible bearings are unconditionally unstable, this finding implies a radical running mode is required for stability.

High Eccentricity

The combination of small L/D and relatively large C/R found in the MIT microengine bearings implies a large eccentricity (*eg.* $\epsilon > 0.90$) is required for stability, particularly at low speed. Such a large eccentricity in a clearance measured in microns leads to an extremely small physical separation between journal and bearing ($\simeq 1\mu m$). Tolerances for allowable contaminant size and, to a lesser extent, surface roughness and journal roundness are therefore also small.

Near-wall operation is put forth as a characteristic feature of plain microfabricated bearings because it is shown in this work that variations in length, diameter, and clearance have a surprisingly weak effect on stability in terms of dimensional running separation between solid surfaces. This finding is traceable to a reduced sensitivity of the minimum stable eccentricity to these parameters when its baseline value is high, as demonstrated in Fig. 3.12. Furthermore, as discussed in Sec. 3.2.1, the consistent trend of increasing minimum eccentricity with clearance, and vice versa, works to cancel attempts to improve the separation via clearance modification alone.

The design charts of Sec. 3.2.1 show that, of the variable parameters in a plain bearing, increasing the length generally brings the most benefit in terms of increasing allowable separation between surfaces. Figure 3.14 shows that this conclusion most often holds even if the clearance increases with the length, as is most often the case when it is produced via deep etching. In this situation, the minimum eccentricity increases with length, but it does so at a slower rate than the clearance increases. The running separation therefore improves, although only slightly.

The benefit of increased length can, however, be canceled if it exacerbates the axial clearance variation often seen in etched bearings. For example, it is shown in Sec. 4.2.3 that a tapered clearance can be modeled as an increase in ϵ_{min} proportional to the axial ΔC divided by the clearance (Eq. 4.9). This parameterization implies that the greater running separation obtained by increasing the length via a fixed aspect ratio etch survives if ΔC increases at no more than a linear rate with C. The benefit can easily be canceled, however, if ΔC grows faster than C as the length increases.

In addition to varying the plain bearing geometric parameters of Fig. 1.3 to increase running separation, varying the bearing radius as a function of location is investigated in this work. While, various noncircular shapes have proven beneficial in macro-scale bearings, their effect on microfabricated bearings has not previously been assessed. The key difference is that the minimum clearance between features is more or less fixed in an etched bearing, thus noncircularity must be obtained solely through introducing clearance increases at various circumferential positions. A noncircular bearing's mean clearance will therefore be larger than its circular equivalent, possibly canceling the performance gain imparted by the shape change. The load capacity was shown to suffer from this cancellation. Conversely, the minimum running separation required for bearing stability improved

despite the clearance increase. In cases where low load capacity can be tolerated, the non-circular bearing shows some promise for achieving running separations comparable to those of macro-scale bearings.

Low Load Capacity

The large C/R - small L/D combination responsible for near-wall operation of microfabricated journal bearings produces another characteristic feature: low load capacity. As shown Sec. 1.3.3, however, microdevices tend to have very low (order 10^{-4}) load parameters from rotor weight. Ability to carry a static load is therefore not necessarily a primary design concern.

In this context, low load capacity is worrisome only in terms of accuracy required to control appropriate side load for stability and resistance to impulsive loading. In terms of the former concern, the high eccentricities required for stability imply high stiffnesses. The load can therefore be overspecified to guarantee stability in view of load-control uncertainty without greatly increasing the running eccentricity and, thus, the drag and danger of crashing. In terms of the latter concern, despite their low static load capacity, microfabricated bearings are shown in Sec. 3.2.5 to tolerate shocks in the thousands of g's. This result is traceable to very low rotor weight, large stiffness at high eccentricity, and squeeze film effects.

As pointed out in Sec. 3.1 low load capacity proves to be an advantage in terms of stability because it implies smaller side-load requirements for producing the required eccentricity. In a turbomachine with side load provided via self-tapped pressures, this translates to reduced bleed-air requirements, increasing machine efficiency. In addition, as shown in Sec. 3.1.2, the low load capacity allows use of a greatly-simplified expression for calculating the bearing drag, simplifying design tradeoffs.

Imbalance

Due to their small size and constraints inherent to available tools, post-fabrication balancing of microrotors is extremely difficult. Imbalance is therefore most easily minimized by careful design and control of the fabrication process. Unfortunately, with clearances comparable to the achievable tolerances on various manufacturing steps, significant imbalance is likely to be an unavoidable feature of microbearings.

In Sec. 3.2.4 a duality between applied load and imbalance level was demonstrated. This situation allows the imbalance tolerance to be adjusted through manipulation of the side-load. In addition, by adjusting the load using the rotor motion's spectral content as a guide, the duality may still be exploited in many cases when the imbalance level is not known *a priori*.

6.4 Recommendations

In terms of improving microbearings, this work indicates a number of areas that merit further investigation.

First, lengthening the bearing appears to improve its operating state in almost all respects. This trend does not always hold, however, for shrinking the clearance. This result indicates that process development effort is most profitably spent on the former issue.

Second, noncircular shapes appear to be a useful idea for microbearings. Because the parameter space is so large, however, only a very small subset of the possibilities were treated in this document. More complex shapes that take advantage of the microfabrication characteristics should be investigated. For machines that spend the majority of their time at a single operating point, the idea of inverse design, where the shape is tailored to produce a desired pressure distribution, may also be useful.

Varying the rotor (as opposed to the bearing) shape, which was entirely neglected in this document, also merits investigation, particularly in view of Fleming and Hamrock's finding that placing herringbone grooves on the rotating member was more effective than placing them on the stationary member [28]. In addition, reshaping both the bearing and rotor, such that the clearance etch is of uniform width, simplifies fabrication considerably and is therefore desirable even if the bearing performance does not improve. An experimental investigation of startup issues may be required in this case.

Third, the load / imbalance duality proposed in this work offers great promise for dealing with possibly large imbalances in microdevices. Issues of starting such a bearing hydrodynamically were not addressed in the current work, however. As shown by Orr [34], this issue may be circumvented via the hydrostatic mechanism of Sec. 5.2. In some devices, such as turbomachines where the bearing supply pressure is provided by the compressor, a hydrostatic startup is not possible without external equipment. The difficulties inherent in hydrodynamic startup should therefore be investigated to enable the design tradeoffs to be made.

Finally, the development of BASICS, or a similar tool that does not rely on lubrication assumptions, should be pushed forward to provide insight into thermal effects on bearings in the MIT microengine. Conditions for the formation of Taylor vortices, or large-scale turbulence, should be examined more quantitatively than was possible in this document because such an investigation may open design space in terms of increased C/R.

Appendix A

Analysis Example

In this appendix, a quantitative example is presented to demonstrate the application of various charts presented in this document and the interaction of various considerations.

For circular, cylindrical bearings near the MIT microengine's design point, a series of densely-populated charts are provided in Appendix C of Orr [34]. In that work, load parameter and attitude angle versus bearing number and minimum eccentricity charts, of the type employed in this appendix, are provided for $0.075 \leq L/D \leq 0.125$ in steps of 0.005.

The baseline parameters to be used in this example are shown below:

$$\begin{aligned} R &= 2mm \\ C &= 10\mu m \\ L &= 300\mu m \\ P_a &= 101325Pa \\ \mu &= 1.8 \times 10^{-5} Pa \cdot s \\ m &= 1 \times 10^{-5} kg \\ \omega &= 210,000 rad/s \end{aligned}$$

which yield the following nondimensional parameters:

$$\begin{aligned} L/D &= 0.075 \\ \bar{M} &= 0.5 \\ \zeta_g &= 0.0008 \\ \Lambda &= 9 \end{aligned}$$

With the above parameters, the minimum stable eccentricity at the design point, as well as during acceleration to this point, can be obtained from the minimum eccentricity chart, described in Sec. 3.2.1. The minimum eccentricity chart for this case is shown in Fig. A.1. On this chart, the operating line during acceleration is indicated by a dashed line, assuming only ω changes during acceleration.

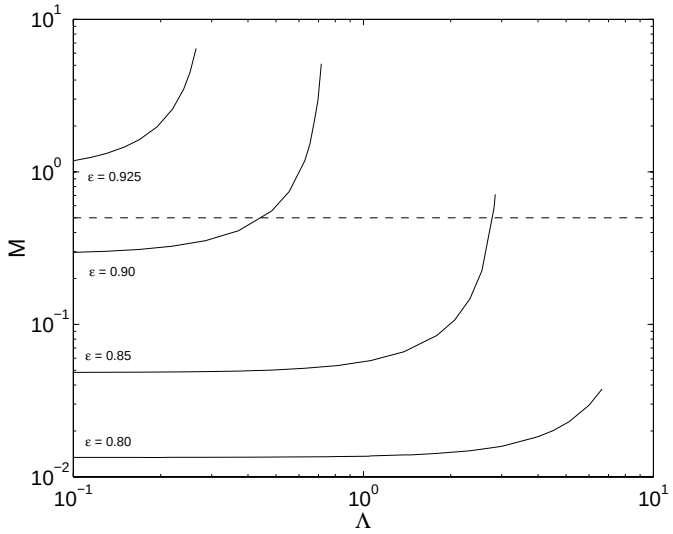

Figure A.1: Minimum eccentricity chart for example case. The operating line during startup is indicated by a dashed line (- - -).

From Fig. A.1 the eccentricity at the design point is approximately 80% and the worst-case (low speed) eccentricity is approximately 91%. The minimum separation between solid surfaces anywhere on the operating line is therefore:

$$(1 - 0.91)10\mu m = 0.9\mu m \tag{A.1}$$

Assuming, for the time being, that this distance is acceptable, the load schedule, used to guarantee the minimum eccentricity at each speed along the operating line, is then constructed. To construct this chart, the ϵ_{min} contour intersecting the operating line at each Λ is determined from Fig. A.1. The load parameter (and attitude angle) associated with each Λ-ϵ pair may then be obtained from the steady-state performance charts, such as those presented in Sec. 3.1.1. The charts for the example case are presented in Fig. A.2 and the resulting load schedule is presented in Fig. A.3.

Assuming the load is to be applied with side-pressurization from two plena of equal size, the pressure schedule may now be constructed. Further assuming that the low side plenum is held at P_a, as is the opposite end, a rearranged two-plenum version of Eq. 5.2 is employed to generate Fig. A.4 from Fig. A.3:

$$\frac{P_H}{P_a} = 2\zeta + 1 \tag{A.2}$$

Two traces are included on Fig. A.4: one for the vertical (non gravity-loaded) rotor case and one for the horizontal (fully gravity-loaded) case. The difference between these cases is simply whether or not ζ_g is subtracted from the required ζ before computing the pressures. As noted elsewhere in this document, the rotor weight is slight with respect to

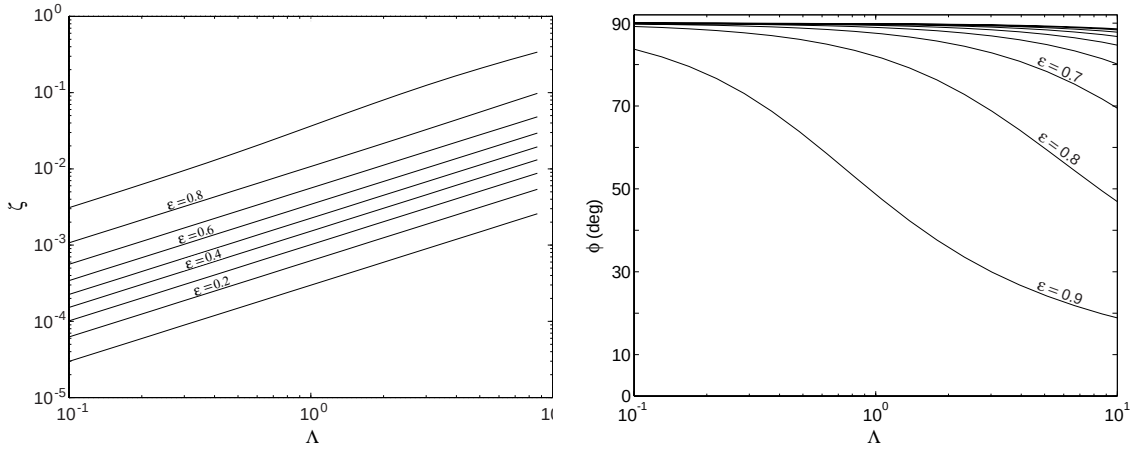

(a) Load Parameter **(b)** Attitude Angle

Figure A.2: Steady-state performance charts for example case.

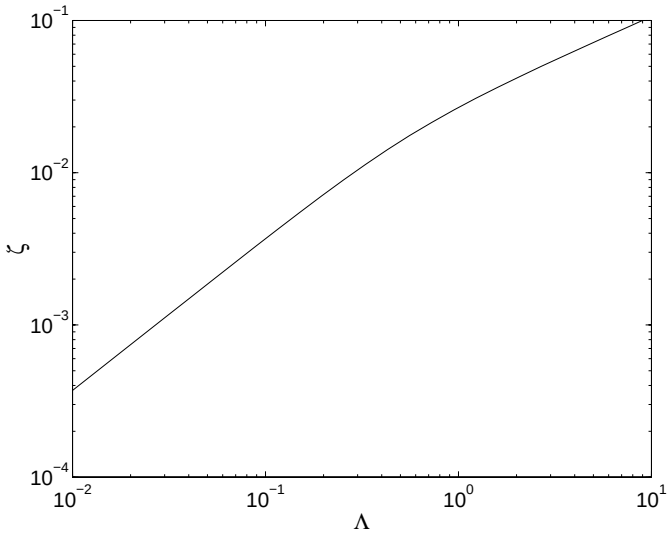

Figure A.3: Load schedule for example case.

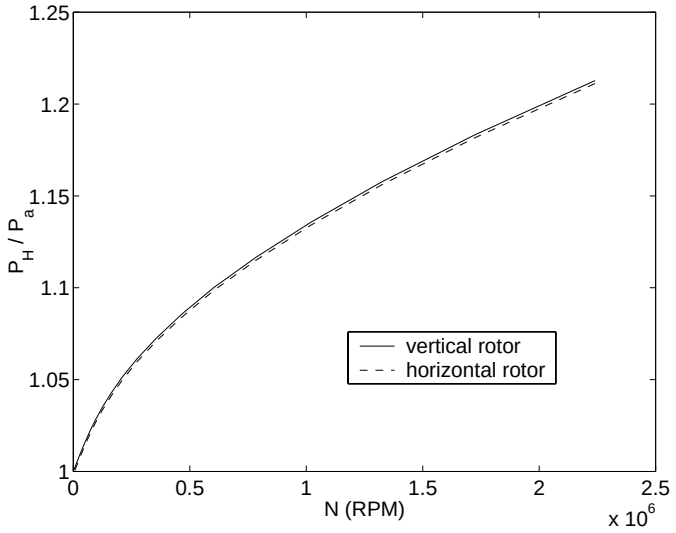

Figure A.4: Pressure schedule for example case.

the required load at most speeds, so there is little difference between the two cases.

Now, to correct for taper, the linear estimate of Eq. 4.9 is applied to each eccentricity on the operating line and a new load is calculated. For example, assuming the clearance reaches $11\mu m$ at one end and the shape is nearly linear, the taper level is $(11-10)/10 = 0.1$. Equation 4.9 then predicts a minimum eccentricity increment of $\Delta\epsilon_{min} = 0.4(0.1) = 0.04$. The worst-case minimum eccentricity then becomes $e_{min} = 0.91 + 0.04 = 0.95$. Similarly, the minimum eccentricity at the design point becomes 84%.

Because the adjusted worst-case eccentricity is large enough to arouse concern about the near-wall effects demonstrated in Sec. 4.2.3, a simulation with taper was run to confirm the adjusted minimum eccentricity. The result

To adjust the load schedule, $\Delta\epsilon_{min}$ is first added to the eccentricities along the operating line. The steady-state taper estimator introduced in Sec. 4.2.2 is then applied to find the associated load parameter. In this scheme, the tapered bearing performance is estimated from that of an equivalent untapered bearing with clearance $\tilde{C}$, where:

$$\frac{\tilde{C}}{C} = 1 + 0.45(0.1) = 1.045 \tag{A.3}$$

Each $\Lambda - \epsilon$ operating point is then recalculated as an $\tilde{\Lambda} - \tilde{\epsilon}$ operating point, where:

$$\tilde{\Lambda} = \Lambda \left(\frac{C}{\tilde{C}}\right)^2 \tag{A.4}$$

$$\tilde{\epsilon} = \epsilon \left(\frac{C}{\tilde{C}}\right) \tag{A.5}$$

The resulting load and pressure schedules are shown in Fig. A.5 and Fig. A.6, respec-

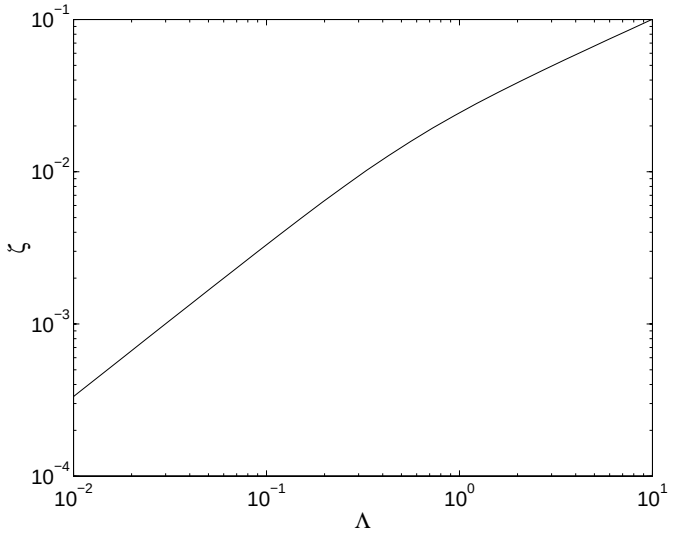

Figure A.5: Load schedule for example case with 10% taper.

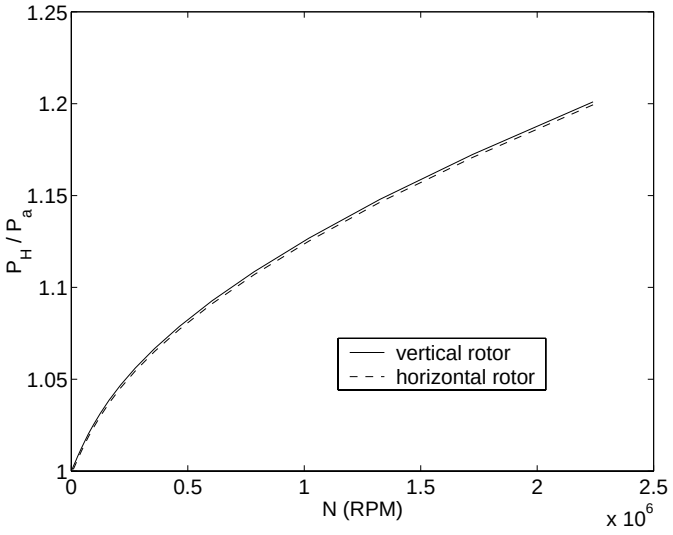

Figure A.6: Pressure schedule for example case with 10% taper.

tively. Notably, despite the fact that taper has increased the eccentricity along the operating line, the required load is actually slightly lower. This result is a consequence of the drastic loss of load capacity in tapered bearings.

Appendix B

Neglected Effects

This chapter examines the major assumptions inherent to the results presented in this document. For macro-scale bearings, this would be a short exercise because these assumptions are often easily justifiable. For microbearings, however, these assumptions are often called into question by an unusual geometry or application. For data presented in nondimensional form, which is the vast majority of this document, assumption breakdown emerges only when certain parameters, for example χ and C/R, are calculated for a given geometry. If these "watchdog" parameters indicate violation of an assumption, it does not mean that the data itself is invalid - it is questionable only when used for that particular case.

B.1 Inertia

When developing the Reynolds equation from the Navier Stokes equations (see, for example, Hamrock [12], Chapter 7), terms of order $(C/R)^2$ and $(C/L)^2$ are dropped. This operation eliminates all the viscous terms except the cross-channel shear stress gradient in the azimuthal and axial directions for the momentum equations in those directions.

For the vast majority of bearings, including microbearings, this is a good assumption. First, with deep-etching techniques, achieving a C/L of at least 1/20 is relatively routine. Second, due to the strong movement of $\bar{M}$ and Λ toward a more difficult position in terms of bearing stability when C/R increases, this ratio is often kept as small as practicable. It is therefore at least as small as C/L in most machines.

Under this assumption, the inertia terms are the smallest remaining members of the momentum equations. While the pressure, time, and shear gradients are order unity, these terms are multiplied by a parameter C/R times the Reynolds number based on clearance and the flow speed at the journal surface, $U = R\omega$. This quantity was introduced earlier as the inertial parameter, χ, where:

$$\chi = \frac{\rho U c}{\mu}\frac{C}{R} = \frac{\rho \omega c^2}{\mu} \tag{B.1}$$

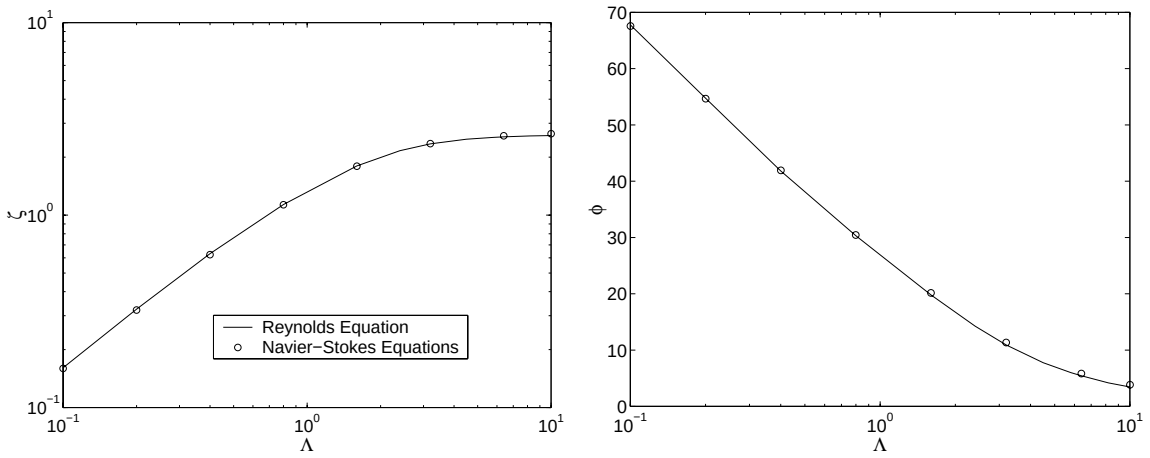

(a) Load Parameter **(b)** Attitude Angle

Figure B.1: Comparison of Navier-Stokes and Reynolds equation calculations for an infinite-length bearing with unity inertial parameter at 80% eccentricity over a range of bearing numbers. The error maxima are -2% for the load parameter and +9% for the attitude angle. The error generally increases with Λ.

Noting that χ is much smaller than unity for typical lubrication flows, the inertial terms are dropped and the Reynolds equation is derived based on the shear and pressure gradient terms alone.

For liquid-filled macro-bearings, due to the large viscosities of liquids, this is a good assumption because inertial parameters of order 10^{-4} are not unusual. For high speed, gas-filled macrobearing, χ is significantly larger, but not yet large enough to arouse concern. For example, an order-of-magnitude analysis assuming rotation rates in tens of thousands RPM and clearances in the tens of microns (single-digit mils) yields:

$$\chi = \frac{(1)(10^3)(10^{-5})^2}{(10^{-5})} = (10^{-2}) \tag{B.2}$$

In the microturbomachines currently being developed at MIT, however, the clearance is a similar order of magnitude as a good macrobearing, but the rotation rates are two orders of magnitude larger. The inertial parameter can therefore be order unity. Consequently, inertial terms have a potential for significant impact on the pressure distribution in these bearings because they reach a similar order of magnitude as the viscous and pressure terms.

The most direct way to measure the effect of the inertial terms is to include them in the governing equations. BASICS, described in Sec. 2.1, was written for this approach by solving the Navier-Stokes equations instead of the Reynolds equation. A BASICS result for infinite-length bearings at $\chi = 1$ and $\epsilon = 0.8$ is compared to a Reynolds equation solution in Fig. B.1.

In Fig. B.1, it may be seen that the error in calculating the steady-state parameters under the inertialess flow assumption is less than 10% for infinite bearings with $\Lambda < 10$. For all cases, the inclusion of inertia decreased ζ and increased ϕ. Except for the highest ζ value, the trend is of increasing error with Λ for both ζ and ϕ.

The conclusion of small contributions to the steady-state variables from first-order inertial terms is supported by DiPrima and Stuart's [77] results for incompressible lubricant in infinite-length bearings. Their analytic method was a small parameter expansion in terms of variables functionally equivalent to C/R and χ. Their analysis could therefore provide corrections for both curvature and inertia.

Nataraj *et al.* [13] also found a negligible contribution of inertia to the steady state variables. Like DiPrima and Stuart, their analysis was a small-parameter expansion in C/R for incompressible lubricants, but it was derived for short bearings with cavitation. It was shown in Fig. 3.3 that this solution provides very good estimate for ζ for the very short bearings treated in this work at a surprisingly large range of ϵ and Λ. It should be noted, however, that this solution does not provide a good estimate for the attitude angle.

Because it retains time derivatives in its momentum equations, the analysis of Nataraj *et al.* is also capable of modeling unsteady effects. Changes in the stiffness and damping coefficients due to inertia were presented in [13]. As with the steady-state parameters, the authors conclude that the changes in coefficients are not very large and could be neglected for the Reynolds numbers they studied, which were as large as 1000. Both steady and unsteady variables for finite-length incompressible bearings are therefore shown to change very little for order-unity inertial parameters.

A straightforward solution to the problem of adding inertial effects to a finite-length compressible gas bearing was presented by Banerjee *et al.* [78] in a "predictor-corrector" framework. In this scheme, the Reynolds equation is solved and the velocity components are recovered from the continuity and inertialess momentum equations. These components are then used to construct inertia terms for the momentum equations. Treating these terms as constants, the momentum equations may be integrated across the clearance as in the standard Reynolds equation development. The resulting Reynolds equation is then solved for the "corrected" pressure in the presence of extra terms from the "predictor" step. If additional accuracy is required, the process can be repeated, through either a more complex equation or an iteration on the current scheme.

Banerjee *et al.* then show that the effect of inertia for an incompressible short bearing is always to increase the net load capacity. Performing calculations for finite-length incompressible bearings with this method, Chen and Chen [79] show that the inertial increase to the load capacity at $\chi = 1.4$ is strongest at moderate eccentricity, but still reaches only 2.1% for an $L/D = 0.5$ bearing at $\epsilon = 0.5$. This peak is only 1.5% for the $L/D = 1$ bearing. Moreover, Chen and Chen show that the side leakage flow rate increases due to inertia. The trends for leakage are quite different than for load capacity. The leakage was shown

to increase with L/D and eccentricity but, again, reached only 3% in the worst case.

While Banerjee *et al.* assume an incompressible bearing later in their paper, which was also assumed by Chen and Chen, their general result is valid for compressible flows. Furthermore, though their analysis neglects the unsteady term in the continuity equation, this term may be added relatively easily because the output from the predictor step is used to recover velocities in terms of pressures. These velocities are carried through the integration to yield velocities at the corrector step which are then inserted into the spatial derivative terms in the continuity equation to produce the Reynolds equation. The time term escapes modification because involves only the density at the corrector time level.

If the time derivative terms in the momentum equations are retained, however, many complications arise in this method. Retention of the time terms is considered necessary if the "squeeze number" is non-negligible:

$$\sigma_s = \frac{\rho c^2}{t_o \mu} \tag{B.3}$$

where t_o is a reference time. If the inverse rotational frequency is used for the reference time, which is a reasonable choice for journal bearings, the squeeze number becomes identical to the inertial parameter. It is thus appropriate to keep the temporal terms in the momentum equations. Unfortunately, this addition causes the corrector-step velocities to contain mixed second derivatives with temporal and spatial components, which considerably complicates the recovery of needed information from the predictor step.

Because many previous researchers have found that order-unity inertial parameters have negligible impact on both the steady and unsteady bearing performance for incompressible flow, and BASICS supports this conclusion for steady flow in infinite-length compressible bearings, it is unlikely that the effort required to negotiate these complications is worthwhile. Not only is compressibility unlikely to significantly worsen the problem for finite-length bearings, but the very short bearings treated in this work behave largely as incompressible bearings due to their large side-leakage.

B.2 3-D Vortices

A literature search for Couette flow between rotating cylinders yields a surprising quantity of papers for a problem whose incompressible case can be solved analytically and whose compressible case is easily treated numerically with finite difference techniques. Closer inspection reveals that the interest centers around a secondary flow that appears in the form of toroidal vortices under certain conditions. Such a flow is known as "Taylor-Couette" flow because the first successful treatment of this problem was due to Taylor [80], who showed that vortices appear in concentric cylinders when a quantity, now known as the

"Taylor number" and given by:

$$Ta = \frac{\rho^2 R \omega^2 C^3}{\mu^2} \tag{B.4}$$

reaches a critical value of approximately 1700.

From a journal bearing perspective, the formation of these vortices is important because they are a large-scale feature in the flowfield that is not represented in the Reynolds equation. Furthermore, the vortices themselves can be unstable and lead to fully-turbulent flow. Though modeling turbulent bearings is possible, it involves the use of empirically-derived constants, leading to considerable uncertainty [81]. Moreover, turbulent bearings have a larger drag and thus increased power consumption.

The infrequent appearance of these vortices in conventional bearings can be explained if the Taylor number is re-expressed in terms of quantities used elsewhere in this document:

$$Ta = \chi^2 \frac{R}{C} \tag{B.5}$$

Thus, for conventional bearings where C/R is on the order of $1/1000$, the Taylor number reaches the critical value only if χ becomes order unity. As shown in the previous section, however, χ is typically orders of magnitude smaller than unity for conventional bearings.

Remembering that χ was shown to be of order unity for microturbomachine bearings, Eq. B.5 appears to indicate that Taylor vortices will form in these devices. Fortunately, three characteristics of these bearings act to prevent such formation: larger C/R, large ϵ, and compressibility.

First, microbearings tend to have C/R of order 10^{-2} instead of 10^{-3} due to an interplay of design constraints outlined in Sec. 1.3. This order-of-magnitude increase C/R raises the threshold χ for the initiation of Taylor vortices by a factor of $\sqrt{10}$, or slightly more than 3.

Second, the critical Taylor number of 1700 was obtained for concentric cylinders. As shown in Chap. 3, however, hydrodynamic journal bearings must be displaced to some eccentricity to avoid whirling. The effect of this displacement on Ta_{crit} has been the subject of experiments and several analytic efforts, four of which are compared in Fig. 9-3.1 in Gross *et al.* [82]. From this figure, where their Taylor number is the square root of the version used in this document, it can be seen that operating at eccentricities above 80%, which is usually a necessity for microbearings, increases the critical Taylor number by approximately a factor of two.

Third, Hatay *et al.* [83] showed that compressibility has a stabilizing effect if the gap spacing is "small." In their work, "small" was defined as a ratio of outer cylinder radius to inner cylinder radius of 0.82. In the nomenclature of this document, this corresponds to $1-C/R < 0.82$, a condition which is met by almost any practical journal bearing.

Finally, Hatay *et al.* [83] also showed that heat flux from the outer to the inner cylinder has a stabilizing effect on the flow. In the MIT microengine, where the combustor surrounds the bearing, Ta_{crit} will therefore be increased.

In sum, despite the order-unity inertial parameter typical of microbearings, it is unlikely that Taylor vortices will form due to several factors that increase the critical Taylor number.

B.3 Temperature Variation

Most bearing analysis tools, including SPECTRES, assume isothermal flow. This assumption enables temperatures that appear when densities are replaced with pressures via the ideal gas law to be brought outside the derivatives and canceled, leaving the Reynolds equation with pressure as the sole dependent variable. Moreover, assumption of constant temperature removes the energy equation from the system and allows viscosity to be brought outside integrals and derivatives.

Toward developing a straightforward method for assessing the importance of temperature variation, Elrod and Burgdorfer [44] derived an estimate for the maximum temperature at the point of maximum pressure in an infinite-length bearing. This choice of location causes the pressure gradient to vanish and considerably simplifies the equations. A closed-form temperature estimate can then be derived:

$$\frac{T_{max} - T_w}{T_w} \leq \frac{\gamma - 1}{2} Pr M^2 \simeq \frac{M^2}{6} \tag{B.6}$$

where T_w is the wall temperature of both journal and bearing and M is the Mach number at the journal surface. Pr is the Prandtl number and γ is the ratio of specific heats, which are 0.72 and 1.4, respectively, for air.

Elrod and Burgdorfer note that this equation does not contain information as to the maximum temperature anywhere in the bearing. It does, however, give a maximum at a very important point which, they argue, should be indicative of values occurring elsewhere in the film.

To test this estimate, a sample bearing temperature distribution from BASICS is presented in Fig. B.2. In this case, ϵ=0.8, Λ=0.8, M=0.31, Re=1000, κ=0.001, and χ=1.0. The gap is greatly exaggerated for visibility and the figure is oriented such that the load points vertically downward. The temperature at the journal and bearing walls were set equal and the distribution is normalized by the wall value.

The appearance of this distribution is somewhat typical of bearing flows. Notably, the temperature and pressure maxima do not coincide. This observation may be understood in the context of isothermal walls: the point of maximum pressure is near the point of minimum height, where the walls are best able to remove heat from the fluid volume. The temperature maximum is therefore found upstream of the minimum height where the fluid is being compressed but the walls are further apart. In addition, the maximum temperature does not occur in the channel center; it occurs closer to the journal surface, where energy is being added to the fluid via viscous work.

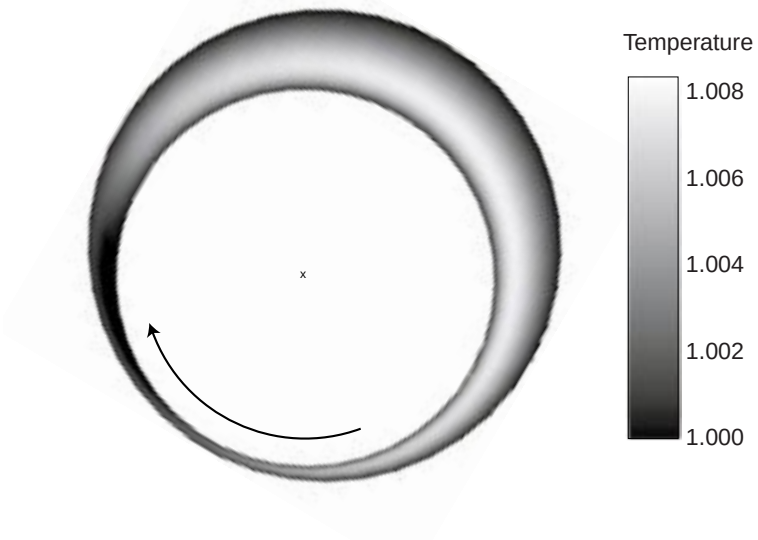

Figure B.2: Temperature distribution for an infinite-length bearing at 80% eccentricity with a tangential Mach number of 0.31.

For these conditions, Eq. B.6 yields $T_{max}/T_w \leq 1.013$ whereas the BASICS result is $T_{max}/T_w \simeq 1.0085$. Elrod and Burgdorfer's estimate therefore appears to yield a very pessimistic upper bound for the T_{max} at P_{max} and, moreover, a pessimistic upper bound for the temperature maximum in the entire bearing.

A second temperature distribution, this time for operating point of an early MIT microengine is shown in Fig. B.3 as a more extreme example. In this case, ϵ=0.6, Λ=3.5, M=1.09, Re=577, κ=0.005, and χ=2.9. The pressure distribution from this case was shown previously in Fig. 2.4.

In this case, Elrod and Burgdorfer's temperature estimate is $T_{max}/T_w \leq 1.17$ while the BASICS result is $T_{max}/T_w \simeq 1.07$. Again, the estimated maximum was pessimistic by approximately a factor of two for the global maximum.

In a microengine, taking the Elrod and Burgdorfer estimate as an upper bound and assuming the rotor speed is held near Mach 1 to maximize the compressor pressure ratio, the temperature variation will be less than 15% through the bearing. Assuming μ has 2/3 power-law dependence on temperature, a viscosity variation of less than 10% should therefore be seen.

This estimate is very pessimistic, not only in the context of the findings presented above with regard to Elrod and Burgdorfer's result, but also because the finite bearing will have significant axial massflow which will act to reduce the maximum temperature. Furthermore, side-loading via axial pressure gradients will increase the massflow. With this situation in mind, thermal effects originating from the bearing operation are unlikely to be significant.

A complication exists in the MIT microengine: as noted previously, the combustor sur-

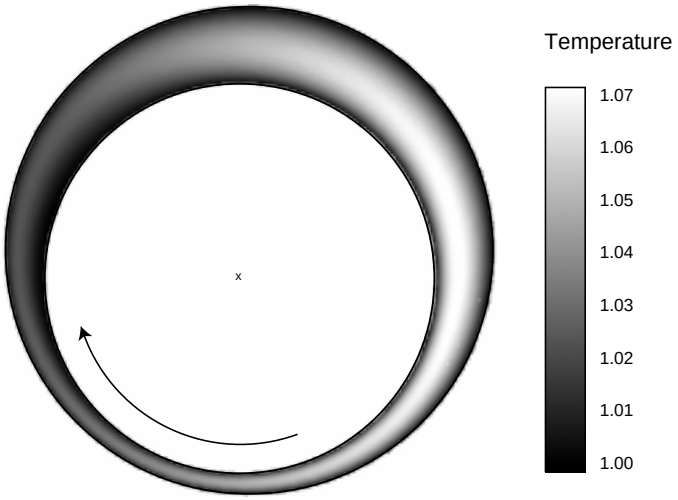

Figure B.3: Temperature distribution for an infinite-length bearing at 60% eccentricity with a tangential Mach number of 1.09.

rounds the bearing. The bearing temperature could therefore be significantly higher than the journal temperature. If this proves to be the case, the thermal effect on bearing performance should be evaluated. Equations for this type of analysis was derived by Kao [84] by including the energy equation in the set before invoking the lubrication assumptions and constructing the governing equations.

B.4 Rarefaction

The Navier-Stokes equations, on which the Reynolds equation is based, computes molecular-scale transport phenomena, such as shear stress, from macroscopic mean variables, such as flow speed. For this technique to be useful, the macroscopic mean must be taken over a volume large enough to contain a statistically sufficient number of molecules, but small enough to capture the flow features of interest. The applicability of this method is thus indicated by the ratio of the mean distance a molecule travels between collisions, known as the mean free path, λ, to a characteristic length in the flowfield, H. This ratio is known as the "Knudsen number" and given by:

$$Kn = \frac{\lambda}{H} \tag{B.7}$$

For journal bearings, H can be taken as the channel height. The mean free path is a function of pressure and temperature:

$$\lambda = \frac{kT}{P\pi\sqrt{2}\sigma^2} \tag{B.8}$$

where k is Boltzmann's constant and σ is the molecular diameter [85].

Based on the Knudsen number, flows may be divided into three categories [86] : If $Kn < 0.01$, the Reynolds equation may be used without modification. If $0.01 < Kn < 0.1$, the Reynolds equation must be redeveloped from the Navier-Stokes equations with a nonzero velocity, known as the slip velocity, at the wall. If $Kn > 0.1$ the continuum representation of the fluid is usually replaced by its molecular counterpart.

Air at standard conditions has a mean of approximately $50\,nm$, so the Reynolds equation may be applied without considering rarefaction if the gap size is greater than approximately $5\mu m$. In a journal bearing running at high eccentricity, however, the channel height may be a fraction of a micron at the location of closest approach. Fortunately, the inverse dependence of Eq. B.8 on pressure prevents rarefaction from becoming an issue in this case because the pressure is elevated significantly at the minimum channel height when running at high eccentricity. The mean free path is thus reduced and rarefaction remains unimportant. Even if Kn is not negligible in this case, the region for which rarefaction is significant is a small portion of the total bearing circumference so it is unlikely to have a notable impact on the overall flowfield.

In a turbomachine, the overall pressure levels tend to be high, so the mean free path will be reduced. In an engine, however, elevated temperatures may reduce, or even reverse this gain. The importance of rarefaction should therefore be reevaluated if the cycle changes significantly.

B.5 Curvature

Though C/R is often viewed in terms of its effect on χ, it appears by itself in several key places in the Reynolds equation development. First, the viscous terms of order $(C/R)^2$ are dropped from the Navier-Stokes equation before χ is introduced to eliminate inertial terms. Second, the channel height is taken to be:

$$h = 1 + \epsilon \cos(\theta) \tag{B.9}$$

whereas the full expression is actually [82]:

$$h = 1 + \epsilon \cos\theta + \frac{R}{C}\left[1 - \left(1 - \sqrt{\epsilon^2 \left(\frac{C}{R}\right)^2 \sin^2\theta}\right)\right] \tag{B.10}$$

Finally, the equations are written in a Cartesian system despite the fact that the geometry is cylindrical. The passage between the journal and bearing is thus "unwrapped" to a linear, varying height channel with the argument that the radius of curvature is large with respect to the channel height, or, again, that C/R is small.

As noted previously, C/R can be of order 10^{-2} for microfabricated bearings, which is an order of magnitude larger than typically seen in macro-scale bearings. During design

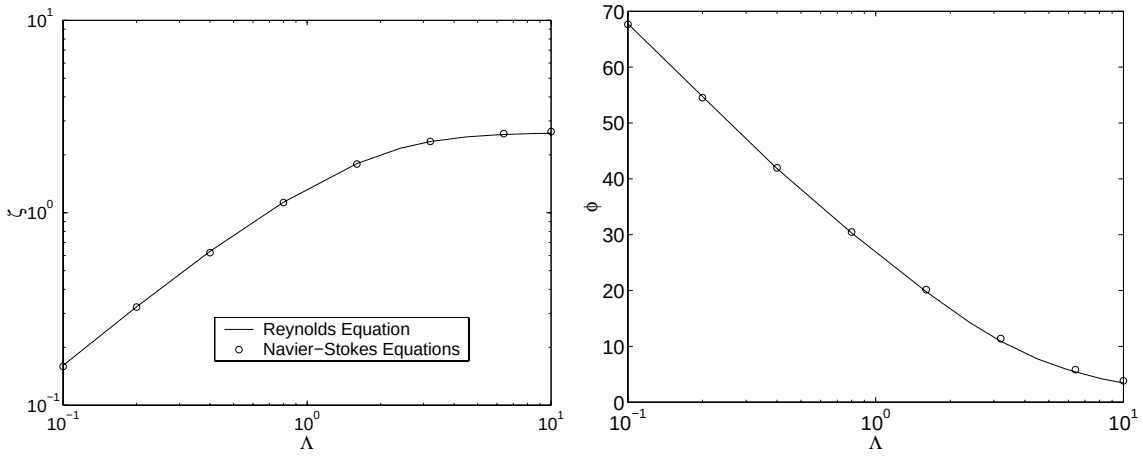

(a) Load Parameter **(b)** Attitude Angle

Figure B.4: Comparison of Navier-Stokes and Reynolds equation calculations for an infinite-length bearing with unity inertial parameter and $C/R = 1/200$ at 80% eccentricity over a range of bearing numbers. No discernible additional error is incurred over the $\chi = 1$, $C/R = 1/1000$ case of Sec. B.1.

iterations, this ratio may increase as the radius is reduced to improve stability via larger L/D (see Fig. 3.13), reduce drag via to smaller circumferential area, or increase the number of devices on a wafer.

In Fig. B.1, the inertial parameter was set to unity while the clearance ratio was held at $1/1000$ to ensure that the observed effects were strictly due to inertia. In Fig. B.4, a similar calculation is performed to evaluate the additional effect of curvature. In this case, the inertial parameter is held at unity and the clearance ratio is increased by a factor of five to $1/200$.

Comparing Figs. B.1 and B.4, it can be seen that little or no additional error is incurred by the increase in C/R. Curvature effects, in isolation from inertial effects, are therefore not likely to be an issue.

B.6 Summary

The impact of several effects commonly neglected in bearing analyses was discussed. These effects are often easily ruled negligible for macro bearings based on certain nondimensional parameters falling into theoretical or empirical ranges. In this case, the nondimensional results presented in this document may be dimensionalized and applied without adjustment. For microfabricated bearings, however, several parameters can exceed the accepted range. The effects they measure must therefore be examined to establish their importance before using results computed without them.

The most glaring boundary-crossing was the nondimensional parameter measuring

the importance of fluid inertia. The lubrication equations are developed by eliminating inertia terms from the nondimensional momentum equations because they are multiplied by an "inertial parameter," χ, while the retained terms are order unity. For macro bearings, χ is usually of order 10^{-3}. For microbearings, however, χ is of order unity. Based on the results of BASICS and several published works it was shown that the inertial effect was negligible for order-unity χ.

Another complication of an order-unity inertial parameter is, due to its close relationship with the Taylor number, it exceeds the value commonly quoted for the formation of toroidal vortices in a rotating Couette flow, of which journal bearings are a special case. Again, by a careful examination of the literature, it was shown that Taylor vortices are not likely to form because the critical Taylor number is increased by compressibility and by running at large eccentricity.

Of the neglected effects, only thermal variation could not be so handily dismissed. This variation is likely unimportant if the journal and bearing surfaces are held at the same temperature but the effect may be significant if heat is flowing through the lubricant. This is a likely situation in the MIT microengine because the bearing is surrounded by a combustor. In this case, thermal effects on the bearing performance should be evaluated, either through BASICS or by a lubrication analysis that does not assume isothermal flow, such as that of Kao [84].

References

[1] F. Dimofte, H. Addy, and Walker J. Preliminary experimental results of a three wave journal air bearing. In *Proceedings of Advanced Earth-to-Orbit Propulsion Technology Conference*, pages 375–384, Marshall Space Flight Center, Huntsville, AL, May 1994. NASA CP 3282, Vol II.

[2] A.H. Epstein, S.D. Senturia, G. Anathasuresh, A. Ayón, K.S. Breuer, K-S Chen, F.E. Ehrich, E. Esteve, L. Frechette, G. Gauba, R. Ghodssi, C. Groshenry, S. Jacobson, J.L. Kerrebrock, J.H. Lang, C-C Lin, A. London, J. Lopata, A. Mehra, J.O Mur Miranda, S. Nagle, D.J. Orr, E.S. Piekos, M.A. Schmidt, G. Shirley, S.M. Spearing, C.S. Tan, Y-S Tzeng, and I.A. Waitz. Micro-heat engines, gas turbines, and rocket engines - the MIT microengine project-. AIAA 97-1773, 28th AIAA Fluid Dynamics Conference, Snowmass Village, CO, Jun 1997.

[3] C.C. Lin. *Development of a Microfabricated Turbine-Driven Air Bearing Rig*. Ph.D. dissertation, Massachusetts Institute of Technology, Department of Mechanical Engineering, June 1999.

[4] T.G. Wiegele. Micro-turbo-generator design and fabrication; a preliminary study. In *Proc. of 31st Intersociety Energy Conversion Engineering Conference*, volume 4, pages 2308–2313, Washington, DC, August 11-16, 1996.

[5] H. Guckel, T.R. Christenson, K.J. Skrobis, T.S. Jung, J. Klein, K.V. Hartojo, and I. Widjaja. A first functional current excited planar rotational magnetic micromotor. In *IEEE Micro Electro Mechanical Systems*, pages 7–11, Fort Lauderdale, FL, February 7-10, 1993.

[6] S.L. Miller, J.J. Sniegowski, G. LaVigne, and P.J. McWhorter. Friction in surface micromachined microengines. In *Proceedings of the Smart electronics and MEMS Conference*, pages 197–204, San Diego, CA, Feb. 28-29, 1996. SPIE.

[7] J. O. Mur Miranda. Feasibility of electrostatic bearings for micro turbo machinery. M.Eng. thesis, Massachusetts Institute of Technology, Department of Electrical Engineering and Computer Science, December 1997.

[8] H. C. Rothe. Air bearings for guidance components of ballistic missiles and their production aspects. In *First Int. Symp. Gas-Lubricated Bearings*, page 68, Washington, D.C., October 1959.

[9] A large tank of liquid helium for nuclear experiments. *New Scientist*, (325):277, 1963.

[10] G.L. Agrawal. Foil air / gas bearing technology - an overview. ASME 97-GT-347, International Gas Turbine & Aeroengine Congress & Exhibition, Orlando, FL, June 1997.

[11] A.A. Raimondi. A numerical solution for the gas lubricated full journal bearing of finite length. *ASLE Transactions*, 4:131–155, 1961.

[12] B.J. Hamrock. *Fundamentals of Fluid Film Lubricaton*. McGraw-Hill Series in Mechanical Engineering. McGraw-Hill, Inc., New York, 1994.

[13] C. Nataraj, H. Ashrafiuon, and N.K. Arakere. Effect of fluid inertia on journal bearing parameters. *Tribology Trans.*, 37:784–792, 1994.

[14] O. Reynolds. On the theory of lubrication and its application to Mr. Beuchamp Tower's experiments, including an experimental determination of the viscosity of olive oil. *Philos. Trans. R. Soc.*, 177:157–234, 1886.

[15] G. Belforte, T. Raparelli, and V. Viktorov. Theoretical investigation of fluid inertia effects and stability of self-acting gas journal bearings. *Journal of Tribology*, 121:836–843, 1999.

[16] H.S. Cheng and C.H.T. Pan. Stability analysis of gas-lubricated, self-acting, plain, cylindrical, journal bearings of finite length, using Galerkin's method. *J. Basic Engineering*, 87(1):185–192, March 1965.

[17] C.W. Ng. Linearized PH stability theory for finite length, self-acting gas-lubricated, plain journal bearings. *Journal of Basic Engineering*, 0:559–567, September 1965.

[18] J.S. Ausman. On the behavior of gas-lubricated journal bearings subjected to sinusoidally time-varying loads. *J. Basic Engineering*, pages 589–603, September 1965.

[19] C.H.T. Pan. Spectral analysis of gas bearing systems for stability studies. In T.C. Huang and M.W. Johnson, Jr, editors, *Proc. Ninth Midwestern Mechanics Conference*, volume 3 of *Developments in Mechanics*, pages 431–447, Madison, WI, Aug. 16-18 1965. John Wiley and Sons, Inc.

[20] G.M. Rentzepis and B. Sternlicht. On the stability of rotors in cylindrical journal bearings. *Journal of Basic Engineering*, 84(3):521–532, December 1962.

[21] C.H.T. Pan and B. Sternlicht. Comparison between theories and experiments for the threshold of instability of rigid rotor in self-acting, plain-cylindrical journal bearings. *J. Basic Engineering*, 86:321–327, June 1964.

[22] A.A. Ayón, K.-S. Chen, K.A. Lohner, S.M Spearing, H.H. Sawin, and M.A. Schmidt. Deep reactive ion etching of silicon. Invited presentation, Materials Research Society Fall Meeting, Boston, MA, Nov 30 - Dec 4, 1999.

[23] Y.B. Gianchandani and K. Najafi. Micron-sized, high aspect ratio bulk silicon micromechanical devices. In *Proc. Fifth IEEE Workshop of Micro Electro Mechanical Systems*, pages 208–213, Travemünde, Germany, 4-7 February 1992.

[24] W.H. Juan and S.W. Pang. High-aspect-ratio Si etching for microsensor fabrication. *Journal of Vacuum Science and Technology A*, 13(3):834–838, 1995.

[25] F. Lärmer and A. Schilp. Method of anisotropically etching silicon. U.S. Patent 5501893, Robert Bosch, Gmbh, 1996.

[26] D.B. Reynolds and W.A. Gross. Experimental investigation of whirl in self-acting air-lubricated journal bearings. *ASLE Transactions*, 5:392–403, 1962.

[27] D.D. Fuller. A review of the state-of-the-art for the design of self-acting gas-lubricated bearings. *J. Lubrication Technology*, 91(1):1–16, January 1969.

[28] D.P. Fleming and B.J. Hamrock. Optimization of self-acting herringbone journal bearing for maximum stability. In *Proc. of the 6th Gas Bearing Symposium*, pages c1–1 – 12, Southampton University, March 1974.

[29] F.R. Archibald and B.J. Hamrock. The Rayleigh step bearing applied to a gas-lubricated journal of finite length. *Journal of Lubrication Technology*, 89(1):38–46, January 1967.

[30] Florin Dimofte. Wave journal bearing with compressible lubricant – part I: The wave bearing concept and a comparison to the plain circular bearing. *Tribology Trans.*, 38(1):153–160, 1995.

[31] J.L. Kerrebrock. *Aircraft engines and gas turbines*. MIT Press, Cambridge, first edition, 1977.

[32] A. Padmanabhan, M. Sheplak, and K.S. Breuer M.A. Schmidt. Micromachined sensors for static and dynamic shear-stress measurements in aerodynamic flows. In *IEEE Transducers '97 Conference*, Chicago, IL, June 1997.

[33] MESA – Sandia's largest project ever – wins DOE nod. Sandia National Laboratories News Release, September 21, 1999.

[34] D.J. Orr. *Macro-Scale Investigation of High Speed Gas Bearings for MEMS Devices*. Ph.D. dissertation, Massachusetts Institute of Technology, Department of Aeronautics and Astronautics, February 2000.

[35] J.S. Ausman. The fluid dynamic theory of gas-lubricated bearings. *Trans. ASME*, 79:1218–1224, 1957.

[36] J.S. Ausman. An improved analytical solution for self-acting, gas-lubricated journal bearings of finite length. *J. Basic Engineering*, 83(2):188–194, 1961.

[37] W.A. Gross and E.C. Zachmanoglou. Perturbation solutions for gas-lubricating films. *Journal of Basic Engineering*, pages 139–144, June 1961.

[38] F. Dimofte. Fast methods to numerically integrate the Reynolds equation for gas fluid films. NASA Technical Memorandum 105415, NASA Lewis Research Center, 1992.

[39] H.S. Cheng and P.R. Trumpler. Stability of the high speed journal bearing under steady load 2. the compressible film. *Journal of Engineering for Industry*, 85:274–280, 1963.

[40] S.A. Jacobson. Personal communication.

[41] V. Castelli and H.G. Elrod. Solution of the stability problem for 360 deg. self-acting, gas-lubricated bearings. *J. Basic Engineering*, 87(1):199–212, March 1965.

[42] S.H. Crandall. The instability mechanism responsible for oil whirl and oil whip. In *Proceedings of the Fourth Greek National Congress on Mechanics*, pages 659–672, Democritus Univ. of Thrace, Xanthi, 1995.

[43] H. Hashimoto, S. Wada, and M. Sumitomo. The effects of fluid inertia forces on the dynamic behavior of short journal bearings in the superlaminar flow regime. *J. Tribology*, 110:539–547, July 1988.

[44] H.G. Elrod, Jr. and A. Burgdorfer. Refinements of the theory of the infinitely-long self-acting gas-lubricated journal bearing. In *Proc. First Annual International Symposium on Gas-Lubricated Bearings*, pages 93–118, Washington, D.C., October 1959. Superintendant of Documents, U.S. Government Printing Office.

[45] W.J. Harrison. The hydrodynamical theory of lubrication with special reference to air as a lubricant. *Trans. Cambridge, Philosophical Society*, 22:39–54, 1913.

[46] F.M. White. *Viscous Fluid Flow*. McGraw-Hill, New York, NY, 2 edition, 1991.

[47] C. Tan, Y. Tzeng, I. Waitz, R. Walker, D.J. Orr, S. Senturia, A. Ayón, J. Mur Miranda, E. Piekos, C. Lin, A. Epstein, M. Spearing, G. Anathasuresh, K. Breuer, K.-S. Chen, F. Ehrich, E. Esteve, G. Gauba, S. Jacobson, J. Lang, A. Mehta, S. Nagle, and M. Schmidt. Micro gas turbine generators. Interim Progress Report 33888CH-MUR, U.S. Army Research Office, Research Triangle Park, NC, January 1997.

[48] J.P. Boyd. Chebyshev & fourier spectral methods. In C.A. Brebbia and S.A. Orszag, editors, *Lecture Notes in Engineering*, volume 49. Springer-Verlag, New York, 1989.

[49] S. Wolfram. *The Mathematica Book*. Wolfram Media, Inc., Champaign, IL, third edition, 1996.

[50] B.J. Hamrock. *Fundamentals of Fluid Film Lubricaton*, section 10.2, pages 230–234. McGraw-Hill, Inc., New York, 1994.

[51] E.S. Piekos and K.S. Breuer. Pseudospectral orbit simulation of nonideal gas-lubricated journal bearings for microfabricated turbomachines. *J. Tribology*, 121(3):604–609, July 1999.

[52] R.L. Coleman. A brief comparison of the accuracy of time-dependent integration schemes for the reynolds equation. *J. Lubrication Technology*, 94(4):331–334, October 1972.

[53] B. Sternlicht and L.W. Winn. On the load capacity and stability of rotors in self-acting gas lubricated plain cylindrical journal bearings. *J. Basic Engineering, Trans ASME, Series D*, 85:503–512, 1963.

[54] B. Sternlict and R.C. Elwell. Synchonous whirl in plain journal bearings. ONR Report 61GL37, General Electric Co., Schenectady, NY, January 1961.

[55] S.M. Spearing. Personal communication.

[56] J.W. Lund. Calculation of stiffness and damping properties of gas bearings. *J. Lubrication Technology, Transactions ASME*, 90:793–801, 1968.

[57] F. Dimofte. Effect of fluid compressibility on journal bearing performance. *Tribology Transactions*, 36(3):341–350, 1993.

[58] C.H.T. Pan and B. Sternlicht. On the translatory whirl motion of a vertical rotor in plain cylindrical gas-dynamic journal bearings. *Journal of Basic Engineering*, 84(1):152–158, March 1962.

[59] P. Hollis and D.L. Taylor. Hopf bifurcation to limit cycles in fluid film bearings. *ASME Journal of Lubrication Technology*, 108(2):184–189, April 1986.

[60] D. S. Wilson. The effect of geometry variations on hydrodynamic bearing performance. *ASLE Transactions*, 9:411–419, 1966.

[61] M.T.M Cooijmans, H.J.H Brouwers, D.H. van Campen, and A. de Kraker. Limit cycle predictions of a nonlinear journal-bearing system. *ASME Journal of Engineering for Industry*, 112:168–171, May 1990.

[62] F.W. Ocvirk. Short-bearing approximation for full journal bearings. NACA Technical Note 2808, Cornell University, October 1952.

[63] F.F. Ehrich. Sum and difference frequencies in vibration of high speed rotating machinery. *Journal of Engineering for Industry*, pages 181–184, February 1972.

[64] A.A. Ayón, R. Braff, C.C. Lin, H.H. Sawin, and M.A. Schmidt. Characterization of a time multiplexed inductively coupled plasma etcher. *Journal of the Electrochemical Society*, 146(1):339–349, January 1999.

[65] Florin Dimofte. Wave journal bearing with compressible lubricant – part II: A comparison of the wave bearing with a wave-groobe bearing and a lobe bearing. *Tribology Trans.*, 38(2):364–372, 1995.

[66] M. Lavender. Some practical results on the stability of noncircular aerodynamic journal bearings. In *Proceedings of the Gas Bearing Symposium*, University of Southampton, April 1967.

[67] Florin Dimofte. Wave journal bearing – part I: Analysis. Contractor Report 195431, Lewis Research Center, Toledo, Ohio, January 1995.

[68] A.A. Ayón. Personal communication.

[69] O.C. Brewster. High speed rotor. US Patent 2,603,539, July 1952.

[70] C.C. Lin, R. Ghodssi, A.A. Ayón, D.Z. Chen, S. Jacobson, K.S. Breuer, A.H. Epstein, and M.A. Schmidt. Fabrication and characterization of a micro turbine/bearing rig. presentation, MEMS '99, Orlando, FL, January 1999.

[71] K.S. Breuer. Personal communication.

[72] J.E.R. Coney and M.A.I. El-Shaarawi. A contribution to the numerical solution of developing laminar flow in the entrance region of concentric annuli with rotation inner walls. *Journal of Fluids Engineering*, pages 333–340, December 1974.

[73] M.S. Bhatti and C.W. Savery. Heat transfer in the entrance region of a straight channel: laminar flow with uniform wall heat flux. Paper 76-HT-20, ASME-AIChE Heat Transfer Conference, St. Louis, MO, August 1976.

[74] G.S. Beavers, E.M. Sparrow, and R.A. Magnuson. Experiments on hydrodynamically dveloping flow in rectangular ducts of arbitrary aspect ratio. *International Journal of Heat and Mass Transfer*, 15:689–70, 1970.

[75] R.H. Larson and H.H. Richardson. A preliminary study of whirl instability for pressurized gas bearings. *Journal of Basic Engineering*, pages 522–520, December 1962.

[76] N. Savoulides. Low order models for hybrid gas bearings. S.M. thesis, Massachusetts Institute of Technology, Department of Aeronautics and Astronautics, February 2000.

[77] R.C. DiPrima and J.T. Stuart. Flow between eccentric rotating cylinders. *Journal of Lubrication Technology*, 94:266–274, July 1972.

[78] M.B. Banerjee, R.G. Shandil, S.P. Katyal, G.S. Dube, T.S. Pal, and K Banerjee. A nonlinear theory of hydrodynamic lubrication. *Journal of Mathematical Analysis and Applications*, 117(1):48–56, July 1986.

[79] C-H Chen and C-K Chen. The influence of fluid inertia on the operating characteristics of finite journal bearings. *Wear*, 131:229–240, 1989.

[80] G.I. Taylor. Stability of a viscous liquid contained between two rotating cylinders. *Philosophical Transactions, Series A.*, 223:289–343, 1923.

[81] V.N. Constantinescu. Analysis of bearings operating in turbulent regime. *Journal of Basic Engineering*, pages 139–151, March 1962.

[82] W.A. Gross, L.A. Matsch, V. Castelli, A. Eschel, J.H. Vohr, and M. Wildmann. *Fluid Film Lubrication*. Wiley-Interscience, New York, 1980.

[83] F.F. Hatay, S. Biringen, E. Erlebacher, and W.E. Zorumski. Stability of high-speed compressible rotating Couette flow. *Physics of Fluids A*, 5(2):393–404, February 1993.

[84] H-C Kao. A theory of self-acting, gas-lubricated bearings with heat transfer through surfaces. *Journal of Basic Engineering*, pages 324–328, June 1963.

[85] G.A. Bird. *Molecular Gas Dynamics and the Direct Simulation of Gas Flows*. Oxford Engineering Science. Oxford University Press, New York, NY, 1994.

[86] S.A. Schaff and P.L. Chambre. *Fundamentals of Gas Dynamics*, chapter H. Princeton University Press, Princeton, NJ, 1958.